MPM SCIENTIFIC JOURNAL

ISSN 1605-2730
E-ISSN 1605-8119

MATERIALS PHYSICS AND MECHANICS

Vol. 53, No. 5, 2025

MATERIALS PHYSICS AND MECHANICS

"Materials Physics and Mechanics" Editorial Office:
Phone: +7(812)552 77 78, ext. 224 **E-mail:** mpmjournal@spbstu.ru **Web-site:** http://www.mpm.spbstu.ru

International scientific journal "**Materials Physics and Mechanics**" is published by Peter the Great St. Petersburg Polytechnic University in collaboration with Institute for Problems for Mechanical Engineering in the Russian Academy of Sciences in both hard copy and electronic versions. The journal provides an international medium for the publication of reviews and original research papers written in English and focused on the following topics:

- Mechanics of composite and nanostructured materials.
- Physics of strength and plasticity of composite and nanostructured materials.
- Mechanics of deformation and fracture processes in conventional materials (solids).
- Physics of strength and plasticity of conventional materials (solids).
- Physics and mechanics of defects in composite, nanostructured, and conventional materials.
- Mechanics and physics of materials in coupled fields.

Owner organizations: Peter the Great St. Petersburg Polytechnic University; Institute of Problems of Mechanical Engineering RAS.

Materials Physics and Mechanics is indexed in Chemical Abstracts, Cambridge Scientific Abstracts, Web of Science Emerging Sources Citation Index (ESCI) and Elsevier Bibliographic Databases (in particular, SCOPUS).

МЕХАНИКА И ФИЗИКА МАТЕРИАЛОВ

Materials Physics and Mechanics

Том 53, номер 5, 2025 год

Учредители:
ФГАОУ ВО «Санкт-Петербургский политехнический университет Петра Великого»
ФГБУН «Институт проблем машиноведения Российской академии наук»

Тел.: +7(812)552 77 78, доб. 224 **E-mail:** mpmjournal@spbstu.ru **Web-site:** http://www.mpm.spbstu.ru

Тематика журнала

Международный научный журнал "Materials Physics and Mechanics" издается Санкт-Петербургским политехническим университетом Петра Великого в сотрудничестве с Институтом проблем машиноведения Российской академии наук в печатном виде и электронной форме. Журнал публикует обзорные и оригинальные научные статьи на английском языке по следующим тематикам:

- Механика композиционных и наноструктурированных материалов.
- Физика прочности и пластичности композиционных и наноструктурированных материалов.
- Механика процессов деформации и разрушения в традиционных материалах (твердых телах).
- Физика прочности и пластичности традиционных материалов (твердых тел).
- Физика и механика дефектов в композиционных, наноструктурированных и традиционных материалах.
- Механика и физика материалов в связанных полях.

Редколлегия принимает статьи, которые нигде ранее не опубликованы и не направлены для опубликования в другие научные издания. Все представляемые в редакцию журнала "Механика и физика материалов" статьи рецензируются. Статьи могут отправляться авторам на доработку. Не принятые к опубликованию статьи авторам не возвращаются.

Журнал "Механика и физика материалов" ("Materials Physics and Mechanics") включен в систему цитирования Web of Science Emerging Sources Citation Index (ESCI), SCOPUS и РИНЦ.

Contents

MATERIALS PHYSICS AND MECHANICS REVIEW

Submitted: August 19, 2025 **Revised: September 8, 2025** **Accepted: September 25, 2025**

Micromechanics of misfit stress relaxation in heterogeneous crystalline nanostructures: a review

M.Yu. Gutkin [1–3]✉, A.L. Kolesnikova [1,2], S.A. Krasnitckii [2], K.N. Mikaelyan [1], D.A. Petrov [1], A.E. Romanov [2,4], A.M. Smirnov [2]

[1] Institute for Problems in Mechanical Engineering, Russian Academy of Sciences, St. Petersburg, Russia

[2] ITMO University, St. Petersburg, Russia

[3] Peter the Great St. Petersburg Polytechnic University, St. Petersburg, Russia

[4] Ioffe Institute, St. Petersburg, Russia

✉ m.y.gutkin@gmail.com

ABSTRACT

Theoretical models of misfit stress relaxation in heterogeneous crystalline nanostructures are reviewed in brief. It is shown that the main channel of relaxation is the formation of misfit dislocations. Some mathematical tools for continuum modeling of misfit stress relaxation through generation of discrete dislocations in spherical and cylindrical nanostructures are considered with special attention to the strain energies of the dislocations and the energies of elastic interaction between them. The critical conditions and energy barriers for the formation of prismatic dislocation loops and straight edge misfit dislocations in core-shell nanoparticles and nanowires with various types of cores, in Janus nanoparticles and nanowires, in axially inhomogeneous nanowires with transverse interfaces, and in free-standing composite nanolayers are discussed.

KEYWORDS

misfit stress • heterogeneous nanostructures • stress relaxation • misfit dislocations • Janus nanoparticles Janus nanowires • free-standing composite nanolayers • dislocation loops core-shell nanoparticles core-shell nanowires

Funding. *The authors are thankful to the Ministry of Education and Science of the Russian Federation for support under the state assignment No. 124041100008-5 for the Institute for Problems in Mechanical Engineering of the Russian Academy of Sciences.*

Citation: Gutkin MYu, Kolesnikova AL, Krasnitckii SA, Mikaelyan KN, Petrov DA, Romanov AE, Smirnov AM. Micromechanics of misfit stress relaxation in heterogeneous crystalline nanostructures: a review. *Materials Physics and Mechanics*. 2025;53(5): 1–34.
http://dx.doi.org/10.18149/MPM.5352025_1

Introduction

Heterogeneous crystalline nanostructures serve as the basis of modern devices in nano- and microelectronics, optoelectronics, photonics, etc. It is well known that their physical properties and performance characteristics strongly depend on elastic misfit strains caused by differences in crystal lattice parameters. Under certain conditions, the misfit strains and stresses relax through the formation of various defects [1–5], which can lead to a significant deterioration in the properties of nanostructures. The most common way of such relaxation is the formation of misfit dislocations (MDs) at the interfaces. Theoretical and experimental studies of relaxation processes with the formation of MDs

have been carried out since the mid-twentieth century (see, for example, some earlier papers [6,7] and more recent books [8–13] and reviews [14–27]). However, the discussion of the sources, mechanisms, and critical conditions for the appearance of MDs in real inhomogeneous crystalline nanostructures is still of great interest [25–27].

The present paper offers a brief overview of very recent theoretical models of misfit stress relaxation in inhomogeneous crystalline nanostructures – composite nanoparticles, nanowires and nanolayers.

Mathematical tools for continuum modeling of misfit stress relaxation through generation of discrete dislocations

The invention and comparison of different relaxation micromechanisms lead to the conclusion that, in the vast majority of cases, the main channel of relaxation is the formation of various dislocation configurations [1,2,28]. To determine and analyze the critical conditions for their formation, some novel mathematical tools were developed.
In particular, new analytical solutions of the boundary problems in the theory of elasticity for circular prismatic dislocation loops in a hollow elastic sphere [29] and in an elastic cylinder [30] were obtained. Solutions were found for the strain energy of such loops [29,30] and for the energies of pair elastic interaction between them [30,31]. The stress fields and strain energy of a circular prismatic dislocation loop surrounding a cylindrical cavity in an infinite elastic medium were calculated [32] as well. All these solutions were found by using the classical methods of the elasticity theory, which were described in detail by Lurie [33]. Since the analytical formulas for the elastic fields are rather cumbersome, here we show the expressions for strain and interaction energies only that are of primary importance for theoretical modeling of the misfit-stress relaxation micromechanisms.

In the case of a circular prismatic dislocation loop placed axisymmetrically in a hollow elastic sphere (Fig. 1(a)), the elastic strain energy of the system is given by the superpositions [29]:

$$E_{\text{el}} = {}^{\infty}E - \pi b \int_0^c \tilde{\sigma}_{zz}|_{z=z_0} r dr, \; |z_0| \geq a_p, \tag{1}$$

$$E_{\text{el}} = {}^{\infty}E - \frac{Gb^2 c_p^2}{(1-\nu)c} \mathrm{D}\left(\frac{c_p}{c}\right) - \pi b \int_0^c \tilde{\sigma}_{zz}|_{z=z_0} r dr, \; |z_0| < a_p, \tag{2}$$

where ${}^{\infty}E$ is the elastic strain energy of the loop in an infinite elastic medium, b is the Burgers vector magnitude of the loop, c is the loop radius, z_0 is its position in the sphere, a_p is the radius of the cavity in the center of the sphere, G and ν are the shear modulus and the Poisson ratio, respectively, of the sphere material, $c_p = (a_p^2 - z_0^2)^{1/2}$, $\mathrm{D}(k) = \int_0^{\pi/2} \sin^2 t \, (1 - k^2 \sin^2 t)^{-1/2} dt$ is the elliptic integral [34], and $\tilde{\sigma}_{zz}$ is the axial component of the additional stress tensor that provides the fulfilment of traction-free boundary conditions on the inner and outer surfaces of the hollow sphere.

The elastic strain energy ${}^{\infty}E$ reads [35,36]:

$${}^{\infty}E = \frac{\pi G b^2 c}{2(1-\nu)} J(1,1;0)|_{r=c-r_{core}, z=z_0}, \tag{3}$$

where $J(1,1;0)|_{r=c-r_{core},z=z_0} = \int_0^{\infty} J_1(\kappa) J_1(\kappa(1 - r_{core}/c)) d\kappa$ is the Lipschitz-Hankel integral [37], $J_1(t)$ is the Bessel function of the first order, and r_{core} is the dislocation core radius. When $c >> r_{core}$, Eq. (3) is well approximated by the following equation:

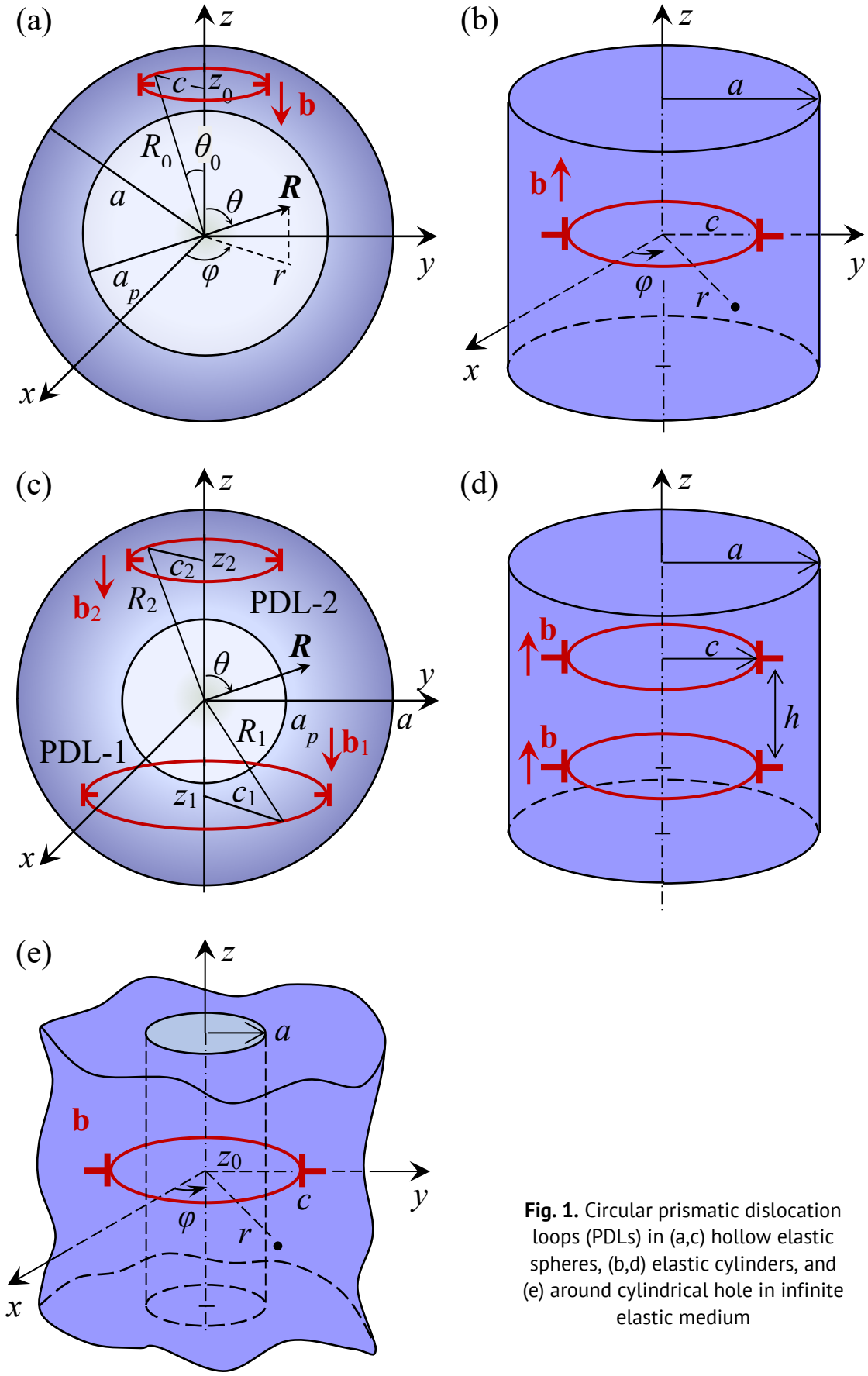

Fig. 1. Circular prismatic dislocation loops (PDLs) in (a,c) hollow elastic spheres, (b,d) elastic cylinders, and (e) around cylindrical hole in infinite elastic medium

$$^{\infty}E = \frac{Gb^2c}{2(1-\nu)}\ln\left(\frac{8c}{r_{core}} - 2\right). \quad (4)$$

The additional axial stress $\tilde{\sigma}_{zz}$ [29] is:

$$\tilde{\sigma}_{zz} = \tilde{\sigma}_{RR}\cos^2\theta + \tilde{\sigma}_{\theta\theta}\sin^2\theta - \tilde{\sigma}_{R\theta}\sin 2\theta, \quad (5)$$

with $\tilde{\sigma}_{RR} = 2G\sum_{k=0}^{\infty}\Big[A_k^{(1)}(k+1)(k^2-k-2-2\nu)R^k + B_k^{(1)}k(k-1)R^{k-2} - \frac{C_k^{(2)}k}{R^{k+1}}(k^2+3k-2\nu) + \frac{D_k^{(2)}(k+1)(k+2)}{R^{k+3}}\Big]P_k(\cos\theta)$, $\tilde{\sigma}_{R\theta} = 2G\sum_{k=0}^{\infty}\Big[A_k^{(1)}(k^2+2k-1+2\nu)R^k + B_k^{(1)}(k-1)R^{k-2} + \frac{C_k^{(2)}}{R^{k+1}}(k^2-2+2\nu) - \frac{D_k^{(2)}(k+2)}{R^{k+3}}\Big]\frac{dP_k(\cos\theta)}{d\theta}$, $\tilde{\sigma}_{\theta\theta} = 2G\sum_{k=0}^{\infty}\Big\{\Big[-A_k^{(1)}(k+1)(k^2+4k+2+2\nu)R^k - B_k^{(1)}k^2R^{k-2} + \frac{C_k^{(2)}k}{R^{k+1}}(k^2-2k-1+2\nu) - \frac{D_k^{(2)}(k+1)^2}{R^{k+3}}\Big]P_k(\cos\theta) - \Big[A_k^{(1)}(k+5-4\nu)R^k + B_k^{(1)}R^{k-2} + \frac{C_k^{(2)}}{R^{k+1}}(-k+4-4\nu) + \frac{D_k^{(2)}}{R^{k+3}}\Big]\frac{dP_k(\cos\theta)}{d\theta}\cot\theta\Big\}$.

Here R is the radial coordinate (see Fig. 1(a)), θ is the polar angle, and $P_k(t)$ are the Legendre polynomials. The coefficients $A_k^{(1)}, B_k^{(1)}, C_k^{(2)}$, and $D_k^{(2)}$ are found from the free-traction boundary conditions of the problem [29].

The graphical representation of the elastic strain energy E_{el} is given in [29]. When a circular prismatic dislocation loop is placed axisymmetrically in an elastic cylinder (Fig. 1(b)), the elastic strain energy of the system is given by the superposition [30]:

$$E_{el} = {}^{\infty}E - \frac{Gb^2at^2}{1-\nu}\int_0^{\infty}\frac{s^2t^2I_0^2(ts)+wI_1^2(ts)-2stI_1(ts)I_0(ts)[wI_1(s)K_1(s)+s^2I_0(s)K_0(s)]}{s^2I_0^2(s)-wI_1^2(s)}ds, \quad (6)$$

where $t = c/a$, $w = s^2 + 2(1-\nu)$, $I_{0,1}(\kappa)$ and $K_{0,1}(\kappa)$ are the modified Bessel functions of the first kind and the Macdonald functions, respectively.

The graphical representations of the elastic strain energy E_{el} for the circular prismatic dislocation loops in a hollow sphere and in a cylinder are given in [29,30].

The energy of pair elastic interaction between two coaxial circular prismatic dislocation loops (denoted as PDL-1 and PDL-2) in a hollow sphere (Fig. 1(c)) can be written as a sum [31]:

$$E_{int} = {}^{\infty}E_{int} + {}^{*}E_{int}, \quad (7)$$

where the first term, ${}^{\infty}E_{int}$, is the interaction energy of the loops in an infinite elastic medium, while the second term, ${}^{*}E_{int}$, is caused by the effect of the inner and outer free surfaces of the sphere.

As shown in [31], the term ${}^{\infty}E_{int}$ reads:

$$^{\infty}E_{int} = \frac{\pi Gb_1b_2}{1-\nu}\Big[rJ(1,1;0) + \frac{|z-z_2|}{c_2}rJ(1,1;1)\Big]\begin{matrix} r=c_1 \\ r=\xi \end{matrix}\Big| z=z_1, \quad (8)$$

where b_1 and b_2 are the Burgers vector magnitudes of the loops, c_1 and c_2 are their radii, z_1 and z_2 are their coordinates with respect to the sphere center (Fig. 1(c)); $\xi = 0$ for $z_1 \geqslant a_p$, and $\xi = \sqrt{a_p^2 - z_1^2}$ for $z_1 < a_p$, and $J(m,n;p) = \int_0^{\infty}J_m(\kappa)J_n(\kappa r/c_2)\exp[-\kappa|z-z_2|/c_2]\kappa^p d\kappa$.

The term ${}^{*}E_{int}$ is given by [31]:

$$^{*}E_{int} = \frac{\pi Gb_1b_2}{1-\nu}\sum_{n=0}^{+\infty}\Big[A_n^{(2)}\frac{2(n+1)(1+\nu-2n\nu-2n^2)}{2n-1}Q_{n,1} + A_{n+2}^{(2)}\frac{(n+2)(n+3)(2n^2+9n+7)}{2n+3}{}_{n,2}I_{int} + B_{n+2}^{(2)}(n+1)(n+2)Q_{n,1} - C_n^{(2)}\frac{2n[2n^2+2n(2-\nu)+1-3\nu]}{2n+3}T_{n,1} - -C_{n-2}^{(2)}\frac{n(n-2)(2n^2-7n+5)}{2n-1}T_{n,3} + D_{n-2}^{(2)}n(n-1)T_{n,3}\Big], \quad (9)$$

where $A_n^{(2)}$, $B_n^{(2)}$, $C_n^{(2)}$, and $D_n^{(2)}$ are the coefficients determined in [29] from the boundary conditions on the free inner and outer spherical surfaces, $Q_{n,l}$ and $T_{n,l}$ are the following polynomials:

$$Q_{n,l} = \sum_{s=0}^{[n/2]} \frac{(-1)^s}{2^{n(s+l)}} \binom{n}{s} \binom{2n-2s}{n} z_1^{n-2s} (R_1^{2(s+l)} - \zeta^{2(s+l)}), \tag{10a}$$

$$T_{n,l} = \sum_{s=0}^{[n/2]} \frac{(-1)^s}{2^{n(-2k+2s+l)}} \binom{n}{s} \binom{2n-2s}{n} z_1^{n-2s} (R_1^{-2k+2s+l} - \zeta^{-2k+2s+l}). \tag{10b}$$

Here $[n/2]$ denotes the greatest integer $\leq n/2$, $\binom{n}{s}$ are the binomial coefficients, and $\zeta = z_1$ for $z_1 \geqslant a_p$, and $\zeta = a_p$ for $z_1 < a_p$.

In a cylinder of radius a (Fig. 1(d)), the energy of pair elastic interaction between two identical axisymmetric circular prismatic dislocation loops of radius c with the Burgers vector magnitude b and spacing h is given by the sum (7), the terms of which can be written as follows [30]:

$${}^{\infty}E_{\text{int}} = \frac{\pi G b^2 c}{1-\nu} \left(J(1,1;0) \rightleftarrows|_{z=h} + \frac{h}{c} J(1,1;1)|_{z=h} \right), \tag{11a}$$

$${}^{*}E_{\text{int}} = \frac{2Gb^2ct}{1-\nu} \int_0^{\infty} \frac{s^2t^2I_0^2(ts) + wI_1^2(ts) - 2stI_1(ts)I_0(ts)[wI_1(s)K_1(s) + s^2I_0(s)K_0(s)]}{s^2I_0^2(s) - wI_1^2(s)} \cos\frac{hs}{a} ds\,. \tag{11b}$$

The interaction energies for the circular prismatic dislocation loops in a hollow sphere and in a cylinder are illustrated in detail by maps [31] and plots [30], respectively.

The total (including the energy of the dislocation core) energy of a circular prismatic dislocation loop surrounding a cylindrical cavity in an infinite elastic medium (Fig. 1(e)) [32] is:

$$E_t = \frac{Gb^2c}{2(1-\nu)} \left\{ \ln\frac{1.08\gamma c}{b} - \frac{2}{t}\mathbf{D}\left(\frac{1}{t}\right) - 2\int_0^{\infty} \{(-2A_1\nu + B_1\beta)[K_1(\beta) - tK_1(\beta t)] + \right.$$
$$\left. + A_1\beta[K_2(\beta) - t^2K_2(\beta t)]\} d\beta \right\}, \tag{12}$$

where the first term is the total energy of the loop in an infinite elastic medium [36,38], γ is the core energy parameter ranging from 1 for metals to 4 for semiconductors [38] and the coefficients A_1 and B_1 are given by the following equations [32]:

$$A_1 = \pm \frac{K_1(\beta t)[wI_1(\beta)K_1(\beta) + \beta^2 I_0(\beta)K_0(\beta)] - \beta t K_0(\beta t)}{wK_1^2(\beta) - \beta^2 K_0^2(\beta)}, \tag{13a}$$

$$B_1 = \pm \left\{ \frac{tK_0(\beta t)[wI_1(\beta)K_1(\beta) + \beta^2 I_0(\beta)K_0(\beta) + 2 - 2\nu]}{wK_1^2(\beta) - \beta^2 K_0^2(\beta)} + \right.$$
$$\left. + \frac{K_1(\beta t)\{2(\nu-1)[\beta^2 I_0(\beta)K_0(\beta) + wI_1(\beta)K_1(\beta)] - w\}}{\beta[wK_1^2(\beta) - \beta^2 K_0^2(\beta)]} \right\}. \tag{13b}$$

Here $w = \beta^2 + 2(1-\nu)$.

The energy plots illustrating Eq. (12) are represented in Ref. [32] in detail.

Critical conditions for the onset of misfit dislocations in core-shell nanoparticles

Using the solutions for the self strain energies of circular prismatic dislocation loops placed in elastic bodies of different geometry (see the previous section), the critical conditions necessary for the formation of circular prismatic misfit dislocation loops (MDLs) at the interfaces in core-shell nanoparticles with different types of cores were determined. In particular, the critical conditions for the formation of MDLs in solid [39,40] and hollow [41] single-crystalline and in solid decahedral [42] spherical nanoparticles were considered. To model the latter, a new solution for the elastic fields of a wedge disclination in an elastic sphere [43] was used. The cases of cores in the form of a

solid [39,42] and hollow [41] sphere, as well as in the form of a hemisphere resting on the equatorial plane of a nanoparticle [40] were investigated.

Within the continuum approach, the calculation scheme was based on the assumption that the difference in the total energy of the system under study ΔE due to the onset of the first MDL can be approximated by the following general formula [44]:

$$\Delta E = E_{\mathrm{el}} + E_{\mathrm{c}} + E_{\mathrm{int}}, \tag{14}$$

where E_{el} is the elastic strain energy of the MDL in the system, E_{c} is the energy of the MDL core, and E_{int} is the energy of interaction of the MDL with the initial misfit stress in the system before the MDL appearance there.

The formation of the first MDL is energetically favorable if $\Delta E < 0$. Therefore, the equation $\Delta E = 0$ gives the critical conditions for its onset in the system. Since the energy difference ΔE (more precisely, its third term E_{int}) is always in linear proportion with the misfit parameter f (here we assume for definiteness that $f > 0$), this equation is always simply resolved with respect to a critical misfit f_c given by:

$$f_c = -\frac{E_{\mathrm{el}}+E_{\mathrm{c}}}{E^*_{\mathrm{int}}}, \tag{15}$$

where $E^*_{int} = E_{int}/f$. Thus, the critical (necessary) condition for the formation of the first MDL in the system can be written as $f > f_{\mathrm{c}}$. As a result, the analyzes of the system stability with respect to its transition from the coherent state (with no MDL) to the partly relaxed (semicoherent) state with a MDL comes down to studying the dependences of the critical misfit f_c on other parameters (geometric, material, etc.) of the system.

Consider, for example, the case of a spherically symmetric core-shell nanoparticle studied in [39]. It was assumed that the nanoparticle consisted of an elastically isotropic core and an elastically isotropic shell with identical elastic moduli but different lattice parameters a_1 and a_2 (Fig. 2(a)). The lattice misfit was defined by the parameter $f = 2(a_1 - a_2)/(a_1 + a_2) > 0$. The outer and inner radii of the shell were denoted by a and R_0, respectively. During the coherent growth of the shell on the core, misfit strains and stresses should appear in the core-shell nanoparticle [1,2]. For some values of the system parameters f, a, and R_0, the interface was supposed to transform into a semicoherent state corresponding to the formation of a misfit dislocation at it. Owing to the spherical

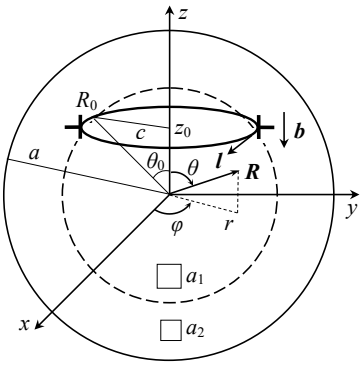

Fig. 2. Model of a circular MDL with the Burgers vector **b** and the tangent vector ***l*** at the interface in a core-shell nanoparticle. The spherical (R, φ, θ), cylindrical (r, φ, z) and Cartesian (x, y, z) coordinate systems are shown. The geometric parameters of the system are the nanoparticle radius a, the nanoparticle core radius R_0, the MDL radius c, and the MDL coordinate z_0. The lattice parameters a_1 and a_2 satisfy the inequality $a_1 > a_2$. Adopted from [39]

symmetry of the system, it was expected the formation of a vacancy (for $f > 0$) MDL around the core, which would partially compensate the lattice misfit. It is worth noting that earlier this problem got an approximate solution [2,12] for the case when the MDL was located in the equatorial plane of the nanoparticle and the core and shell were characterized by different elastic moduli.

In the elastically homogeneous case [39], the first term $E_{\rm el}$of the energy difference ΔE given by Eq. (14) can be derived from Eq. (1) in the limiting case of $a_p \to 0$. The second and third terms of ΔE are [39]:

$$E_{\rm c} \approx \frac{Gcb^2 Z}{2(1-\nu)}, \tag{16}$$

$$E_{\rm int} = -\frac{4\pi}{3}\frac{1+\nu}{1-\nu} Gbc^2 f\left(1 - \frac{{R_0}^3}{a^3}\right), \tag{17}$$

where $Z = \ln\alpha$ and the parameter α can vary in the range from 1 to 4 when $r_{core} = b$ [38]. In numerical calculations of [39], it was assumed that $Z = 1$.

Introduction of Eq. (1) at $a_p \to 0$ with Eqs. (4), (5), (16) and (17) to Eq. (15) gave an analytical formula for the critical misfit f_c [39]. Figure 3 shows the dependences of f_c on the principal geometric parameters of the system: (a) the normalized position z_0/R_0 of the MDL for the two different outer radii of the nanoparticles $a = 50b$ (solid curves) and $200b$ (dashed curves) with different values of the normalized core radius R_0/a and (b) the normalized core radius R_0/a for different values of the nanoparticle radius a at $z_0 = 0$ (here the solid and dashed curves correspond to the strict [39] and approximate [2,12] solutions, respectively). Each of these curves separates the phase space (R_0/a, f_c) into two regions. In the region under the curve, the MDL formation is energetically unfavorable, while in the region above the curve, it is energetically favorable. As is seen from Fig. 3(a), for any value of R_0/a, the minimum value of f_c is reached for the MDL position in the equatorial plane of the nanoparticle ($z_0 = 0$). Therefore, the first MDLs are expected to form in equatorial sections of the nanoparticles.

In Fig. 3(b), the dashed curves correspond to the approximate solutions obtained in [2,12] for a thin shell on a massive core ($R_0/a \to 1$) and for a massive shell on a small core ($R_0/a \ll 1$). It is seen that the strict solution (15) coincides almost completely with the approximate solution for large nanoparticles and differs significantly from it for small nanoparticles, when the approximate solution somewhat overestimates the critical misfit parameter f_c.

For a fixed misfit parameter f, which, in the diagram (R_0/a, f_c), is represented by the horizontal line, the points of intersection $f = f_c$ determine the critical values of the normalized core radius $\tilde{R}_0 = R_0/a$. The critical normalized radii $\tilde{R}_{0,\,c1}$ and $\tilde{R}_{0,\,c2}$ are such that the generation of an MDL is possible only in the range $\tilde{R}_{0,\,c1} < \tilde{R}_0 < \tilde{R}_{0,\,c2}$ and impossible neither for the extremely small core ($\tilde{R}_0 < \tilde{R}_{0,\,c1}$) nor for the extremely thin shell ($\tilde{R}_0 > \tilde{R}_{0,\,c2}$). For example, at $f_c = 0.01$ and $a = 200b$, the critical values of the normalized radii of the cores are $\tilde{R}_{0,c1} \approx 0.225$ and $\tilde{R}_{0,c2} \approx 0.935$ (Fig. 3(b)). In absolute units, these estimates give $R_{0,c1} \approx 45b$ and $R_{0,c2} \approx 187b$.

It is also seen from Fig. 3(b) that, for a given particle size, there is a minimum critical misfit $f_{c,\min}$, such that at $f < f_{c,\min}$, in the particle with a radius a the MDL generation is energetically unfavorable for any value of the ratio R_0/a. For example, $f_{c,\min} \approx 0.005$ for the curve with $a = 200b$ and $f_{c,\min} \approx 0.014$ for the curve with $a = 50b$.

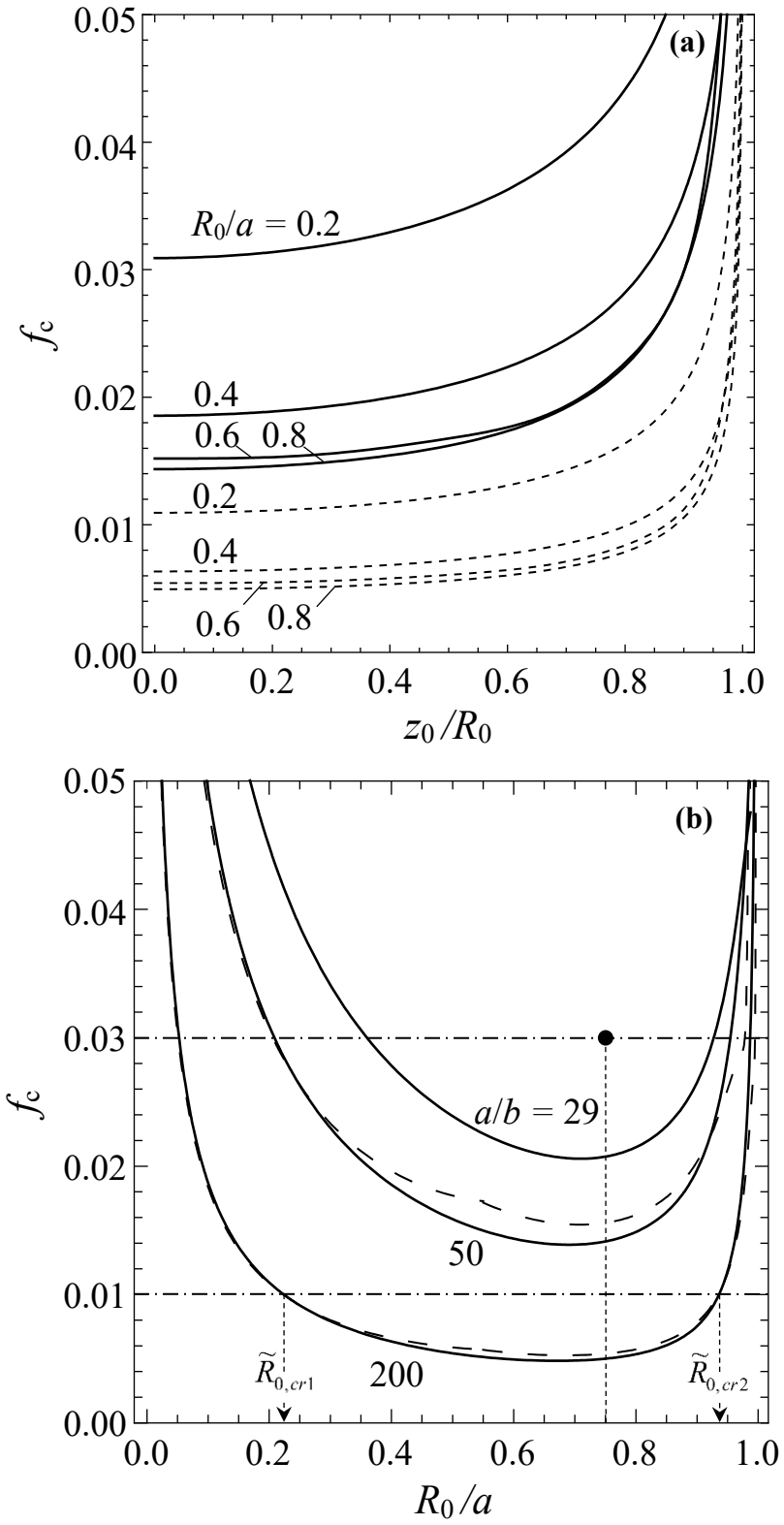

Fig. 3. Dependences of the critical misfit f_c on the geometric parameters of the system: (a) the normalized MDL position z_0/R_0 for the nanoparticle radii $a = 50b$ (solid curves) and $200b$ (dashed curves) with different values of the normalized core radius R_0/a and (b) the normalized core radius R_0/a for different values of the nanoparticle radius a at $z_0 = 0$ (the solid and dashed curves correspond to the strict [39] and approximate [2,12] solutions, respectively). The point (0.75, 0.03) corresponds to the experimental observation of a perfect MD in the Au-$FePt_3$ nanoparticle with radius $a = 29b$ [45]. Adopted from [39]

The point with coordinates (0.75, 0.03) in Fig. 3(b) corresponds to the experimental observation of a perfect edge MD in the Au-$FePt_3$ nanoparticle with radius a = 29b [45]. It is seen that this point lies in the region $f > f_c(R_0/a)$ where the generation of MDLs was predicted by the calculations [39].

A similar problem for a hollow core-shell nanoparticle was solved in work [41]. Figure 4 shows the corresponding model of a circular MDL placed at the core-shell interface in the plane $z = z_0$. In this case, the difference in the total energy of the system ΔE due to the onset of the first MDL was approximated by Eq. (14), in which the first term was given by Eqs. (1) and (2), the second term by Eq. (16) and the third term by [41]:

$$E_{int} = -\frac{4\pi}{3}\frac{1+\nu^2}{1-\nu}\left(1-\frac{R_0^3}{a^3}\right)\frac{1-(a_p/R_0)^3}{1-(a_p/a)^3}. \quad (18)$$

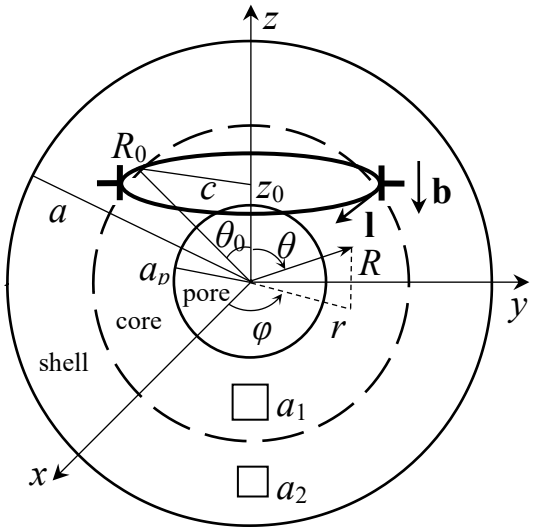

Fig. 4. Model of a circular MDL with the Burgers vector **b** and the tangent vector $\boldsymbol{l}$ at the interface in a hollow core-shell nanoparticle. The spherical (R, φ, θ), cylindrical (r, φ, z) and Cartesian (x, y, z) coordinate systems are shown. The geometric parameters of the system are the nanoparticle radius a, the nanoparticle core radius R_0, the pore radius a_p, the MDL radius c, and the MDL coordinate z_0. The lattice parameters a_1 and a_2 satisfy the inequality $a_1 > a_2$. Adopted from [41]

In the limit $a_p \to 0$, Eq. (18) transforms to Eq. (17). As a result, the critical condition for the MDL formation is given in this case by the inequality $f > f_c$, where the critical misfit f_c is determined by Eq. (15).

Figure 5(a) shows the dependence $f_c(z_0/R_0)$ for $a = 100b$, $R_0/a = 0.8$, and different values of the ratio a_p/a. It is seen that f_c increases both with z_0/R_0 and a_p/a ratios. It means that the most favorable position of the MDL is in the equatorial plane of a hollow core-shell nanoparticle as is also the case with solid core-shell nanoparticles [39]. It is also seen than both the MDL shift from the equatorial plane and pore growth in the core decrease the energetic preference of the MDL generation in hollow core-shell nanoparticles.

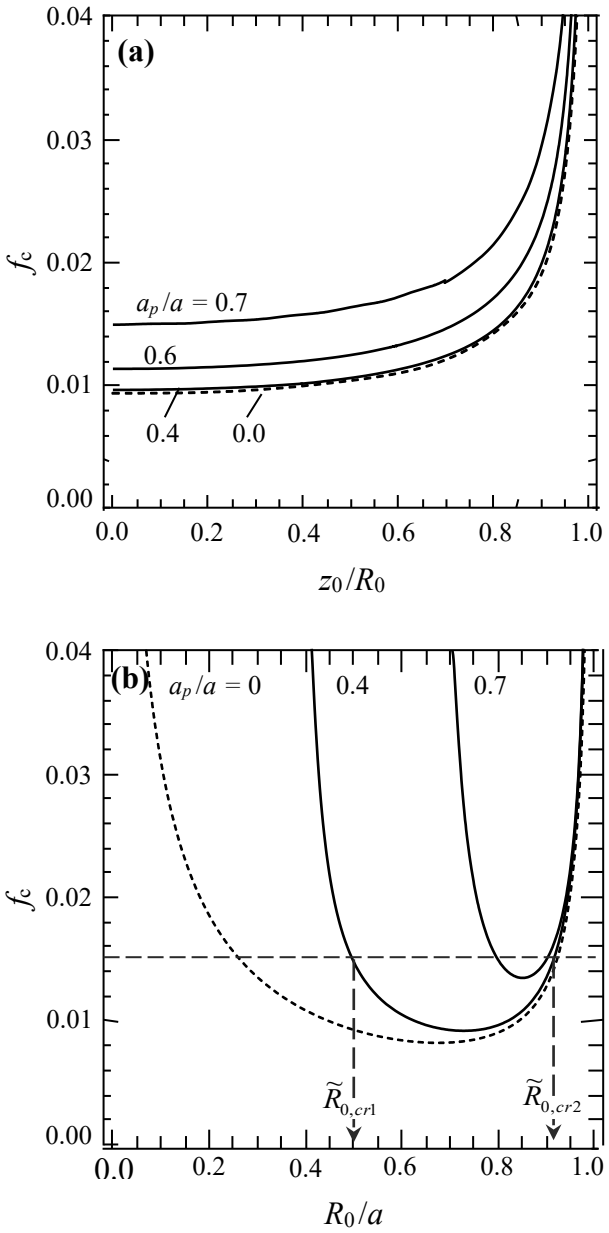

Fig. 5. Dependence of the critical misfit f_c of a hollow core-shell nanoparticle with outer radius $a = 100b$ on (a) the normalized MDL position z_0/R_0 for the fixed normalized core radius $R_0/a = 0.8$, and (b) the normalized core radius R_0/a for the equatorial position ($z_0 = 0$) of the MDL, for different values of the normalized pore radius a_p/a. The dashed curves correspond to full core-shell nanoparticles. Adopted from [41]

Figure 5(b) illustrates the effect of the $R_0/a = \tilde{R}_0$ ratio on the critical misfit f_c. Here the curves $f_c(\tilde{R}_0)$ were plotted for $a = 100b$, $z_0 = 0$, and different values of a_p/a. They have minima which give the minimal critical misfit $f_{c,\min}$ such that no MDL can form at $f < f_{c,\min}$for any $\tilde{R}_0$. For $f > f_{c,\min}$, there is a range $\tilde{R}_{0,\,c1} < \tilde{R}_0 < \tilde{R}_{0,\,c2}$, in which MDL generation is energetically favorable. When $\tilde{R}_0 < \tilde{R}_{0,\,c1}$ or $\tilde{R}_0 > \tilde{R}_{0,\,c2}$, the coherent state of the nanoparticle is more preferable. With raising *f*, this range increases. Similar results were reported earlier for MDLs in solid core-shell nanoparticles [39] (see also the above

discussion of Fig. 3(b)) and straight MDs in solid core-shell nanowires [46] and at the interface between a (nano)tube and surrounding infinite matrix [47]. As is seen, the pore strongly affects the curves $f_c(\tilde{R}_0)$: they become narrower with increasing the pore radius a_p, and $f_{c,min}$ increases as well. As a result, the range $(\tilde{R}_{0,c1}, \tilde{R}_{0,c2})$ decreases. Thus, the region of parameter values, in which the MDL formation is energetically favorable, drastically shrinks.

The most important practical issues from the model [41] are the dependences of the minimal critical misfit $f_{c,min}$ and the critical shell thickness $h_c = a(1 - \tilde{R}_{0,c2})$ on the ratio a_p/a (Fig. 6). It is seen from Fig. 6 that both $f_{c,min}$ and h_c weakly depend on the a_p/a ratio until it reaches the value of about 0.8. However, when $a_p/a > 0.8$, they drastically grow with a_p/a. The authors of [41] concluded on a great potential in developing coherent (MD free) hollow core-shell nanoparticles by using cores in the form of thin-wall shells with the inner-to-outer radii ratio larger than 0.8.

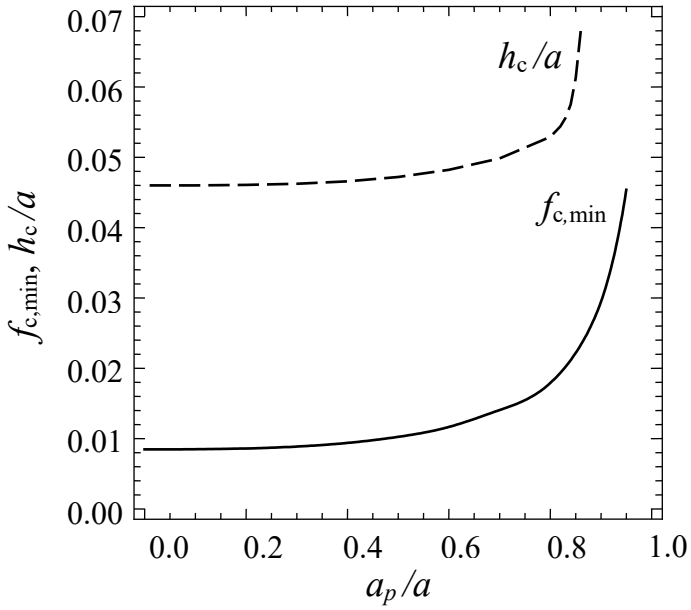

Fig. 6. Dependences of the minimal critical misfit $f_{c,min}$ and the critical shell thickness h_c (at $f = 0.02$) on the inner-to-outer radii ratio a_p/a for $a = 100b$ and $z_0 = 0$. Adopted from [41]

The solid and hollow core-shell nanoparticles considered in [39,41] were supposed single crystalline (solid and hollow SC-CSNPs). Krauchanka et al. [42] extended this energetic approach to the case of solid decahedral core-shell nanoparticles (Dh-CSNPs). Indeed, the most of bimetallic CSNPs contain noble metals (Au, Ag, Pt and Pd) whose nanoparticles are well known to be so-called pentagonal nanoparticles (PNPs) in the greater part of their populations.

PNPs are multiply-twinned crystalline particles in the shape of either decahedron or icosahedron, or of close morphologies [48–51]. As a result, PNPs possess five-fold symmetry axes that are absent in bulk single crystals and pass through quintuple junctions of twin boundaries. These axes can be described in terms of positive partial wedge disclinations (WDs). For example, decahedral particles (DhPs) contain one WD [52], while icosahedral particles (IcPs) contain six WDs [53]. Due to these WDs, PNPs are

elastically strained and store high strain energy that can relax through generation of various lattice defects [48,50,51].

The elastic model of a spherical DhP can be given by a partial positive WD piercing the elastic sphere [43]. In solid DhPs, the WD stress relaxation was shown to occur through the generation of axisymmetric circular PDLs [54]. For hollow DhPs, a model was suggested that described the formation of multiple cracks at the twin boundaries with subsequent agglomeration of the initial cracks into a unite five-foldstar crack [55].

For a Dh-CSNP that is a DhP covered with a shell of another crystalline material, the superpositions of the WD and misfit strains and stresses were expected [42]. The stress/strain state of a WD axially pierced an elastic sphere (Fig. 7(a)) was given in [43]. The authors [43] showed that in the area around the line of a positive WD is hydrostatically compressed, while the peripheral area of the sphere is hydrostatically stretched. They suggested that stress relaxation in the system could naturally include nucleation of vacancies at the stretched surface of the sphere, their migration to the compressed region around the WD line, and their coagulation with formation of a circular PDL of vacancy type [54].

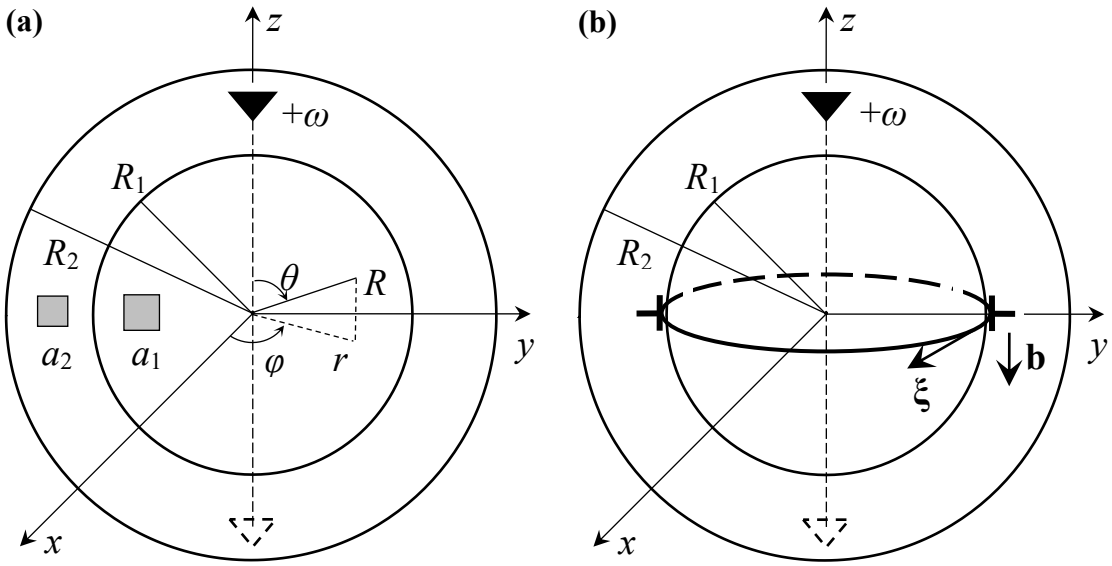

Fig. 7. Model of a Dh-CSNP in its (a) initial and (b) partially relaxed states. The Cartesian (x, y, z), cylindrical (r, φ, z) and spherical (R, ϑ, φ) coordinate systems are shown. Adopted from [43]

In a Dh-CSNP with $f > 0$ (Fig. 7(a)), the formation of such a PDL could be effective for both the WD and misfit stress/strain states (Fig. 7(b)). Since the equatorial planes are the most favorable positions for MDLs and PDLs in SC-CSNPs [39,41] and DhPs [54], respectively, it was suggested that the equatorial plane is the most favorable position of a MDL in a Dh-CSNP, too [43]. In this case, the total energy change caused by the partial relaxation in a Dh-CSNP reads [43]:

$$\Delta E = E_{\mathrm{c}} + E_{\mathrm{el}} + E_{\mathrm{int},\nabla} + E_{\mathrm{int,f}} + E_{\mathrm{st}}, \tag{19}$$

where the first two terms are the core and strain energies of the MDL, respectively, as before; $E_{\mathrm{int}\nabla}$ and $E_{\mathrm{int,f}}$ are the energies of interaction of the MDL with the WD and

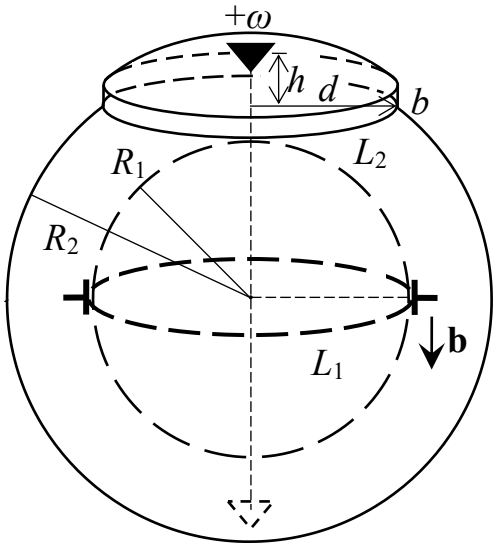

Fig. 8. Formation of a circular MDL of length L_1 with the Burgers vector **b** in the Dh-CSNP leads to the formation of a monolayer with a step of radius d, height b and length L_2 around a pole on the free surface of the shell. Adopted from [43]

misfit stresses, respectively; and E_{st} is the energy of the atomic step that forms on the Dh-CSNP free surface in the process of the generation of vacancies needed for the MDL creation (Fig. 8).

The interaction energy $E_{\text{int},\nabla}$ is [54]:

$$W_{\text{int},\nabla} = 2\pi DbR_1^2\omega \left[\nu \ln\frac{t}{2} + \frac{21+\nu(238+125\nu)}{30(7+5\nu)} - \frac{(7+\nu)(1+3\nu)}{8(7+5\nu)}t^2 - \right.$$
$$\left. - \sum_{m=2}^{+\infty}\left(\tilde{A}_m\frac{(2m+1)(2m^2+4m+1+\nu)}{m+1} + \tilde{B}_m\frac{2m}{t^2}\right) t^{2m}P_{2m}(0)\right]. \quad (20)$$

where R_1 and R_2 are the core and shell radii, respectively, of the Dh-CSNP (Fig. 7), $t = R_1/R_2$, ω is the strength of the WD, $\tilde{A}_m = \frac{\sigma_m - 2m\tau_m}{2s_m}$, $\tilde{B}_m = -\frac{p_m\sigma_m + 2q_m\tau_m}{2(2m-1)s_m}$, $\sigma_m = (2m - -1)(m+1)\tau_m - \frac{4m+1}{2m(2m+1)}$, $\tau_m = \frac{(1-2\nu)(4m+1)}{2(m-1)m(2m+1)(2m+3)}$, $s_m = 1+\nu+2m(1+2m+2\nu)$, $p_m = = 2\nu - 1 + 4m(1+m)$, $q_m = 1+\nu-4m^3+(3+2\nu)m$, and $m = 2,3,4, \ldots$.

The interaction energy $E_{\text{int,f}}$ is given by [54] $E_{\text{int,f}} = -(8/3)\pi^2 Df(1+\nu)bR_1^2(1-t^3)$. The surface step energy E_{st} was estimated as [54] $E_{\text{st}} \approx \kappa\pi Db^2R_1\sqrt{1-t^2/4}$ with $\kappa \leq 1$. It is worth noting that the terms like E_{st} have never been accounted for in previous theoretical models of MD formation. The authors [54] showed that it may give a strong effect on the critical conditions for this process.

When the critical conditions are formulated as in the aforementioned models [39,41] in terms of the misfit parameter value as $f > f_c$, where f_c is the minimal value of the lattice misfit for which the generation of a MDL becomes energetically favorable, the equation $\Delta E = 0$ gives [54]:

$$f_c = \frac{3(E_c + E_{\text{el}} + E_{\text{int},\nabla} + E_{\text{st}})}{8\pi^2(1+\nu)DbR_1^2(1-t^3)}. \quad (21)$$

Figure 9 shows the dependence of f_c on the ratio t for the following set of material parameters: $\alpha = e$ (an average value in the range from 1 to 5 [38]), $\kappa = 1$, $\omega = 7°20' \approx$ ≈ 0.128 rad, and $\nu = 0.3$, for three different values of the normalized shell radius

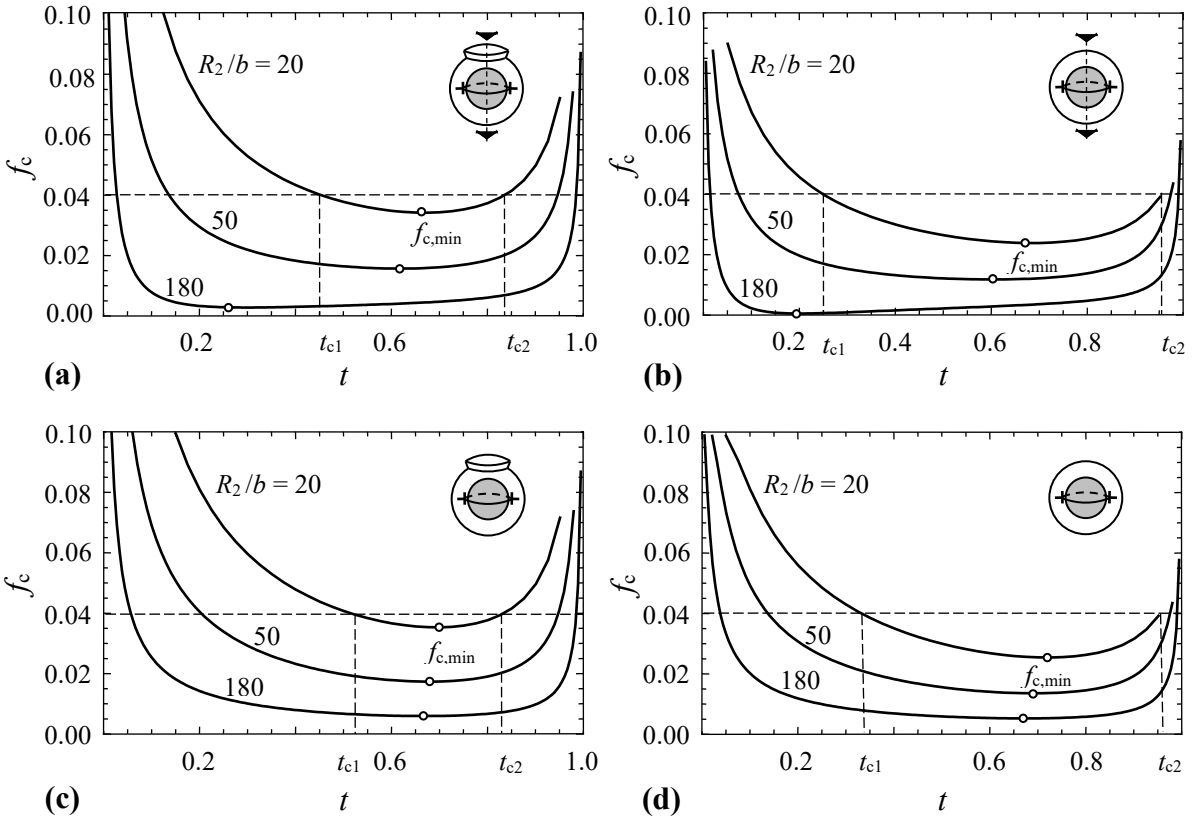

Fig. 9. The dependence of critical misfit parameter f_c on the ratio $t = R_1/R_2$ at $\alpha = e$ for nanoparticles of different size (R_2/b = 20, 50, and 180) and type, (a,b) Dh-CSNPs and (c,d) SC-CSNPs, with (a,c) and with no (b,d) account for the surface step energy. Adopted from [43]

$\frac{R_2}{b} = 20, 50$, and 180 in two cases: Fig. 9(a,b) for a Dh-CSNP (with $\omega = 0.128$ rad) and, for comparison, Fig. 9(c,d) for a SC-CSNP (with $\omega = 0$). Figures 9(a) and 9(c) illustrate the results obtained with taking into account the surface step energy term E_{st}, while Figs. 9(b) and 9(d) show those obtained without this term. One can see that the curves $f_c(t)$ are qualitatively similar for all the cases under consideration. They are also similar to the dependences calculated earlier in [39,41] (see Figs. 3(b) and 5(b)).

However, the values of the critical parameters $f_{c,min}$, t_{c1} and t_{c2} are quite different for these cases. For example, for Dh-CSNPs of radius $\frac{R_2}{b} = 20, 50$, and 180 (Fig. 9(a)), the minimum critical misfit $f_{c,min}$ ~ 0.034, 0.016, and 0.003, respectively, while in the case of SC-CSNPs of the same radii (Fig. 9(c)), $f_{c,min}$ ~ 0.036, 0.018, and 0.006, respectively. Thus, the relative difference in the $f_{c,min}$ values increase as ~ 5.9, 12.5, and 100 % with increasing value of R_2/b.

It is also seen that the interval $[t_{c1}, t_{c2}]$ where the MDL formation is energetically favorable for a given $f > f_{c,min}$ is also larger for Dh-CSNPs than for SC-CSNPs. For example, at $R_2/b = 20$ and $f = 0.04$, it is approximately $[0.45, 0.83]$ for Dh-CSNPs (Fig. 9(a)) and $[0.52, 0.83]$ for SC-CSNPs (Fig. 9(c)). As noted in [43], the interval widening in Dh-CSNPs results from the diminishing t_{c1}, while the value of t_{c2} remains practically the same for any fixed value of R_2/b. This means that t_{c1} is strongly affected by the

interaction of MDLs with WDs, modeling the five-fold symmetry axes in Dh-CSNPs, while t_{c2} is mainly controlled by the misfit relaxation in the Dh-CSNPs and SC-CSNPs.

The authors [43] also noted the different positions of the points of minimum of curves $f_c(t)$ for Dh-CSNPs and SC-CSNPs. For Dh-CSNPs, this position significantly shifts to the region of smaller t with an increase in R_2, from ~ 0.67 for $R_2 = 20b$ to ~ 0.26 for $R_2 = 180b$ (Fig. 9(a)). In contrast, this position remains almost the same, in the range of $t \approx 0.67 - 0.70$, for SC-CSNPs.

It was finally concluded [43] from Fig. 9 that Dh-CSNPs should be noticeably less stable with respect to the formation of MDLs than SC-CSNPs in the case of $f > 0$. The account for the surface step energy leads to significant correction of the $f_c(t)$ plots when the shell radius R_2 is relatively small, when the surface energy contribution E_{st} becomes comparable with other energy terms in Eqs. (19) and (21).

A comparison of the theoretical results [43] with experimental observations of perfect MDs in Dh-CSNPs and SC-CSNPs is shown in Fig. 10. In particular, Ding et al. [45] observed MDs in Au-$FePt_3$ Dh-CSNP and SC-CSNP with $f \approx 0.03$, $t \approx 0.67$ and 0.75, and $R_2 \approx 16b$ and $15b$, respectively. The corresponding blue and black points lie a little higher the blue and black curves $f_c(t)$ plotted at $\alpha = 1$ for these values of R_2, and well fall into the intervals $[t_{c1}, t_{c2}]$ for these curves at $f = 0.03$. Khanal et al. [56] observed three similar MDs in an Au-CuS_2 Dh-CSNP with $f \approx 0.11$, $t \approx 0.8$ and $R_2 \approx 74b$. The corresponding red point lies much higher the red curve $f_c(t)$ plotted at $\alpha = 1$ for this value of R_2, and obviously well falls into the interval $[t_{c1}, t_{c2}]$ for this curve at $f = 0.11$. Thus, the results of the theoretical model [43] were in a good accordance with available experimental observations of perfect MDs in Dh-CSNPs and SC-CSNPs.

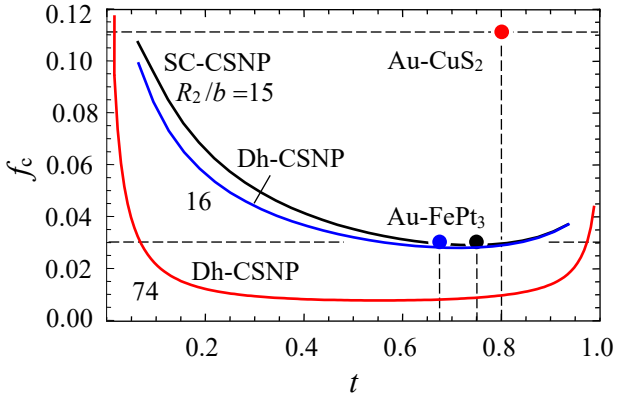

Fig. 10. Theoretical curves $f_c(t)$ for Dh-CSNPs with shell radii $R_2 = 16\,b$ (blue) and $74\,b$ (red), and SC-CSNPs with shell radius $R_2 = 15\,b$ (black), plotted for $\alpha = 1$. Experimental points (0.67, 0.03) and (0.75, 0.03) correspond to observation of perfect MDs in Au-$FePt_3$ Dh-CSNPs and SC-CSNPs, respectively [45]. Experimental point (0.8, 0.11) corresponds to observation of perfect MDs in an Au-CuS_2 Dh-CSNP [56]. Adopted from [43]

The case of a solid core in the form of a hemisphere resting on the equatorial plane of a SC-CSNP (Fig. 11) was investigated in [40]. As before, for definiteness, it was assumed that $a_1 > a_2$ and, therefore, $f > 0$. The misfit stress relaxation was supposed to occur through the transition of the SC-CSNP from the initial coherent state with no misfit defects (Fig. 11(a)) to a partly relaxed semi-coherent state, in which case a circular

prismatic MDL forms at the core-shell interface (Fig. 11(b)). The initial coherent strain/stress state in such a SC-CSNP was calculated by Kolesnikova at al. [57]. Based on this solution, the authors [40] assumed that, for $f > 0$, the MDL should be of vacancy type and could form from vacancies which nucleate on the free surface of the SC-CSNP, in the polar region of higher positive values of the elastic dilatation, and migrate to the dilatationally compressed core (see Fig. 4 in [57]).

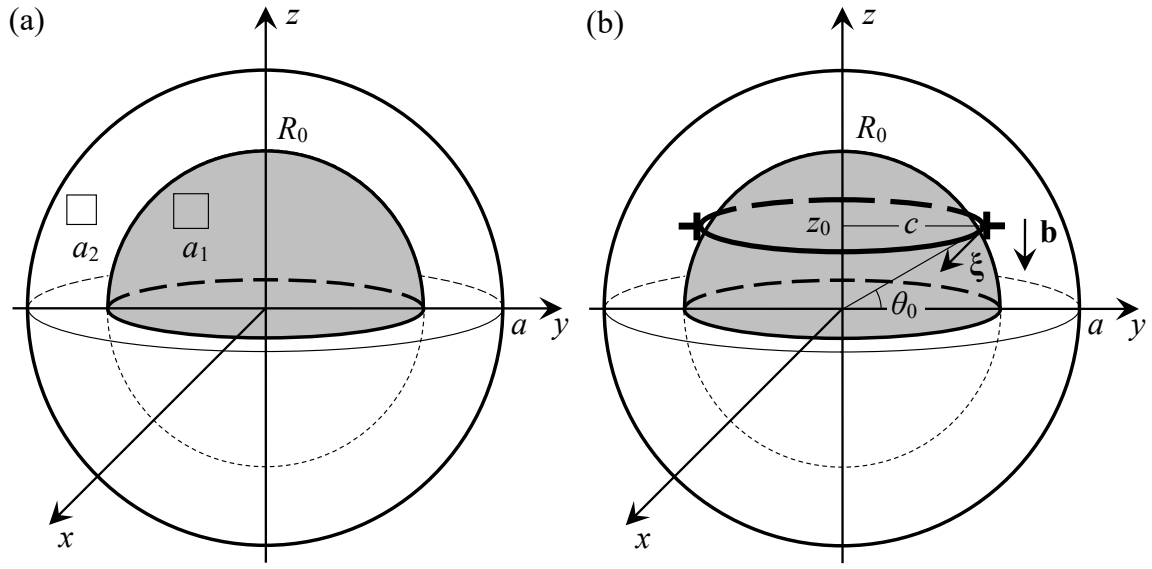

Fig. 11. Model of a SC-CSNP with an axisymmetrical semispherical core in its (a) initially coherent and (b) partially relaxed states. Adopted from [40]

The necessary condition for the MDL formation was given in [40] by the inequality $\Delta E < 0$, where the energy change ΔE is determined by Eq. (14). The first two terms on the right hand side of this equation are the strain and core energies, respectively, of the MDL as before, while the third term is the energy E_{int} of elastic interaction of the MDL with the misfit stress field in the SC-CSNP with a semispherical core. The latter was found as the work spent to generate the MDL in the axial misfit stress σ_{zz} through the integral [40]:

$$E_{\text{int}} = -\backslash\pi bz\,{}^{2}_{0}\int_0^{\theta_0}\sigma_{zz}(z=z_0)\frac{\sin\theta}{\cos^3\theta}d\theta\,, \qquad (22)$$

where b is the Burgers vector magnitude of the MDL, z_0 is the MDL position with respect to the equatorial plane of the SC-CSNP (Fig. 11(b)), and θ_0 is the angular coordinate of the MDL line.

The authors [40] calculated numerically the energy change ΔE for a model SC-CSNP with radius $a = 200b$ and Poisson ratio $\nu = 0.3$. Figure 12 shows the dependence of ΔE on the normalized coordinate z_0/R_0 of the MDL plane (here R_0 is the core radius) for different values of the misfit f and the ratio R_0/a .

In the case, when $f = 0.02$ and R_0/a is varied from 0.1 to 0.99 (Fig. 12(a)), the curves allow to predict the energetically favorable ($\Delta E < 0$) formation of the MDLs in SC-CSNPs with hemispherical cores of normalized radius $R_0/a = 0.2\ldots0.9$. The most favorable (optimal) position $z_{0,opt}$ of the MDL is clearly indicated by the minimum at the energy

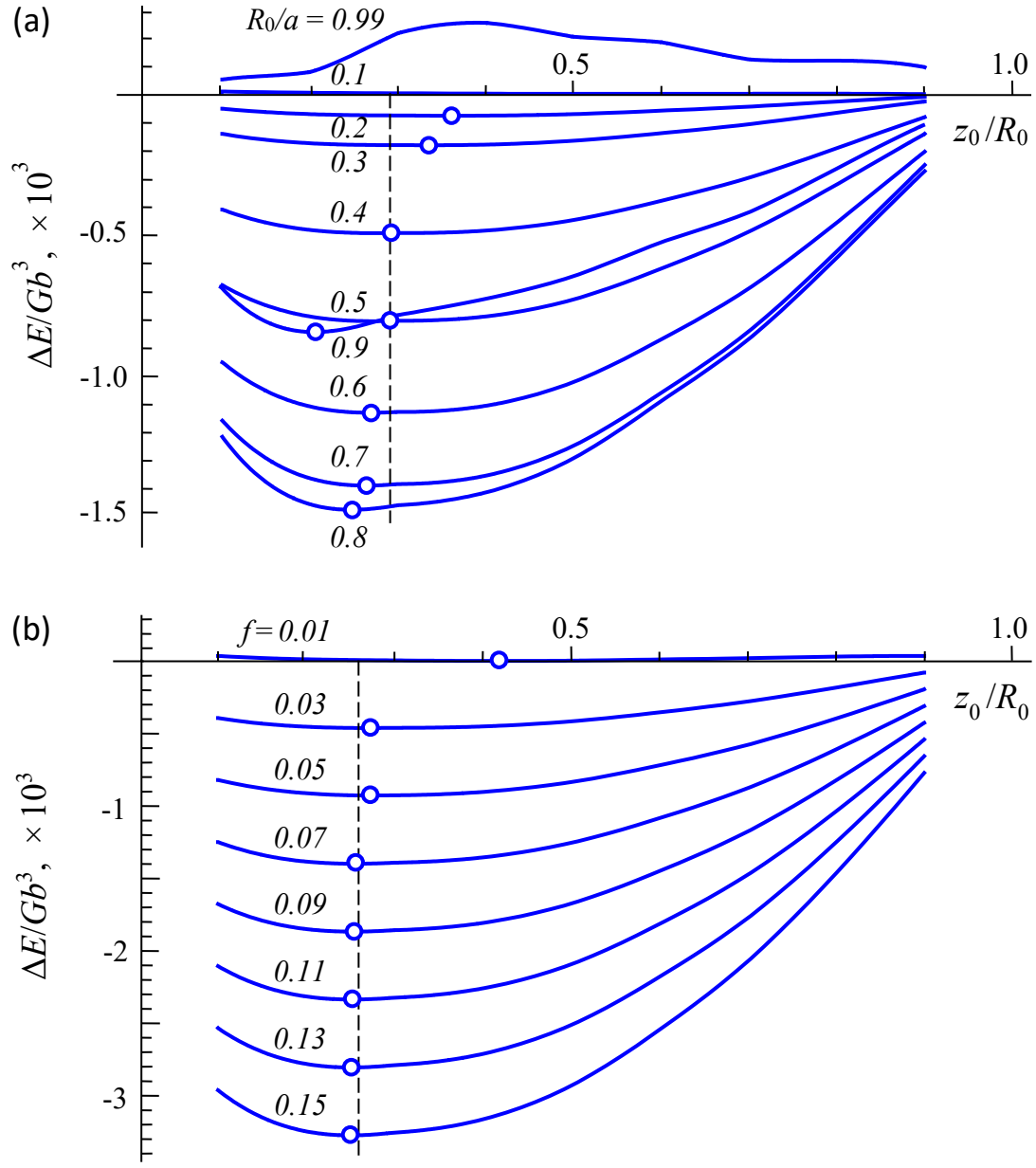

Fig. 12. Dependence of the energy change ΔE on the normalized coordinate of the MDL z_0/R_0 for (a) $f = 0.02$ and different values of the ratio R_0/a, and (b) $R_0/a = 0.3$ and different values of the misfit *f*. The small circles indicate the minima on the curves. Adopted from [40]

curves. For $R_0/a = 0.2$, it is $z_{0,opt} \approx 0.36R_0$; for $R_0/a = 0.3$, it is $z_{0,opt} \approx 0.33R_0$; for larger values of the ratio, $R_0/a = 0.4$ and 0.5, it remains approximately constant, $z_{0,opt} \approx 0.30R_0$; and then it slightly decreases again with R_0/a. Finally, at $R_0/a = 0.9$, it falls down to $z_{0,opt} \approx 0.20R_0$. For either very fine ($R_0/a = 0.1$) or very coarse ($R_0/a = 0.99$) cores, the MDL formation is not energetically favorable ($\Delta E \geq 0$). It was also noted in [40] that the energy gain $|\Delta E_{\min}|$, caused by the MDL generation, increases with the ratio R_0/a in its interval from 0.2 to 0.8 and then drastically drops at $R_0/a = 0.9$.

In the case, when $R_0/a = 0.3$ and *f* is varied from 0.01 to 0.15 (Fig. 12(b)), the misfit value $f = 0.01$ can be treated as the critical one for this value of the ratio R_0/a.

The corresponding curve has a minimum at $z_0/R_0 \approx 0.42$ where $\Delta E = 0$. At higher values of f (here from 0.03 to 0.15), $\Delta E < 0$ for any value of z_0/R_0. It is of interest that all these curves have minima approximately at the same point $z_0/R_0 \approx 0.26$. As it concluded in [40], for $R_0/a = 0.3$ and any $f \geq 0.02$ (see also Fig. 12(a)), the optimal position of the MDL is $z_{0,opt} \approx 0.26R_0$. It is also seen that the energy gain $|\Delta E_{\min}|$ monotonously increases with the misfit $f > f_c \approx 0.01$.

A detailed study of the optimal position $z_{0,opt}$ in dependence on the misfit f and the ratio R_0/a for $a = 200b$ and $\nu = 0.3$ (see Fig. 4 in [40]) showed that, for a wide range of the model parameters, $z_{0,opt}/R_0$ is close to 0.3. Then, taking $z_0/R_0 = 0.3$, the authors [40] considered the dependence of the energy change ΔE on the ratio R_0/a for different values of the misfit f in the interval from 0.001 to 0.030 (Fig. 13). The corresponding non-monotonous curves $\Delta E(R_0/a)$ may have one or two extremum points in dependence on f. When f is relatively small (here $f = 0.001$), the curve has a maximum (here at $R_0/a \approx 0.9$), and $\Delta E > 0$ for any value of R_0/a, which means that no MDL can form around the core. At a larger value of f (here at $f = 0.004$), the maximum shifts to the region of smaller R_0/a (here to the point $R_0/a \approx 0.46$), while a minimum appears on the curve (here at $R_0/a \approx 0.7$) , although $\Delta E > 0$ still always. Then, at a critical misfit value f_c (here $f_c = 0.0055$), the energy change ΔE becomes negative in the region of its minimum (here at $R_0/a \approx 0.74$) , which means that a MDL can form around the core in such a SC-CSNP. The positions of the maxima strongly depend on f, shifting to smaller values of R_0/a with increasing f, while the positions of the minima slightly shift to greater values of R_0/a, remaining however in the range from $R_0/a \approx 0.74$ to ≈ 0.78.

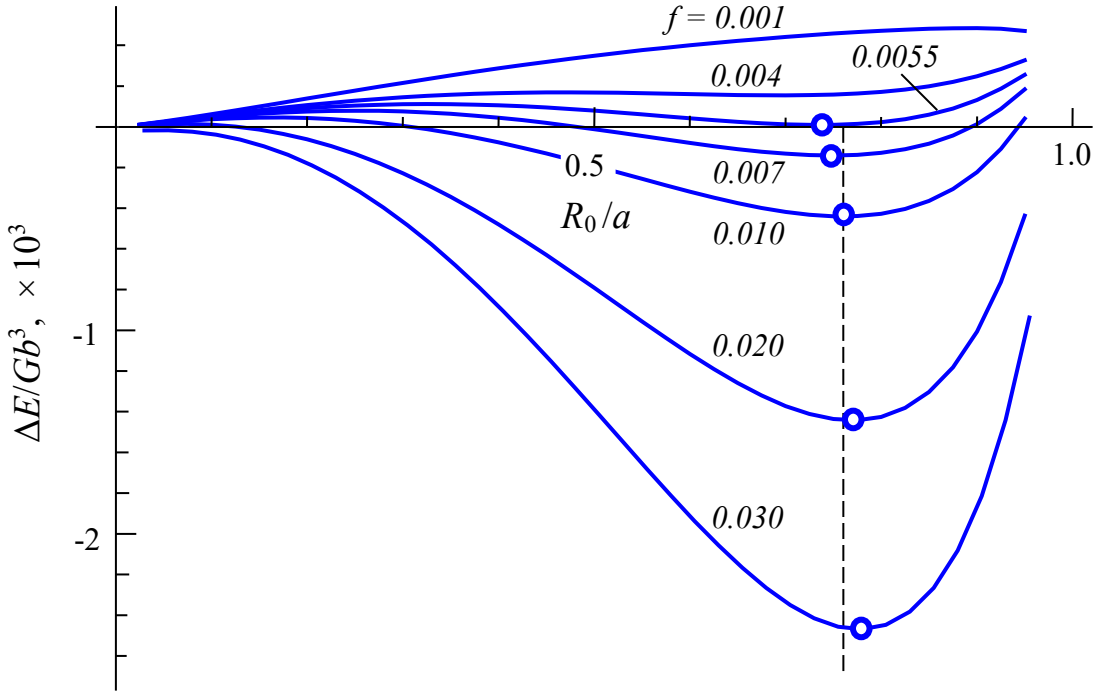

Fig. 13. Dependence of the energy change ΔE on the ratio R_0/a for the normalized position $z_0/R_0 = 0.3$ of the MDL and different values of the misfit strain f. Adopted from [40]

For $f > f_c$, there is an interval of R_0/a values, where $\Delta E < 0$, in which a MDL can form. Outside this interval, $\Delta E > 0$ and no MDL can nucleate. The boundaries of this interval can be considered as critical values of the ratio R_0/a, $(R_0/a)_{c1}$ and $(R_0/a)_{c2}$, for a given value of f. When f increases, $(R_0/a)_{c1}$ decreases, while $(R_0/a)_{c2}$ increases. These conclusions of [40] are rather similar to those obtained earlier for axially symmetric core-shell nanowires [46] and CSNPs with centered spherical cores [2,39,41,42].

When f is significantly larger then f_c (here at $f = 0.02$), the upper boundary $(R_0/a)_{c2}$ of the interval practically disappears, while its lower boundary $(R_0/a)_{c1}$ still exists. However, when $f >> f_c$ (here at $f = 0.03$), both the maximum on the curve $\Delta E(R_0/a)$ and the critical interval disappear, which means that a MDL can form for any value of R_0/a.

Since the point of minimum on the curve $\Delta E(R_0/a)$ remains almost the same, at $R_0/a \approx 0.76 \approx 3/4$ (Fig. 13), the authors [40] concluded that SC-CSNPs with the ratio $R_0/a \approx 3/4$ are the less stable to the MDL formation because in this case, the appearance of MDLs leads to the biggest energy gain $|\Delta E_{\min}|$ of the system. They also noted that their additional calculations showed that this result did not change for other values of the SC-CSNP radius a.

Figure 14 shows the diagrams $f_c(R_0/a)$ plotted in [40] for the SC-CSNPs with semispherical (solid red curves) and, for comparison, spherical (dashed blue curves) cores [39] for $z_0/R_0 = 0.3$ and different values of the normalized radius a/b of the SC-CSNP. The region under (above) the curve corresponds to the case when the MDL formation is not (is) energetically favorable. Similar diagrams were constructed and discussed in detail for different models describing the critical conditions of MD generation in the past [2,39,41,42,46] (see also Figs. 3(b), 5(b), 9, and 10 in the present review). In Fig. 14, the curves $f_c(R_0/a)$ for SC-CSNPs with semispherical cores lie above the corresponding curves for SC-CSNPs with spherical cores in the range of $R_0/a < 0.9$. It means that in this range, the SC-CSNPs with semispherical cores are more stable with respect to MDL generation than the SC-CSNPs with spherical cores. However, at $R_0/a \approx 0.9$, the curves for semispherical and spherical cores meet, which means that the SC-CSNPs with semispherical and spherical cores become equally stable (unstable) with respect to MDL generation. The authors [40] did not consider the range of $R_0/a > 0.9$ because the misfit stress fields [57] poorly converge near the free surface of the SC-CSNP.

It is worth noting that, for SC-CSNPs with semispherical cores, the formation of a straight MD at the core base along the diameter of a SC-CSNP was also considered [58]. In this case, the recently found solution of the boundary-value problem in the elasticity theory for a straight edge dislocation in an elastic sphere [59] was used. It was shown that for relatively small cores, the formation of a straight MD at the core base is less favorable than the formation of a circular MDL around the spherical part of the core/shell interface. However, for cores whose radii are close to the shell radius, both of these mechanisms are approximately equivalent. The authors [58] explained it by the facts that for small cores, the self-energy of a MDL is significantly less than for a straight dislocation intersecting a SC-CSNP, and on the other hand, for large cores, the elastic fields of the MDL are too strongly screened by the free surface, which significantly reduces the interaction energy of the MDL with the misfit stress field. Therefore, as the core radius tends to the shell radius, the formation of a MDL becomes less favorable than the formation of a straight MD.

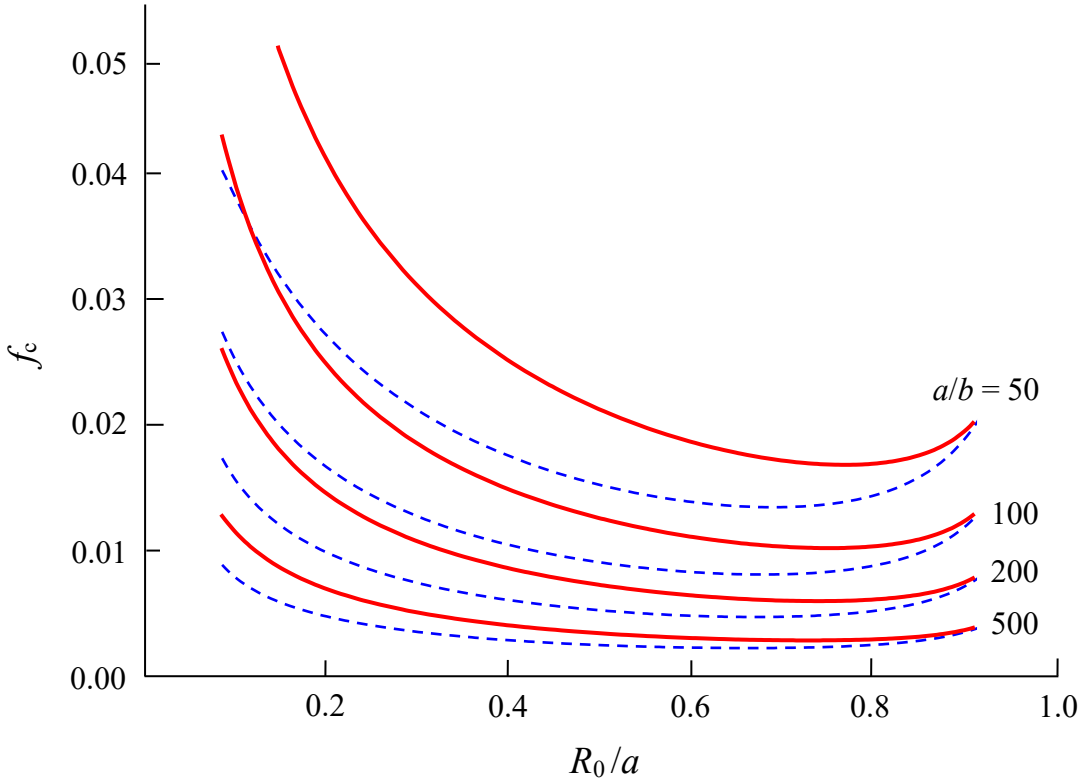

Fig. 14. Dependence of the critical misfit f_c on the ratio R_0/a for $z_0/R_0 = 0.3$, $\nu = 0.3$ and different values of the normalized radius a/b of the nanoparticle. The solid (red) curves show the solution for a semispherical core, while the dashed (blue) curves for a spherical core. Adopted from [40]

In all the aforementioned models, the critical conditions for the onset of already formed MDLs in CSNPs were analyzed. However, neither the physical processes of MDL nucleation and formation nor the energy barriers, which could accompany these processes, were considered. To overcome these drawbacks, the authors of [60] suggested a model of nucleation of an initial defect configuration capable to develop in a final configuration of the first closed MDL around the core. They assumed that the initial defect configuration could be a small PDL nucleating from either the inner or outer boundary in the SC-CSNP and propagating into its core or into its shell. The critical conditions for nucleation of such a PDL were calculated by using Eqs. (14) and (15) with appropriate formulas for the energy terms [60]. In particular, the approximation of the classical linear isotropic theory of elasticity was used with the assumptions that the core and the shell had identical elastic moduli and that the shell thickness *h* was substantially smaller than the outer radius of the SC-CSNP *R*: *h* << *R*. With the latter assumption, the authors [60] passed in calculation of the strain energy term from the spherical to planar geometry of the problem and considered a rectangular PDL. In this case, the solution for the strain energy of a rectangular PDL located in a plane perpendicular to the plane of the free surface of the elastic half-space [61] was used.

Thus, the authors [60] calculated the critical conditions for relaxation of misfit stresses in SC-CSNPs through the generation of rectangular PDLs at either the internal core-shell interface or the outer free surface with their subsequent propagation into the core or into the shell in the cases where the PDLs have the shape of a square or are

extended along or across the interface. As a result, they investigated the necessary conditions for the generation of PDLs of nine types classified according to the shape of the PDL and the position of its formation. It was shown that such PDLs can form when the misfit f exceeds a critical value that depends on R, h, the PDL formation position, and the shape of PDLs. For a PDL generating in the shell, this condition holds when h either lies in a specific range of small values or (for a larger value of f) is less than a critical value. For a PDL generating in the core, h should exceed a critical value. It was also shown that the PDLs elongated along the core-shell interface are formed easier. When the shell grows on the core of a fixed radius, the energetically more preferable generation of a PDL occurs first from the free surface into the bulk of the shell, then from the interface into the shell, and finally from the interface into the core of the SC-CSNP.

The model [60] of misfit stress relaxation through generation of rectangular PDLs in SC-CSNPs was later extended to various heterogeneous nanostructures. In particular, PDL generation in heteronanostructures of spherical (solid [62,63] and hollow [62–64] SC-CSNPs), infinite cylindrical (solid [63–67] and hollow [63,64] core-shell nanowires), flat (bi- and tri-nanolayers [63,64]), and finite-length tubular [68] geometry was analyzed. Departing from the calculations of the misfit stress fields in the heteronanostructures, the authors investigated changes in their energies caused by the formation of PDLs in different regions of them, revealed the regions of the energetically more preferable generation of the PDLs and specified the optimum shape of the PDLs. Gutkin and Smirnov [63,64] compared the critical conditions for the onset of the most energetically favorable PDLs in different heteronanostructures and ranged the relative stabilities of these nanostructures against PDL formation. They concluded hollow nanostructures are always more stable than their solid counterparts, the cylindrical nanostructures are more stable than the symmetric flat tri-nanolayers, the spherical nanostructures are more stable than the cylindrical ones, and the flat bi-nanolayers are the most stable nanostructures among those under consideration.

Critical conditions for misfit dislocation generation in composite nanowires

Critical conditions for MD generation in composite nanowires of different architectures have remained in the focus of many authors for a long time (see, for example, books [11–13] and reviews [22–27,69]). The main segments in this field are theoretical models for: straight MDs [46,70–74], circular [30,70,75–80] and elliptic [81] MDLs, and rectangular PDLs [63,64] in core-shell nanowires (CSNWs) with cylindrical cores; straight MDs [82] and rectangular PDLs [65–67] in CSNWs with prismatic cores of hexagonal, squared and triangular cross section; straight MDs [47,83,84], circular MDLs [32] and rectangular PDLs [63,64] at/in nanotubes embedded to infinite matrix; straight MDs [85–87] and circular PDLs [88] in axially-inhomogeneous nanowires with transverse interfaces; straight MDs in bilayer nanowires with planar interfaces [89–93]; circular MDLs around axially symmetric finite-length cylindrical inclusions in nanowires [28].

Since the most of these models have been extendedly reviewed in recent years [24–27,69], here we briefly consider only some fresh results [91–93] which have been reported in conference talks but not published in regular journals yet.

Figure 15 shows a model [91] of the cross-section of a bilayer nanowire with a flat longitudinal interface in the initial coherent and partly relaxed states. The nanowire was supposed elastically isotropic and homogeneous. The initial coherent state in this case is different from those considered in earlier models [89,90] where the one-dimensional lattice misfit along the x-axis was assumed and modeled through a continuous distribution of virtual edge dislocations with infinitesimal Burgers vectors $\delta\mathbf{b} = \delta b\mathbf{e}_x$ (here δb is the infinitesimal Burgers vector magnitude and $\mathbf{e}_x$ is the ort of the x-axis). In models [91–93], the authors considered the general case of three-dimensional lattice misfit $f = 2(a_2 - a_1)/(a_2 + a_1)$ and solved the corresponding boundary-value problem in the classical theory of elasticity.

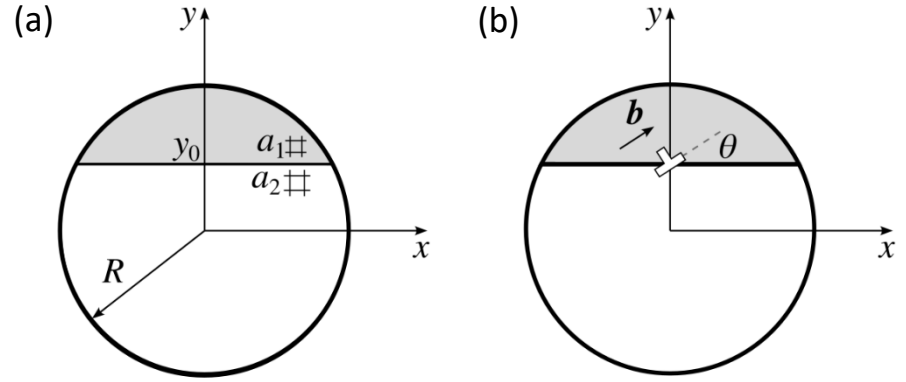

Fig. 15. Cross-section of a bilayer nanowire in (a) the initial coherent state and (b) the partly relaxed state with a misfit dislocation. Here a_1 and a_2 are the lattice parameters in the nanowire layers, R is the nanowire radius, $y = y_0$ is the interface position, $\boldsymbol{b}$ is the Burgers vector of the misfit dislocation, and ϑ is the angle between the Burgers vector and the interface plane. Adopted from [91]

The onset of the first straight edge MD at the interface (Fig. 15(b)) needs the fulfillment of the common inequality $\Delta W = W_{\mathrm{el}} + W_{\mathrm{c}} + W_{\mathrm{int}}$, where ΔW is the energy change caused by the generation of the MD, W_{el} is the MD strain energy, W_{c} is its core energy, and W_{int} is the energy of interaction of the MD with the initial misfit stress in the nanowire. All these energy terms are calculated per unit length of the MD. Then the critical misfit follows from the equation $\Delta W = 0$ as [91]:

$$f_{\mathrm{c}} = \frac{3g(t)}{8(1+\nu)s\cos\theta}\left(\ln\alpha\, s + \ln(1-t^2) + t^2\cos^2\theta - \frac{3-4\nu}{4(1-\nu)}\right), \tag{23}$$

where $s = R/b$, $t = y_0/R$, α is the dislocation core energy parameter [38], ν is the Poisson ratio, and $g(t)$ is the dimensionless function equal to 1 for $t = 0$ and given by:

$$g(t) = \frac{2t^3}{3(1-t^4)(\arcsin t - t\sqrt{1-t^2})}, \text{ for } 0 < |t| < 1. \tag{24}$$

Figure 16 shows the dependence of the critical misfit f_{c} on the normalized position t of the interface for different values of radius R at $\nu = 0.3$, $\alpha = e$ (here e is the base of natural logarithm), and $\theta = 30°$. As is seen, the critical misfit f_{c} depends on both the nanowire radius R and interface position y_0. It increases with a decrease in R and behaves non-monotonously with an increase in y_0: f_{c} slowly decreases with y_0 at relatively small values of y_0, reaches its minimum value $f_{\mathrm{c,min}}$ at some intermediate value of y_0 varying from roughly $0.48R$ in the range of relatively large values of R (here for $R \geq 50b$) to roughly $(0.50–0.54)R$ at smaller values of R (here at $R = 25b$ and $10b$), and then increases

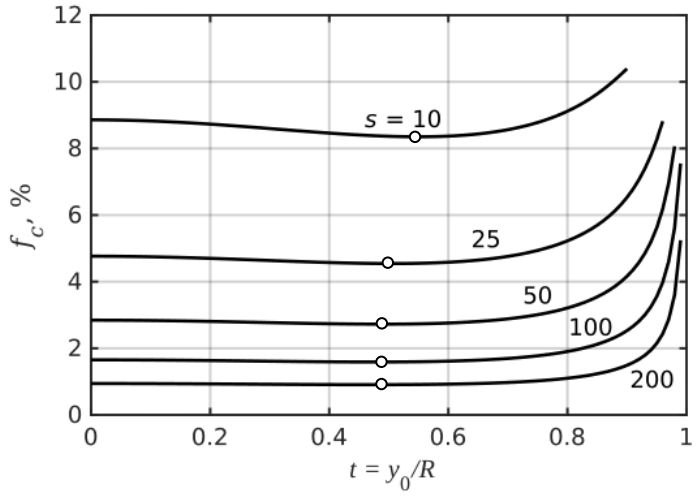

Fig. 16. Dependence of the critical misfit f_c on the normalized position t of the interface for different values of the normalized radius $s = R/b$ at $\nu = 0.3$, $\alpha = e$, and $\theta = 30°$. The open dots indicate the minima of the curves. Adopted from [91]

with y_0, especially fast when $y_0 \geq 0.8R$. Thus, it was shown in [91] that bilayer nanowires with asymmetric position $y_0 \approx R/2$ of the interface are the most unstable with respect to MD generation.

The misfit stress relaxation in the same model system (Fig. 15(a)) through the formation of equilibrium discrete ensembles of edge MDs was considered in [92]. The number and arrangement of MDs were chosen to minimize the energy W of the system per unit area of the interface. As a result, the dependence of this energy W on the misfit f was studied for $R = h$ and $2h$, where $h = R - y_0$ is the maximum thickness of the 'upper' layer, and compared with that for a thin flat epilayer of thickness h on a thick substrate (Fig. 17). It is seen that, for a given value of h, the misfit relaxation with increasing f in the nanowire begins expectedly later than, for example, in a thin flat epilayer on a thick substrate. On the other hand, it was also shown [92] that, at a sufficiently high level of f (here for f > 20 %) the density of the MD ensemble is practically independent on the configuration of the system.

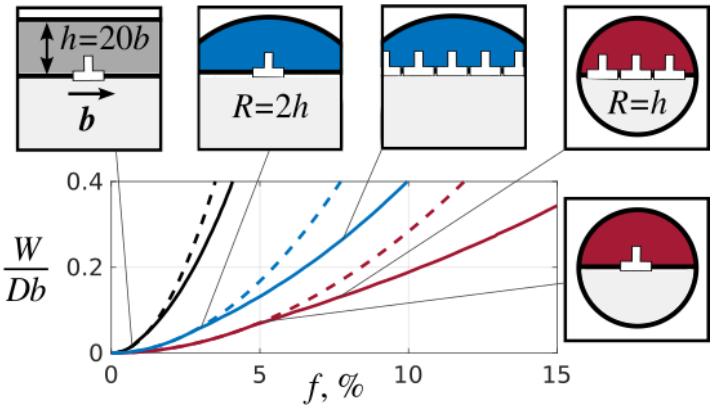

Fig. 17. Dependence of the energy W on the misfit f for $h = 20b$. Here $D = G/[2\pi(1-\nu)]$, G is the shear modulus, ν is the Poisson ratio, and b is the Burgers vector magnitude of the misfit dislocations. The dashed curves show similar dependences for the corresponding systems in the coherent state (with no MDs). Adopted from [92]

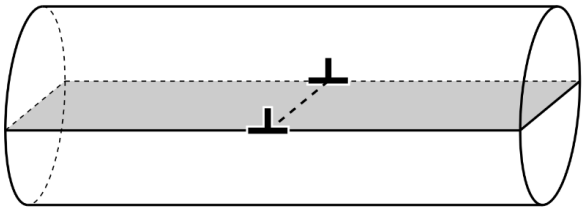

Fig. 18. A straight edge MD piercing a symmetrical bilayer nanowire normally to its axis. Based on results given in [93]

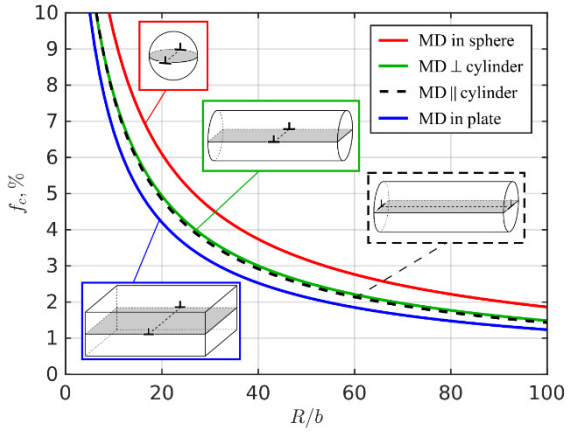

Fig. 19. Dependence of the critical misfit f_c for the formation of straight edge MDs in different Janus nanostructures – a symmetrical bilayer cylinder of radius R, a sphere of radius R and a plate of thickness $2R$ – on their normalized characteristic size R/b at $\nu = 0.3$ and $\alpha = e$. Based on results given in [93]

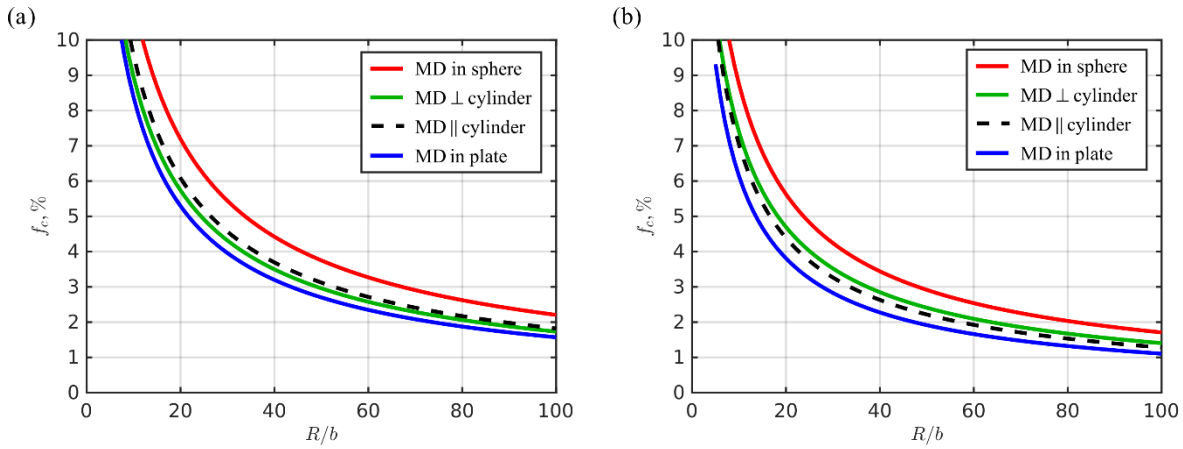

Fig. 20. Dependence of the critical misfit f_c for the formation of straight edge MDs in different Janus nanostructures – a symmetrical bilayer cylinder of radius R, a sphere of radius R and a plate of thickness $2R$ – on their normalized characteristic size R/b at $\alpha = e$ and (a) $\nu = 0$ and (b) $\nu = 0.49$. Based on results given in [93]

MD lines in models [89–92] were parallel to the nanowire axes. Obviously, it would be also reasonable to consider the nonparallel case. However, modeling of such configurations is hindered by the lack of analytical solutions for the boundary-value elastic problems on cylinders with straight dislocations piercing the free surface of the cylinders. Thus, calculating the dislocation strain energy W_{el} becomes a matter of numerical approximations. On the other hand, the interaction energy W_{int} can still be obtained

analytically with the aforementioned solution for the misfit stress-field of a bilayer nanowire [92]. In such a manner, the misfit stress relaxation in a symmetrical bilayer cylinder via the formation of an edge MD perpendicular to the cylinder axis (Fig. 18) was considered in [93]. The strain energy W_{el} was calculated with the finite element method and verified by comparison with several well-known analytical solutions for other systems. The results show that the values for the critical misfit f_c for both the parallel and perpendicular MDs in a symmetrical bilayer cylinder are rather close (Fig. 19). However, it is of interest that the exact relation between those two cases depends on the Poisson ratio ν (Fig. 20): for $\nu = 0$, the perpendicular MD is more preferable than the parallel one, while for $\nu = 0.49$ it is vice versa, and for intermediate values (here for $\nu \approx 0.3$, see Fig. 19), the critical misfits are practically equal. In any case, both the critical misfits for a bilayer cylinder of radius R lie between the critical misfit values for a symmetrical bilayer plate of thickness $2R$ and a Janus sphere of radius R. Thus, comparing different architectures of Janus nanostructures, one can conclude that the Janus plate is less stable to the MD generation than the Janus cylinder, while the latter is less stable in this respect than the Janus sphere. This result well corresponds to the earlier comparison of the stability of different misfitting nanostructures to the formation of small rectangular PDLs [63,64].

Theoretical models for misfit dislocations in free-standing composite nanolayers

The theoretical models describing the elastic fields and strain energy of MDs, and critical conditions for their generation in free-standing composite nanolayers were suggested and studied by a number of authors. In particular, they considered: straight edge MDs in misfitting bi- [44,94–102], tri- [102,103], and multilayers [94] with two free surfaces and either different [44,94–96,99–102] or equal [96,98,103] elastic constants, isotropic [44,94–98,103] and anisotropic [99–102]; a periodic set of straight screw interfacial MDs normally piercing the free surfaces of a plate-like heterogeneous bicrystal with different isotropic elastic moduli [104,105]; dipoles of straight edge MDs in the interfaces of a lamellar inclusion piercing a nanolayer normally to its free surfaces [106,107]; a circular MDL in the interface of a circular cylindrical inclusion piercing a nanolayer normally to its free surfaces [108]; straight edge MDs in a nanolayer with an embedded nanowire of rectangular cross section with the faces parallel and normal to the nanolayer free surfaces [109]. It is worth noting that model nanostructures in works [106–109] were assumed elastically isotropic and homogeneous.

Some of the authors concentrated their attention on the calculation of elastic fields of some presumed periodic configurations of MDs at the interfaces [94,95,97,99,100,104,105], while the others also analyzed the energetics of partly relaxed nanolayers with MDs [44,96,98,101–103,106–109], the critical conditions for the onset of MD generation process [44,96,103,106–109], and the energy barriers for its realization [103,109]. The discussion of the critical conditions was based on the calculation of the energy changes accompanied the MD appearance in the misfitting nanolayers as was also the case with composite nanoparticles and nanowires (see the previous sections). The differences were in the self-strained energies of MDs and the energies of their interaction with the initial misfit stresses that were found according to the geometry of the nanolayers under study. Moreover, the earlier models [44,94–100] were already reviewed in book [11]. To avoid

repeating, here we consider in more details only the most recent models [103,109] dealing with analyzing possible mechanism of MD generation with corresponding critical conditions and energy barriers.

Mikaelyan et al. [109] suggested a model of misfit stress relaxation in and around a nanowire of rectangular cross section embedded in a nanolayer in such a way that opposite faces of the nanowire are parallel or normal to the nanolayer surfaces (Fig. 21). Within the model, an edge of the nanowire, which is closer to the nanolayer surface, emits a dipole of edge dislocations, either perfect or partial, which glide along the nanowire face normal to the free surfaces of the nanolayer. One of these dislocations glides from the nanowire edge to the free surface, while the other one glides to the middle of the nanowire face. Based on the earlier solutions of the boundary-value problems in the theory of elasticity for a rectangular dilatational inclusion in a thin layer [110] and for an edge dislocation in a thin two-layer plate [111], the authors calculated the total energy change ΔW caused by the dislocation emission and analyzed it with the help of energy maps built in coordinates of emitted dislocations x_1 and x_2.

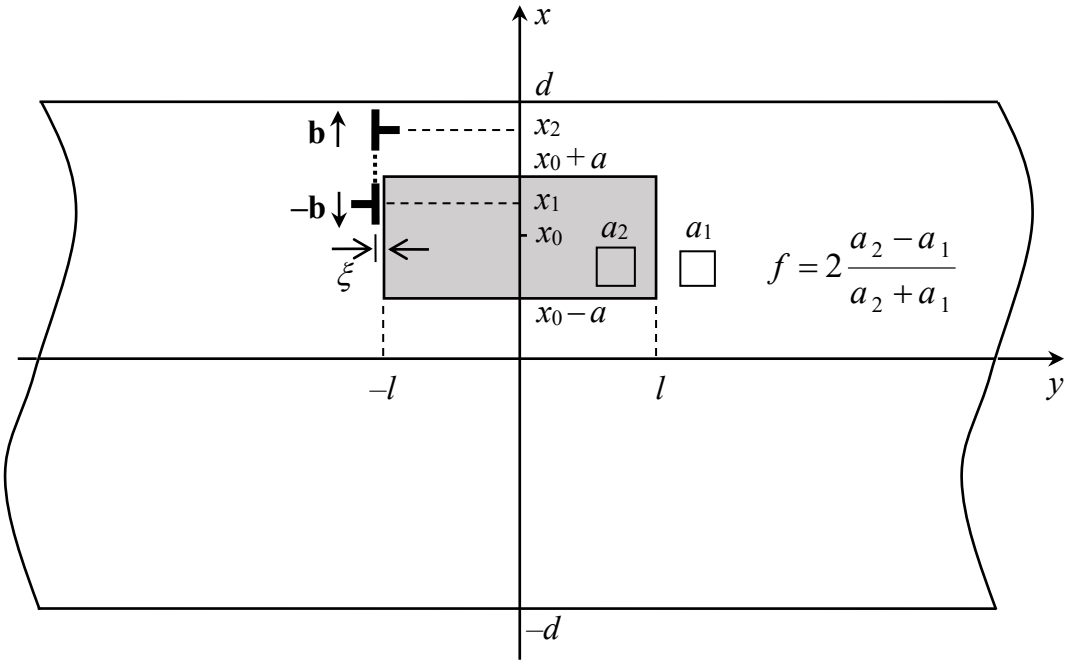

Fig. 21. Misfit stress relaxation near a nanowire having a rectangular cross section with sizes $2l \times 2a$, embedded in a nanolayer of thickness $2d$, through the emission of a dipole of edge dislocations with Burgers vectors $\pm\boldsymbol{b}$ from one of two nanowire edges which are closer to the free surface of the nanolayer. Adopted from [109]

Figure 22 shows some examples of these energy maps $\Delta W(x_1, x_2)$ plotted for a model nanostructure of a Ge nanowire embedded in a Si nanolayer with the following set of the material parameters: the misfit value $f = 0.042$, the shear modulus $G = 60$ GPa, the Poisson ratio $\nu = 0.26$ and the stacking fault energy $\gamma_{SF} = 0.069$ Jm^{-2} (for the case of emission of partial dislocations). The Burgers vector magnitudes for partial and perfect dislocations were $b = 0.23$ and 0.46 nm, respectively. For the sake of definiteness, the authors [109] fixed the position of the nanowire center in the nanolayer as $x_0 = 25$ nm.

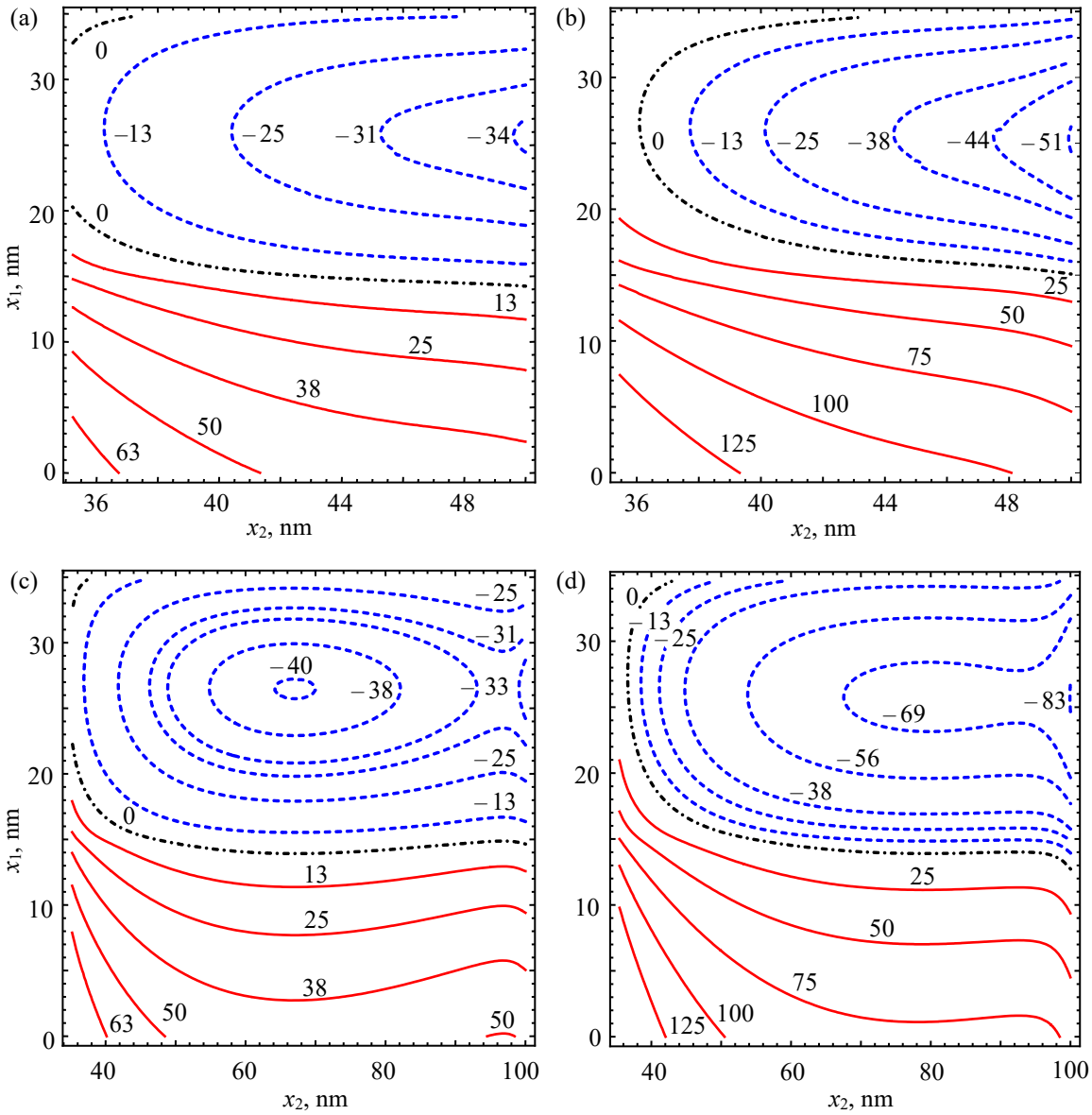

Fig. 22. The maps of the energy change $\Delta W(x_1, x_2)$ in the coordinates of emitted dislocations for the model nanostructure of a Ge nanowire embedded in a Si nanolayer for (a, c) partial and (b, d) perfect dislocations at $x_0 = 25$ nm, $2a = 20$ nm, $2l = 50$ nm, and $2d = 100$ nm (a, b) and 200 nm (c, d). The energy values are given in eV/nm. Adopted from [109]

They also assumed that the crystalline lattices of the nanowire and nanolayer materials were oriented in such a manner that the glide plane of the dislocations was of {111}-type, that is the plane of easy slip for partial (Shockley) dislocations.

With these assumptions, the authors [109] chose the sizes of the nanowire cross section as $2l = 50$ nm and $2a = 20$ nm and plotted the energy maps $\Delta W(x_1, x_2)$ for partial (Fig. 22(a,c)) and perfect (Fig. 22(b,d)) dislocations for two typical values of the nanolayer thickness $2d = 100$ nm (Fig. 22(a,b)) and 200 nm (Fig. 22(c,d)). The starting points of dislocation emission were assumed to be $x_{10} = x_0 + a - b = (35 - b)$ nm and $x_{20} = x_0 + a + b = (35 + b)$ nm, so after emission the coordinate x_1 decreased, while the coordinate x_2 increased. In a map, these starting points give a point $(x_{10}, x_{20}) = (35 - b, 35 + b)$ which lies near the top left corner of the map. As is seen, this point is situated in the region

of positive values of ΔW, and the value of $\Delta W(x_{10}, x_{20})$ may be considered as an energy barrier W_{em} for dislocation emission. The calculations showed [109] that for partial dislocations, W_{em} is about 2.8 eV/nm for $2d = 100$ nm and 3.0 eV/nm for $2d = 200$ nm; for perfect dislocations, W_{em} is about 13.1 eV/nm for $2d = 100$ nm and 13.4 eV/nm for $2d = 200$ nm. Thus, the authors [109] concluded that the energy barrier strongly depends on the type of emitted dislocations but weakly depends on the nanolayer thickness. On the other hand, they also showed that W_{em} weakly depends on the nanowire size.

Figure 23 shows the dependence of W_{em} on d for two different values of $2l$, $2l = 10$ and 50 nm, at $2a = 20$ nm. As is seen from Fig. 23, W_{em} increases with a decrease in the nanowire size. This is so because the misfit shear stress at the points of dislocation emission increases with the nanowire size [112]. The authors [109] concluded that, in general, the nucleation of partial dislocations is much more probable than that of perfect dislocations in this model system of Ge nanowire in Si nanolayer. In particular, at $W_{em} \approx 3$ eV/nm, the partial dislocations can be emitted even at room temperature in this system. In contrast, the emission of perfect dislocations with $W_{em} \approx 13$ eV/nm is possible only at much higher temperatures.

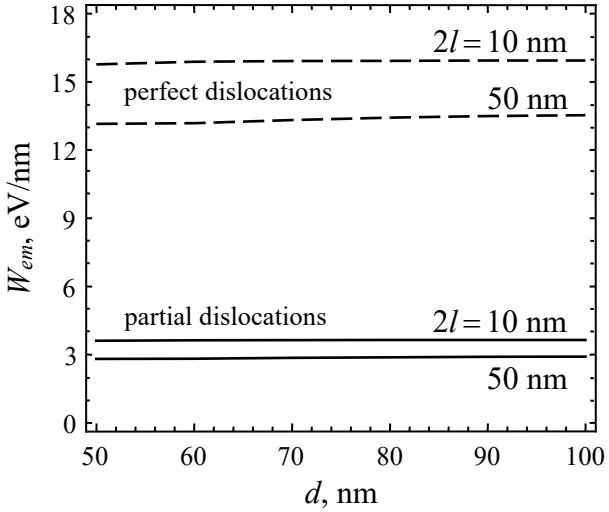

Fig. 23. Dependence of the energy barrier W_{em} on the nanolayer half-thickness d for partial and perfect dislocations at the following values of the system parameters: $x_0 = 25$ nm, $2a = 20$ nm, and $2l = 10$ and 50 nm. Adopted from [109]

It is evident from the energy maps in Fig. 22 that if the dislocation dipole nucleate, the dislocations start to feel at once driving thermodynamic forces which stimulate their glide to the opposite directions. In a map, their motion is reflected by the trajectory which follows the maximum gradient of the function $\Delta W(x_1, x_2)$ and tends to the minimum of this function. In the case of partial dislocations, this minimum can be localized either on the right margin of the map (Fig. 22(a)) or in its central region (Fig. 22(c)). The first situation is characteristic for a relatively thin nanolayer (here with the thickness $2d = 100$ nm) when one dislocation (with coordinate x_1; the authors [109] called it x_1-dislocation) reaches its stable equilibrium position $x_{1eq} \approx 26$ nm at the middle of the nanowire face, while the other dislocation (with coordinate x_2; the authors [109] called it x_2-dislocation) achieves its stable equilibrium position $x_{2eq} = 50$ nm on the free

surface of the nanolayer. The second situation is characteristic for a relatively thick nanolayer ($2d = 200$ nm) when the x_1-dislocation also reaches its stable equilibrium position $x_{1eq} \approx 26$ nm at the middle of the nanowire face, while the x_2-dislocation stops inside the nanolayer, at the stable equilibrium position $x_{2eq} = 67$ nm.

In the case of perfect dislocations, the minimum of function $\Delta W(x_1, x_2)$ was always localized on the right margin of the map (Figs. 22(b,d)). As follows from its position, the x_1-dislocation reaches its stable equilibrium position $x_{1eq} \approx 25$ nm at the middle of the nanowire face, while the x_2-dislocation glides to its stable equilibrium positions $x_{2eq} = 50$ nm (for $2d = 100$ nm) and 100 nm (for $2d = 200$ nm) on the free surface of the nanolayer.

Thus, the calculations of [109] show that perfect dislocations (if they can overcome the energy barrier for their nucleation) must occupy two stable equilibrium positions, one in the middle of the nanowire face and the other one on the free surface of the nanolayer. This situation does not depend on the nanowire and nanolayer sizes. In the case of partial dislocations, whose nucleation is much more probable than that of perfect ones, one dislocation must always occupy its stable equilibrium position at the middle of the nanowire face, while the equilibrium position of the second dislocation depends on the nanowire and nanolayer sizes.

Colin [103] considered a model of misfit strain relaxation in a three-layer structure through the climb of one and two straight edge dislocations from the 'upper' free surface (Fig. 24). He calculated the equilibrium positions of the dislocations, the energy barriers for their climb to the interface, and the critical misfit values for their generation under the assumptions that the second dislocation climbs in the same path as the first one and that the effects of the 'lower' free surface on the dislocation stresses can be neglected.

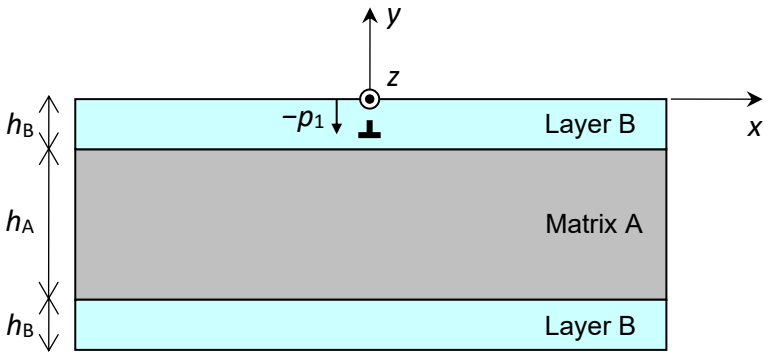

Fig. 24. Two layers of material B and thickness h_B cover a matrix of material A and thickness h_A. An edge dislocation with Burgers vector **b** = (b, 0) lies at a position (0,$-p_1$) in the upper layer. Adapted from [103]

Conclusions

In general, it is shown that both classical and novel methods of the theory of spatial elasticity in combination with the micromechanics of defects form an effective approach which allows adequate description of the relaxation of misfit stresses in various inhomogeneous crystalline nanostructures – composite nanoparticles, nanowires and nanolayers. In recent decades, many new theoretical models have been elaborated within this approach. Significant progress has been achieved in describing the dislocation

mechanisms, the energy barriers, and the critical conditions of misfit stress relaxation in newly considered misfitting nanostructures such as solid and hollow core-shell nanoparticles and nanowires, core-shell nanowires with faceted cores, Janus nanoparticles and nanowires, spherical nanoparticles with semispherical cores, axially-inhomogeneous nanowires with planar transverse interfaces, embedded nanotubes, and free-standing nanolayers with embedded nanowires. Based on these achievements, one can conclude that the relative stability of different misfitting nanostructures to stress relaxation through generation of MDs increases with a decrease in the dimension of the nanostructures having the same characteristic sizes: the planar nanolayers (quasi 2D-nanostructures) are less stable than the cylindrical ones (quasi 1D-nanostructures), and the latter are less stable than the spherical ones (quasi 0D-nanostructures). Generation of partial MDs needs lower energy barriers to overcome than that of perfect MDs, although perfect MDs provide more effective relaxation of misfit stresses than partial MDs.

Among the problems of special interest in the nearest future, the following research areas can be noted:

1. further development of theoretical models of misfit stress relaxation in already analyzed nanostructures with special attention to the calculation of energy barriers for MD formation and equilibrium densities of MDs belonging to different families (for example, straight MDs and MDLs in core-shell nanowires);
2. comparative studying (when suitable and possible) the models for generation of partial and perfect MDs in various misfitting nanostructures;
3. invention of effective approaches for analytical modeling the misfit stress relaxation in faceted core-shell nanowires and nanoparticles;
4. formulation and solution of new boundary-value problems in the theory of elasticity for straight dislocations and disclinations shifted from the axial position in bulk, hollow and inhomogeneous spheres;
5. solution of new boundary-value problems in the theory of elasticity to determine misfit stress fields in inhomogeneous crystalline nanostructures with diffuse interfaces;
6. development of theoretical models for misfit stress relaxation in inhomogeneous crystalline nanostructures with diffuse interfaces.

It is expected that any progress in dealing with these problems will allow to obtain new results that will be useful for better understanding the behavior of defects, stress relaxation and related phenomena in real device nanostructures.

CRediT authorship contribution statement

Mikhail Yu. Gutkin: writing – review & editing, writing – original draft; **Anna L. Kolesnikova**: conceptualization; **Stanislav A. Krasnitckii**: data curation; **Kristina N. Mikaelyan**: data curation; **Dmitrii A. Petrov**: data curation; **Alexey E. Romanov**: supervision; **Andrei M. Smirnov**: writing – review & editing.

Conflict of interest

The authors declare that they have no conflict of interest.

References

1. Trusov LI, Tanakov MYu, Gryaznov VG, Kaprelov AM, Romanov AE. Relaxation of elastic stresses in overlayed microcrystals. *J. Cryst. Growth.* 1991;114(1–2): 133–140.
2. Gutkin MYu. Misfit stress relaxation in composite nanoparticles. *Intern. J. Eng. Sci.* 2012;61: 59–74.
3. Sneed BT, Young AP, Tsung CK. Building up strain in colloidal metal nanoparticle catalysts. *Nanoscale.* 2015;7(29): 12248.
4. Zhang Y, Wu J, Aagesen M, Liu H. III–V nanowires and nanowire optoelectronic devices. *J. Phys. D: Appl. Phys.* 2015;48(46): 463001.
5. Zhao J, Chen B, Wang F. Shedding light on the role of misfit strain in controlling core-shell nanocrystals. *Adv. Mater.* 2020;32(46): 2004142.
6. Frank FC, Van der Merwe J.H. One-dimensional dislocations. I. Static theory. *Proc. Roy. Soc. London A.* 1949;198(1053): 205–225.
7. Matthews JW. Defects associated with the accommodation of misfit between crystals. *J. Vac. Sci. Technol.* 1975;12(1): 126–133.
8. Tkhorik YuA, Khazan LS. *Plastic Deformation and Misfit Dislocations in Heteroepitaxial Systems*. Kiev: Naukova Dumka; 1983. (In Russian)
9. Milvidskii MG, Osvenskii VB. *Structural Defects in Epitaxial Layers of Semiconductors*. Moscow: Metallurgia; 1985. (In Russian)
10. Freund LB, Suresh S. *Thin Film Materials. Stress. Defect Formation and Surface Evolution*. Cambridge: Cambridge University Press; 2003.
11. Gutkin MYu, Ovid'ko IA. *Physical Mechanics of Deformed Nanostructures. Vol. II. Nanolayered Structures*. Saint-Petersburg: Yanus; 2005. (In Russian)
12. Gutkin MYu. *Strength and Plasticity of Nanocomposites: Textbook*. Saint-Petersburg: Izdatel'stvo Politekhnicheskogo universiteta; 2011. (In Russian)
13. Ovid'ko IA, Sheinerman AG. *Mechanics of Nanowires and Nanostructured Films*. Saint-Petersburg: Exlibris-Nord; 2011. (In Russian)
14. Matthews JW, Blakeslee AE. Defects in epitaxial multilayers: I. Misfit dislocations. *J. Cryst. Growth.* 1974;27: 118–125.
15. Matthews JW, Blakeslee AE. Defects in epitaxial multilayers: II. Dislocation pile-ups, threading dislocations, slip lines and cracks. *J. Cryst. Growth.* 1975;29(3): 273–280.
16. Matthews JW, Blakeslee AE. Defects in epitaxial multilayers: III. Preparation of almost perfect multilayers. *J. Cryst. Growth.* 1976;32(2): 265–273.
17. Van der Merwe JH. The role of lattice misfit in epitaxy. *CRC Crit. Rev. Sol. State Mater. Sci.* 1978;7(3): 209–231.
18. Schwartzman AF, Sinclair R. Metastable and equilibrium defect structure of II-VI/GaAs interfaces. *J. Electron. Mater.* 1991;20: 805–814.
19. Gutkin MYu, Kolesnikova AL, Romanov AE. Misfit dislocations and other defects in thin films. *Mater. Sci. Eng. A.* 1993;164(1–2): 433–437.
20. Beanland R, Dunstan DJ, Goodhew PJ. Plastic relaxation and relaxed buffer layers for semiconductor epitaxy. *Adv. Phys.* 1996;45(2): 87–146.
21. Jain SC, Harker AH, Cowley RA. Misfit strain and misfit dislocations in lattice mismatched epitaxial layers and other systems. *Philos. Mag. A.* 1997;75(6): 1461–1515.
22. Ovid'ko IA, Sheinerman AG. Misfit dislocations in nanocomposites with quantum dots, nanowires and their ensembles. *Adv. Phys.* 2006;55(7–8): 627–689.
23. Kavanagh KL. Misfit dislocations in nanowire heterostructures. *Semicond. Sci. Technol.* 2010;25(2): 024006.
24. Glas F. Strain in nanowires and nanowire heterostructures. *Semicond. Semimet.* 2015;93: 79–123.
25. Gutkin MYu, Kolesnikova AL, Romanov AE. Nanomechanics of stress relaxation in composite low-dimensional structures. In: Altenbach H, Öchsner A. (eds.) *Encyclopedia of Continuum Mechanics*. Berlin: Springer; 2020. p.1778–1799.
26. Smirnov AM, Krasnitckii SA, Rochas SS, Gutkin MYu. Critical conditions of dislocation generation in core-shell nanowires: A review. *Rev. Adv. Mater. Technol.* 2020;2(3): 19–43.
27. Romanov AE, Kolesnikova AL, Gutkin MY. Internal stresses and structural defects in nanowires. *Mech. Solids.* 2022;57(8): 1987–2004.
28. Gutkin MYu, Kuzmin KV, Sheinerman AG. Misfit stresses and relaxation mechanisms in a nanowire containing a coaxial cylindrical inclusion of finite length. *Phys. Stat. Sol. B.* 2011; 248(7): 1651–1657.
29. Kolesnikova AL, Gutkin MYu, Krasnitckii SA, Romanov AE. Circular prismatic dislocation loops in elastic bodies with spherical free surfaces. *Intern. J. Sol. Struct.* 2013;50(10): 1839–1857.

30. Chernakov AP, Kolesnikova AL, Gutkin MYu, Romanov AE. Periodic array of misfit dislocation loops and stress relaxation in core-shell nanowires. *Intern. J. Eng. Sci.* 2020;156(10): 103367.
31. Krasnitckii SA, Smirnov AM, Gutkin MYu. Pair interaction of coaxial circular prismatic dislocation loops in elastic solids with spherical surfaces. *Materials Physics and Mechanics*. 2020;44(1): 116–124.
32. Kolesnikova AL, Chernakov AP, Gutkin MYu, Romanov AE. Prismatic dislocation loops in crystalline materials with empty and coated channels. *Europ. J. Mech. – A/Solids.* 2022;94(10): 104612.
33. Lurie AI. *Spatial Problems of Theory of Elasticity*. Moscow: State Publishing House of Scientific and Technical Literature; 1955. (In Russian)
34. Prudnikov AP, Brychkov YuA, Marichev OI. *Integrals and Series. Special Functions*. Moscow: Nauka; 1983. (In Russian).
35. Dundurs J, Salamon NJ. Circular prismatic dislocation loop in a two-phase material. *Phys. Stat. Sol. B.* 1972;50: 125–133.
36. Kolesnikova AL, Romanov AE. *Circular dislocation-disclination loops and their application to boundary problem solution in the theory of defects*. Leningrad: Preprint No. 1019, Ioffe Physico-Technical Institute; 1986. (In Russian).
37. Eason G, Noble B, Sneddon IN. On certain integrals of Lipschitz-Hankel type involving products of Bessel functions. *Philos. Trans. Roy. Soc. Lond. A.* 1955;247: 529–551.
38. Hirth JP, Lothe J. *Theory of Dislocations*. New York: John Wiley & Sons; 1982.
39. Gutkin MYu, Kolesnikova AL, Krasnitckii SA, Romanov AE. Misfit dislocation loops in composite core-shell nanoparticles. *Phys. Solid State.* 2014;56(4): 723–730.
40. Gutkin MYu, Kolesnikova AL, Mikheev DS, Romanov AE. Misfit stresses and their relaxation by misfit dislocation loops in core-shell nanoparticles with truncated spherical cores. *Europ. J. Mech. / A Solids*. 2020;81: 103967.
41. Gutkin MYu, Kolesnikova AL, Krasnitckii SA, Romanov AE, Shalkovskii AG. Misfit dislocation loops in hollow core-shell nanoparticles. *Scripta Mater.* 2014;83: 1–4.
42. Krauchanka MYu, Krasnitckii SA, Gutkin MYu, Kolesnikova AL, Romanov AE. Circular loops of misfit dislocations in decahedral core-shell nanoparticles. *Scripta Mater.* 2019;167: 81–85.
43. Kolesnikova AL, Gutkin MYu, Proskura AV, Morozov NF, Romanov AE. Elastic fields of straight wedge disclinations axially piercing bodies with spherical free surfaces. *Int. J. Sol. Struct.* 2016;99: 82–96.
44. Gutkin MYu, Romanov AE. Misfit dislocations in a thin two-phase heteroepitaxial plate. *Phys. Stat. Sol. (A).* 1992;129(2): 117–126.
45. Ding Y, Sun X, Wang ZL, Sun S. Misfit dislocations in multimetallic core-shelled nanoparticles. *Appl. Phys. Lett.* 2012;100(11): 111603.
46. Gutkin MYu, Ovid'ko IA, Sheinerman AG. Misfit dislocations in wire composite solids. *J. Phys.: Condens. Matter.* 2000;12(25): 5391–5401.
47. Sheinerman AG, Gutkin MYu. Misfit dislocations in a hollow cylindrical film grown on a hole surface. *Scripta Mater.* 2001;45(1): 81–87.
48. Gryaznov VG, Heidenreich J, Kaprelov AM, Nepijko SA, Romanov AE, Urban J. Pentagonal symmetry and disclinations in small particles. *Cryst. Res. Technol.* 1999;34(9): 1091–1119.
49. Koga K, Sugawara K. Population statistics of gold nanoparticle morphologies: direct determination by HREM observations. *Surf. Sci.* 2003;529(1–2): 23–35.
50. Hofmeister H. Fivefold twinned nanoparticles. In: Nalwa HS. (ed.) *Encyclopedia of Nanoscience and Nanotechnology*. Stevenson Ranch: American Scientific Publishers; 2004. p.431–452.
51. Marks LD, Peng L. Nanoparticle shape, thermodynamics and kinetics. *J. Phys.: Condensed Matter.* 2016;28(5): 053001.
52. De Wit R. Partial disclinations. *J. Phys. C Solid State Phys.* 1972;5(5): 529–534.
53. Howie A, Marks LD. Elastic strains and the energy balance for multiply twinned particles. *Philos. Mag. A.* 1984;49(1): 95–109.
54. Krauchanka MYu, Krasnitckii SA, Gutkin MYu, Kolesnikova AL, Romanov AE, Aifantis EC. Generation of circular prismatic dislocation loops in decahedral small particles. *Scr. Mater.* 2018;146: 77–81.
55. Gutkin MYu, Kolesnikova AL, Yasnikov IS, Vikarchuk AA, Aifantis EC, Romanov AE. Fracture of hollow multiply-twinned particles under chemical etching. *Europ. J. Mech. /A Solids.* 2018;6: 133–139.
56. Khanal S, Casillas G, Bhattarai N, Velázquez-Salazar JJ, Santiago U, Ponce A, Mejía-Rosales S, José-Yacamán M. CuS_2-passivated Au-core, Au_3Cu-shell nanoparticles analyzed by atomistic-resolution Cs-corrected STEM. *Langmuir*. 2013;29(29): 9231–9239.
57. Kolesnikova AL, Gutkin MYu, Krasnitckii SA, Smirnov AM, Dorogov MV, Serebryakova VS, Romanov AE, Aifantis EC. On the elastic description of a spherical Janus particle. *Rev. Adv. Mater. Sci.* 2018;57(1/2): 246–256.

58. Petrov DA, Gutkin MYu, Kolesnikova AL, Romanov AE. Critical conditions for the formation of straight misfit dislocations in composite nanoparticles. In: *Proceedings of the 66th International Conference on Actual Problems of Strength (APP-2023), Zelenogorsk, St. Petersburg, 2023*. St. Petersburg: Izdatel'stvo VVM; 2023. p.27.
59. Petrov DA, Gutkin MYu, Kolesnikova AL, Romanov AE. Edge dislocation in an elastic sphere. *Intern. J. Eng. Sci.* 2025;210: 104226.
60. Gutkin MYu, Smirnov AM. Generation of rectangular prismatic dislocation loops in shells and cores of composite nanoparticles. *Phys. Solid State*. 2014;56(4): 731–738.
61. Gutkin MYu, Ovid'ko IA, Sheinerman AG. Misfit dislocations in composites with nano-wires. *J. Phys.: Condensed Matter*. 2003;15: 3539–3554.
62. Gutkin MYu, Krasnitckii SA, Smirnov AM, Kolesnikova AL, Romanov AE. Dislocation loops in solid and hollow semiconductor and metal nanoheterostructures. *Phys. Solid State*. 2015;57(6): 1177–1182.
63. Gutkin MYu, Smirnov AM. Initial stages of misfit stress relaxation through the formation of prismatic dislocation loops in GaN-Ga_2O_3 composite nanostructures. *Phys. Solid State*. 2016;58(8): 1611–1621.
64. Gutkin MYu, Smirnov AM. Initial stages of misfit stress relaxation in composite nanostructures through generation of rectangular prismatic dislocation loops. *Acta Mater*. 2015;88: 91–101.
65. Krasnitckii SA, Kolomoetc DR, Smirnov AM, Gutkin MYu. Misfit stress relaxation in composite core-shell nanowires with parallelepipedal cores by rectangular prismatic dislocation loops. *J. Phys.: Conf. Ser*. 2018;993: 012021.
66. Krasnitckii SA, Smirnov AM, Mynbaev KD, Zhigilei LV, Gutkin MYu. Axial misfit stress relaxation in core-shell nanowires with hexagonal core via nucleation of rectangular prismatic dislocation loops. *Materials Physics and Mechanics*. 2019;42(6): 776–783.
67. Krasnitckii SA, Smirnov AM, Gutkin MYu. Axial misfit stress relaxation in core-shell nanowires with polyhedral cores through the nucleation of misfit prismatic dislocation loops. *J. Mater. Sci*. 2020;55: 9198–9210.
68. Gutkin MYu, Mordasova EA, Kolesnikova AL, Romanov AE. Misfit stress relaxation at boundaries of finite-length tubular inclusions through the generation of prismatic dislocation loops. In: Altenbach H, Bruno G, Eremeyev VA, Gutkin MYu, Müller WH. (eds.) *Mechanics of Heterogeneous Materials. Advanced Structured Materials*. Cham: Springer; 2023. p.139–157.
69. Gutkin MYu, Kolesnikova AL, Krasnitckii SA, Mikaelyan KN, Mikheev DS, Petrov DA, Romanov AE, Smirnov AM, Chernakov AP. Dislocation mechanisms of misfit stress relaxation in crystalline nanoheterostructures. *Phys. Met. Metallogr*. 2024;125(1): 1211–1218.
70. Raychaudhuri S, Yu ET. Critical dimensions in coherently strained coaxial nanowire heterostructures. *J. Appl. Phys*. 2006;99(11): 114308.
71. Zhao YX, Fang QH, Liu YW. Edge misfit dislocations in core–shell nanowire with surface/ interface effects and different elastic constants. *Int. J. Mech. Sci*. 2013;74: 173–184.
72. Enzevaee C, Gutkin MYu, Shodja HM. Surface/interface effects on the formation of misfit dislocation in a core–shell nanowire. *Philos. Mag*. 2014;94(5): 492–519.
73. Wang X, Pan E, Chung PW. Misfit dislocation dipoles in wire composite solids. *Int. J. Plast*. 2010;26(9): 1415–1420.
74. Arjmand M, Benjamin C, Szlufarska I. Analytical elastoplastic analysis of heteroepitaxial core-shell nanowires. *AIP Advances*. 2019;9(5): 055119.
75. Ovid'ko IA, Sheinerman AG. Misfit dislocation loops in composite nanowires. *Philos. Mag*. 2004;84(20): 2103–2118.
76. Aifantis KE, Kolesnikova AL, Romanov AE. Nucleation of misfit dislocations and plastic deformation in core/shell nanowires. *Philos. Mag*. 2007;87(30): 4731–4757.
77. Colin J. Prismatic dislocation loops in strained core-shell nanowire heterostructures. *Phys. Rev. B*. 2010;82(5): 054118.
78. Haapamaki CM, Baugh J, LaPierre RR. Critical shell thickness for InAs-$Al_xIn_{1-x}As$(P) core-shell nanowires. *J. Appl. Phys*. 2012;112(12): 124305.
79. Salehzadeh O, Kavanagh KL, Watkins SP. Geometric limits of coherent III-V core/shell nanowires. *J. Appl. Phys*. 2013;114(5): 054301.
80. Colin J. Circular dislocation loop in a three-layer nanowire. *Int. J. Solids Struct*. 2015;63: 114–120.
81. Chu HJ, Wang J, Zhou CZ, Beyerlein IJ. *Self*-energy of elliptical dislocation loops in anisotropic crystals and its application for defect-free core/shell nanowires. *Acta Mater*. 2011;59(18): 7114–7124.
82. Smirnov AM, Krasnitckii SA, Gutkin MYu. Generation of misfit dislocations in a core-shell nanowire near the edge of prismatic core. *Acta Mater*. 2020;186: 494–510.
83. Fang QH, Chen JH, Wen PH, Liu YW. Misfit dislocations in an annular strained film grown on a cylindrical nanopore surface. *Scr. Mater*. 2009;60(6): 395–398.

84. Zhao YX, Fang QH, Liu YW. Edge misfit dislocation formation at the interface of a nanopore and infinite substrate with surface/interface effects. *Philos. Mag.* 2012;92(34): 4230–4249.
85. Ertekin E, Greaney PA, Chrzan DC, Sands TD. Equilibrium limits of coherency in strained nanowire heterostructures. *J. Appl. Phys.* 2005;97(11): 114325.
86. Glas F. Critical dimensions for the plastic relaxation of strained axial heterostructures in free-standing nanowires. *Phys. Rev. B*. 2006;74(12): 121302.
87. Ye H, Yu Z. Plastic relaxation of mixed dislocation in axial nanowire heterostructures using Peach-Koehler approach. *Phys. Stat. Sol. RRL*. 2014;8(5): 445–448.
88. Kolesnikova AL, Chernakov AP, Gutkin MYu, Romanov AE. Misfit strain induced out-of-interface prismatic dislocation loops in axially inhomogeneous hybrid nanowires. *Extr. Mech. Lett.* 2022;56(10): 101861.
89. Nabarro FRN. The force between misfit dislocations. *Philos. Mag.* 1970;22(178): 803–808.
90. Ovid'ko IA, Sheinerman AG. Perfect, partial, and split dislocations in quantum dots. *Phys. Rev. B*. 2002;66(24): 245309.
91. Petrov DA, Gutkin MYu. Critical conditions of misfit dislocation formation in a bilayer cylinder. In: Zaytsev DV. (ed.) *Abstracts of the LXVII International Conference "Advanced Problems of Strength" (April 2–5, 2024, Yekaterinburg, Russia)*. Yekaterinburg: Izd-vo UGGU; 2024. p.70–72. (In Russian)
92. Petrov DA, Gutkin MYu. Longitudinal misfit dislocations in a bilayer nanowire. In: Straumal BB. (ed.) *Physics of Condensed Matter: Abstracts of the IV International Conference (June 2-6, 2025, Chernogolovka, Russia)*. Chernogolovka; 2025. p.144. (In Russian)
93. Petrov DA, Gutkin MYu. Critical conditions for the formation of longitudinal and transverse misfit dislocations in a symmetrical bilayer cylinder. In: Yurlova NA. (ed.) *XXIV Winter School on Continuum Mechanics (February 24-28, 2025, Perm', Russia). Book of Abstracts*. Perm: Izd-vo ICMM UB RAS; 2025. p.220. (In Russian)
94. Bonnet R. Elasticity theory of straight dislocations in a multilayer. *Phys. Rev. B*. 1996;53(16): 10978–10982.
95. Bonnet R. A thin bicrystal deformed by a two period network of misfit dislocations. *Compt. Rend. Acad. Sci., Ser. II*. 1999;327(13): 1331–1336.
96. Zhang TY, Lee S, Guido LJ, Hsueh CH. Criteria for formation of interface dislocations in a finite thickness epilayer deposited on a substrate. *J. Appl. Phys.* 1999;85(11): 7579–7586.
97. Bonnet R. A biperiodic network of misfit dislocations in a thin bicrystalline foil. *Phys. Stat. Sol. A*. 2000;180(2): 487–497.
98. Wang SD. Energy of an array of dislocations in a strained epitaxial layer deposited on a finite substrate. *J. Appl. Phys.* 2000;88(12): 7089–7094.
99. Outtas T, Adami L, Derardja A, Madani S, Bonnet R. Anisotropic elastic field of a thin bicrystal deformed by a biperiodic network of misfit dislocations. *Phys. Stat. Sol. A*. 2001;188(3): 1041–1045.
100. Outtas T, Adamia L, Bonnet R. A biperiodic interfacial pattern of misfit dislocation interacting with both free surfaces of a thin bicrystalline sandwich. *Solid State Sciences*. 2002;4(2): 161–166.
101. Vattré A. Mechanical interactions between semicoherent heterophase interfaces and free surfaces in crystalline bilayers. *Acta Mater.* 2015;93: 46–59.
102. Vattré A. Elastic interactions between interface dislocations and internal stresses in finite-thickness nanolayered materials. *Acta Mater.* 2016;114: 184–197.
103. Colin J. Dislocation climbing in a three-layer structure. *Acta Mech.* 2024; 235: 5661–5672.
104. Neily S, Ghabri H, Youssef S, Bonnet R. Screw heterointerfacial dislocations piercing a thin plate. *Comptes Rendus Physique.* 2018;19(5): 341–346.
105. Ghabri H, Neily S, Youssef S, Bonnet R. Screw misfit dislocations perpendicular to one or two free surfaces. *Philos. Mag. Lett.* 2018;98(6): 227–239.
106. Colin J. Misfit dislocation formation in stressed nanofilms. *Philos. Mag. Lett.* 2014;94(4): 189–197.
107. Colin J. Equilibrium positions of misfit dislocations in a nanolayer embedded in a matrix. *Intern. J. Sol. Struct.* 2016;81: 393–398.
108. Colin J. Formation of a prismatic dislocation loop in the interface of a circular cylindrical inclusion embedded in a thin slab. *J. Appl. Mech.* 2016;83(2): 021006.
109. Mikaelyan KN, Gutkin MYu, Borodin EN, Romanov AE. Dislocation emission from the edge of a misfitting nanowire embedded in a free-standing nanolayer. *Intern. J. Sol. Struct.* 2019;161: 127–135.
110. Malyshev KL, Gutkin MYu, Romanov AE, Sitnikova AA, Sorokin LM. *Dislocation models and diffraction contrast of rod-like defects in silicon. Preprint No.1109*. Leningrad: A.F. Ioffe Physico-Technical Institute; 1987. (In Russian).
111. Gutkin MYu, Romanov AE. Straight edge dislocations in a thin two-phase plate. I. Elastic stress fields. *Phys. Stat. Sol. A*. 1991;125(1): 107–125.
112. Gutkin MYu. Elastic behavior of defects in nanomaterials. I. Models for infinite and semi-infinite media. *Rev. Adv. Mater. Sci.* 2006;13(2): 125–161.

MATERIALS PHYSICS AND MECHANICS RESEARCH ARTICLE

Submitted: October 17, 2025 **Revised: November 11, 2025** **Accepted: November 20, 2025**

A model for the temperature dependence of the fracture strength of ceramic matrix composites

A.G. Sheinerman [1,2] ✉

[1] St. Petersburg State University, St. Petersburg, Russia

[2] Institute for Problems in Mechanical Engineering, St. Petersburg, Russia

✉ asheinerman@gmail.com

ABSTRACT

High fracture strength at elevated temperatures is a crucial characteristic of ceramic matrix composites for applications in extreme heat environments. Here we suggest a model that describes the temperature dependence of the fracture strength of particulate-reinforced ceramic matrix composites. Within the model, the variation of the fracture strength with temperature is given by the competition of the temperature dependences of the thermal stresses and cohesive strength of the matrix. It is demonstrated that the temperature dependence of the fracture strength can have a maximum if the coefficient of thermal expansion of the filler is significantly smaller than that of the matrix. The results of the model agree with experimental data and confirm that a small coefficient of thermal expansion difference between the matrix and the filler is beneficial for a high fracture strength of ceramic matrix composites.

KEYWORDS

high-temperature ceramics • ceramic matrix composites • fracture • strength • thermal stresses

Funding. *The work is supported by the Russian Science Foundation (grant 23-19-00236).*

Citation: Sheinerman AG. A model for the temperature dependence of the fracture strength of ceramic matrix composites. *Materials Physics and Mechanics*. 2025;53(5): 35–41.
http://dx.doi.org/10.18149/MPM.5352025_2

Introduction

Due to their high strength, oxidation resistance, and high-temperature stability high-temperature ceramics and ceramic matrix composites are increasingly used in extreme environments, such as gas turbines, rocket nozzles, and hypersonic vehicle leading edges [1–3]. Among these, ultra-high-temperature ceramics (UHTCs) based on diborides (ZrB_2, HfB_2) and carbides (HfC, TaC) exhibit outstanding melting points (> 3000 °C), high stiffness, and resistance to ablation and thermal shock [4,5]. The incorporation of reinforcements such as SiC, ZrC, and carbon fibers produces UHTC-based composites that combine high temperature capability with improved fracture toughness and damage tolerance [6,7].

However, the fracture strength and toughness of high- and ultrahigh-temperature ceramics and ceramic composites strongly vary with temperature [8–20]. While some researchers report on a monotonous decrease in the fracture toughness [16] and flexural strength [8,10,17] of ceramics and ceramic matrix composites, others [9–16,18] demonstrate the presence of maxima in such dependences at certain temperatures. The enhanced strength or toughness of such materials was attributed to the formation of core-

shell structures [11,17], the relaxation of thermal mismatch stresses [8,10], the brittle-to-ductile transition in one of the phases [11] or to the healing of microcracks [17].

The effect of the thermal mismatch stresses on the temperature dependence of the flexural strength of composite ceramics has also been addressed theoretically in [21–23], which considered the nucleation and growth of cracks at spherical particles but have not demonstrated the possibility for the growth of the fracture strength with temperature. In [24], the effect of the thermal mismatch stresses on the temperature dependence of fracture toughness has been considered for ceramic matrix composites containing long parallel whiskers. The solution used in[24] adopts the concept [25] of crack growth in a two-dimensional periodic stress field and the assumption that the coefficient of thermal expansion (CTE) creates compressive stresses in the matrix [26], which is valid if the CTE of the matrix is smaller than that of particles. In contrast to [24], in the present paper, we consider the situation of particulate reinforced ceramic matrix composites and focus on the case where the CTE of the matrix is larger than that of particles. The aim of the present paper is to suggest a model that describes the temperature dependence of the fracture strength of particulate reinforced ceramic matrix composites.

Model

Consider a composite ceramic solid that consists of an elastically isotropic ceramic matrix and elastically isotropic ceramic particles and is subject to a uniaxial tensile load σ_0 (Fig. 1). Within the model, we assume that all the particles are identical and represent spheres of radius R. Let the thermal stresses, associated with the cooling of the ceramic composite after sintering and the difference of the CTE of the particles and the matrix, act in the composite solid. We focus on the case where the thermal stresses in the particles are compressive. Let a mode I crack propagate across the ceramic solid. The compressive thermal stresses acting inside the particles hinder crack growth across them. In this case, when the crack front approaches a particle, the crack can grow in three different ways: it can cut the particle (Fig. 2(a)), change its direction and bend the particle (Fig. 2(b)) or envelope the particle, which will eventually produce a bridge in the crack wake (Fig. 2(c)). The mode of crack growth should depend on the stress level, as well as on how far the crack plane lies from the "equator" of the particle. (The closer the crack plane to a particle pole, the easier the crack to bend around the particle due to the smaller deflection angle.) Here we focus on the case where the compressive stresses acting in

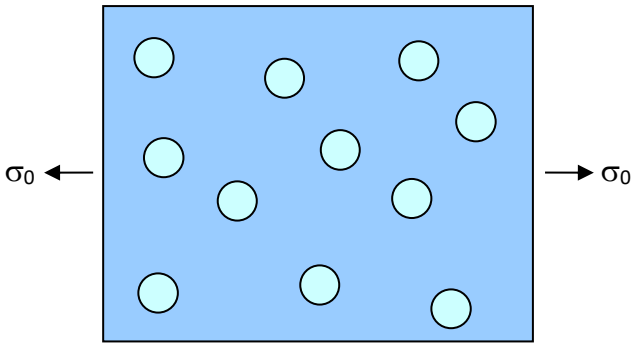

Fig. 1. A ceramic composite solid containing spherical particles under a uniaxial tensile load σ_0

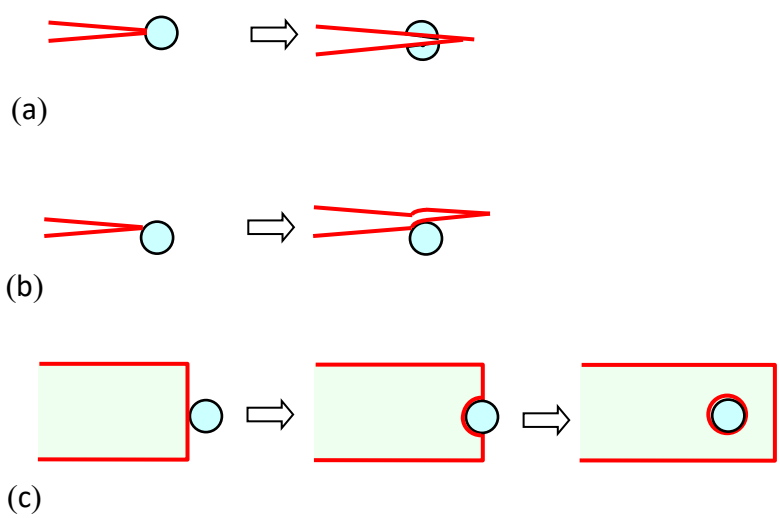

Fig. 2. Three modes of crack interaction with a spherical particle: (a) the crack cuts the particle; (b) the crack deflects and bends around the particle; (c) the crack envelops the particle, which eventually produces a bridge in the crack wake. Figures (a) and (b) display the plane normal to the crack plane, while figure (c) shows the crack plane

the particles are large enough to prevent cutting and assume that the crack does not cut the particles. Under this assumption, the crack propagates only inside the matrix, where tensile thermal stresses act in addition to the applied tensile stress σ_0. These stresses are temperature-dependent and promote crack growth inside the matrix. (It should be noted here that crack deflection and crack bridging hamper crack growth, and so particles can inhibit crack propagation, even though their thermal stresses promote crack growth.)

To calculate the effect of the thermal stresses on crack growth inside the matrix, as a first approximation, we employ the mean field theory, that is, treat the crack as advancing in a spatially uniform stress field equal to the average stress field acting in the matrix (and in those particles which are cut by the crack) in the crack plane. Within this theory, it is sufficient to consider the matrix as a homogeneously stressed medium, which is filled by the particles bypassed by the crack and characterized by the volume fraction f_V. The average stress field acting in the homogeneously stressed matrix incorporates the tensile stress σ_0 normal to the crack plane and the average thermal mismatch stress $\bar{\sigma}_{ij}^m$, where *i*,*j*=*x*,*y*,*z*, and *x, y* and *z* are the coordinate axes of a Cartesian coordinate system. In the following, we assume that the crack plane coincides with the (*xy*) plane of the coordinate system.

We assume that the fracture of the ceramic composite solid occurs when the total tensile stress acting in the direction normal to the macroscopic direction of crack propagation reaches a critical stress σ_c, which is temperature-dependent and incorporates the effects of crack bridging or crack deflection. This implies that the fracture criterion has the form $\sigma_0 + \bar{\sigma}_{zz}^m = \sigma_c$. We assume that the stress σ_c does not depend on the crack length. (For the case of crack bridging, this assumption is valid if the crack length exceeds the length of the bridging zone.) On the other hand, the condition of fracture can also be presented as $\sigma_0 = \sigma_f$, where σ_f is the fracture strength. From the two latter relations one obtains:

$$\sigma_f = \sigma_c - \bar{\sigma}_{zz}^m. \quad (1)$$

For elastically isotropic spherical particles characterized by the Young modulus E_p and Poisson's ratio ν_p in an elastically isotropic matrix with the Young modulus E_m and Poisson's ratio ν_m, the average stress $\bar{\sigma}_{zz}^m$ is given [26] by:

$$\bar{\sigma}_{zz}^m = \frac{2\delta f_V E_m \varepsilon_0}{(1-f_V)(\delta+2)(1+\nu_m)+3\delta f_V(1-\nu_m)}, \quad (2)$$

where $\delta = (1+\nu_m)E_p/[(1-2\nu_p)E_m]$, $\varepsilon_0 = \int_T^{T_s}[\alpha_m(T') - \alpha_p(T')]\,dT'$ and T_s is the sintering temperature.

To calculate the temperature dependence of the fracture strength σ_f, we employ the following equation for the critical stress σ_c [27]:

$$\sigma_c(T) = \sigma_c(T_0)\left\{\frac{E(T)}{E(T_0)}\left[1 - \frac{\int_{T_0}^{T} c_p(T')dT'}{\int_{T_0}^{Tm} c_p(T')dT' + \Delta H_m}\right]\right\}^{1/2}, \quad (3)$$

where T_0 is the arbitrary temperature, whose choice does not affect the critical stress $\sigma_c(T)$, T_m is the melting temperature, $E(T)$ is the Young modulus of the composite, $c_p(T)$ is the specific heat capacity, ΔH_m is the specific heat of melting. The Young modulus of the composite can be roughly estimated using the mixture rule as $E = E_p f_V + E_m(1-f_V)$.

Using Eqs. (1)–(3), let us calculate the temperature dependence of the fracture strength σ_f for the case of α-SiC particles in a ZrB_2 matrix. To do so, we exploit the following temperature dependence of the model parameters [23]:

$$E_m(T) = 507 - [2.54T + 1.9(T - 0.363T_m + |T - 0.363T_m|)]\exp[-T_m/T], \quad (4)$$

$$E_p(T) = 460 - 0.04T\exp[-962/T], \quad (5)$$

$$c_p(T) = 64.18 + 9.41\times10^{-3}T - 16.57\times10^{5}T^{-2}, \quad (6)$$

where E_m and E_p are given in GPa, T is given in K, $c_p$is given in $\mathrm{J/(mol\cdot K)}$.

The temperature dependence of the CTE can be written based on the experimental data [28,29] as:

$$\alpha_p(T) = (0.882 + 8.974\times10^{-3}T - 5.680\times10^{-6}T^2 + 1.264\times10^{-9}T^3)\times10^{-6}, \quad (7)$$

$$\alpha_m(T) = (6.40 + 7.65\times10^{-4}T - 3.62\times10^{-7}T^2 + 9.67\times10^{-11}T^3)\times10^{-6}, \quad (8)$$

where α_p and α_m are given in K^{-1}. We also put $\nu_m = 0.14$ [30], $\nu_p = 0.19$ [31], T_m = 3323 K [23], T_s=2223 K [23], T_0=300 K. Since the values of $\sigma_c(T_0)$ and ΔH_m for these composites are not known, they have been chosen to fit the calculated curve and the experimental data as follows: $\sigma_c(T_0) = 1.05$ GPa, $\Delta H_m = 50$ KJ/mol.

Results

The temperature dependence of the fracture strength σ_f is presented in Fig. 3(a), for ZrB_2–30 % SiC composite (with $f_V = 0.3$). The squares in this figure depict the experimental data from [10]. It is seen in Fig. 3(a) that the fracture strength first increases and then decreases with temperature and that the calculated curve agrees with the experimental data. An increase in σ_f with temperature up to 500 °C is related to a decrease in the thermal stresses. Since these stresses promote crack propagation, their decrease hinders crack growth and thereby increases the fracture strength σ_f. At the same time, an increase in σ_f with temperature due to a reduction of thermal stresses competes with a decrease in the fracture strength due to the reduction of the cohesive strength (which manifests itself by a decrease in the critical stress σ_c with temperature). Above a

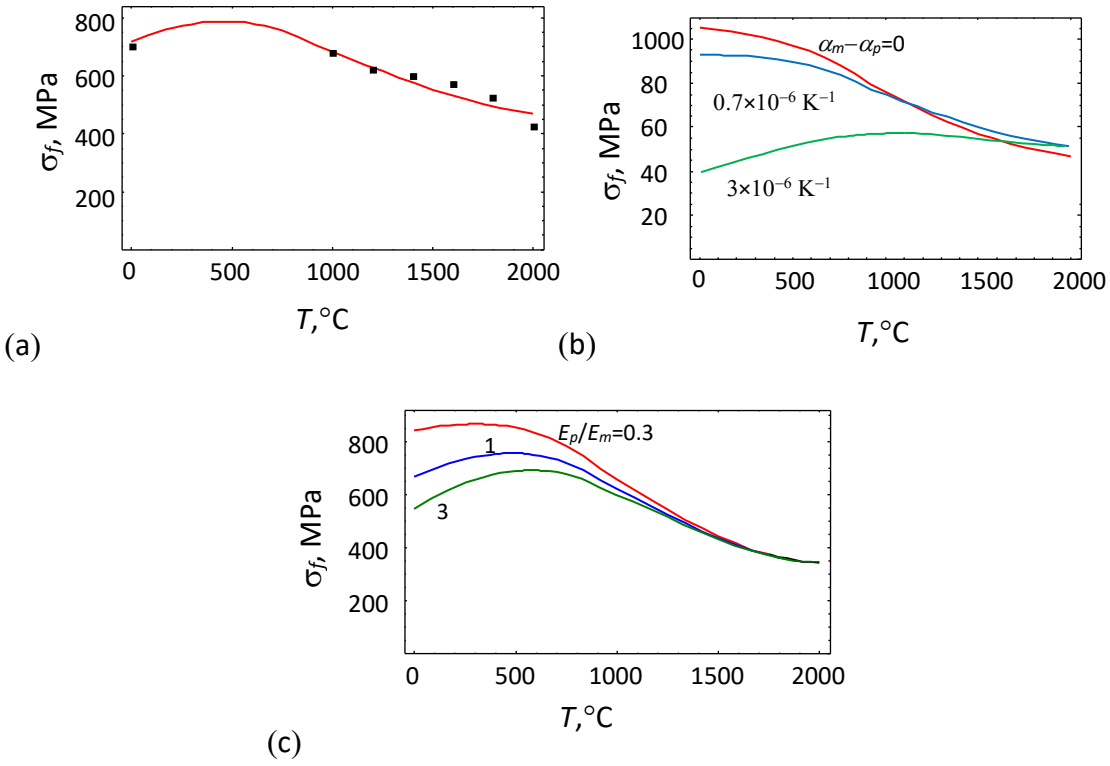

Fig. 3. Dependence of the fracture strength σ_f on temperature T, for the case of the ZrB_2–30 % SiC composite (a), for various values of $\alpha_m - \alpha_p$ (b), and for various values of E_p/E_m (c). The squares in figure (a) show the experimental data [10] for ZrB_2–30 % SiC–2 % B_4C

certain temperature (500 °C for the case shown in Fig. 3(a)) the latter factor (a reduction of the cohesive strength with temperature) becomes dominant, which leads to a decrease in the fracture strength σ_f with increasing temperature.

To demonstrate further that the presence of a maximum on the temperature dependence of the fracture strength σ_f is associated with the thermal stresses, Fig. 3(b) illustrates the model situation where the CTE α_m and α_p do not depend on temperature. Figure 3 displays the fracture strength σ_f vs temperature T for various values of the difference $\alpha_m - \alpha_p$ and the values of the other parameters specified above. It is seen in Fig. 3(b) that in the situation where the thermal stresses are absent ($\alpha_m - \alpha_p = 0$) or relatively small ($\alpha_m - \alpha_p = 0.7 \times 10^{-6}\ K^{-1}$), the fracture strength σ_f monotonously decreases with an increase in temperature. In contrast, if the thermal stresses are large enough ($\alpha_m - \alpha_p = 3 \times 10^{-6}\ K^{-1}$), the curve $\sigma_f(T)$ has a maximum.

The thermal stresses also depend on the ratio E_p/E_m of the Young moduli of the particles and the matrix. To elucidate the effect of the elastic moduli on fracture strength σ_f, Fig. 3(c) shows the model situation where the ratio E_p/E_m is temperature independent. The dependences of the fracture strength σ_f on temperature T for various values of E_p/E_m and the values of the other parameters specified above are presented in Fig. 3(c). This figure shows that the fracture strength σ_f increases with a decrease in E_p/E_m. This points to the effectiveness of a decrease in the Young modulus of the particles compared to that of the matrix for an increase in the fracture strength of ceramic matrix composites. At the same time, if the Young modulus of the particles becomes too small, their cohesive

strength significantly decreases, and cracks stop to bypass particles. This, in turn, eliminates strengthening via crack deflection and bridging. Therefore, the maximum fracture strength should be achieved at intermediate values of the particle Young modulus, which are sufficiently small to reduce the thermal mismatch stresses but also sufficiently high to provide strengthening via crack deflection and bridging.

Conclusions

Thus, in the present paper, we have suggested a model that explains the experimentally observed non-monotonous temperature dependences of the fracture strength of ceramic matrix composites. Within the model, such dependences can be observed if the CTE of the matrix is significantly larger than that of the particles and if the crack cannot cut all the particles. The model also demonstrates that although moderate compressive thermal mismatch stresses in particles can be beneficial for toughening via crack deflection and bridging, high compressive stresses inside particles (that originate if the CTE of the matrix significantly exceeds that of the particles) can reduce the fracture strength of ceramic matrix composites. The high compressive stresses can be reduced by choosing the filler with a smaller CTE mismatch or smaller Young modulus.

CRediT authorship contribution statement

Alexander G. Sheinerman: writing – review & editing, writing – original draft; conceptualization; investigation.

Conflict of interest

The author declares that he has no conflict of interest.

References

1. Sun J, Ye D, Zou J, Chen X, Wang Y, Yuan J, Liang H, Qu H, Binner J, Bai J. A review on additive manufacturing of ceramic matrix composites. *Journal of Materials Science and Technology.* 2023;138: 1–16.
2. Karadimas G, Salonitis K. Ceramic matrix composites for aero engine applications—A review. *Applied Sciences.* 2023;13(5): 3017.
3. Chen Q, Bai S, Ye Y. Highly thermal conductive silicon carbide ceramic matrix composites for thermal management: A review. *Journal of Inorganic Materials.* 2023;38(6): 634–646.
4. Gao R, Wang S, Zhou T, Jiang T, Lu L, Wen Q, Tao S, Xiong X. Research progress on ultrahigh-temperature ceramics modified C/C composites. *Materials.* 2025;18(16): 3891.
5. Baier L, Friess M, Hensch N, Leisner V. Development of ultra-high temperature ceramic matrix composites for hypersonic applications via reactive melt infiltration and mechanical testing under high temperature. *CEAS Space Journal.* 2024;17: 635–644.
6. Lindner F, Puchas G, Wich F, Hariri S, Schafföner S. Ceramic matrix composites (CMC) for high-temperature structural applications. *Journal of the European Ceramic Society.* 2024;45: 116978.
7. Park MS, Gu J, Lee H, Lee SH, Feng L, Fahrenholtz WG. Cf/SiC ceramic matrix composites with extraordinary thermomechanical properties up to 2000 °C. *Nanomaterials.* 2023;14(1): 72.
8. Melendez-Martinez JJ, Dominguez-Rodriguez A, Monteverde F, Melandri C, De Portu G. Characterisation and high temperature mechanical properties of zirconium boride-based materials. *Journal of the European Ceramic Society.* 2002;22(14–15): 2543–2549.
9. Neuman EW, Hilmas GE, Fahrenholtz WG. Mechanical behavior of zirconium diboride–silicon carbide ceramics at elevated temperature in air. *Journal of the European Ceramic Society.* 2013;33(15-16): 2889–2899.

10. Neuman EW, Hilmas G.E., Fahrenholtz W.G. Mechanical behavior of zirconium diboride–silicon carbide–boron carbide ceramics up to 2200 °C. *Journal of the European Ceramic Society.* 2015;35(2): 463–476.
11. Neuman EW, Hilmas GE, Fahrenholtz WG. Ultra-high temperature mechanical properties of a zirconium diboride–zirconium carbide ceramic. *Journal of the American Ceramic Society.* 2016;99(2): 597–603.
12.Silvestroni L, Kleebe HJ, Fahrenholtz WG, Watts J. Super-strong materials for temperatures exceeding 2000 °C. *Scientific Reports.* 2017;7: 40730.
13. Best JP, Wehrs J, Polyakov M, Morstein M, Michler J. High temperature fracture toughness of ceramic coatings evaluated using micro-pillar splitting. *Scripta Materialia.* 2019;162: 190–194.
14. Wang H, Huang Z, Qi J, Wang J. A new methodology to obtain the fracture toughness of YAG transparent ceramics. *Journal of Advanced Ceramics.* 2019;8: 418–426.
15. Mao W, Wang Y, Huang H, Zeng L, Wang Y, Lv L, Feng B, Zou C, Dai C, Tang Q, Fang D. In situ characterizations of mechanical behaviors of freestanding coatings by bending tests under different temperatures based on digital image correlation. *Journal of the European Ceramic Society.* 2020;40(2): 491–502.
16. Liu C, Cai C, Xie J, Guo W, Qin H, Gao P, Xiao H. Effect of surface brittle-to-ductile transition on high-temperature thermal shock resistance of Al_2O_3 ceramics. *Ceramics International.* 2022;48(14): 20627–20638.
17. Wu Q, Cao K, Sun Y, Li C, Yang L, Zhou YC. Temperature-dependent fracture behaviour of superstructure $Hf_6Ta_2O_{17}$ from ambient temperature to 1600 °C. *Ceramics International.* 2022;48(21): 31461–31469.
18. Feng L, Fahrenholtz WG, Hilmas GE, Zhou Y, Bai J. Strength retention of single-phase high-entropy diboride ceramics up to 2000 °C. *Journal of the American Ceramic Society.* 2024;107(3): 1895–1904.
19. Gutkin MYu, Krasnitckii SA, Skiba NV. Formation of liquid-like inclusions near pores in amorphous intercrystalline layers in high-temperature ceramics. *Materials Physics and Mechanics.* 2024;52(6): 8–16.
20. Krasnitckii SA, Sheinerman AG, Gutkin MYu. Brittle vs ductile fracture behavior in ceramic materials at elevated temperature. *Materials Physics and Mechanics.* 2024;52(2): 82–89.
21. Li W, Wang R, Li D, Fang D. A thermodamage strength theoretical model of ceramic materials taking into account the effect of residual stress. *Advances in Materials Science and Engineering.* 2012;2012: 490516.
22. Wang R, Li W, Ji B, Fang D. Fracture strength of the particulate-reinforced ultra-high temperature ceramics based on a temperature-dependent fracture toughness model. *Journal of the Mechanics and Physics of Solids.* 2017;107: 365–378.
23. Gu M, Wu C, Chen X, Wan Y, Liu Y, Zhou S, Cai H, Jia B, Wang R, Li W. Stress-induced microcracking and fracture characterization for ultra-high-temperature ceramic matrix composites at high temperatures. *Materials.* 2022;15(20): 7074.
24. Shao J, Li W, Kou H, Deng Y. Temperature dependent fracture toughness model for whisker-reinforced ceramic matrix composites. *Journal of the American Ceramic Society.* 2022;105(6): 4348–4359.
25. Cutler RA, Virkar AV. The effect of binder thickness and residual stresses on the fracture toughness of cemented carbides. *Journal of Materials Science.* 1985;20: 3557–3573.
26. Taya M, Hayashi S, Kobayashi AS, Yoon H. Toughening of a particulate-reinforced ceramic-matrix composite by thermal residual stress. *Journal of the American Ceramic Society.* 1990;73(5): 1382–1391.
27. Cheng T, Fang D, Yang Y. The temperature-dependent surface energy of ceramic single crystals. *Journal of the American Ceramic Society.* 2017;100: 1598–1605.
28. Stockmeier M, Müller R, Sakwe SA, Wellmann PJ, Magerl A. On the lattice parameters of silicon carbide. *Journal of Applied Physics.* 2009;105:033511.
29. Zimmermann JW, Hilmas GE, Fahrenholtz WG, Dinwiddie RB, Porter WD, Wang H. Thermophysical properties of ZrB_2 and ZrB_2–SiC ceramics. *Journal of the American Ceramic Society.* 2008;91: 1405–1411.
30. Wang HY, Xue FY, Zhao NH, Li DJ. First-principles calculation of elastic properties of TiB_2 and ZrB_2. *Advanced Materials Research.* 2010;150–151: 40–43.
31. Shackelford JF, Alexander W. *Materials Science and Engineering Handbook*. Boca Raton: CRC Press; 2001.

MATERIALS PHYSICS AND MECHANICS RESEARCH ARTICLE

Submitted: October 29, 2025 **Revised: November 18, 2025** **Accepted: December 03, 2025**

Band gap engineering with strains induced by quantum dots in semiconductors nanowires

Nguyen Van Tuyen [1,2], A.L. Kolesnikova [1,3], M.Yu. Gutkin [1,3,4], A.E. Romanov [1,5,6] ✉

[1] ITMO University, St. Petersburg, Russia

[2] Sao Do University, Hai Phong City, Vietnam

[3] Institute for Problems in Mechanical Engineering, Russian Academy of Sciences, St. Petersburg, Russia

[4] Peter the Great St. Petersburg Polytechnic University, St. Petersburg, Russia

[5] Ioffe Institute, Russian Academy of Sciences, St. Petersburg, Russia

[6] Togliatti State University, Togliatti, Russia

✉ aeromanov@itmo.ru

ABSTRACT

This work examines the influence of quantum dots embedded in semiconductor nanowires with lattice parameters different from those of the surrounding nanowire material on the nanowire band gap. Using the found analytical formulas for the elastic fields of cylindrical, hemispherical, and conical inclusions simulating quantum dots and located along the nanowire symmetry axis, the maps of the elastic dilations are depicted and the regions of their extremes near the nanowire surface are identified. Calculations are performed within the framework of the isotropic linear theory of elasticity. For GaN nanowires containing axisymmetric quantum dots of varying shapes and compositions, the deformation potentials and corresponding changes in the band gap in the nanowire regions of elastic dilation extremes are calculated. The dependence of local change in the band gap in GaN nanowires on the lattice mismatch parameter between the quantum dots and NWs are presented. It is shown that the semiconductor nanowire band structure depends on the quantum dot shape, material, and size, and the band gap of GaN nanowires can locally vary by approximately 10 % of its tabulated value. The response of the band gap of a semiconductor nanowire to the elastic field of quantum dot embedded in this wire allows one to nanowire band gap engineering by varying the parameters of the quantum dot.

KEYWORDS

semiconductor nanowire • quantum dot • elastic fields • deformation potential • band gap

Funding. *AK and MG are thankful to the Ministry of Education and Science of the Russian Federation for support under the state assignment No. 124041100008-5 for the Institute for Problems in Mechanical Engineering of the Russian Academy of Sciences.*

Citation: Nguyen Van Tuyen, Kolesnikova AL, Gutkin MYu, Romanov AE. Band gap engineering with strains induced by quantum dots in semiconductors nanowires. *Materials Physics and Mechanics*. 2025;53(5): 42–49. http://dx.doi.org/10.18149/MPM.5352025_3

Introduction

With the development of modern science and technology, quantum dots are playing an increasingly important role in electronics, optoelectronics, photonics and other applications [1,2]. Quantum dots (QDs) are tiny semiconductor particles, typically ranging in size from 2 to 10 nanometers, possessing unique optical and electronic properties due to quantum mechanical effects [3–5]. The optical and electronic properties of QDs are determined by their size and shape, which allows for precise control of light emission and

Publisher: Peter the Great St. Petersburg Polytechnic University

absorption [6,7]. Crystalline QDs embedded in the matrix of another crystalline material possess an elastic field [8–10] depending on QD and matrix shape, material and size. This results in the emergence of a deformation potential in the QDs themselves and the surrounding matrix. This deformation potential influences the formation of the band structure of the QDs and the matrix [11–14]. QDs embedded in nanowires (NW) uniquely combine the tunable optical properties of QDs with the unique electronic and optoelectronic characteristics of the nanowires, enabling precise control of the quantum-optical behavior of the semiconductor wire heterostructure. This makes them highly promising for applications in quantum photonics, optoelectronics, and sensors [15–17]. As mentioned above, the strain induced by the presence of QDs in NW strongly affects the band structure of the nanowires. Detailed studies of the influence of QD strain on the band structure of nanowires can be found in a few papers [18–20].

In this paper, using our analytical calculations, we briefly analyze the elastic strain field of cylindrical, hemispherical, and conical QDs in nanowire. Then, in the framework of the **k·p** perturbation theory approach, we study the effect of QD induced strains on the electronic band gap of GaN nanowires.

Elastic field of the quantum dot in the wire

The QD buried in material matrix can be modeled by an elastic dilatational inclusion (DI) with an eigenstrain ${}^{\mathrm{DI}}\varepsilon_{ii}^{*}$ due to the mismatch between the lattice constants of the QD and the surrounding crystal matrix:

$${}^{\mathrm{DI}}\varepsilon_{ii}^{*} = \varepsilon^{*}\delta(\Omega), \tag{1}$$

where $\delta(\Omega) = \begin{cases} 1, & \boldsymbol{r} \in \Omega \\ 0, & \boldsymbol{r} \notin \Omega \end{cases}$, Ω is the DI region. There is no summation of i in ${}^{\mathrm{DI}}\varepsilon_{ii}^{*}$, i is a coordinate in any orthogonal coordinate system.

In Eq. (1), misfit parameter ε^{*} is found using the following relationship (see, for example, [21,22]):

$$\varepsilon^{*} = \frac{a_{QD} - a_m}{a_m}, \tag{2}$$

where a_{QD} and a_m are the lattice constants of QD and surrounding matrix in the absence of strains. For the crystal lattice parameters, a and c of wurtzite structure $In_xGa_{1-x}N$, Vegard's law is applied [23,24]:

$$a_{\mathrm{In}_x\mathrm{Ga}_{1-x}N} = x \cdot a_{\mathrm{InN}} + (1-x) \cdot a_{\mathrm{GaN}},\ c_{\mathrm{In}_x\mathrm{Ga}_{1-x}N} = x \cdot c_{\mathrm{InN}} + (1-x) \cdot c_{\mathrm{GaN}}. \tag{3a,b}$$

In our consideration, QDs are axially symmetric DIs of the cylinder, hemisphere and cone shapes (Fig. 1). To calculate the elastic fields of DIs in NW, we model DIs as a set of infinitesimally thin coaxial disks (DDs) of radius c with eigenstrain ${}^{DD}\varepsilon_{ii}^{*}$ [25–27], uniformly distributed with a constant density ρ along the axis of symmetry:

$${}^{\mathrm{DD}}\varepsilon_{ii}^{*} = bH\left(1 - \frac{r}{c}\right)\delta(z - z_0), \tag{4}$$

$${}^{\mathrm{DI}}\varepsilon_{ii}^{*} = \int_{z_1}^{z_2} {}^{\mathrm{DD}}\varepsilon_{ii}^{*}(r, z - z_0)\rho dz_0 = \int_{z_1}^{z_2} bH\left(1 - \frac{r}{c}\right)\delta(z - z_0)\rho dz_0 = \varepsilon^{*}\delta(\Omega), \tag{5}$$

where b is a coefficient with the dimension of length, $H(\zeta) = \begin{cases} 1, \zeta > 0 \\ 0, \zeta < 0 \end{cases}$ is the Heaviside step function, $\delta(z)$ is the Dirac delta-function, c is the radius of the disk, z_0 is the coordinate of disk, and $[z_1, z_2]$ is an extent of DI along the z-axis.

In this approach, the elastic fields of DIs are obtained by integrating the

corresponding components of the elastic fields of infinitesimal thin DDs in NW, found by us earlier [28,29].

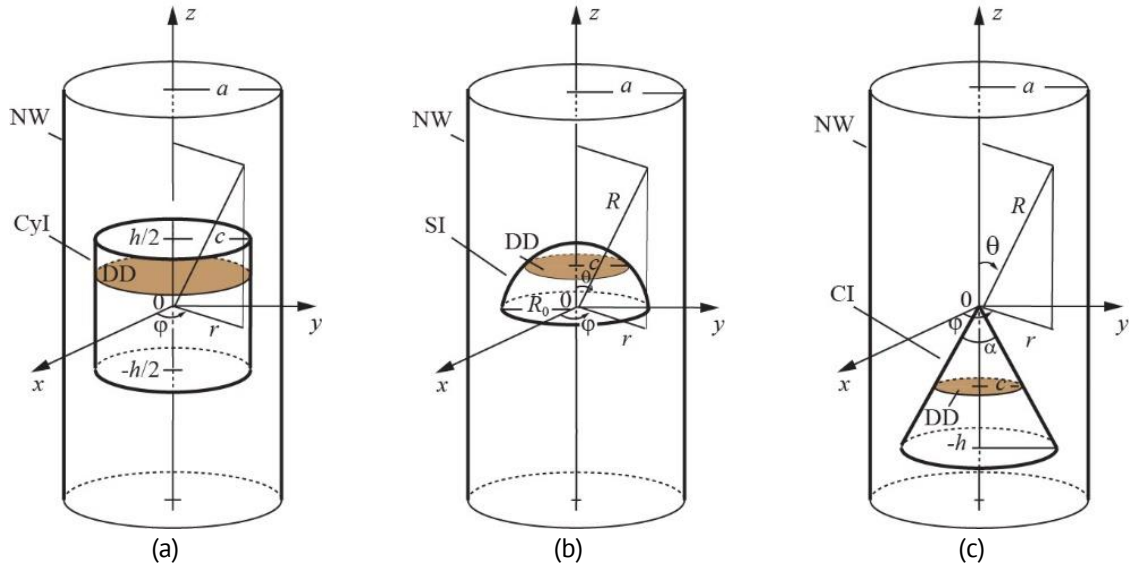

Fig. 1. Quantum dots modeled by the dilatational inclusions in the shape of a cylinder - CyI (a), a hemisphere - SI (b), and a cone - CI (c), embedded in a circular nanowire - NW. The cartesian (x, y, z), cylindrical (r, φ, z), and spherical (R, θ, φ) coordinate systems are shown. Dilatational disks – DDs, which are used to "assemble" the inclusions, are also depicted

The elastic fields (displacements ${}^{\mathrm{DI}}u_i$, strains ${}^{\mathrm{DI}}\varepsilon_{ij}$, and stresses ${}^{\mathrm{DI}}\sigma_{ij}$) of DI in NW include two parts: the first part corresponds to DI in infinite elastic space, the second part corresponds to the contribution of the free surface of NW, see [28,29] and [30], in which DD and DI have the same radius as NW.

For example, total displacements ${}^{\mathrm{DI}}u_i$ of DI are calculated by the following equation:

$${}^{\mathrm{DI}}u_i = \int_{z_1}^{z_2} {}^{\mathrm{DD}}u_i(r, z - z_0)\rho dz_0 = {}^{\infty\mathrm{DI}}u_i + {}^{\mathrm{imDI}}u_i. \quad (6)$$

where ${}^{\infty\mathrm{DI}}u_i$ and ${}^{\mathrm{imDI}}u_i$ are displacements of DI in an infinite elastic media and image part due to effect of free lateral surface of NW, respectively [28,29]. Note that all the fields found have an analytical representation in the form of integrals or series.

Based on Eq. (6), we can find elastic strains for axially symmetric DI by the following expressions in the cylindrical (r, φ, z) and spherical (R, θ, φ) coordinate systems:

$${}^{\mathrm{DI}}\varepsilon_{rr} = \frac{\partial {}^{\mathrm{DI}}u_r}{\partial r} - \varepsilon^* \delta(\Omega),\ {}^{\mathrm{DI}}\varepsilon_{\varphi\varphi} = \frac{{}^{\mathrm{DI}}u_r}{r} - \varepsilon^* \delta(\Omega), \quad (7a,b)$$

$${}^{\mathrm{DI}}\varepsilon_{zz} = \frac{\partial {}^{\mathrm{DI}}u_z}{\partial z} - \varepsilon^* \delta(\Omega),\ {}^{\mathrm{DI}}\varepsilon_{rz} = \frac{1}{2}\left(\frac{\partial {}^{\mathrm{DI}}u_r}{\partial z} + \frac{\partial {}^{\mathrm{DI}}u_z}{\partial r}\right), \quad (7c,d)$$

$${}^{\mathrm{DI}}\varepsilon_{RR} = \frac{\partial {}^{\mathrm{DI}}u_R}{\partial R} - \varepsilon^* \delta(\Omega),\ {}^{\mathrm{DI}}\varepsilon_{\theta\theta} = \frac{1}{R}\frac{\partial {}^{\mathrm{DI}}u_\theta}{\partial \theta} + \frac{{}^{\mathrm{DI}}u_R}{R} - \varepsilon^* \delta(\Omega), \quad (8a,b)$$

$${}^{\mathrm{DI}}\varepsilon_{\varphi\varphi} = \frac{{}^{\mathrm{DI}}u_\theta}{R} cot\,\theta + \frac{{}^{\mathrm{DI}}u_R}{R} - \varepsilon^* \delta(\Omega),\ {}^{\mathrm{DI}}\varepsilon_{R\theta} = \frac{1}{2}\left(\frac{1}{R}\frac{\partial {}^{\mathrm{DI}}u_R}{\partial \theta} + \frac{\partial {}^{\mathrm{DI}}u_\theta}{\partial R} - \frac{{}^{\mathrm{DI}}u_\theta}{R}\right). \quad (8c,d)$$

The elastic hydrostatic strain of DI in NW is determined by following equation:

$${}^{\mathrm{DI}}\Delta = {}^{\mathrm{DI}}\varepsilon_{rr} + {}^{\mathrm{DI}}\varepsilon_{\varphi\varphi} + {}^{\mathrm{DI}}\varepsilon_{zz} = {}^{\mathrm{DI}}\varepsilon_{RR} + {}^{\mathrm{DI}}\varepsilon_{\theta\theta} + {}^{\mathrm{DI}}\varepsilon_{\varphi\varphi}. \quad (9)$$

From Eq. (9), we can depict the maps of the distribution of the elastic hydrostatic strains for considered QDs in NW as it is shown in Fig. 2.

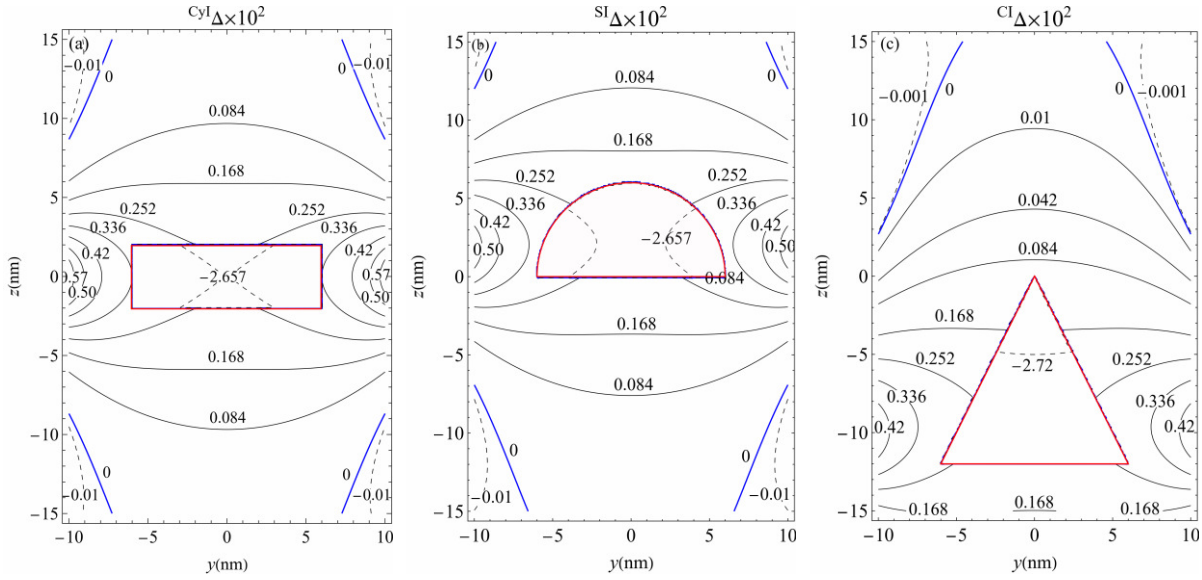

(a) (b) (c)

Fig. 2. The maps of elastic hydrostatic strains due to $In_{0.2}Ga_{0.8}N$ quantum dots (QDs) in GaN nanowire (NW): (a) cylindrical QD, (b) hemispherical QD, and (c) conical QD. The parameters for calculations: the volume of the base of QD $V = 144\pi$ nm^3; NW radius and the radius of QD base are 10 and 6 nm, respectively; the Poisson ratio of GaN $v = 0.234$ [22]; the misfit parameter of $In_{0.2}Ga_{0.8}N$ in GaN matrix is $\varepsilon^* = 0.021$

Effect of the strain on the NW band gap

The influence of strain of QD on the band structure is evaluated using the **k·p** perturbation approach proposed by Bir and Pikus [11]. In unstrained wurtzite GaN, there are three closely spaced top valence bands (VB) at the center of the Brillouin zone, commonly referred to as heavy-hole (HH), light-hole (LH), and crystal-field split-off hole (CH) [14,31]. These VB states have atomic *p*-orbital character, in contrast to the bottom conduction band (CB), which has atomic *s*-orbital character. The presence of QDs in the material matrix creates a strain field, thereby changing the band structure of the material through the deformation potential. Since the large band gap of GaN reduces the interaction of CB and VB states, the Hamiltonian for the strain dependence of VB can be separately given by the 6 × 6 matrix [11]:

$$H^v(k,\varepsilon) = \begin{pmatrix} F & 0 & -H^* & 0 & K^* & 0 \\ 0 & G & \Delta & -H^* & 0 & K^* \\ -H & \Delta & \lambda & 0 & I^* & 0 \\ 0 & -H & 0 & \lambda & \Delta & I^* \\ K & 0 & I & \Delta & G & 0 \\ 0 & K & 0 & I & 0 & F \end{pmatrix}. \quad (10)$$

Here $\Delta = \sqrt{2}\Delta_3$, $F = \Delta_1 + \Delta_2 + \lambda + \theta$; $G = \Delta_1 - \Delta_2 + \lambda + \theta$, $K = A_5 k_+^2 + D_5\varepsilon_+$, $H = i(A_6 k_z k_+ + A_7 k_+ + D_6\varepsilon_{z+})$, $I = i(A_6 k_z k_+ - A_7 k_+ + D_6\varepsilon_{z+})$, $\lambda = A_1 k_z^2 + A_2 k_\perp^2 + +D_1\varepsilon_{zz} + D_2(\varepsilon_{xx} + \varepsilon_{yy})$, $\theta = A_3 k_z^2 + A_4 k_\perp^2 + D_3\varepsilon_{zz} + D_4(\varepsilon_{xx} + \varepsilon_{yy})$, $k_\pm = k_x \pm ik_y$, $k_\perp^2 = k_x^2 + k_y^2$, $k_\pm = k_x \pm ik_y$, $\varepsilon_{z\pm} = \varepsilon_{xz} \pm i\varepsilon_{yz}$, $\varepsilon_\pm = \varepsilon_{xx} - \varepsilon_{yy} \pm 2i\varepsilon_{xy}$, $\varepsilon_\perp = \varepsilon_{xx} + \varepsilon_{yy}$, where parameters D_j (j = 1–6) denote the deformation potentials VB, and A_j (j = 1 to 7) are equivalent to the Luttinger parameters [31], parameter Δ_1 is the crystal-field parameter, while Δ_2 and Δ_3 are the spin-orbit energy parameters. The diagonalization of the matrix (10) yields the three distinct VB maxima $E_{v,j}$.

The edge of conduction band E_c (due to strain) can be expressed as [14,32]:

$$E_c = \frac{\hbar^2 k_z^2}{2m_{e||}} + \frac{\hbar^2 (k_x^2 + k_y^2)}{2m_{e\perp}} + \alpha_{\|}\varepsilon_{zz} + \alpha_{\perp}(\varepsilon_{xx} + \varepsilon_{yy}), \quad (11)$$

where k_x, k_y, k_z are components of wave vector on direction of the x, y, z axes respectively; respect $\alpha_{\perp}$, $\alpha_{\|}$ and $m_{e\|}$,$m_{e\perp}$ denote the CB deformation potentials and electron effective mass, respectively. Here we only consider the ground energy state (**k** = 0), so Eqs. (10) and (11) are much simplified. The band structure parameters for wurtzite GaN are presented in Table 1.

Table 1. Band structure parameters for wurtzite GaN [33]

Parameters	Values, eV	Parameters	Values, eV
E_g	3.479	D_1	- 41.4
D_{cr}	0.010	D_2	- 33.3
D_{SO}	0.015	D_3	8.2
$\Delta_1 = \Delta_{cr}$	0.022	D_4	- 4.1
$\Delta_2 = \Delta_3 = \Delta_{SO}/3$	0.005	D_5	- 4.7
$\alpha_{\|\|}$	- 44.5	D_6	- 7.5
$\alpha_{\perp}$	- 44.5		

The strains influence both valence and conduction bands via Eqs. (10) and (11), therefore the band gap of material changes due to the strains. The strong change of band gap is near the lateral surface of NW. The distribution of the change of band gap ΔE_g^{def} along lateral surface of NW is shown in Fig. 3.

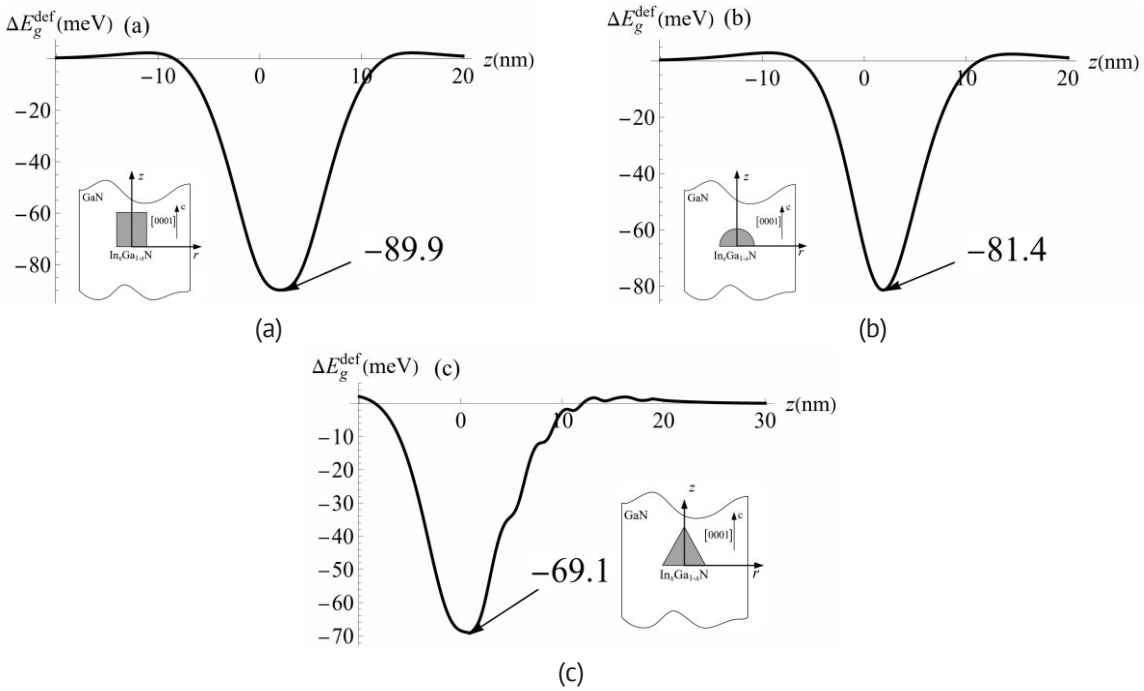

Fig. 3. The distribution of the change of the band gap $\Delta E_g^{\mathrm{def}}$ of GaN nanowire (NW) due to the presence of the $In_{0.2}Ga_{0.8}N$ quantum dot (QD), along free surface of NW. (a) cylindrical QD, (b) hemispherical QD, and (c) conical QD. The parameters for calculations: the volume of the base of QD $V = 144\pi$ nm^3; NW radius and the radius of QD base are 10 nm and 6 nm, respectively; the Poisson ratio of GaN $v = 0.234$ [22]; the misfit parameter of $In_{0.2}Ga_{0.8}N$ quantum dot in GaN matrix is $\varepsilon^* = 0.021$

The changes of band gaps GaN nanowire depend on the QD misfit parameter ε^* and shape as shown in Fig. 4. In addition, the band gap depends on the ratio of the sizes of the quantum dot and nanowire.

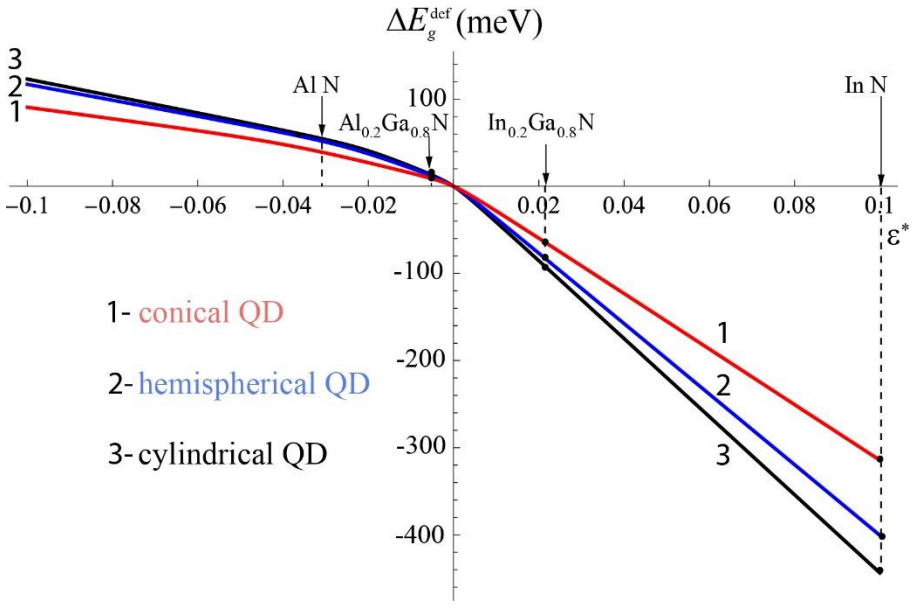

Fig. 4. The dependence of maximum band gap change under lateral surface of the GaN nanowire (NW) containing quantum dot (QD) on misfit parameter ε^*. The parameters for calculations: the volume of QD $V = 144\pi$ nm^3; the radius of the QD base and NW radius are 6 and 10 nm, respectively; the Poisson ratio $\nu = 0.234$ [22]. The arrows indicate QDs corresponding to the selected misfit parameters

Discussions and Conclusions

In this study, using the found analytical formulas for the elastic fields of cylindrical, hemispherical, and conical inclusions simulating QDs and located along the semiconductor NW symmetry axis, the maps of the elastic dilations are depicted and the regions of their extremes near the NW free surface are identified. Calculations are performed within the framework of the isotropic linear theory of elasticity. For GaN nanowires containing axisymmetric QDs of varying shapes and compositions, the changes of the band gap in the NW regions of elastic dilation extremes are calculated. The analysis demonstrates that the contribution of the free surface to the elastic fields, as well as the band structure, depend on the QD shape, material and size. The band gap near the free surface of the semiconductor nanowire changes most strongly for a cylindrical QD (Fig. 4). The change of semiconductor NW band gap depends linearly on the positive misfit parameter ($\varepsilon^* > 0$) between QD and NW, for the case of $\varepsilon^* < 0$, the dependence is nonlinear (Fig. 4). It is shown that the band gap of GaN nanowires can locally vary by approximately 10% of the tabulated value.

The response of the band gap of a semiconductor nanowire to the elastic field of a quantum dot embedded in this wire allows one to band gap engineering of the nanowire by varying the shape, material, and size of the quantum dot.

CRediT authorship contribution statement

Nguyen Van Tuyen **:** data curation; **Anna L. Kolesnikova** : writing – review & editing, writing – original draft; **Mikhail Yu. Gutkin** : conceptualization; **Alexey E. Romanov** : supervision.

Conflict of interest

The authors declare that they have no conflict of interest.

References

1. Deshmukh A, Bhaiswar J, Kapse V, Meghe D. Quantum dots: a brief review. In: Thejo Kalyani N, Dhoble SJ, Michalska-domańska M, Vengadaesvaran B, Nagabhushana H, Arof AK (eds.) *Quantum Dots*. Woodhead Publishing; 2023. p.41–66.
2. Efros AL, Brus LE. Nanocrystal quantum dots: From discovery to modern development. *American Chemical Society Nano*. 2021;15(4): 6192–6210.
3. García de Arquer FP, Talapin DV, Klimov VI, Arakawa Y, Bayer M, Sargent EH. Semiconductor quantum dots: Technological progress and future challenges. *Science*. 2021; 373(6555): eaaz8541.
4. Schmidt HM, Weller H. Quantum size effects in semiconductor crystallites: Calculation of the energy spectrum for the confined exciton. *Chemical Physics Letters*. 1986;129(6): 615–618.
5. Park SH, Morgan RA, Hu YZ, Lindberg M, Koch SW, Peyghambarian N. Nonlinear optical properties of quantum-confined CdSe microcrystallites. *Journal of the Optical Society of America B*. 1990;7(10): 2097–2105.
6. Liu Y, Bose S, Fan W. Effect of size and shape on electronic and optical properties of CdSe quantum dots. *Optik*. 2018;155: 242–250.
7. Ngo CY, Yoon SF, Fan WJ, Chua SJ. Effects of size and shape on electronic states of quantum dots. *Physical Review Journals B*. 2006;74(24): 245331.
8. Grundmann M, Stier O, Bimberg D. InAs/GaAs pyramidal quantum dots: Strain distribution, optical phonons, and electronic structure. *Physical Review B*. 1995;52(16): 11969–11981.
9. Pan E, Yang B. Elastic and piezoelectric fields in a substrate AlN due to a buried quantum dot. *Journal of Applied Physics*. 2003;93(5): 2435–2439.
10. Romanov AE, Beltz GE, Fischer WT, Petroff PM, Speck JS. Elastic fields of quantum dots in subsurface layers. *Journal of Applied Physics*. 2001;89(8): 4523–4531.
11. Bir GL, Pikus GE. *Symmetry and Strain-Induced Effects in Semiconductors*. New York: Wiley; 1974.
12. Zhang A, Luo S, Ouyang G, Yang G. Strain-induced optical absorption properties of semiconductor nanocrystals. *Journal of Chemical Physics*. 2013;138(24): 244702.
13. Romanov AE, Baker TJ, Nakamura S, Speck JS. Strain-induced polarization in wurtzite III-nitride semipolar layers. *Journal of Applied Physics*. 2006;100(2): 023522.
14. Chuang SL, Chang CS. K·p method for strained wurtzite semiconductors. *Physical Review B*. 1996;54(4): 2491–2504.
15. Reimer ME, Akopian N, Barkelid M, Bulgarini G, Heeres R, Hocevar M, Witek BJ, Bakkers EPAM, Zwiller V. Single semiconductor quantum dots in nanowires: growth, optics, and devices, in quantum dots. In: Tartakovskii A. (ed.) *Quantum Dots*. Cambridge: Cambridge University Press; 2012. p.21–40.
16. Björk MT, Thelander C, Hansen AE, Jensen LE, Larsson MW, Wellenberg LR, Samuelson L. Few-electron quantum dots in nanowires. *Nano Letters*. 2004;4(9): 1621–1625.
17. Francaviglia L, Fontana Y, i Morral AF. Quantum dots in nanowires. In: Dayeh SA, i Morral AF, Jagadish Ch. (eds.) *Semiconductors and Semimetals*. Elsevier; 2016. p.159–184.
18. Deng J, Yu J, Hao Z, Kang J, Lu B, Wang L, Sun C, Han Y, Xiong B, Wang J, Li H, Luo Y. Disk-shaped GaN quantum dots embedded in AlN nanowires for room-temperature single-photon emitters applicable to quantum information technology. *ACS Applied Nano Materials*. 2022;5(3): 4000–4008.
19. Bouwes Bavinck M, Zieliński M, Witek BJ, Zehender T, Bakkers EPA.M, Zwiller V. Controlling a nanowire quantum dot band gap using a straining dielectric envelope. *Nano Letters*. 2012;12(12): 6206–6211.
20. Kremer PE, Dada AC, Kumar P, Ma Y, Kumar S, Clarke E, Gerardot BD. Strain-tunable quantum dot embedded in a nanowire antenna. *Physical Review B*. 2014;90(20): 201408.

21. Waltereit P, Romanov AE, Speck JS. Electronic properties of GaN induced by a subsurface stressor. *Applied Physics Letters*. 2002;81(25): 4754–4756.
22. Romanov AE, Waltereit P, Speck JS. Buried stressors in nitride semiconductors: Influence on electronic properties. *Journal of Applied Physics*. 2005;97(4): 043708.
23. Denton AR, Ashcroft NW. Vegard's law. *Physical Review A*. 1991;43(6): 3161–3164.
24. Vegard L. Die Konstitution der Mischkristalle und die Raumfüllung der Atome. *Zeitschrift für Physik*. 1921;5(1): 17–26.
25. Kolesnikova AL, Soroka RM, Romanov AE. Defects in the elastic continuum: classification, fields and physical analogies. *Materials Physics and Mechanics*. 2013;17(1): 71–91. (In Russian)
26. Kolesnikova AL, Gutkin MYu, Romanov AE. Analytical elastic models of finite cylindrical and truncated spherical inclusions. *International Journal of Solids and Structures*. 2018;143: 59–72.
27. Nguyen Van Tuyen, Kolesnikova AL, Romanov AE. Isotropic elasticity of dilatational conical inclusion. An analytical approach. *International Journal of Solids and Structure*. 2024;294: 112735.
28. Kolesnikova AL, Nguyen Van Tuyen, Gutkin MYu, Romanov AE. General approach to the calculation of elastic properties of axially symmetric quantum dots in nanowires. *Pisma v Zhurnal Tekhnicheskoi Fiziki*. 2024;50(6): 28–32. (In Russian)
29. Kolesnikova AL, Nguyen Van Tuyen, Gutkin MYu, Romanov AE. Dilatational disk and finite cylindrical inclusion in elastic nanowire. *International Journal of Engineering Science*. 2025;206: 104169.
30. Kolesnikova AL, Romanov AE, Gutkin MYu, Bougrov VE. Multi-step dilatational inclusion in an elastically isotropic cylinder. *Materials Physics and Mechanics*. 2021;47(5): 697–705.
31. Willatzen M, Lew Yan Voon LC. *The k·p Method*. Berlin: Springer; 2009.
32. Chuang SL. *Physics of Optoelectronic Devices*. New York: John Wiley; 1995.
33. Ghosh S, Waltereit P, Brandt O, Grahn HT, Ploog KH. Electronic band structure of wurtzite GaN under biaxial strain in the M plane investigated with photoreflectance spectroscopy. *Physical Review B*. 2002;65(7): 075202.

MATERIALS PHYSICS AND MECHANICS RESEARCH ARTICLE

Submitted: June 21, 2025 **Revised: September 8, 2025** **Accepted: November 4, 2025**

Strength characteristics of additively manufactured meta-biomaterials made of titanium alloy under cyclic loading

L.B. Maslov [1,2], A.I. Borovkov [1], L.S. Nezhinskaya [1], M.A. Zhmaylo [1]✉, F.D. Tarasenko [1]

[1] Peter the Great St. Petersburg Polytechnic University, St. Petersburg, Russia

[2] Ivanovo State Power Engineering University n.a. V.I. Lenin, Ivanovo, Russia

✉ zhmaylo@compmechlab.com

ABSTRACT

The study considers the fatigue strength of additively manufactured specimens made of metamaterials based on Ti-6Al-4V titanium alloy. The study presents results of full-scale tests for two types of meta-biomaterials: lattice and surface. Dynamic tests were performed in a symmetrical tension-compression cycle at room temperature. The goal of the tests was to construct an S-N curve, which was used to determine the fatigue limit of the metamaterial. We found that the results of numerical simulation differ significantly from the full-scale tests, showing a trend toward overestimated fatigue life. The surface roughness parameter of the specimen was introduced, allowing to achieve better agreement between the results of full-scale tests and numerical simulations.

KEYWORDS

metamaterial • titanium alloy • lattice structures • surface structures • fatigue strength • finite element analysis

Funding. *The research was funded by the Russian Science Foundation (project No. 23-19-00882), https://rscf.ru/project/23-19-00882.*

Citation: Maslov LB, Borovkov AI, Nezhinskaya LS, Zhmaylo MA, Tarasenko FD. Strength characteristics of additively manufactured meta-biomaterials made of titanium alloy under cyclic loading. *Materials Physics and Mechanics*. 2025;53(5): 50–73.
http://dx.doi.org/10.18149/MPM.5352025_4

Introduction

Structures created in various branches of modern high-tech engineering (aerospace, automotive, aircraft, shipbuilding, etc.) require materials combining high strength with resistance to cyclic loads. Titanium alloys, in particular Ti-6Al-4V (or its Russian equivalent VT6), have remained a key structural material for several decades due to the optimal ratio of strength, corrosion resistance and durability under dynamic loads [1]. Metamaterials based on the Ti-6Al-4V alloy have also been the focus of considerable attention in modern biomedical technologies, in particular, in traumatology, orthopaedics and regenerative medicine, due to biocompatibility, lightness and strength of titanium.

Metamaterials with an artificially produced periodic structure exhibit unique mechanical characteristics, including negative Poisson's ratios, controlled anisotropy and good fatigue strength compared with traditional solid materials with isotropic properties. The designed elastic and strength properties of lattice and surface metamaterials based on Ti-6Al-4V titanium alloy expand their scope of application in the aerospace industry,

biomedicine and other fields with demand for materials with unique mechanical properties [2].

As additive technologies are gaining increasing popularity [3], new approaches must be developed to evaluating the strength characteristics of metal-based metamaterials. The physical behaviour of Ti-6Al-4V alloy serving as a base material for 3D printing of metamaterials has been comprehensively explored to study various additive technologies for manufacturing tests specimens, such as electron beam melting (EBM), selective laser melting (SLM), laser powder bed fusion (LPBF) [4]. It was found that the mechanical properties of additively manufactured titanium alloy after appropriate thermal treatment were within the standard range of parameter values for solid materials fabricated by conventional methods [5,6].

Material fatigue is understood as the gradual accumulation of damage in the material under the influence of variable stresses, typically below the yield point, leading to cracking and fracture [7]. The fatigue strength of materials under variable cyclic loading largely depends on the time evolution of stresses; the loads considered are typically periodic. It was experimentally established that the number of cycles to failure depends not only on the magnitude of the maximum absolute stress but also on the stress amplitude of the cycle. The larger this quantity at constant maximum stress, the fewer loading cycles the material can withstand. For many materials, there is a maximum cycle stress at which the material can withstand an infinite number of load cycles. The highest absolute stress in the cycle at which fatigue failure does not yet occur is called the fatigue limit of the material. The fatigue limit of the material is determined by testing identical specimens at different values of maximum stress with a constant asymmetry coefficient, recording the number of cycles at which failure occurs in each specimen. The number of cycles that the specimen or part can withstand before failure characterizes the fatigue life of the material.

High-cycle fatigue occurs at stresses well below the yield point. In this case, the material is elastically deformed, so its properties are satisfactorily described by Hooke's law. Since most materials have a complex multicomponent structure (grains, pores, non-metallic inclusions, etc.), alternating local plastic deformation, which is called microplastic, occurs in individual microvolumes under elastic deformation of a sufficiently large volume. As this deformation is repeated for multiple cycles, microscopic cracks start to evolve. The boundary between low-cycle and high-cycle fatigue is not clearly defined. The fatigue life of 10^5 cycles can be selected as the threshold for Ti-6Al-4V alloy [8].

Traditional experimental methods for evaluating the fatigue characteristics of metals include symmetric cyclic loading controlling the number of cycles to failure, which allows to construct Wöhler fatigue curves, or the so-called S-N (stress-number) curves [9]. The maximum cycle stress at which the specimen is tested is plotted along the ordinate, and the number of cycles that the specimen can withstand until failure is plotted along the abscissa. According to standard approaches to fatigue strength testing, at least fifteen identical specimens are tested to build a fatigue curve and determine the fatigue limit.

Studies show that fatigue life strongly depends on the microstructure: coarse-grained structures show higher resistance to crack initiation, while fine-grained structures show higher resistance to crack propagation [10]. The fatigue characteristics of Ti-6Al-4V fabricated by the traditional technique and laser power bed fusion (LPBF) are compared in [11].

It was found that additively manufactured specimens have 15–20 % lower fatigue life due to the presence of pores and residual stresses. This confirms the need for post-treatment (thermal or mechanical) to improve performance.

A distinctive characteristic of metamaterials is that their properties are architecture-dependent. Lattice structures can exhibit greater fatigue strength compared to classical solid materials with the same density. However, the location of the crack initiation site becomes critical, as failure generally begins in the connections between strut elements. Failure in even a small number of struts in a lattice structure greatly reduces the load-bearing capacity of the structure [12].

Additive manufacturing of products from metamaterials often faces problems with fatigue strength, primarily due to manufacturing quality. Despite high accuracy of modern 3D printers, internal defects occur in the material at the micro, meso, and macro levels during the printing process [13]. Such defects often have a significant influence on the mechanical characteristics and behaviour of the metamaterial during its service life [14]. Depending on the geometric location and shape, these defects negatively affect the strength and other mechanical properties of the complex structure of the metamaterial as a whole [15].

The complex architecture of metamaterials makes classical experimental testing methods too cumbersome, which stimulates the development of computational approaches to evaluating the strength properties of complex elastic structures. Numerical technologies actively pursued to study mechanical fatigue include mathematical modelling methods such as finite element analysis (FEA), discrete element method (DEM) for modelling fracture in brittle structures and multilevel modelling at micro, meso, and macroscales. The crystal plasticity finite element method (CPFEM) accounting for plasticity and crack kinetics for metal alloys allows to build models characterizing grain orientation and dislocation dynamics to predict fatigue life with a small error in comparison with full-scale tests [16].

Despite the progress made in this area, several major issues remain unresolved. Crucial aspects of fatigue testing include the scale effect on test results (real designs exhibit significant differences from laboratory specimens in cyclic loading); the influence of defects, for example, randomly distributed pores in the volume of additively manufactured material; the effect of dynamic loading rate, which is critical for components of turbines, rockets, and airplanes.

A promising direction is integration of machine learning, for example, neural network predictions of fatigue life based on microstructural data. For example, the machine learning method was used in [17] to study the influence of location, size and morphology of defects inside the structure to improve the prediction of fatigue life.

The full-scale tests and simulations carried out in this paper to obtain the strength characteristics of additively manufactured metamaterials under cyclic loading used the following unit cells of a meta-biomaterial based on Ti-6Al-4V alloy: gyroid, a surface-based meta-biomaterial, and diamond, a lattice-based meta-biomaterial. All metamaterials have three porosity values of 30, 50, and 70 %. High-cycle tests are performed to evaluate the parameters characterizing fatigue in the metamaterial under the influence of long-term loads with amplitudes below the yield strength.

Materials and Methods

The base material was a Ti-6Al-4V alloy in the form of spherical powder with particle sizes from 15 to 53 μm with a chemical composition of 90.02 wt. % Ti, 6.01 wt. % Al, 3.89 wt. % V, 0.08 wt. % Fe. The alloy is widely used in surgical operations to replace bone structures with artificial components due to its high strength properties, chemical stability and biocompatibility. It can be used to manufacture parts with thin elements and complex geometries, also well suited to manufacturing products whose mass should be minimal.

Geometric models

To evaluate the fatigue characteristics of metamaterials with complex internal structure, it is important to understand the behaviour of the solid material from which the metamaterial is fabricated. The mechanical behaviour and representative values of elastic and strength properties of the biocompatible Ti-6Al-4V alloy are well known, available in Russian [6] and foreign [5,10] reference books and databases of materials. In this study, we carried out an experimental evaluation of the mechanical properties of solid material additively manufactured with a 3D printer to assess the reliability of the test results for metamaterials obtained by similar technologies.

We considered solid specimens for cyclic loading tests, whose shape and dimensions are standardized in GOST 25.502-79 [18]. The specimen models were built in the SolidWorks CAD software. The appearance and geometric characteristics (total length of 108 mm, thickness of 3 mm, length and radius of the gauge section of 28 and 25 mm, respectively) of the model are shown in Fig. 1.

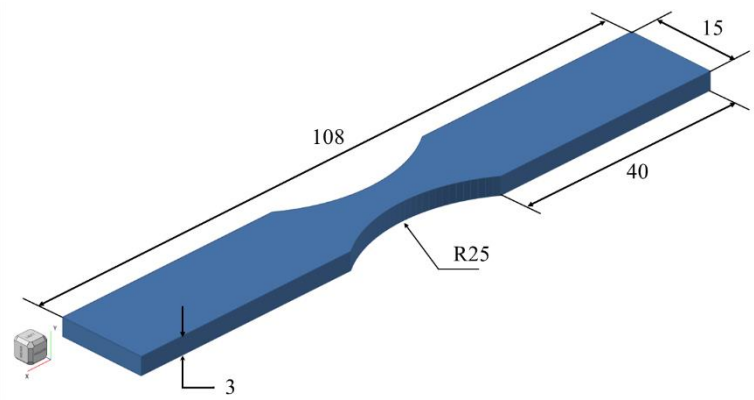

Fig. 1. Solid specimen for fatigue tests

The following types known from the literature were selected as representative volume elements (RVE's), or unit cells, of the fabricated metamaterials: diamond, a cell composed of short struts making up a diamond crystal lattice; gyroid, a cell based on triply periodic minimal surfaces (TPMS).

The volume fractions of solid material were taken to be 30, 50 and 70 %. The variation in porosity of RVE's and, accordingly, specimens of the metamaterial is regulated by the diameter of the struts making up the diamond lattice metamaterial or by the thickness of the 'trabeculae' formed by periodically repeating surfaces shifted by a fixed

distance relative to each other in the case of the metamaterial based on TPMS. In the latter case, the introduced thickness is the characteristic transverse dimension of curved solid shell elements forming surface-based metamaterials.

The following factors were taken into account to design CAD models of the specimens for printing:

1. at least five unit cells had to be included along all axes of the gauge section of the specimen to minimize the influence of local factors on the overall deformation behaviour;
2. minimum thickness of the RVE was limited to 1 mm for additive manufacturing to reduce the impact of manufacturing defects on experimental results;
3. grip section for specimens subjected to tensile loading was substantially long, at least 42 mm;
4. specimen stiffness in the grip section was at least 1.5 times as high as that in the gauge section;
5. material for the specimens had to be used judiciously to reduce the manufacturing costs.

Geometric models of metamaterial cells were built in the Altair Inspire 2023 software, allowing to create models of periodic porous structures of various topologies (Fig. 2). Unit cells of lattice and surface metamaterials and the construction of their models are described in our earlier studies [19,20].

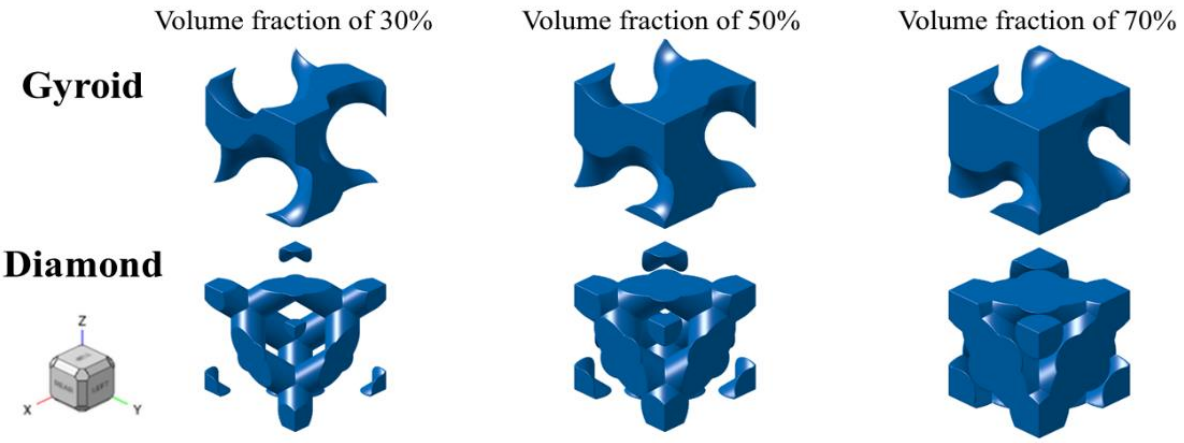

Fig. 2. CAD models of unit cells for constructing gyroid and diamond metamaterials with three volume fractions of solid material: 30, 50 and 70 %

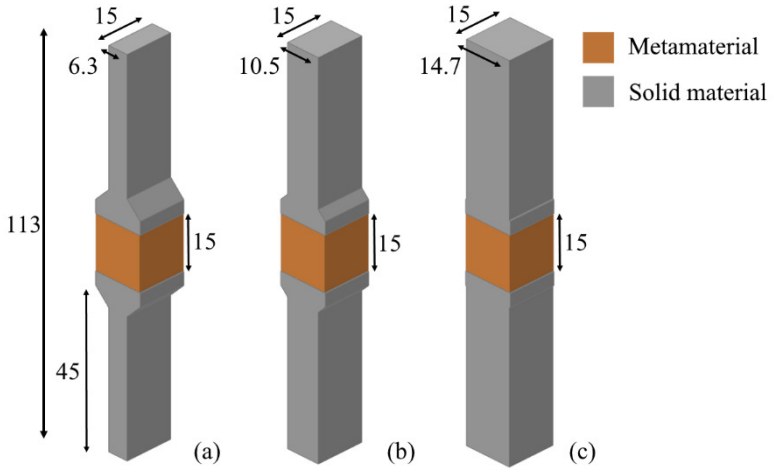

Fig. 3. Characteristic shape and dimensions of specimens for cyclic loading tests: (a) specimen with 30 % volume fraction of solid material, (b) specimen with 50 % volume fraction of solid material, (c) specimen with 70 % volume fraction of solid material

The two basic 3D structures (diamond, gyroid) with three characteristic porosities (30, 50 and 70 %) were used to build 3D CAD models, necessary for 3D printing of specimens for subsequent mechanical testing. The characteristic (including overall) dimensions and shape of the specimens for cyclic loading are shown in Fig. 3.

The given volume of the metamaterial (Fig. 4) with the dimensions of 15 × 15 × 15 mm^3 and a unit cell size of 3 × 3 × 3 mm^3 was designed in Altair Inspire 2023 and complemented by massive solid grips with a length of 45 mm, with the cross-sectional area of the grip exceeding the effective area of the specimen's gauge section by at least 1.5 times (Fig. 5). Such a restriction ensures that failure occurs within the gauge section of the specimen, allowing to correctly evaluate the deformation in the metamaterial, eliminating the influence of solid grips.

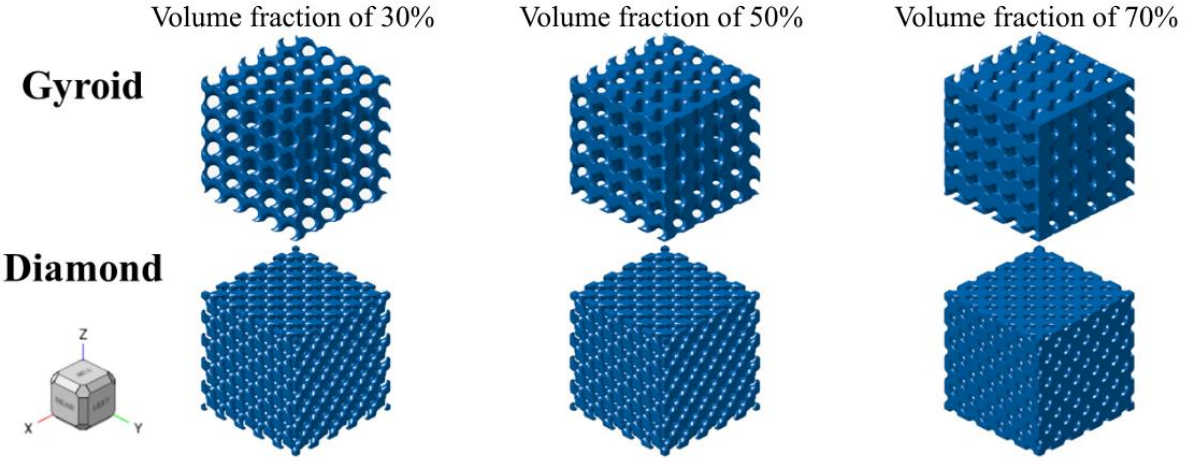

Fig. 4. CAD models of metamaterial specimens (gyroid, diamond) with three volume fractions of solid material (30, 50 and 70 %)

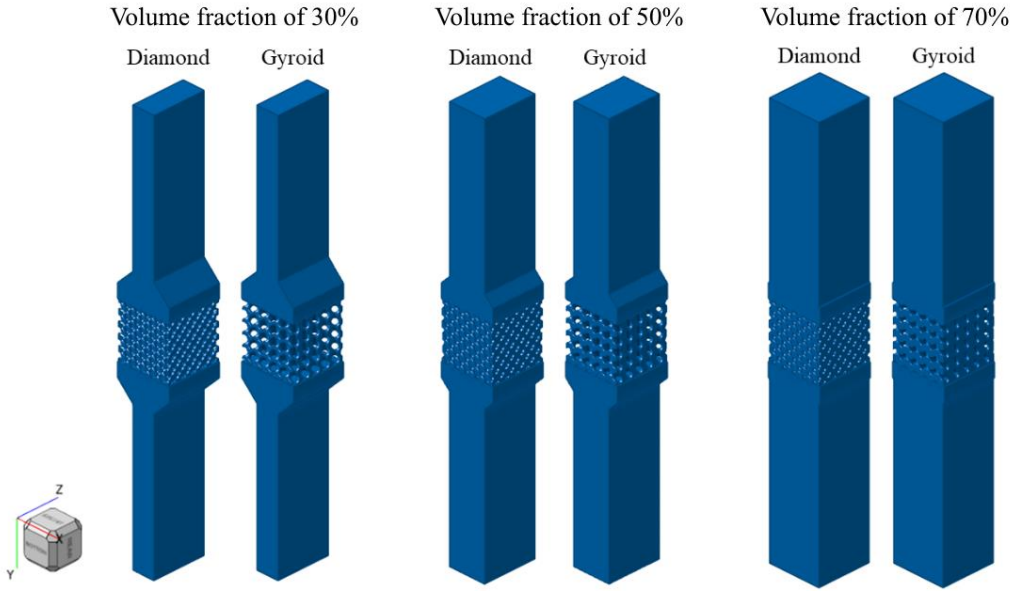

Fig. 5. CAD models of metamaterial specimens (diamond and gyroid) with three volume fractions of solid material (30, 50 and 70%) for full-scale tests on cyclic loading

The lattice-based diamond structure was designed with the strut thickness set equal to 0.4, 0.56, 0.71 mm for volume fractions of 30, 50 and 70 %, respectively. The surface-based gyroid structure is designed with the required volume fraction set from 0 to 1, where 0 is the absence of material and 1 is solid material. In our case, the volume fractions were 0.3, 0.5 and 0.7. The obtained minimum thicknesses of the "trabeculae" for the gyroid structure were 0.97, 35 and 1.87 mm.

Specimens for full-scale tests

Solid specimens (15 pieces) from additive titanium alloy for testing were additively manufactured by selective laser melting on a Concept Laser M2 industrial 3D printer (GE Additive, Germany) with the printing area of 250 × 250× 280 mm^3 (Fig. 6). A biocompatible Ti-6Al-4V powder was used for 3D printing of specimens from additive material.

(a) (b)

Fig. 6. 3D-printing equipment and prepared Ti-6Al-4V specimens: (a) Concept Laser M2 industrial 3D printer, (b) 3D-printed solid specimens for testing

The metamaterial specimens based on the designed geometric models were prepared by SLM from biocompatible Ti-6Al-4V powder also using the Concept Laser M2 printer. A series of specimens with three volume fractions was prepared for each of the two types of metamaterials for cyclic loading tests. Examples of additively produced specimens are shown in Fig. 7. A total of 12 specimens (2 identical specimens of each type) were printed for full-scale tests of metamaterials.

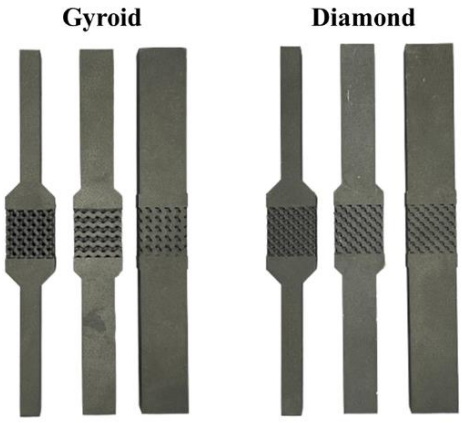

Fig. 7. Front view of printed metamaterial specimens based on Ti-6Al-4V alloy (gyroid and diamond) with three volume fractions of solid material (30, 50 and 70 %) for full-scale tests on cyclic loading

Evaluation of material density

Because the metamaterial specimens for full-scale testing are manufactured additively and have a complex structure, their volume and geometric characteristics differ from the nominal characteristics of the corresponding CAD models. The specimens for full-scale tests are dry-weighed, with the actual porosity of the meta-biomaterial subsequently determined, which allows to adjust the geometry of the specimen model to reproduce the experiments in a simulation environment and bring the model parameters closer to the characteristics of the printed specimen.

To calculate the actual volume fraction, or volume content, of solid material in a metamaterial, in addition to the mass of the samples, the density of the titanium alloy used in printing the samples is determined. By weighing fifteen solid samples of the same type made for fatigue testing and calculating the average mass of one sample and based on the sample volume known from its digital model, simple calculations can be used to obtain the density of the solid material based on the additive titanium alloy. Then, to calculate the value of the actual volume fraction of the solid phase of the metamaterial of each sample, it is necessary to consider the lattice structure of the metamaterial without taking into account the grips added to the metamaterial sample for its attachment in the testing machine.

$$\varphi = \frac{\rho_{lattice}}{\rho_{Ti6Al4Vi}}, \quad (1)$$

$$\rho_{lattice} = \frac{m_{lattice}}{V_{lattice}}, \quad (2)$$

$$m_{lattice} = m_{sample} - m_{grips}, \quad (3)$$

$$m_{grips} = V_{grips} \cdot \rho_{Ti-6Al-4V}, \quad (4)$$

where φ is the volume fraction of the solid phase of the metamaterial; $\rho_{lattice}$ is the effective density of the metamaterial, defined as the ratio of the mass of the metamaterial specimen under consideration to its overall volume; $\rho_{Ti-6Al-4V}$ is the actual density of the Ti-6Al-4V titanium alloy used; $m_{lattice}$ is the mass of the metamaterial specimen under consideration, in this study in the form of the cube of 15 × 15 × 15 mm^3; $V_{lattice}$ is the overall volume of the metamaterial specimen under consideration, equal to 3.375 mm^3; respectively, m_{sample} is the mass of the entire printed test specimen consisting of the cube of metamaterial and additional grips; m_{grips} is the mass of additional solid titanium alloy grips for attaching the specimen in the machine added to the metamaterial specimen; V_{grips} is the volume of the additional grips.

After the relative density of the periodic structure of the specimens is determined, the numerical model is corrected to take into account the obtained volume fractions and is used for reproducing full-scale tests in the simulation environment. In the case of lattice specimens, the thickness of the strut is varied in accordance with the obtained relative density of the meta-biomaterial; in the case of the surface structure, the geometry is adjusted directly by setting the actual volume fraction.

Testing procedure for determining fatigue properties

The purpose of the cyclic tests was to construct the S-N curve to subsequently determine the fatigue limit of the solid material. In our case, tests were carried out for 15 solid specimens up to their fracture under various loads. Cyclic loading tests to determine the

fatigue properties at room temperature were carried out on a Zwick Roell AMSLER 100 machine (Fig. 8) with testXpert V12.3 software. A resonant system with variable loading frequency was used in the experiments, allowing to adjust the loading frequency to ensure stable loading in the selected range.

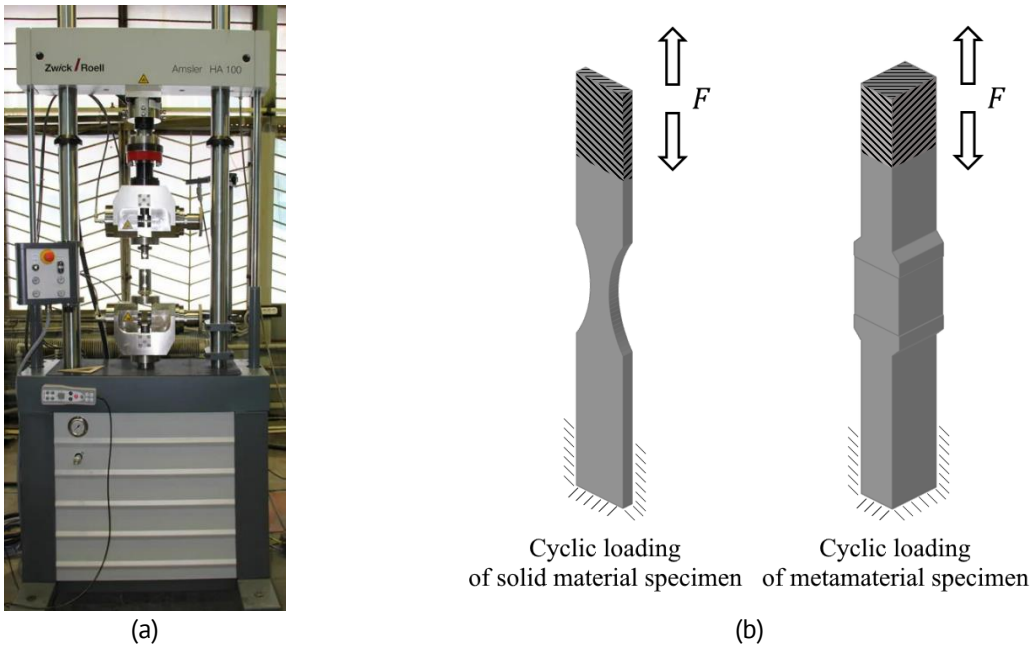

Fig. 8. Experimental equipment and loading conditions for cyclic loading tests: (a) Zwick Roell AMSLER 100 system, (b) loading conditions for solid specimens and metamaterial specimens

The uniaxial stress state of the test specimen is characterized by the load cycle asymmetry coefficient $R = \sigma_{max}/\sigma_{min}$, where σ_{min} and σ_{max} are the minimum and maximum values of stresses applied to the specimen in the load cycle. Tests for constructing the S-N curve and determining the fatigue characteristics of the solid material are usually carried out with a symmetrical tension-compression cycle, when $\sigma_{min} = -\sigma_{max}$. For each tested specimen, the loading amplitude, the number of fracture cycles, and the cyclogram were recorded. Testing of one speciment before reaching the destruction forms one point of the S-N curve in the coordinates "force – number of loading cycles".

According to GOST 25.502-79 [18], at least 15 identical specimens are tested to build a fatigue curve and determine the fatigue limit corresponding to a 50 % probability of failure. At least three specimens are tested within the 0.95–1.05 fatigue limit stress range, corresponding to a 50 % probability of failure, and at least half of them must not fracture within the selected number of test cycles. In our case, the number of cycles for determining the fatigue limit is taken equal to 2 million.

The test results are used to plot points on the axes corresponding to the number of cycles versus stress amplitude in log-log coordinates. The fatigue curve is plotted in log-log coordinates based on the test results of the specimens after processing the experimental data using the least squares method. The left, inclined branch of the fatigue curve is described by the equation of the form:

$$\sigma_a(N) = A \cdot N^{-B}, \quad (5)$$

where $\sigma_a(N)$, MPa, is the stress amplitude of the cycle; A is the coefficient corresponding to the maximum stress that the material can withstand in one loading stage, approximately corresponding to the intersection of the curve with the ordinate axis; N is the fatigue life expressed as the number of cycles for a given stress amplitude; B is the exponent characterizing the slope of the straight line plotted in log-log coordinates using the least squares method from the points corresponding to the test results.

The right branch of the fatigue curve is a horizontal straight line. The coefficients of the obtained fatigue curve are calculated in the postprocessing software, provided together with the experimental data for each specimen. The experimental data is processed based on the technique described in [21].

One of the main factors influencing the results of high-cycle fatigue testing for metamaterials is the surface roughness in the gauge section. Additive manufacturing technologies using metal powders provide a relatively low quality of the surface, with local structural defects observed. A possible solution to this problem is mechanical processing of the obtained specimens. However, such processing was not included in the experimental plan, since the goal of this study was not to obtain the most durable specimens through additional manipulations, but rather to determine the mechanical characteristics of meta-biomaterials under conditions best reproducing their real-life cycle.

In view of this, the following factors were taken into account to determine the fatigue properties of metamaterials: more predictable, reproducible behaviour close to solid material for specimens with the high volume fraction, which is why such specimens were tested first; the yield strengths found in previous experiments for similar specimens [22], allowing to evaluate the upper bound for the load amplitude multiplied by 0.8; accounting for the S-N curve obtained for solid material and the fatigue limit.

After a series of preliminary experiments was conducted and the first results were obtained, we found that the most effective technique for predicting the stress amplitude turned out to be the comparing the yield strength ratios for the solid and the metamaterial with the fatigue limit ratios for the same specimens. The tests were repeated for 2 million cycles. After that, the specimen was considered unfractured. In some cases, the duration of the test was increased to assess whether the selected bound was correct.

Finite element models of metamaterials and specimens

Computational mathematical models based on the finite element method were developed based on the prepared 3D CAD models of the specimens made of solid material and two types of metamaterials. Full-scale tests on fatigue strength were reproduced in a simulation environment in two stages. The first stage was uniaxial tension for each metamaterial specimen in the Abaqus software, describing a half-cycle (symmetric tension-compression cycle) of the fatigue test. The procedures for developing the numerical models and performing the simulations were done in Abaqus. The problems were solved on a workstation equipped with Intel Xeon Silver 4210R processor (2.4 GHz, 12 cores).

Finite element meshes for the models of metamaterials considered are given in Fig. 9, schematically showing the kinematic boundary conditions of the solved problem on tension of a deformable solid by the displacements set along the specimen axis. Fixed

zero displacements of the mesh nodes at one end of the specimen simulate rigid fixation of the specimen in the grips of the testing machine, while the given non-zero component of the displacements along the specimen axis simulates the movements of the crosshead.

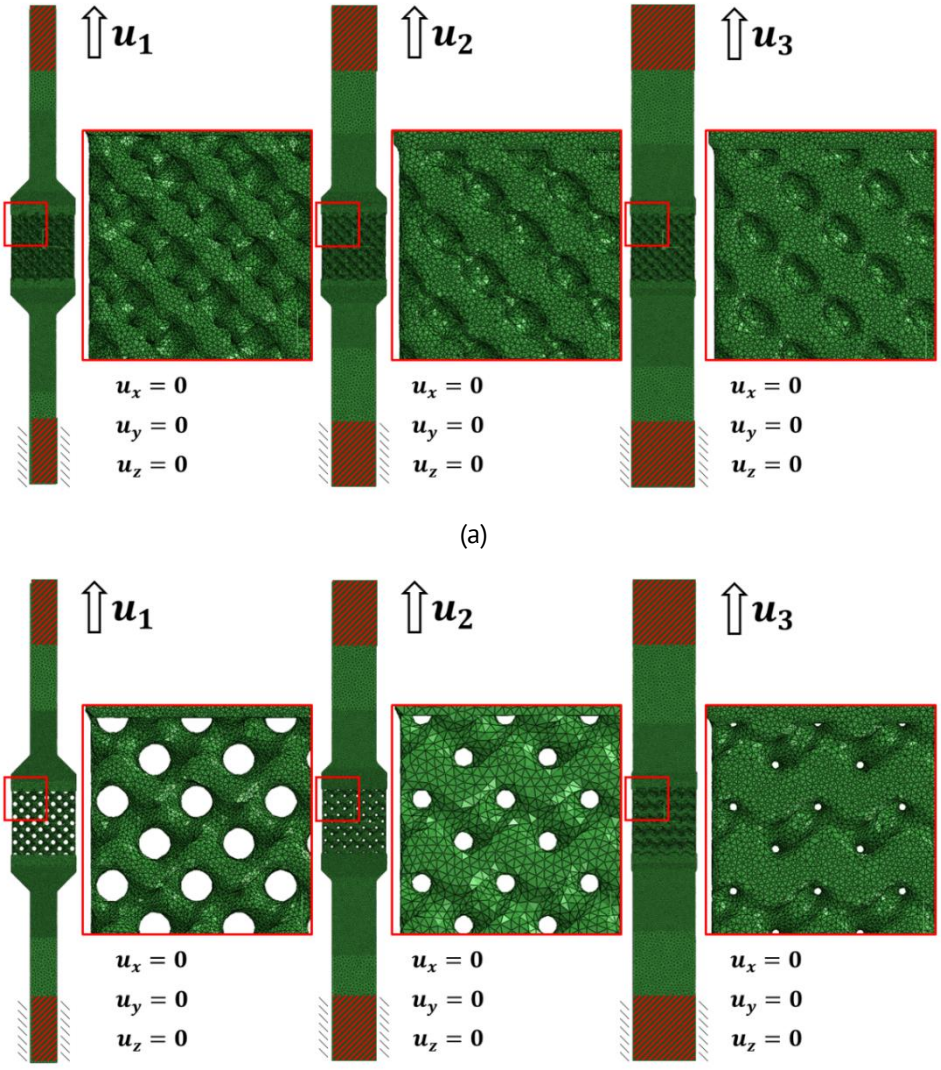

Fig. 9. Schematics for design of numerical tests on uniaxial tension of metamaterial specimens and fragments of finite element mesh: (a) diamond, (b) gyroid. The specimens with 30, 50 and 70 % volume contents of titanium alloy are shown from left to right

The load application region is kinematically coupled to the reference point, for which a non-zero displacement in the longitudinal direction is set. The displacement value is selected so that the final deformation of the specimen's gauge corresponds to the deformation obtained in the full-scale test. The displacement value during the tensile tests varies linearly from zero to a maximum equal to 3, 4, and 5 mm for specimens with the metamaterials of the considered volume fractions (Fig. 9).

In the case of numerical tests of the metamaterial, the size of the finite element in the gauge section of the metamaterial specimens was 0.1 mm due to geometric complexity of the internal structure. The quantitative characteristics of the finite element meshes are given in Table 1. The resulting files with the computational results are

imported from Abaqus into the Altair HyperLife environment for the second stage of simulation evaluating the fatigue properties of the model.

Table 1. Quantitative characteristics of finite element models of metamaterial specimens for numerical simulations

Specimen	Nodes	Elements
Diamond, 30%	304 396	1 210 275
Gyroid, 30%	249 756	988 563
Diamond, 50%	297 937	1 232 168
Gyroid, 50%	96 911	402 611
Diamond, 70%	299 051	1 266 728
Gyroid, 70%	261 777	1 104 826

Simulation procedure for high-cycle fatigue tests

Numerical simulations reproducing the fatigue tests were performed in the Altair HyperLife 2023.1 fatigue analysis software, using basic solvers, including support for post-processing of stress results from the Abaqus environment. Setting up fatigue tests in the computational environment requires importing a solver file with the results of finite element analysis of the specimen, specifying the parameters of the material model and specifying the fatigue curve for a symmetrical loading cycle. The files with the results of quasi-static simulations for uniaxial tension of diamond and gyroid specimens with the volume fractions of 30, 50 and 70 % of solid material were taken as input files for fatigue analysis.

Loading steps from Abaqus are recognised in Altair HyperLife, each step corresponding to a specific force, which is a response to the displacement applied to the specimen during the simulation of uniaxial tension. The loading step for the numerical test is selected in accordance with the load applied in the full-scale test. If necessary, the load is multiplied by a factor so that it exactly matches the load during the full-scale test. The load selected for the simulation at the compression stage is multiplied by a negative factor. Thus, two peak loading points are determined in the tension-compression cycle.

To assess fatigue, a symmetrical loading cycle is set by indication of the maximum tensile and compressive loads. The loads for numerical fatigue tests were selected in accordance with the value of the load during a full-scale fatigue test. In the computational assessment of fatigue characteristics, the fatigue strength estimation method was used with Goodman correction of average stresses under uniaxial loading.

In Altair HyperLife, any user-defined S-N curve must be specified for a symmetrical loading cycle, and should consist of two linear sections defining the relationship between the durability N_f and the amplitude of stresses during a symmetrical loading cycle:

$$S(N_f) = \begin{cases} S_1 \left(N_f\right)^{-b_1}, \ N_f \le N_{limit} \\ FL \left(N_f\right)^{-b_2}, \ N_f > N_{limit} \end{cases}, \quad (6)$$

where S is the stress amplitude of the symmetrical cycle (σ_a in Eq. (5)), S_1 is the coefficient of fatigue strength, N_{limit} is the maximum number of cycles before failure, FL is the fatigue limit, b_1 and b_2 are the first and second fatigue strength indicators equal to the slope coefficients of straight lines on a logarithmic scale.

The previously introduced fatigue equation (5) describes the left branch of the S-N curve (Fig. 11), constructed according to Eq. (6), if we take the coefficients $b_1 = B$ and

$S_1 = A$. In addition, for certainty, Fig. 10 shows a view of the fatigue curve with a horizontal right-hand branch corresponding to the exponent $b_2 = 0$, which is a frequently used model case when describing the phenomenon of fatigue in metals.

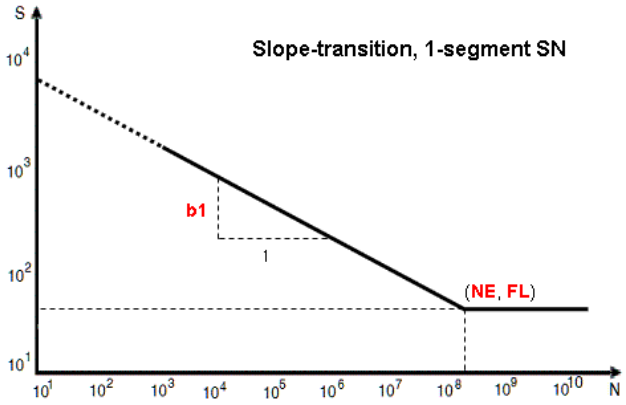

Fig. 10. Scheme of one-segment SN curve

The parameters set for the material model are elastic modulus, Poisson's ratio, ultimate tensile strength of the material, the characteristics of the fatigue curve, namely, the exponent B, the maximum number of cycles to failure N_{limit} and the fatigue limit FL. In our case, elastic modulus was 105 803 MPa, Poisson's ratio was 0.3 and ultimate tensile strength of the material was 906 MPa [22]. The mean computational time to evaluate the fatigue characteristics of one specimen with Altair HyperLife software on an Intel Xeon Silver 4210R processor is 1.8 h.

Results and Discussion

Evaluation of geometric parameters and density

The specimens made of the additively manufactured titanium alloy were subjected to measurements of the geometric dimensions and weighing to assess the quality of 3D printing. The actual dimensions of the specimens are given in Table 2. The mean cross-sectional area in the narrowest point of the gauge section was 17.9 mm^2, and the density of the titanium alloy was 4 305 kg/m^3.

Table 2. Geometric characteristics of solid specimens

Specimen	Gauge thickness *h*, mm	Gauge width *b*, mm	Cross-sectional area *A*, mm^2	Specimen	Gauge thickness *h*, mm	Gauge width *b*, mm	Cross-sectional area *A*, mm^2
1	2.99	5.99	17.91	9	2.98	5.97	17.79
2	3.02	5.99	18.09	10	2.98	5.96	17.76
3	2.98	6.00	17.88	11	2.99	5.99	17.91
4	3.00	6.01	18.03	12	2.99	6.00	17.94
5	2.99	5.98	17.88	13	2.97	5.98	17.76
6	3.00	5.97	17.91	14	2.98	5.98	17.82
7	3.01	6.01	18.09	15	2.97	5.98	17.76
8	2.99	6.00	17.94	–	–	–	–

Specimens of the diamond and gyroid types with three volume fractions of solid material – 30, 50 and 70 % – were printed for the full-scale tests (two identical specimens of each type, 12 specimens in total). The overall dimensions of the gauge cross-section of the metamaterial specimens are given in Table 3. The actual mass of specimen types was determined as the arithmetic mean of the masses of the specimen type entities (Table 4).

Table 3. Geometric characteristics of gauge section of metamaterial specimens

Specimen	Specimen ID	Overall gauge thickness h, mm	Overall gauge width b, mm
1	FD-70-1	14.89	14.61
2	FD-70-2	14.96	14.59
3	FG-70-1	14.90	14.61
4	FG-70-2	14.95	14.61
5	FD-50-1	15.28	14.90
6	FD-50-2	15.29	14.92
7	FG-50-1	15.29	14.91
8	FG-50-2	15.25	14.88
9	FD-30-1	15.03	14.98
10	FD-30-2	15.07	14.97
11	FG-30-1	15.29	14.84
12	FG-30-2	15.21	14.91

Table 4. Actual mass of specimens for fatigue tests

Volume fraction, %	Mass of diamond specimens, g	Mass of gyroid specimens, g
30	54.5	52.4
50	79.9	78.1
70	105.2	104.9

The actual volume fraction of each specimen differs from the nominal value by no more than 5 % (Table 5). The exception is the diamond with the nominal volume fraction of 30 %. Because thinner structural elements were included in this type of meta-biomaterial compared to specimens of other types, the volume fraction of the diamond 30 % specimen was deliberately exceeded by 27.5 % compared to the target at the stage when the model was constructed for printing, since the minimum thickness of the strut was set at 1 mm (radius of 0.5 mm).

Table 5. Actual volume fractions of metamaterial specimens

Volume fraction, %	Volume fraction of diamond specimens, %	Volume fraction of gyroid specimens, %
30	45.7	31.5
50	63.8	51.7
70	72.9	70.8

Results of cyclic tests for specimens made of solid material

The results of the cyclic tests performed with 15 specimens made of additively manufactured Ti-6Al-4V alloy are given in Table 6, including the cyclic load frequency, the load amplitude (also converted to longitudinal stress occurring in the narrowest point of the specimen's gauge section) and fatigue life expressed as the number of loading cycles

that the specimen withstood. The rows are sorted in descending order from the highest load applied to the lowest. One of the prepared specimens (specimen 3) was used only for calibrating the equipment, so its experimental characteristics are not given in Table 6.

Table 6. Parameters of cyclic tests for solid specimens

Load amplitude, F_a, kN	**Stress amplitude, σ_a, MPa**	**Fatigue life, N_f, cycles**	**Test frequency, f,Hz**	**Specimen**	**Note**
13.43	750	2 492	66.7	1	–
9.04	500	9 315	67.5	2	–
7.66	430	31 407	66.8	14	–
7.16	400	49 363	71.3	11	–
5.41	300	180 259	68.0	4	–
4.84	270	195 001	67.9	6	–
4.44	250	769 413	66.8	15	–
4.34	240	403 988	67.5	7	–
4.3	242	–	66.7	13	No failure after 3 877 783 cycles
4.16	232	–	67.9	12	No failure after 4 000 020 cycles
4.13	230	382 689	67.7	8	
4	225	–	68.6	10	No failure after 4 000 008 cycles
3.93	220	–	68.0	5	No failure after 4 000 007 cycles
3.74	210	–	67.5	9	No failure after 4 000 000 cycles
–	–	–	–	3	Reference specimen

The appearance of the specimens after completion of the tests is shown in Fig. 11. As can be seen from the photographs, several specimens (specimens 5, 9, 10, 12, 13) remained intact after reaching the maximum number of loading cycles. The experimental data for the remaining specimens – the values of the stress amplitude of the loading cycle and the number of loading cycles that the specimen could withstand – are plotted in log-log coordinates (Fig. 12). Fatigue failure expectedly occurred in the smallest gauge cross-section, where maximum normal stresses occur along the longitudinal axis of the specimen.

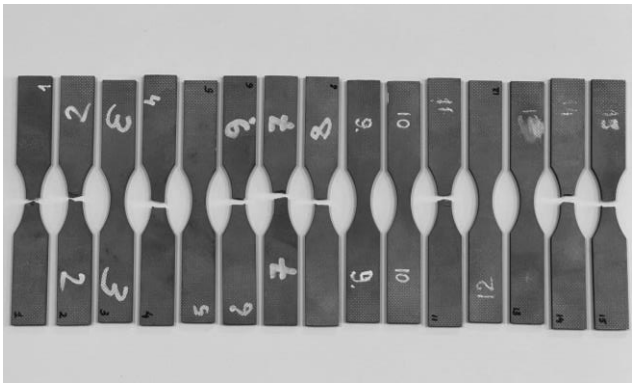

Fig. 11. Solid specimens after fatigue tests

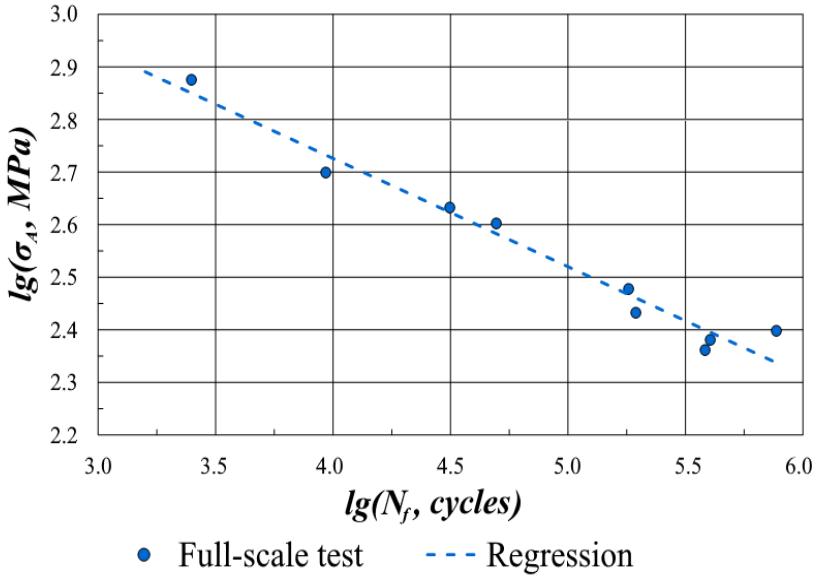

Fig. 12. Experimental results of cyclic tests of solid samples and the regression line in log-log coordinates

A regression dependence was constructed from the experimental points, satisfactorily approximating the linear dependence of the number of loading cycles that the material can withstand on the stresses in the material. The regression coefficients give the values of the exponent B and the amplitude of the fatigue curve of the material (Table 7). The fatigue limit of the Ti-6Al-4V alloy, equal to 213 MPa, was also determined, which is significantly less than the yield strength generally characterizing the strength properties of the material under static loading. Notably, high-cycle failure has a significantly probabilistic nature, and cases when two specimens exhibited significant difference in fatigue life under the same load were observed in full-scale tests.

Table 7. Equation coefficients for inclined branch of fatigue curve for solid material

Fatigue limit after 2 million cycles, FL, MPa	**Equation coefficients for horizontal branch of fatigue curve $\sigma_a(N) = A \cdot N^{-B}$**		
	A, MPa	**B**	**Fatigue life at knee point N_{limit}, cycles**
213	3 547.2	0.206	861 778

Results of cyclic tests of metamaterial specimens

The results of cyclic tests for metamaterial specimens made of additively manufactured Ti-6Al-4V alloy are given in Table 8 and photographs of the specimens after the completion of the tests are shown in Fig. 13. Analysing the results, we found that not all specimens failed under the given cyclic loading: in fact, not only specimens with the high volume fraction of solid material but also specimens with a 30 % volume fraction did not fail.

Table 8 gives the type of specimen, loading cycle frequency, load amplitude (including amplitude converted to longitudinal stress occurring in the narrowest gauge cross-section of the specimen), fatigue life found expressed as the number of loading cycles that the specimen can withstand. The cycle frequency was chosen slightly higher compared to tests of solid materials to shorten the duration of the experiment. Three

specimens did not fail when the maximum number of loading cycles was reached, two of which were specimens with the highest porosity. One specimen failed outside the gauge section, which may be due to a printing defect or stress concentration occurring in the transition zone.

Table 8. Results of full-scale tests for metamaterial specimens

Specimen ID	Load amplitude F_a, N	Fatigue life N_f, cycles	Test frequency, f, Hz	Specimen	Note
FD-70-1	7 000	2 000 000	113.5	1	No failure
FD-70-2	30 000	27 092	129.4	2	–
FD-50-1	8 500	3 818 281	97	5	–
FD-50-2	10 000	1 954 603	96.5	6	–
FD-30-1	5 700	103 175	81.2	9	Failure outside gauge section
FD-30-2	5 100	4 000 083	84.2	10	No failure
FG-70-1	9 500	1 048 331	107.1	3	–
FG-70-2	9 500	638 703	107.2	4	–
FG-50-1	5 100	1 040 982	94.1	7	–
FG-50-2	5 100	799 347	94.2	8	–
FG-30-1	2 100	4 000 000	75.7	11	No failure
FG-30-2	2 500	524 977	75.6	12	–

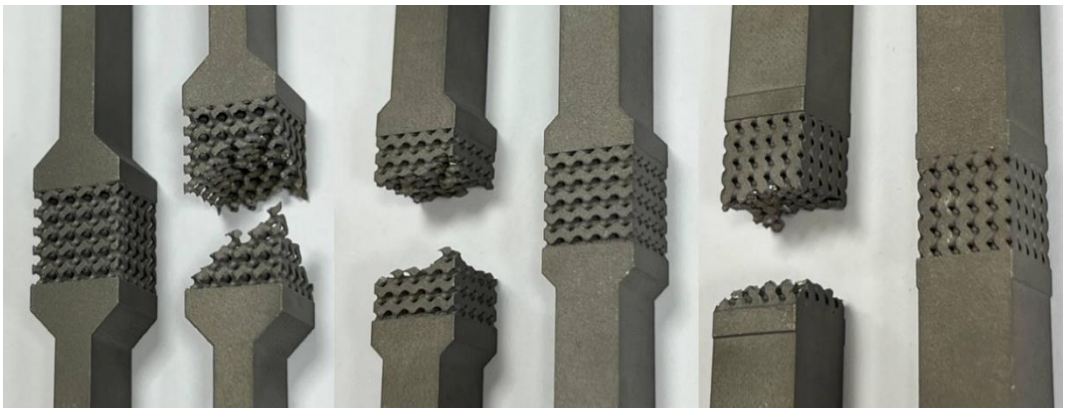

(a)

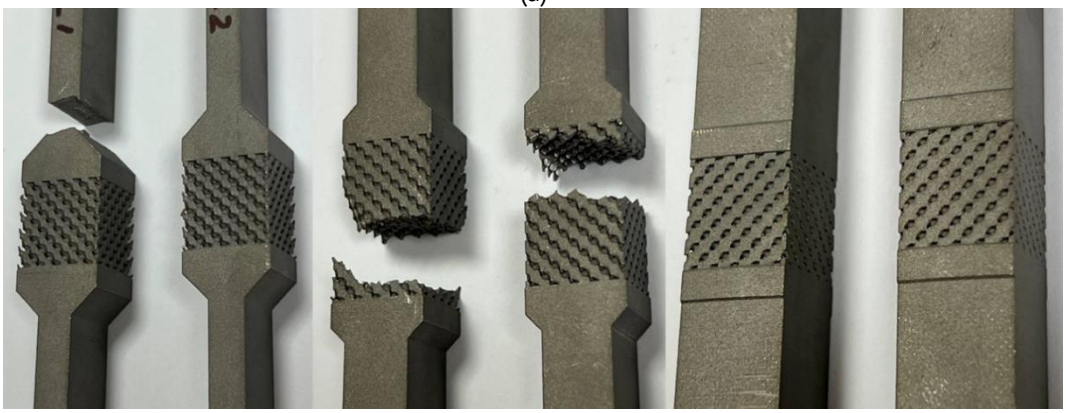

(b)

Fig. 13. Photographs of specimens after full-scale fatigue tests at time of failure or after reaching the maximum number of loading cycles without failure: (a) from left to right, gyroid specimens, 2 specimens for each volume fraction (30, 50 and 70 %) of solid material, (b) from left to right, diamond specimens, 2 specimens for each volume fraction (30, 50 and 70 %) of solid material

Thus, the presence of a stress concentrator in the grip section of the specimen in the transition from a wider to a thinner part is an essential factor for evaluating the number of cycles to failure in some specimens. Moreover, the selected load turned out to be low for some specimens.

Simulation results for metamaterial specimens

Numerical analysis of the maximum number of loading cycles (i.e., fatigue life in Altair HyperLife terms) was carried out based on static analysis of the stress-strain state of the specimens (Fig. 14).

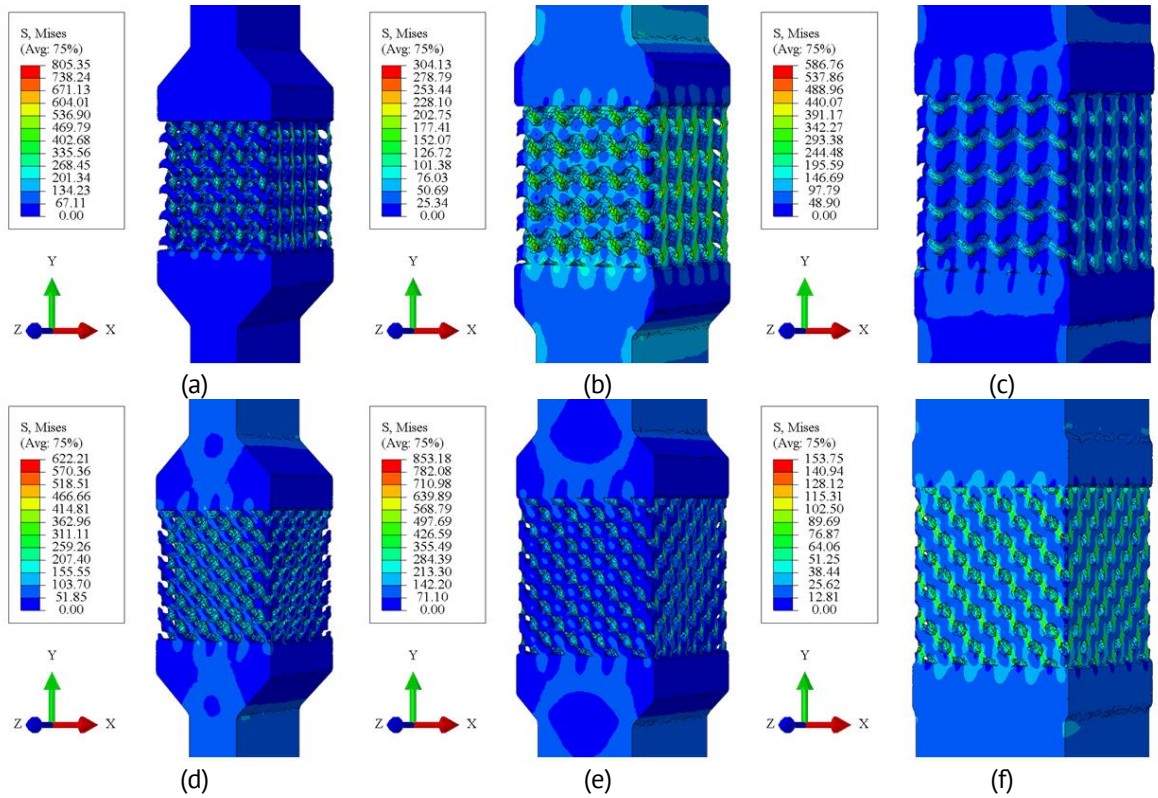

Fig. 14. Distribution of von Mises stress intensity (MPa) for metamaterial specimens with various volume fractions at selected step for analysis in Altair Hyperlife: (a) gyroid 30 %, (b) gyroid 50 %, (c) gyroid 70 %, (d) diamond 30 %, (e) diamond 50 %, (f) diamond 70 %

Figure 15 shows the results as the distribution of the life span, i.e., fatigue life. As can be seen from the fatigue life fields (Fig. 15), all specimens withstood a cyclic load coinciding with the load set during full-scale tests. However, the obtained theoretical values of fatigue life for each specimen turned out to be significantly higher in comparison with the values obtained during full-scale tests. Numerical analysis indicated that the failure did not occur in the specimens.

In view of the above, a parameter C_{finish} responsible for surface roughness of the specimen was introduced into the calculations of the number of cycles to failure (Fig. 16). In this case, the fatigue limit is multiplied by this parameter: $FL' = FL \cdot C_{finish}$.

As already mentioned above, high-cycle fatigue failure is considerably probabilistic in nature, and cases when two specimens had a significant difference in fatigue life at the same load were observed in full-scale tests. Numerical simulation methods do not

allow to detect the precise time of loss of integrity for the specimen, instead providing only the fatigue life for each individual finite element.

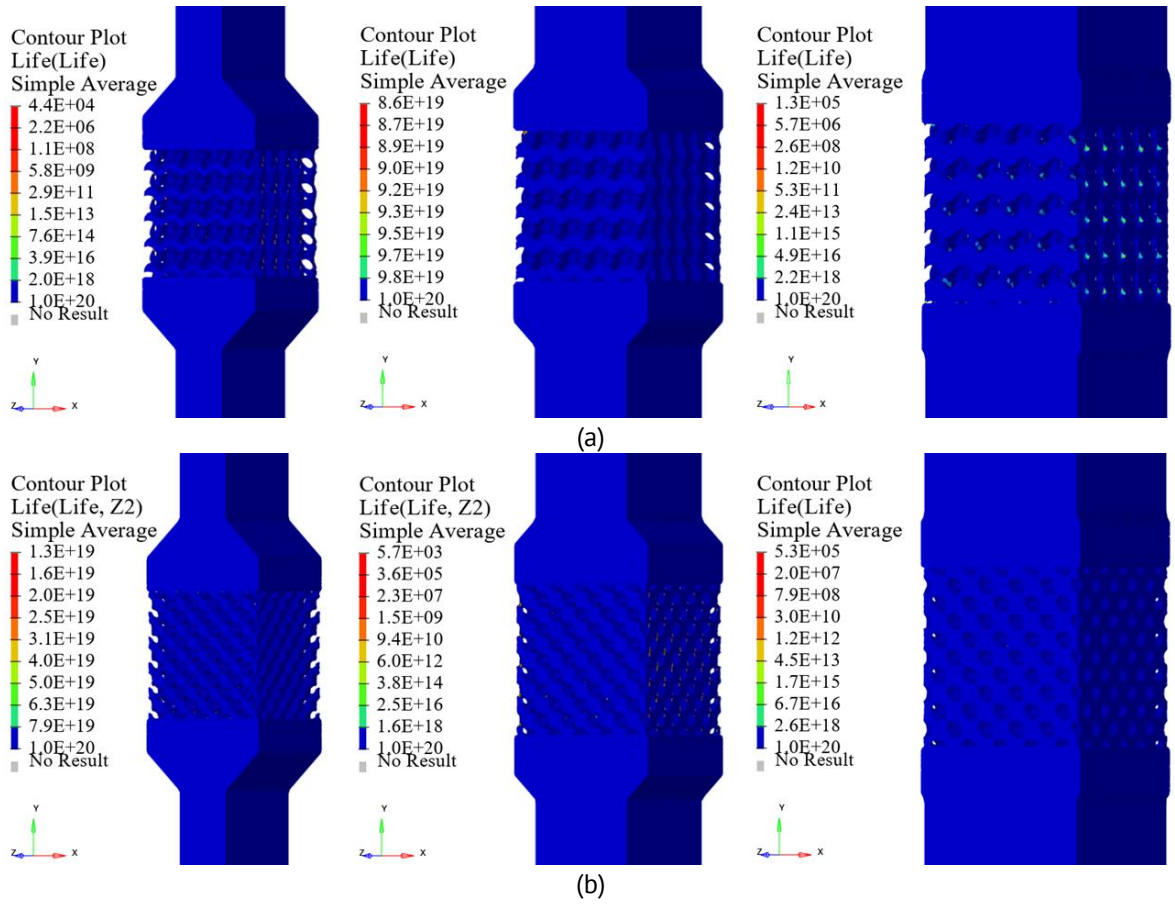

Fig. 15. Numerical estimates for fatigue life based on simulations: (a) from left to right, gyroid specimens with 30, 50 and 70 % volume fractions of solid material, (b) from left to right, diamond specimens with 30, 50 and 70 % volume fractions of solid material

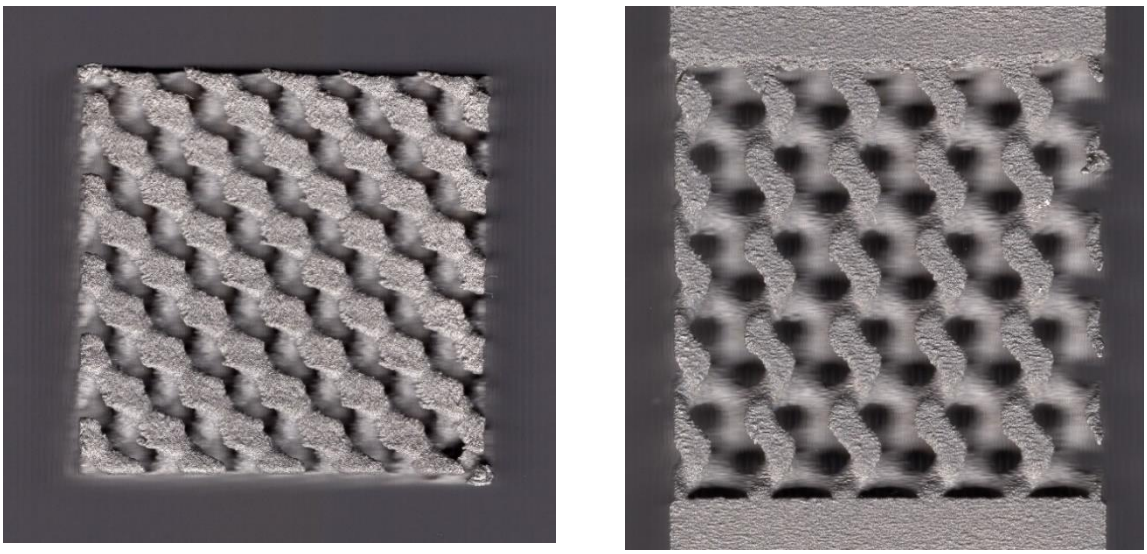

Fig. 16. Photographs for surface of typical specimens, demonstrating poor surface quality of metamaterials obtained by 3D printing

The results of fatigue tests are significantly affected by the surface quality of the specimens and the presence of microcracks and other defects. In the case when meta-biomaterial is produced using additive technologies, this effect becomes key due to the high ratio of surface area to the volume in comparison with conventional solid structures. When cyclic loading with a low amplitude is used to determine the fatigue limit of the material and plot the S-N curve with a large number of cycles (more than 2 million), theoretically extending to a horizontal section, the accuracy of predicting the fatigue life also decreases.

Due to the features of cyclic testing described above, the following approach was used to calibrate the fatigue curve:

1. range of values limited by two obtained results was considered for full-scale tests at a fixed load;
2. adequacy of calibration of the S-N curve was estimated entirely based on the results for all full-scale tests performed;
3. additional parameter C_{finish} was introduced to account for the effect of the surface finish quality;
4. loss of integrity was assumed to occur in the specimen if a significant number of elements (about 50 %) with a fatigue life below the considered value were found in the gauge section at a considered time.

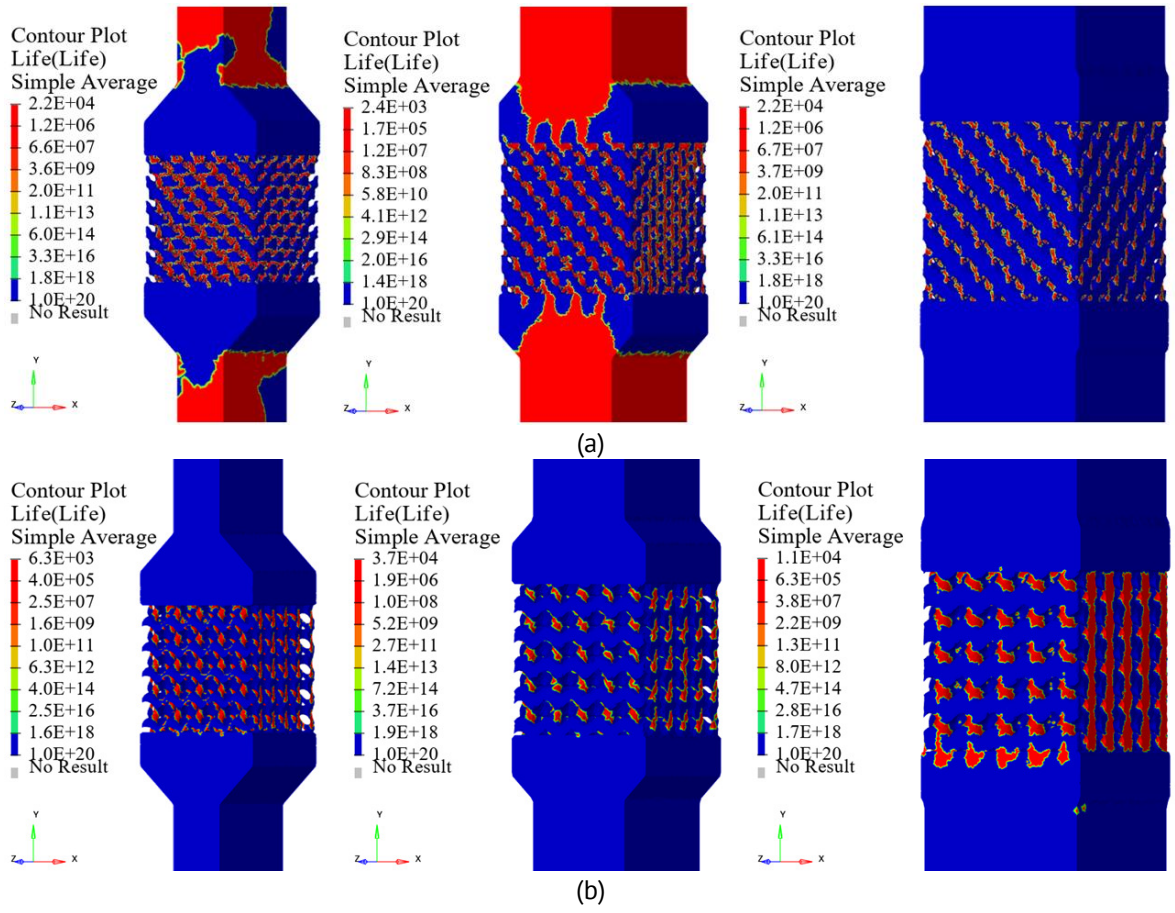

Fig. 17. Numerical estimates for fatigue life based on simulations accounting for the surface roughness parameter: (a) from left to right, gyroid specimens with 30, 50 and 70 % volume fractions of solid material, (b) from left to right, diamond specimens with 30, 50 and 70 % volume fractions of solid material

As a result, we obtained a fitted fatigue model of the material for further calculations with a coefficient of 0.25 accounting for the influence of surface roughness. The simulation results for each full-scale test performed are shown in Fig. 17.

A comparison of the results of full-scale fatigue tests and numerical simulations taking into account the roughness parameter introduced into the numerical model is presented in Table 9. The numerical tests evaluated the volume percentage of the elements in the gauge section of the metamaterial specimen that can withstand the number of cycles obtained during the corresponding full-scale test. This volume did not include the elements in the grips, only the elements in the gauge section. The percentages obtained are listed in the last column of Table 9.

Table 9. Comparison of results of full-scale and numerical (with roughness parameter) fatigue tests

Specimen	Specimen type	Load amplitude F_a, N	Number of cycles to failure for specimen in full-scale tests	Volume percentage of gauge section in FEA model of the specimen withstanding the corresponding number of cycles in full-scale test, %
1	FD-70-1	7 000	2 000 000	63.8
3	FG-70-1	9 500	1 048 331	49.6
4	FG-70-2	9 500	638 703	57.5
6	FD-50-2	10 000	1 954 603	22.6
7	FG-50-1	5 100	1 040 982	67.0
8	FG-50-2	5 100	799 347	67.0
10	FD-30-2	5 100	4 000 083	33.3
12	FG-30-2	2 500	524 977	72.7

Analysing the results of numerical fatigue tests, we observe that the mean percentage of elements in the gauge section that did not fail is 52.4 % for all specimens, with the target value of 50 %. Thus, we estimate the difference between the results of full-scale and numerical fatigue tests as 4.8 %. The degree of agreement between the results allows to conclude that this model of solid material can offer high fidelity in numerical fatigue tests of meta-biomaterial specimens manufactured by additive technologies from Ti-6Al-4V alloy, allowing to expand the range of approaches to numerical analysis of fatigue.

Discussion

Studying the fatigue characteristics of the specimens made of solid titanium and metamaterials, fabricated by selective laser melting, we detected several major trends for further detailed discussion in the context of existing theory.

The obtained values of the fatigue limit for solid Ti-6Al-4V (213 MPa for 2 million cycles) are consistent with the data given in [5,6,23], where values in the range of 200–250 MPa were observed for similar test conditions (symmetrical cycle, $R = -1$). However, there was a significant variance in the results for metamaterials. This can be explained by increased sensitivity of metamaterials to surface defects.

Weighing shows that the actual volume fractions of metamaterials differed from the nominal ones by 5–27 %, which is typical for SLM technologies due to incomplete melting of powder and the presence of pores. It was also noted in [24] that non-optimal

parameter selection of laser melting (for example, insufficient laser power or scan speed) cause porosity and microcracks, reducing the fatigue limit by 15–40 %. Similar conclusions are presented in [25], where the fatigue limit for SLM-printed Ti-6Al-4V turned out to be 25 % lower than that of conventional alloy due to internal defects. Furthermore, the surface roughness that was not taken into account in the initial numerical models considerably influences the simulation results in our case. Introducing a correction factor ($C_{finish} = 0.25$) allowed to reduce the discrepancy between the experimental and computational data to 4.8 %. The effect of the microstructure on the fatigue life of the specimen was also considered in [26].

Using the Goodman approach to mean stress correction in Altair HyperLife yielded good agreement with experimental data after fitting. However, the same as in [27], there were limitations in predicting the fatigue life in the horizontal branch of the S-N curve (after N_{limit}). This is due to probabilistic nature of failure in the region of high-cycle fatigue, where microstructural defects play the dominant role. To improve the simulation accuracy in future studies, it is advisable to include probabilistic methods similar to those proposed in [28].

The Gyroid specimens exhibited more predictable behaviour under cyclic loading compared to Diamond, which is consistent with the results provided in [29] for similar structures. The authors explain this by a uniform stress distribution in Gyroid structures, while stresses in Diamond structures tend to concentrate in the connections between the struts. The study also established that cracking begins to accelerate after reaching maximum strength, resulting in a noticeable deterioration in mechanical properties. For Diamond structures, it is recommended to increase the volume fraction of the elements by 20-30% as reinforcement against fatigue failure [30].

Based on the data obtained and literature analysis, optimization of printing parameters can be proposed to increase the fatigue life of material specimens, for example, preheating the platform to reduce residual stresses as in [31], surface post-treatment, which, according to the data in [32], significantly improves the surface quality of the specimen and, accordingly, slows down cracking in the surface layer. Hybrid models combining machine learning and finite element analysis to account for the stochastic nature of defects can also help improve fatigue life and the prediction quality [33].

Conclusion

The paper reports on the fatigue properties of additively produced metamaterial specimens based on the biocompatible titanium alloy Ti-6Al-4V, using experimental and theoretical approaches using the finite element method. Dynamic full-scale tests were carried out under high-cycle loading below the yield strength of the material.

The fatigue curves obtained experimentally were used to determine the fatigue limits and other characteristics of additively produced solid titanium alloy and the metamaterials based on it. Finite element models of the considered metamaterials were also developed and numerical simulation of the obtained specimens was carried out to evaluate the fatigue life of the specimens taking into account the obtained mechanical properties of the additive titanium alloy. The results of full-scale and numerical tests exhibit qualitatively similar dynamic behaviour. Hypothetically, the discrepancies in

numerical and experimental data are due to the observed printing defects of metamaterials with complex internal structure as well as to poor surface quality of the metamaterials resulting from 3D printing.

While full-scale tests remain the gold standard, their high cost and duration have triggered the search for numerical methods based on computational models. The study confirmed the feasibility of using simulation approaches to predict the fatigue characteristics of titanium metamaterials. Importantly, the surface roughness and possible manufacturing defects should be carefully monitored in additive manufacturing of metamaterials to achieve high accuracy.

Accounting for microstructure and defects is crucial for titanium alloys, while a key aspect for metamaterials is to accurately describe the geometry and damage. In view of this, we can conclude from the results obtained that numerical tests for metamaterials with a low volume fraction (30 %) require additional fitting due to increased sensitivity to defects; in the case of lattice structures, it is important to minimize stress concentrators in the interfaces between the gauge and the grip sections. Further research might focus on integrating machine learning to account for the variability in the properties induced by SLM additive manufacturing.

CRediT authorship contribution statement

Leonid B. Maslov: writing – original draft, writing – review & editing; **Aleksey I. Borovkov**: supervision; **Liliya S. Nezhinskaya**: investigation, conceptualization, writing – original draft; **Mikhail A. Zhmaylo**: data curation, writing – review & editing; **Fedor D. Tarasenko**: investigation.

Conflict of interest

The authors declare that they have no conflict of interest.

References

1. Boyer RR. An overview on the use of titanium in the aerospace industry. *Materials Science and Engineering A-structural Materials Properties Microstructure and Processing.* 1996;213: 103–114.
2. Dudescu MC, Vilau C. Mechanical behaviour of 3D-printed metamaterials with tunable stiffness. *The Romanian Journal of Technical Sciences. Applied Mechanics.* 2019;64(2): 153–161.
3. Lewandowski JJ, Seifi M. Metal Additive Manufacturing: A review of mechanical properties. *Annual Review of Materials Research.* 2016;46(1): 151–186.
4. Bartolomeu F, Gasik M, Silva FS, Miranda G. Mechanical properties of Ti6Al4V fabricated by laser powder bed fusion: a review focused on the processing and microstructural parameters influence on the final properties. *Metals.* 2022;12: 986.
5. Boyer R, Welsch G, Collings EW. *Materials Properties Handbook: Titanium Alloys.* ASM International; 1994.
6. Chernavsky SA, Reshchikov VF. *Metalworker's Handbook. Vol.* 2. Moscow: Mashinostroenie; 1976. (In Russian)
7. Feodosyev VI. *Strength of Materials.* Moscow: Bauman Moscow State Technical University Publishing House, 2018. (In Russian)
8. Akahori T, Niinomi M, Fukui H, Ogawac M, Toda H. Improvement in fatigue characteristics of newly developed beta type titanium alloy for biomedical applications by thermo-mechanical treatments. *Materials Science and Engineering: C.* 2005;3: 248–254.
9. Gunawarman, Niinomi M, Akahori T, Souma T, Ikeda M, Toda H, Terashima K. Fatigue characteristics of low cost β titanium alloys for healthcare and medical applications. *Materials Transactions.* 2005;46(7): 1570–1577.

10. Lütjering G, Williams JC. *Titanium*. Berlin: Springer, 2007.
11. Sterling A, Shamsaei N, Torries D, Thompson SM. Fatigue behaviour of additively manufactured Ti-6Al-4V. *Procedia Engineering*. 2015;133: 576–589.
12. Arcari A, Apetre NA, Strickland EP, Michopoulos J. On the assessment of low cycle fatigue performance of octet-based structural metamaterial. *International Journal of Fatigue*. 2025;197(8): 108936.
13. Li PY, Sun WB, Zhang W, Ma YE. Effect of geometric defects on the mechanical properties of additive manufactured Ti6Al4V lattice structures. *Thin-Walled Structures*. 2024;205(15): 112497.
14. Rodrigues JP, Thanumoorthy RS, Manjhi SK, Sekar P, Perumal DA, Bontha S, Balan ASS. Hybrid additive manufacturing of ER70S6 steel and Inconel 625: A study on microstructure and mechanical properties. *Materials Today Communications*. 2023;37: 106977.
15. Liu L, Kamm PH, García-Moreno F, Banhart J, Pasini D. Elastic and failure response of imperfect three-dimensional metallic lattices: the role of geometric defects induced by selective laser melting. *Journal of the Mechanics and Physics of Solids*. 2017;107: 160–184.
16. Yaghoobi M, Chen Z, Sundararaghavan V, Daly S, Allison JE. Crystal plasticity finite element modeling of extension twinning in we43 mg alloys: calibration and validation. *Integrating Materials and Manufacturing Innovation*. 2021;10: 488–507.
17. Bao H, Wu S, Wu Z, Kang G, Peng X, Withers PJ. A machine-learning fatigue life prediction approach of additively manufactured metals. *Engineering Fracture Mechanics*. 2021;242: 107508.
18. Interstate Standard. GOST 25.502-79. *Strength analysis and testing in machine building. Methods of metals mechanical testing. Methods of fatigue testing*. Moscow: Standardinform; 2005. (In Russian)
19. Borovkov AI, Maslov LB, Zhmaylo MA, Tarasenko FD, Nezhinskaya LS. Elastic properties of additively produced metamaterials based on lattice structures. *Materials Physics and Mechanics*. 2023;51(7): 42–62.
20. Borovkov AI, Maslov LB, Zhmaylo MA, Tarasenko FD, Nezhinskaya LS. Finite element analysis of elastic properties of metamaterials based on triply periodic minimal surfaces. *Materials Physics and Mechanics*. 2024;52(2): 11–29.
21. Troshchenko VT, Sosnovsky LA. *Fatigue Resistance of Metals and Alloys*. Kyiv: Naukova Dumka; 1987. (In Russian)
22. Nezhinskaya LS, Borovkov AI, Maslov LB, Zhmailo MA, Tarasenko FD. Study of elastic-plastic properties of meta-biomaterials. Natural and virtual tests. In: *Proc. XXIV Winter School on Continuum Mechanics Perm, February 24–28, 2025*. Perm: PFRC UB RAS; 2025. p.198–199. (In Russian)
23. Leyens C, Peters M. *Titanium and Titanium Alloys: Fundamentals and Applications*. Weinheim: Wiley-VCH, 2003.
24. DebRoy T, Wei HL, Zuback JS, Mukherjee T, Elmer JW, Milewski JO, Beesea AM, Wilson-Heida A, De A, Zhang W. Additive manufacturing of metallic components – Process, structure and properties. *Progress in Materials Science*. 2018;92(3): 112–224.
25. Leuders S, Thöne M, Riemer A, Niendorf T, Tröster T, Richard HA, Maier HJ. On the mechanical behaviour of titanium alloy TiAl6V4 manufactured by selective laser melting: Fatigue resistance and crack growth performance. *International Journal of Fatigue*. 2013;48: 300–307.
26. Wang H, Zhou K, Tian Z, Xie D, Yang Y, He Y, Wang L, Lv F, Shen L. Fatigue performance at ultra-low porosity of Ti6Al4V produced by laser powder bed fusion after post heat treatment. *SSRN* [Preprint] 2022. Available from: dx.doi.org/10.2139/ssrn.4224194.
27. Przybyla C, McDowell D. Microstructure-sensitive extreme-value probabilities of high-cycle fatigue for Ni-base superalloy IN100. *International Journal of Plasticity*. 2010;26(3): 372–394.
28. Fatemi A, Socie D. A critical plane approach to multiaxial fatigue damage. *International Journal of Fatigue*. 1988;10(2): 149–165.
29. Al-Ketan O, Adel Assad M, Abu Al-Rub RK. Mechanical properties of periodic interpenetrating phase composites with novel architected microstructures. *Composite Structures*. 2017(3);176: 9–19.
30. Xu S, Shen J, Zhou S, Huang X, Xie YM. Design of lattice structures with controlled anisotropy. *Materials & Design*. 2016(3);93: 443–447.
31. Vrancken B, Thijs L, Kruth JP, Humbeeck JV. Heat treatment of Ti6Al4V produced by Selective Laser Melting: Microstructure and mechanical properties. *Journal of Alloys and Compounds*. 2012;541: 177–185.
32. Sokolnikov VN, Sukhochev GA, Usov SV, Tochilin IP. Study of the surface layer of a part after a combined mechanical-electrochemical hardening process. *Hardening Coating Technologies*. 2019;15(12): 555–560. (In Russian)
33. Zhan Z, Hu W, Meng Q. Data-driven fatigue life prediction in additive manufactured titanium alloy: A damage mechanics based machine learning framework. *Engineering Fracture Mechanics*. 2021;252(7785): 107850.

MATERIALS PHYSICS AND MECHANICS RESEARCH ARTICLE

Submitted: September 26, 2025 **Revised: November 1, 2025** **Accepted: November 14, 2025**

The design of Zn_2SiO_4 pigments for thermal control coatings

M.M. Mikhailov [1], A.V. Filimonov [2], A.N. Lapin [1], S.A. Yuryev [1] ✉, V.A. Goronchko [1], D.S. Phedosov [1]

[1] Tomsk State University of Control Systems and Radioelectronics, Tomsk, Russia

[2] Peter the Great St. Petersburg Polytechnic University, St. Petersburg, Russia

✉ yusalek@gmail.com

ABSTRACT

Zn_2SiO_4 pigments were synthesized from ZnO and SiO_2 powders obtained from different manufacturers at various concentration ratios and differing in particle size and specific surface area. The optimal values of particle size and specific surface area were determined, thus making it possible to obtain the pigments with a small value of solar absorptance (α_s). The α_s values of the synthesized pigments were compared with other types of pigments used to design thermal control coatings. The study showed that it is possible to synthesize Zn_2SiO_4 powders with high reflectivity in a wide spectral range (200–2500 nm) and a small value of solar absorptance (α_s = 0.077) - significantly lower compared to ZnO powders - using a solid-state method from zinc oxide micropowders and silicon dioxide nanopowders.

KEYWORDS

thermal control coatings • pigments • synthesis • diffuse reflectance spectra • solar absorptance

Funding. *The work was carried out with the financial support of the Ministry of Science and Higher Education of the Russian Federation (Goszadanie No. FEWM-2023-0012).*

Citation: Mikhailov MM, Filimonov AV, Lapin A.N, Yuryev SA, Goronchko VA, Phedosov DS. The design of Zn_2SiO_4 pigments for thermal control coatings. *Materials Physics and Mechanics*. 2025;53(5): 74–82. http://dx.doi.org/10.18149/MPM.5352025_5

Introduction

The temperature of space objects is maintained at a given level by thermal control systems, which include active and passive components [1,2]. The active component is composed of cooling gases, pumps, gas pipelines, and check valves. It is activated in emergencies upon temperature rising [3]. As for the passive thermal control component, it plays the main role in maintaining the temperature at a certain level. It takes the form of a coating applied to thermal control radiators, housings, and individual devices. This coating operates throughout the entire period of orbital flights. Thermal control coatings (TCC) reflect the electromagnetic radiation of the Sun and re-emits the heat generated during the operation of the on-board equipment. The temperature of the objects is solely determined by the absorption of solar energy and by the re-emission of heat released by the on-board equipment. According to the Stefan–Boltzmann law, it can be determined via the following expression: $T \sim k \cdot (\alpha_s/\varepsilon)^{1/4}$, where k is the coefficient comprising the areas of absorbing and emitting surfaces, α_s is the value of solar absorptance, ε is the emissivity of TCC.

If other conditions are kept equal, the temperature is considered proportional to α_s absorption coefficient. Therefore, it is necessary to reduce the value of α_s in order to decrease the area of both TCC and thermal control radiators and to maintain the required temperature. According to international standards [4,5], the values of absorptance should

fall within $\alpha_s \leqslant 0.2$ for TCCs of the optical solar reflector (OSR) class. This requirement is met for the existing conventional TCCs. However, it is necessary to design the coatings with lower α_s values in order to reduce their area, weight, and cost. The TCCs based on dielectric and semiconductor pigments with α_s varying from 0.12 to 0.15 are currently used in thermal control systems [6–8]. To design TCCs with even lower absorption coefficient values, various combinations of components have been recently used in the pigment design. The usage of these components allows one to obtain $\alpha_s \leqslant 0.1$.

The second requirement for modern OSR TCCs is the high stability of absorption coefficient under operating conditions. A number of methods have been recently developed to increase the radiation stability of TCCs, their pigments and binders when they are exposed to solar spectrum quanta and charged particles. These methods are mainly based on three principles:

1. on the modification of TCCs by nanoparticles that act as small-size relaxation centers for primary photo- and radiation defects caused by irradiation;
2. on the modification of TCCs by rare earth elements (REE) that absorb the primary radiation-induced defects;
3. on the formation of protective layers with higher radiation stability on the surface of TCCs. If the composition of TCC includes nanoparticles or SiO_2 particles, which form protective layers on the surface of various compounds [9–12], then it becomes possible to significantly increase the radiation stability of such compounds.

SiO_2 powders have a large band gap [13], therefore, they do not absorb the main part of the solar spectrum and are prone to form protective layers on the surface of inorganic compounds [14]. ZnO powders with a certain particle size distribution show a high reflectance in solar spectrum and sufficient radiation stability when exposed to charged particles and solar spectrum quanta [15–19]. They can be used in the design of highly reflective pigments that can demonstrate stability under ionizing radiation. Therefore, ZnO and SiO_2 powders might appear to be the most suitable components for designing pigments for OSR TCCs.

In view of the above, the purpose of this work was to develop a technology for the synthesis of pigments based on ZnO and SiO_2 powders to be applied in TCCs with ultra-low α_s values.

Materials and Methods

Zn_2SiO_4 powders were synthesized by solid-state method from ZnO micropowder of PA grade (pure for analysis: average particle size 1.3 μm; weight percent of the active ingredient not less than 99.67 %) and silicon dioxide nanopowders of two brands: Aerosil A-300 (particle size of 5–20 nm, specific surface area of 300 m^2/g) and Plasmotherm (particle size of 10–12 nm, specific surface area of 180-220 m^2/g). The ratio of zinc oxide and silica powders was selected to vary from 1:0.35 to 1:0.5. To obtain zinc orthosilicate, ZnO micropowder was mixed with SiO_2 ($nSiO_2$) nanopowder in a ceramic mortar for 20 min. Next, the resulting mixture was heated in a muffle furnace at a temperature of 1100 °C for 2 h. After cooling, the obtained Zn_2SiO_4 powder was ground in a ceramic mortar for 10 min.

X-ray diffraction (XRD) spectra of the powders obtained from $ZnO + nSiO_2$ components were recorded for all their concentration ratios using Shimadzu XRD-6100 X-ray diffractometer. The diffuse reflectance spectra (ρ_λ) were recorded via Shimadzu UV-3600 Plus spectrophotometer with ISR-603 diffuse reflectance attachment within 0.2 to 2.5 μm. Solar absorptance was calculated from ρ_λ spectra using international standards [4,5] and Johnson tables [20].

Results and Discussion

The XRD spectra of Zn_2SiO_4 micropowders (Fig. 1) showed the peaks assigned to willemite – a Zn_2SiO_4 compound in its crystalline modification [21,22]. This modification was in trigonal syngony [23] with space group R-3 [24]. Additionally, the peaks were observed that could be assigned to ZnO crystalline structure in cubic phase [25].

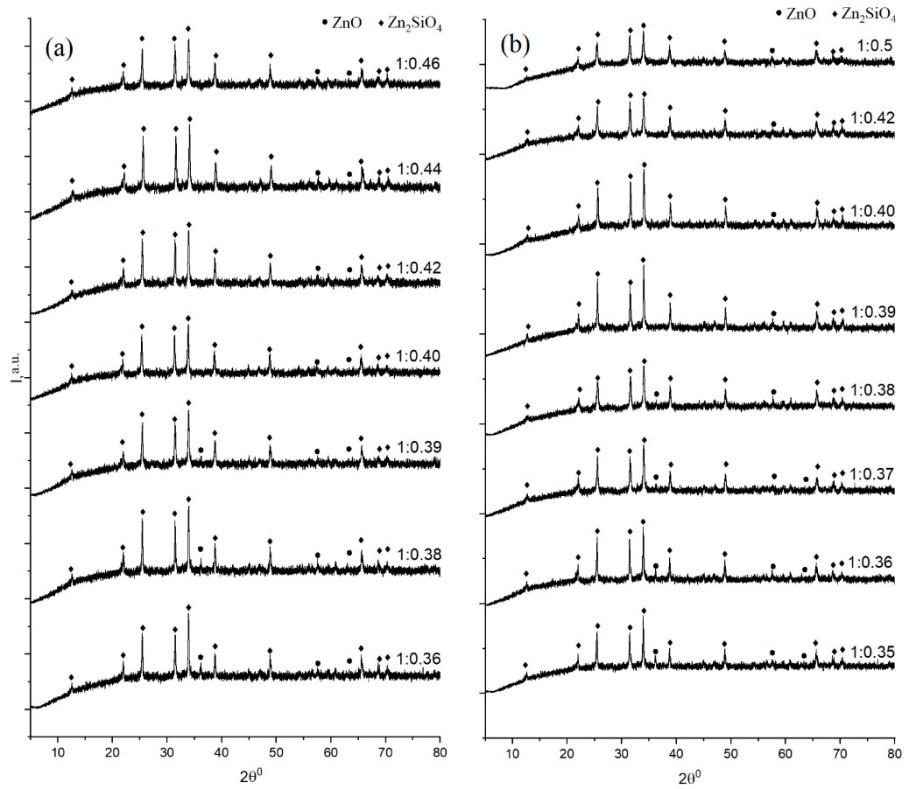

Fig. 1. XRD spectra of Zn_2SiO_4 powders obtained at different concentrations of Plasmotherm (a) and Aerosil (b) SiO_2 brands

Figure 1 demonstrates that the intensity of peaks assigned to willemite increases whereas the intensity of peaks of cubic ZnO decreases with an increase in the concentration of SiO_2 nanopowder (regardless of SiO_2 nanopowder brand). Thus, increasing the amount of the initial SiO_2 nanopowder during synthesis leads to an increase in the concentration of the target compound (willemite).

The diffuse reflection spectra of the powders used in the synthesis (Fig. 2) confirmed that the main absorption edge of the ZnO micropowder was 375 nm, which was consistent with the known values obtained by various authors [26–28]. In the longer wavelength

region, the reflectance increased and reached 93 % at $\lambda \sim 500$ nm. Within $\lambda \geqslant 1000$ nm, it gradually decreased and reached 75 % at $\lambda = 2500$ nm. The bands appeared in the spectrum at 1400, 1740, and 2240 nm, due to the absorption of OH groups sorbed on the powder surface [29–32].

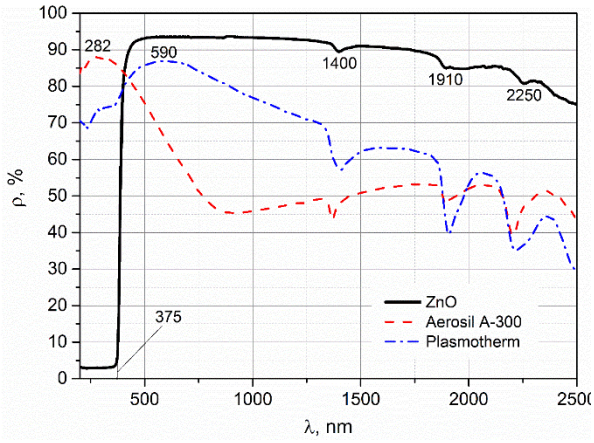

Fig. 2. The diffuse reflectance spectra for ZnO micropowder, Aerosil A-300 nanopowder, and Plasmotherm nanopowder

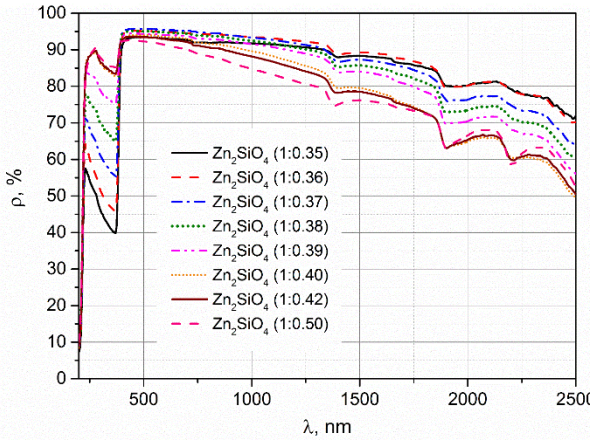

Fig. 3. The diffuse reflectance spectra for Zn_2SiO_4 powders obtained at different concentrations of Aerosil A-300 SiO_2 nanopowder

The ρ_λ spectra of SiO_2 nanopowders of Aerosil A-300 and Plasmotherm brands were characterized by a large band gap, therefore, their main absorption edge was within $\lambda < 200$ nm. The highest value of reflectance for Aerosil A-300 powder was assigned to 282 nm and reached 88 %. It decreased with an increase in the wavelength and reached the lowest value (45 %) at $\lambda = 900$ nm. In the longer wavelength region, the reflectance coefficient slightly increased, while the absorption bands of the OH groups were recorded at 1380, 1910 and 2220 nm similar to the reflectance spectrum of ZnO powder. However, the intensity of these bands for Aerosil A-300 powder was significantly higher.

The ρ_λ spectrum for SiO_2 nanopowder of Plasmotherm brand was different from the one for Aerosil A-300 by the following features: the highest value of reflectance was assigned to 590 nm, that is, it was shifted to the long-wave region; the reflectance coefficient in the longer wavelength region decreased and reached only 30 % at $\lambda = 2500$ nm. Identical absorption bands of OH groups were recorded in the reflectance spectrum of this powder, however, they displayed a much higher intensity.

The reflectance spectra of the obtained Zn_2SiO_4 powders were characterized by the following features. The main absorption edge was clearly visible for ZnO powder at the same wavelength as for the initial powder spectrum (375 nm). The highest value of reflectance was achieved at a slightly lower wavelength (410–430 nm) in comparison with the initial ZnO powder (500 nm). The reflectance coefficient gradually decreased after the highest value and up to 2500 nm. Its lowest value was consistent with the concentration of SiO_2 nanopowder during synthesis: the higher the powder concentration, the lower the reflectance coefficient.

Distinct patterns were traced in the shorter wavelength region from the main absorption edge of ZnO powder ($\lambda = 375$ nm). These patterns were presumably caused by the contribution of SiO_2 nanopowder to the reflectance spectrum of the obtained

compound Zn_2SiO_4. The reflectance increased with a decrease in the wavelength from the main absorption edge of the ZnO powder, reached the highest value, and then decreased. The highest value of reflectance increased with an increase in the concentration of SiO_2 nanopowder, i.e., the reflection spectrum peaked in the short-wave region. For Zn_2SiO_4 powder obtained using Aerosil A-300 nanopowder (Fig. 3), the absolute value of the reflectance was 57, 66, 71, 78, 83, 88, and 88% at the ratio of zinc oxide and silicon dioxide nanopowder concentrations of 1:0.35, 1:0.36, 1:0.37, 1:0.38, 1:0.39, 1:0.40, 1:0.42, 1:0.50, respectively.

The diffuse reflectance spectra of Zn_2SiO_4 powders obtained at different concentrations of Plasmotherm SiO_2 nanopowder (Fig. 4) were qualitatively the same as those for the powders obtained at different concentrations of Aerosil A-300 SiO_2 nanopowder brand (Fig. 2).

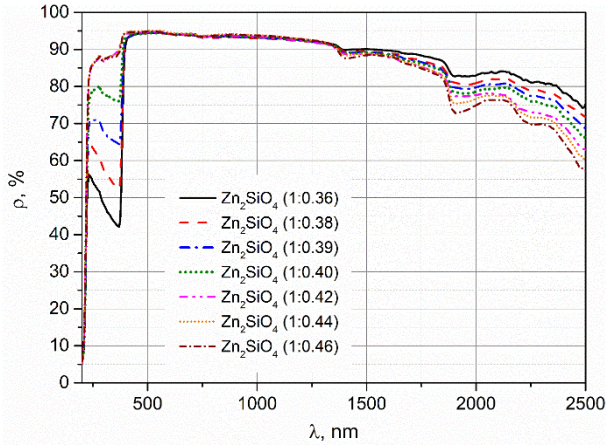

Fig. 4. The diffuse reflectance spectra of Zn_2SiO_4 powders obtained at different concentrations of Plasmotherm SiO_2 nanopowder

The absolute values of the reflectance coefficient in different regions of the spectrum were consistent with the concentration of SiO_2 nanopowder during synthesis. They were slightly different from each other and from their respective values in the spectra of Zn_2SiO_4 powders synthesized using Aerosil A-300 nanopowder. Therefore, it can be concluded that the synthesis of Zn_2SiO_4 powders obtained on the basis of ZnO micropowder and SiO_2 nanopowders of Plasmotherm and Aerosil A-300 brands at different concentrations allowed the authors to obtain pigments with high reflectance in the solar spectrum, depending on both the type of SiO_2 nanopowder and on its concentration. Because solar absorptance is the performance characteristic of TCCs,

Table 1. The correlation between α_s of Zn_2SiO_4 powders and the concentration of SiO_2 nanopowder of Aerosil A-300 brand

ZnO:nSiO_2	1:0.35	1:0.36	1:0.37	1:0.38	1:0.39	1:0.40	1:0.42	1:0.50
α_s	0.120	0.100	0.095	0.098	0.101	0.113	0.120	0.133

Table 2. The correlation between α_s of Zn_2SiO_4 powders and the concentration of SiO_2 nanopowder of Plasmotherm brand

ZnO:nSiO_2	1:0.36	1:0.38	1:0.39	1:0.40	1:0.42	1:0.44	1:0.46
α_s	0.105	0.101	0.094	0.086	0.079	0.077	0.080

it was calculated in relation to the type and concentration of SiO_2 nanopowders used during synthesis. Tables 1 and 2 contain the results of the calculations performed.

Tables 1 and 2 show that an increase in the concentration of SiO_2 nanopowders led to an increase in the absorption coefficient of the two powders obtained. The increase occurred with the lowest α_s values of 0.095 at 1:0.37 for Aerosil A-300 powder and 0.077 at 1:0.44 for Plasmotherm powder. The correlation between α_s and the concentration of SiO_2 nanopowders (Fig. 5) confirmed that the use of Plasmotherm nanopowder made it possible to synthesize Zn_2SiO_4 powders with significantly lower α_s values.

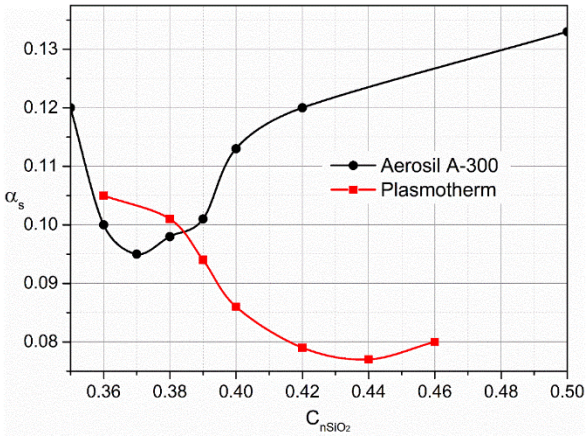

Fig. 5. The correlation between the solar absorptance (α_s) of Zn_2SiO_4 powders obtained and the concentration and type of $nSiO_2$ powders used

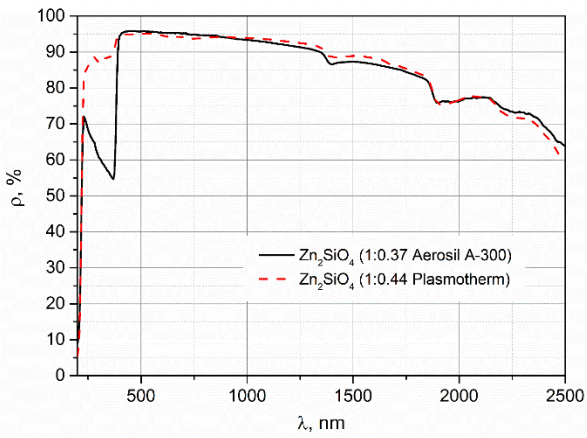

Fig. 6. Diffuse reflectance spectra of Zn_2SiO_4 powders with the lowest α_s values obtained via different types of $nSiO_2$ powder

This difference in α_s values of Zn_2SiO_4 powders was determined by the short-wave region of the diffuse reflectance spectra (Fig. 6). In this region (located at the main absorption edge of ZnO within 375 nm up to 200 nm), the reflectance coefficient of Zn_2SiO_4 powders obtained using Plasmotherm nanopowder was higher compared to the ones obtained using Aerosil nanopowder.

Conclusion

The hypothesis of the present work was that zinc oxide and silica powders could serve as the ideal starting materials for the synthesis of novel pigments to be used in thermal control coatings. Zinc oxide powders have been used as pigments for optical solar reflectors since 1960s both in Russia and in the United States who were managing their own full-scale space programs back then. These powders manifested sufficient radiation stability. Their disadvantage, however, was the large value of absorptance in the initial state ($\alpha_s \sim 0.2$) determined by the semiconductor properties and the main absorption edge. In the short-wave region from the main absorption edge ($\lambda \leqslant 375$ nm), ZnO powders absorbed 94.7 % of the energy from the radiation power of the entire solar spectrum, which is equal to 0.139 $W \cdot cm^{-2}$ [33].

If synthesis is carried out using a ZnO powder with a dielectric powder with a large band gap (e.g., SiO_2 powder), one can obtain a compound that would show a significantly lower absorptance of solar spectrum in the UV region. This work has shown that it is possible to synthesize Zn_2SiO_4 powders with high reflectance and a small value of the

solar absorptance using zinc oxide micropowders and silicon dioxide nanopowders via solid-state method. The solar absoprtance of these powders would be almost 3 times less compared to ZnO powders (α_s = 0.2 and α_s = 0.077, respectively).

Further research will be focused on the study of photo- and radiation stability of the powders obtained. The composition of Zn_2SiO_4 powders allowed the authors to assume that they would demonstrate high radiation stability when exposed to ionizing radiation. The assumption can be grounded on the following factors. The powder contains a simple $nSiO_2$ anion (i.e., not of complex composition). Such anion is unable to decompose into parts under irradiation. Therefore, no additional absorption centers might appear, as was established for complex anions of SO_4^{2-} type in $BaSO_4$ [34,35] powders or CO_3^{2-} anions in $CaCO_3$ [36] powders. If the concentration of $nSiO_2$ allows for forming its monolayer or several layers the surface of grains and granules, then these layers might act: as absorbing layers with high radiation stability [37]; as small-size defects being the relaxation centers for the primary photo- and radiation defects [38].

CRediT authorship contribution statement

Mikhail M. Mikhailov: supervision, conceptualization, writing – original draft, writing – review & editing; **Alexey V. Filimonov**: supervision, writing – review & editing; **Alexey N. Lapin**: data curation, investigation, writing – original draft; **Semyon A. Yuryev:** writing – review & editing, validation; **Vladimir A. Goronchko**: writing – review & editing, visualization; **Dmitriy S. Phedosov:** investigation, visualization.

Conflict of interest

The authors declare that they have no conflict of interest.

References

1. Zhang M, Liu C, Hu R, Hua Y, Yang Z, Wu Q, Guo L. Study on Passive-Active Cooperative Thermal Control Technology for Space Manipulator End Effectors: Design, Simulation, Testing, and On-Orbit Validation. *Case Studies in Thermal Engineering.* 2025;74: 106747.
2. Singh L, Qiu E, Cardin AE, Chen A, Luk TS, Schuller JA, Azad AK. Passive radiative thermal management using phase-change metasurfaces. *Journal of Physics: Photonics.* 2025;7(2): 025028.
3. Anderson L, Swenson C, Mattos B, Fish C, Nunes M, Wright R. Enabling the next generation of advanced small satellites through active thermal control. *Proc. SPIE 13546, Small Satellites Systems and Services Symposium (4S 2024).* SPIE; 2025. p.135462P.
4. ASTM International. *ASTM E490-22 Standard Solar Constant and Zero Air Mass Solar Spectral Irradiance Tables.* ASTM; 2022.
5. ASTM International. *ASTM E903-20 Standard Test Method for Solar Absorptance, Reflectance, and Transmittance of Materials Using Integrating Spheres.* ASTM; 2020.
6. Mikhailov MM, Lapin AN, Sokolovskiy AN, Neshchimenko VV, Yuryev SA. Optical Properties and Photostability of Microsized TiO_2 Powders Modified with its Own Nano-and Hollow Particles. *The Journal of the Astronautical Sciences.* 2023;70(5): 32.
7. Mikhailov MM, Yuryev SA, Lapin AN, Koroleva EY, Goronchko VA. Optical properties of degradation of wollastonite powders under the electron irradiation in vacuum. *Optical Materials.* 2021;119: 111342.
8. Mikhailov MM, Yuryev SA, Lapin AN, Goronchko VA, Mikhailova OA. Optical properties of aluminum oxide powder modified by nanoparticles and prospects for its use in solar power and space industry. *Acta Astronautica.* 2023;212: 483–491.

9. Huseien GF. Potential applications of core-shell nanoparticles in construction industry revisited. *Applied Nano.* 2023;4(2): 75–114.
10. Strapolova VN, Yurtov EV, Muradova AG, Sharapaev AI. Effect of magnetite nanoparticles' modification on optical properties of solar absorber coatings. *Journal of Spacecraft and Rockets.* 2018;55(1): 49–53.
11. Pavlenko VI, Cherkashina NI. Effect of SiO_2 crystal structure on the stability of polymer composites exposed to vacuum ultraviolet radiation. *Acta Astronautica.* 2019;155: 1–9.
12. Bo Z, Gang L, Kangli C, Weimin C. Preparation and space environmental stability of a nano-materials modified thermal control coating. In: Kleiman J. (ed.) *Protection of Materials and Structures from the Space Environment. Astrophysics and Space Science Proceedings, vol 47.* Cham: Springer: 2017. p.433–441.
13. Feng Q, Li B, Xiang X, Deng H, Yang G, Li S, Zu X. Ripple structure and electronic property degradation of Graphene/α-SiO_2 induced by low-Energy self-Ion irradiation. *Computational Materials Science.* 2025;246: 113347.
14. Dworak DP, Soucek MD. Protective space coatings: a ceramer approach for nanoscale materials. *Progress in Organic Coatings.* 2003;47(3–4): 448–457.
15. Kiomarsipour N, Razavi RS, Ghani K. Improvement of spacecraft white thermal control coatings using the new synthesized Zn-MCM-41 pigment. *Dyes and Pigments.* 2013;96(2): 403–406.
16. Rasmidi R, Duinong M, Chee FP. Radiation damage effects on zinc oxide (ZnO) based semiconductor devices–a review. *Radiation Physics and Chemistry.* 2021;184: 109455.
17. Khan M, Alam MS, Ahmed SF. Effect of nickel incorporation on structural and optical properties of zinc oxide thin films deposited by RF/DC sputtering technique. *Materials Physics and Mechanics.* 2023;51(1): 19–32.
18. Torres M, Franco-Urquiza EA, González-García P, Bárcena-Balderas J, Piedra S, Madera-Santana T, Quintana-Owen P. Characterization of epoxy-nanoparticle composites exposed to gamma & UV radiation for aerospace applications. *Nano Hybrids and Composites.* 2019;27: 53–65.
19. Rackauskas S, Talka T, Kauppinen EI, Nasibulin AG. Zinc Oxide Tetrapod Synthesis and Application for UV Sensors. *Materials Physics and Mechanics.* 2012;13(2): 175–180.
20. Johnson FS. The solar constant. *Journal of Atmospheric Sciences.* 1954;11(6): 431–439.
21. Jarý V, Vařák P, Babin V, Hrabovský J, Michalcova A, Volf J, Mrázek J. Scintillation properties of zinc-silicate glass-ceramics based on Zn2SiO4 willemite phase. *Optical Materials.* 2025;162: 116961.
22. Das A, Zając M, Huang WH, Chen CL, Kandasami A, Bittencourt C. The impact of willemite Zn_2SiO_4 phase in B1 to B2 type structural phase transformation in $Cd_xZn_{1-x}O$ composite thin films. *Thin Solid Films.* 2025;812: 140616.
23. Radha A, Wang SF. Influence of ZnB4O7 as an additive on the sintering temperature and microwave dielectric behaviors of Mg_2SiO_4 ceramics. *Ceramics International.* 2025;51(23): 39285–39295.
24. Syahnur FR, Permana MD, Dwiyanti D, Eddy DR, Deawati Y, Takei T, Firdaus ML. Influence of Zn2+ amount on zinc silicate phase from natural silica via hydrothermal synthesis method and evaluation of photocatalytic activity. *Emergent Materials.* 2025;8: 4423–4434.
25. Sokolov PS, Baranov AN, Dobrokhotov ZV, Solozhenko VL. Synthesis and thermal stability of cubic ZnO in the salt nanocomposites. *Russian Chemical Bulletin.* 2010;59(2): 325–328.
26. Secor JA. *Ultrafast Spectroscopy and Energy Transfer in an Organic/Inorganic Composite of Zinc Oxide and Graphite Oxide*. City University of New York; 2016.
27. Ayed S, Belgacem RB, Zayani JO, Matoussi A. Structural and optical properties of ZnO/TiO2 composites. *Superlattices and Microstructures.* 2016;91: 118–128.
28. Mikhailov MM, Lapin AN, Yuryev SA, Goronchko VA. Optical Properties of ZnO Powders Modified with ZnO Nanoparticles. *Russian Physics Journal.* 2022;65(8): 1239–1245.
29. Wilson RH, Nadeau KP, Jaworski FB, Tromberg BJ, Durkin AJ. Review of short-wave infrared spectroscopy and imaging methods for biological tissue characterization. *Journal of Biomedical Optics.* 2015;20(3): 030901.
30. Peng L, Qisui W, Xi L, Chaocan Z. Investigation of the states of water and OH groups on the surface of silica. *Colloids and Surfaces A: Physicochemical and Engineering Aspects.* 2009;334(1–3): 112–115.
31. Zhao D, Chen C, Wang Y, Ji H, Ma W, Zang L, Zhao J. Surface modification of TiO_2 by phosphate: effect on photocatalytic activity and mechanism implication. *The Journal of Physical Chemistry C.* 2008;112(15): 5993–6001.
32. Di Paola A, Bellardita M, Palmisano L, Barbieriková Z, Brezová V. Influence of crystallinity and OH surface density on the photocatalytic activity of TiO_2 powders. *Journal of Photochemistry and Photobiology A: Chemistry.* 2014;273: 59–67.
33. Makarova EA, Kharitonov AV. *Distribution of energy in the spectrum of the Sun and the solar constant*. Moscow: Nauka; 1972. (In Russian)

34. Mikhailov MM, Yuryev SA, Lapin AN. Examining the diffuse reflectance spectra and the radiation stability for the mixtures of $BaSO_4$ micropowders and SiO_2 nanopowders with various specific surface area. *Key Engineering Materials.* 2019;806: 106–112.
35. Sifontes ÁB, Cañizales E, Toro-Mendoza J, Ávila E, Hernández P, Delgado BA, Cruz-Barrios E. Obtaining highly crystalline barium sulphate nanoparticles via chemical precipitation and quenching in absence of polymer stabilizers. *Journal of Nanomaterials.* 2015;2015(1): 510376.
36. Ghadami Jadval Ghadam A, Idrees M. Characterization of $CaCO_3$ nanoparticles synthesized by reverse microemulsion technique in different concentrations of surfactants. *Iranian Journal of Chemistry and Chemical Engineering (IJCCE).* 2013;32(3): 27–35.
37. Ding W, Cheng J, Zhao L, Wang Z, Yang H, Liu Z, Chen M. Determination of intrinsic defects of functional KDP crystals with flawed surfaces and their effect on the optical properties. *Nanoscale.* 2022;14(28): 10041–10050.
38. Pastor E, Sachs M, Selim S, Durrant JR, Bakulin AA, Walsh A. Electronic defects in metal oxide photocatalysts. *Nature Reviews Materials.* 2022;7(7): 503–521.

MATERIALS PHYSICS AND MECHANICS RESEARCH ARTICLE

Submitted: February28, 2025 **Revised: July22, 2025** **Accepted:October23, 2025**

Fabrication and characterization of zinc nitrate doped TiO_2 nanotubes for dye-sensitized solar cells

B. Samran [1], E.N. Timah [2], T Phatungthane[1],P. Thongpanit[1], B. Kadroon[1], S. Photharin[3], S. Chaiwichian[4] ✉

[1] Nakhon Phanom University, Nakhon Phanom, Thailand

[2] Trinity International School, Bangkok, Thailand

[3] Kasetsart University, Sakonnakhon,Thailand

[4] Rajamangala University of Technology Isan, Sakonnakhon, Thailand

✉saranyou530531117@gmail.com

ABSTRACT

Zinc-doped titanium dioxide nanotubes were successfully synthesized, characterized, and tested as materials for energy conversion in dye-sensitized solar cells. The TiO_2 nanotubes were grown through single-face anodization at a constant direct current voltage of 50 V and room temperature on titanium sheets with a thickness of 0.25 mm and purity of 99.7 %. The electrolyte was composed of ethylene glycol, ammonium fluoride (0.3 % wt. NH_4F), and deionized water (2 % v/v H_2O). The titania nanotubes were doped with Zn using $Zn(NO_3)_2$ as the dopant source. The molar ratios of zinc nitrate were varied from 1, 3, 5, and 7 mM. X-ray diffraction, scanning electron microscopy, and ultraviolet-visible spectroscopy (techniques were employed to characterize the Zn-doped titanium dioxide nanotubes. The samples were then tested in dye-sensitized solar cells, and their photoelectric conversion efficiencies were calculated. As a result, amorphous-TiO_2 structure was transformed into the crystalline anatase phase after annealing. The best performance was observed for the 5 mM zinc nitrate sample, with a photoelectric conversion efficiency of 4.96 % and an energy band gap of 3.18 eV. The findings of this research provide valuable insights for ongoing and future studies in the development of renewable energy.

KEYWORDS

renewable energy • DSSCs • TiO_2 nanotubes

Funding. *The authors would like to greatly thank the following for their support: Thailand Science Research and Innovation Fundamental Fund – FF 2024; the Division of Physics, Faculty of Science, Nakhon Phanom University, Muang District, Nakhon Phanom; and Faculty of Industry and Technology, Rajamangala University of Technology Isan.*

Citation: Samran B, Timah EN, Phatungthane T, Thongpanit P, Kadroon B, Photharin S, Chaiwichian S. Fabrication and characterization of zinc nitrate doped TiO_2 nanotubes for dye-sensitized solar cells. *Materials Physics and Mechanics.* 2025;53(5): 83–89.
http://dx.doi.org/10.18149/MPM.5352025_6

Introduction

It was in 1991, when O'Regan and Gratzel [1–3] made their first dye-sensitized solar cells (DSSCs). Since then, there has been huge growth in research on DSSCs. This huge growth can be accounted for due to the following reasons: they are cheap to produce, easy to fabricate, are a source of renewable energy, are environmentally friendly and have high power conversion efficiency [4–10]. Titanium dioxide or titania (TiO_2) nanotubes can be used in DSSCs to improve the photocatalytic performance and resolve the issue of charge recombination [11–14]. However, one challenge encountered with

titania is the large band gap energy of about 3.2 eV. This large band gap restricts solar energy absorption mostly in the UV region. Many reports suggest that this problem can be solved by doping titania with foreign elements. Examples of elements that have been used as dopant in titania include Fe, N, Cu, and Al [15–19].

A.F.Robledo et al.[6], P.Ramos et al. [20] and A. Javed et al. [21] used ZnO nanostructures in DSSCs. Composite nanofibers of ZnO-TiO_2 in DSSCs was reported by C. Qiqi et al. in 2022 [22]. A 1:2 molar ratio of ZnO-TiO_2 was utilized and obtained photoelectric conversion efficiency (PCE) of 3.66 %. There is great room for improvement on this result by doping titania nanotubes (TNT) using zinc nitrate, $Zn(NO_3)_2$, as a source of the dopant element Zn. This research work reports the fabrication and characterization of Zn-doped TNT for DSSCs. The samples were prepared at the molar ratios of zinc nitrate: 1, 3, 5 and 7 mM. The PCE of each sample will be tested in DSSCs.

Materials and Methods

Direct current (DC) anodization technique was used to develop TNT on titanium sheet from Sigma Aldrich. This process was carried out at a constant voltage supplyof 50 V for 2 h at room temperature. The thickness of the each titanium sheet or foil was 0.25 mm thickness and their purity was 99.7 %. The sheets were polished with abrasive paper and degreased by ultrasonic method in isopropanol, deionized water and ethanol. The electrolyte used for the anodization was composed of the following: ethyleneglycol (EG), ammoniumfluoride (0.3 wt. % NH_4F) and deionized water (2 vol. % D.I. H_2O). The molar concentrations of zinc nitrate was varied sequentially -1, 3, 5 and 7 mM. To ensure that the electrolyte was homogenous, we kept the mixture for 5 h prior to anodization. The array for the anodization consist of two electrodes – a copper electrode and a platinum counter electrode, as seen in Fig. 1. With this set up, the electrolyte can only be in contact with one face of the titanium sheet.

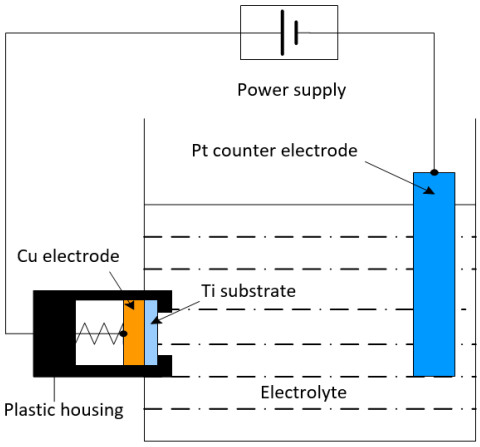

Fig. 1. The schematic diagram of a single-face anodization process

Analysis of the samples was performed before calcination and after anealingin an oven at 450 ºC. The following techniques were used to characterize the samples: X-ray diffraction (XRD), scanning electron microscopy (SEM), and ultraviolet-visible

spectroscopy (UV-VIS). After that, the samples were tested in DSSCs. Totest in DSSCs, the titania nanotubes photoelectrodes were immersed for 24 h at room temperature in 0.5 mM solution of N719 dye and acetonitrile/tert-butanol in a 1:1 mixture. To form the counter electrode, platinum solution (H_2PtCl_6) was dropped on a transparent conducting oxide glass (TCO). After heating the TCO at 80 °C for 30 min, the platinium counter electrode was ready. A sandwich assembly of the Pt electrode and the titania nanotube photoelectrode was incorporated into the DSSCs. The current-voltage (IV) characteristic was then analyzed. The following parameters are fundamental in evaluating the photovoltaic properties of the DSSCs: short-circuit current density (J_{sc}), open-circuit voltage (V_{oc}), fill factor (*FF*) and the photoelectric conversion efficiency PCE (η). These parameters are related via the equations that follows [23,24]:

$$FF = \frac{V_m I_m}{V_{OC} I_{SC}}, \quad (1)$$

$$\eta = \frac{V_m I_m}{P_{in}} = \frac{V_{OC} I_{SC} FF}{P_{in}}, \quad (2)$$

where I_m and V_m are the current and voltage, respectively, at the optimal operating point. Their product gives the maximum output power P_m. The power of the incident light is denoted as Pin.

Results and Discussion

XRD analysis

XRD patterns of the zinc-doped titania nanotubes samples before annealing are displayed in Fig. 2. In Fig. 2, we can see the peaks typical to titanium metal. It is also worth noting that the titania were still in the amorphase phase due to the absence of the anatase phase. On the other hand, Fig. 3 displays XRD patterns after calcinating the samples at 450 °C. It is obvious to see the crystalline anatase phase of TiO_2 which are labelled A. The diffraction peaks for the anatase phase occur at the scattering angles of 25.3, 48.8, 54.2, and 55.1°. These results align perfectly with the works of Hailei Li et al. [25], and Shih-Yu Ho et al. [26].

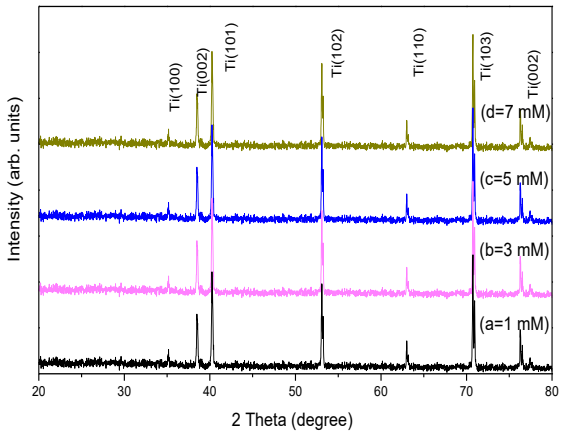

Fig. 2. XRD patterns of Zn-doped TNT before annealing: (a) 1 mM, (b) 3 mM, (c) 5 mM, and (d) 7 mM

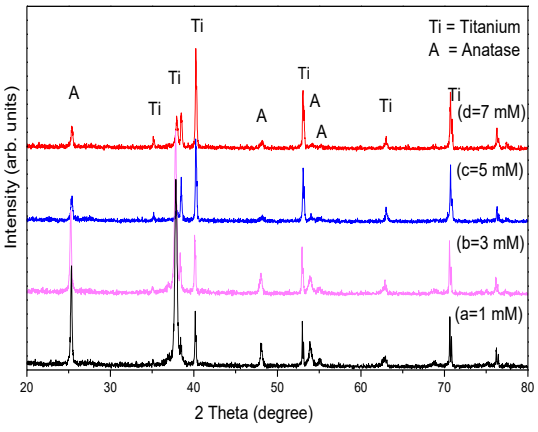

Fig. 3. XRD patterns of Zn-doped TNT after annealing at 450 °C: (a) 1 mM, (b) 3 mM, (c) 5 mM and (d) 7 mM

SEM analysis

The calcinated samples were studied using scanning electron microscopy (SEM). The results presented in Fig. 4 brings to light the changes in the surface morphology of the Zn-doped TNT. The fine structure of the nanotubes gets better with increase in zinc nitrate concentration. However, after 5 mM, the order liness of the nanotube array is heavily disrupted, as seen with the 7 mM sample. A similar result was obtained by X. Chen et al. [27], when varying the concentrations of HCl.

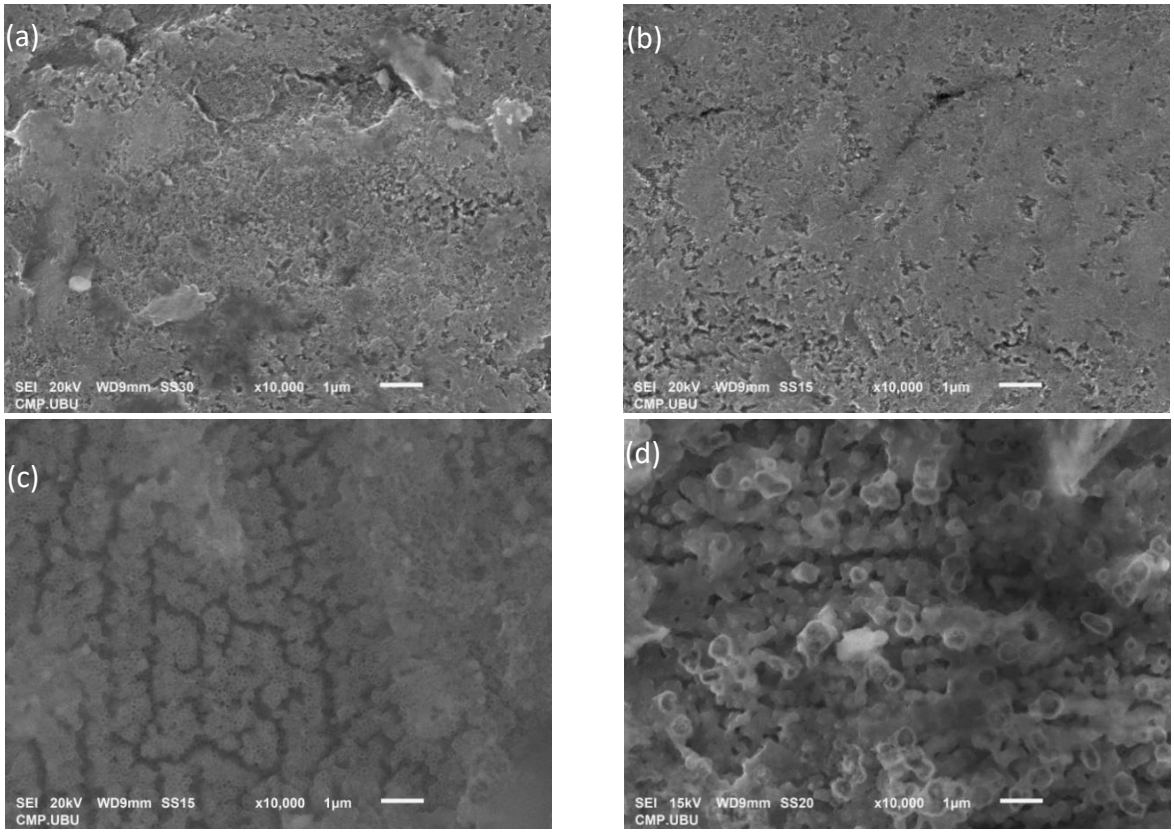

Fig. 4. SEM images of Zn-doped TNT after annealing at 450 ºC: (a) 1 mM, (b) 3 mM, (c) 5 mM and (d) 7 mM

UV-visible spectroscopy analysis

The ultraviolet-visible spectrums of the annealed samples are presented in Fig. 5. The sample with a zinc nitrate concentration of 5 mM had the greatest cut off wavelength (λ_c) of 390 nm. λ_c increased with concentration until 5 mM, and decreased there after at the higher concentration of 7 mM. We can attribute this to the disorderly array of the nanotubes demonstrated in SEM images of Fig. 4(d). A large λ_c implies a smaller energy band gap (E_g), as demonstrated in Table 1 by Eq. (3) [28–30]:

$$E_g = \frac{hc}{\lambda_C} = \frac{1240}{\lambda_C}, \quad (3)$$

where h is the Planck constant (6.626×10^{-34} Js or 4.14×10^{-15} eVs) and c is the speed of light in vacuum (3.00×10^{8} m/s).

Table 1. Energy band gapfrom UV-VIS for different concentrations of Zn-doped TNT after annealing at 450 ºC

Samples	1 mM	3 mM	5 mM	7 mM
λ_c, nm	379	388	390	384
E_g, eV	3.27	3.20	3.18	3.23

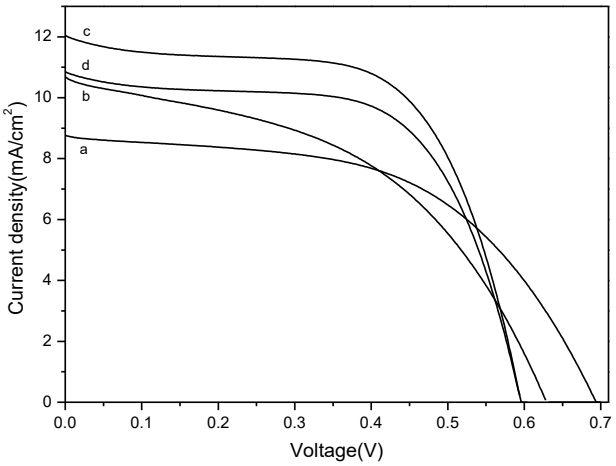

Fig. 5. Current-voltage (IV) characteriztic curves ofZn-doped TNT after annealing at 450 ºC: (a) 1 mM, (b) 3 mM, (c) 5 mM and (d) 7 mM

IV characteristic and photoelectric performance

Figure 5 and Table 2 both reveal that as zinc nitrate concentration increase, the cell efficiency and photocatalytic performance also increase. One explanation to this is that the dopant element Zn serves as charge traps and helps to reduce charge carrierre combination. As more zinc ions replace the titanium ions in the crystal lattice, more charge traps are created. Another reason is that the introduced Zn aid in reducing the band gap energy by forming intermediate energy levels. As a result, the photon absorption of the DSSCs is shifted from the UV region to the Visible light region. This conclusion is supported by the work of Udom T. et al [31]. The 5 mM zinc nitrate sample had the highest PCE of 4.96 %. Because doping reduces the number of trapping states, resulting in a reduction of charge recombination. The efficiency of dye sensitized solar cell of doped Zn-TiO_2 nanotubes obviously declined, which may be due to the formation of recombination centers of photogenerated carriers by the excessive impurity atoms [32]. The cell efficiency at a higher concentration was lower due to a highly distorted and disorganized nanotube array as observed in the SEM images in Fig. 4(d). As a consequence, the charge carrierre combination will be greater, resulting in lower PCE and photocatalytic performance.

Table 2. Photoelectric performance of Zn-doped TNT after annealing at 450 ºC

Samples	J_{sc}, mA/cm^2	V_{oc}, V	*FF*	η, %
1 mM	8.87	0.68	0.53	3.42
3 mM	10.94	0.64	0.49	3.52
5 mM	12.35	0.62	0.64	4.96
7 mM	10.95	0.61	0.62	3.85

Conclusions

Zinc-doped TiO_2 nanotubes were synthesized byDC anodization at 50 V, and their photocatalytic performance were testedin dye-sensitized solar cells (DSSCs). The

electrolyte was composed of ethyleneglycol (EG), ammoniumfluoride (0.3 % wt NH_4F), and deionized water (2 % V H_2O). zinc nitrate was used as the source of the dopant element Zn, and the molar concentrations of zinc nitrate was varied as follows: 1, 3, 5 and 7 mM. The Zn-doped TNT were characterized using several techniques. XRD patterns revealed the transformation of amorphous TiO_2 into the anatase phase after calcination at 450 ºC.The surface morphology and array of the nanotubes were studied using SEM. The nanotubes for the 7 mM sample show highly distorted arrangement. The energy band gaps were determined from the UV-VIS results. The lowest band gap energy of 3.18 eV was obtained for the 5 mM sample. This value can be used to account for the optimal photocatalytic performance of the 5 mM sample when tested in DSSCs. It had the highest PCE of 4.96 %. The results of this research provided significant guidelines for ongoing and future research in the development of sustainable energy.

CRediTauthorshipcontributionstatement

Buagun Samran: conceptualization, data curation, investigation, supervision, writing – review & editing, writing – original draft; **Thanatep Phatungthane**: conceptualization, investigation, supervision, writing – original draft; **Pratya Thongpanit**: conceptualization, investigation, supervision, writing – original draft; **Bhunpawatana Kadroon**: conceptualization, investigation, supervision, writing – original draft; **Saranyoo Chaiwichian**: conceptualization, investigation, supervision, writing – original draft, writing – review & editing.

Conflict of interest

The authors declare that they have no conflict of interest.

References

1. O'Regan B, Grätzel MA low-cost, high-efficiency solar cell based on dye-sensitized colloidal TiO_2films. *Nature.* 1991;353: 737–740.
2. Almansour AI, Kumar RS, Al-Shemaimari KI, Arumugam N. Highly Efficient DSSCs Sensitized Using NIR Responsive Bacteriopheophytine-a and Its Derivatives Extracted from Rhodobacter Sphaeroides Photobacteria. *Molecules.* 2024;29(5): 931.
3. Onah EH, Lethole NL, Mukumba P. Luminescent Materials for Dye-Sensitized Solar Cells: Advances and Directions. *Applied Sciences.* 2024;14(20): 9202.
4. Lin C, Liu Y, Wang G, Li K. Novel Dyes Design Based on First Principles and the Prediction of Energy Conversion Efficiencies of Dye-Sensitized Solar Cells. *ACS Omega.* 2021;6(1): 715–722.
5. Radloff GHC, Naba FM, Ocran-Sarsah DB, Bennett ME, Sterzinger KM, Armstrong AT, Layne O, Dawadi MB. Fabrication and characteristics of high efficient dye-sensitized solar cell with composite dyes. *Digest Journal of Nanomaterials and Biostructures.* 2022;17(2): 457–472.
6. Flota Robledo AG, Enríquez JP, Meza Avendaño CA, Pérez Hernández G, Juárez Gutiérrez PJ. DSSCs based on ZnO photoelectrodes sensitized with natural dyes extracted from the bark of Brazil and Taray. *Journal of Optoelectronic and Biomedical Materials.* 2022;14(2): 29–34.
7. Setyawati H, Hadi MS, Darmokoesoemo, H, Murwani IK, Permana AJ, Rochman F. Modification of Methyl Orange dye as a light harvester on solar cell. *IOP Conference Series Earth and Environmental Science.* 2020;456: 012010.
8. Bobyl AV, Davydov RV, Konkov OI, Kochergin AV, Malevsky DA, Nikitin SE. Accelerated degradation by mechanical load of HIT solar cells encapsulated in flexible plastic. *Material Physics and Mechanics.* 2024;52(4): 1–8.

9. Gusev EYu, Dzhityayeva DZh Yu, Ageyev OA. Effect of PECVD conditions on mechanical stress of silicon films. *Materials Physics and Mechanics.* 2018;37(1): 67–72.
10. VallejoW, Lerma M, Dias-Uríbe C. Dye sensitized solar cells: Meta-analysis of effect sensitizer-type on photovoltaic efficiency. *Heliyon.* 2025;11(1): e41092.
11. Dholam R, Patel N, Adami M, Miotello M. Hydrogen production by photocatalytic water-splitting using Cr- or Fe-doped TiO_2 composite thin films photocatalyst. *International Journal of Hydrogen Energy.* 2009;34(13): 5337–5346.
12. Liu N, Lee KY, Schmuki P. Small diameter TiO_2 nanotubes vs. nanopores in dye sensitized solar cells. *Electrochemistry Communications.* 2011;15(1): 1873–1902.
13. Park H, Kim WR, Jeong HT, Lee JJ, Kim HG, Choi WY. Fabrication of dye-sensitized solar cells by transplanting highly ordered TiO_2 nanotube arrays. *Solar Energy Materials & Solar Cells.* 2011;95(1):184–189.
14. Chen J, Vishart AL, Sauer SPA, Mikkelsen KV. Teoretical investigations of dye-sensitized solar cells. *Journal of Nanotechnology and Nanomaterials.* 2023;4(2): 38–54.
15. Oviedo AM, Thi HT, Van QC, Nguyen HH. Physicochemical properties of Fe-doped $TiO_2$and the application in Dye-sensitized solar cells. *Optical Materials.* 2023;137: 113587.
16. He Z, Que WX, He Y, Hu J, Chen J, Javed HMA, Ji Yu, Li X, Fei D. Electrochemical behavior and photocatalytic performance of nitrogen-doped TiO_2nanotubes arrays powders prepared by combining anodization with solvothermal process. *Ceramics International.*2013;39(5):5545–5552.
17. Momeni MM, Ghayeb Y, Ghonchegi Z. Fabrication and characterization of copper doped TiO_2 nanotube arrays by in situ electrochemical method as efficient visible-light photocatalyst. *Ceramics International.* 2015;41(7):8735–8741.
18. Samran B, Phatungthane T, Timah E, Tipparach U. Synthesis of Aluminum-Doped TiO_2Nanotubes by Anodization Method. *Key Engineering Materials.* 2017;728: 209–214.
19. Rahman S, Haleem A, Siddiq M, Hussain MK, Qamar S, Hameed S, Waris M. Research on dye sensitized solar cells: recent advancement toward the various constituents of dye sensitized solar cells for efficiency enhancement and future prospects. *RSC Advances.* 2023;28: 19508.
20. Ramos P, Flores G, Sánchez E, Candal LA, Hojamberdiev RJ, Estrada M, Rodriguez W. Enhanced photoelectrochemical performance and photocatalytic activity of ZnO/TiO_2 nanostructures fabricated by an electrostatically modified electrospinning. *Applied Surface Science.*2017;426: 844–851.
21. Javed AH,Shahzad N,Khan AM,Ayub M,Iqbal N,Hassan M,Hussain N,Rameel MI,Shahzad MI. Effect of ZnO nanostructures on the performance of dye sensitized solar cells. *Solar Energy.* 2021;230: 492–500.
22. Chang Q, Xu J, Han Y, Ehrmann A, He TH, Zheng RP. Photoelectric Performance Optimization of Dye-Sensitized Solar Cells Based on ZnO-TiO_2 Composite Nanofibers. *Journal of Nanomaterials.* 2022;2022(1): 7356943.
23. Li S, Liu YM, Zhang G, Zhao XZ, Yin J. The role of the TiO_2nanotube array morphologies in the dye-sensitized solar cells. *Thin Solid Films.* 2011;520(2): 689–693.
24. Kim SS, Yum JH, Sung YE. Improved performance of a dye-sensitized solar cell using a TiO_2/ZnO/Eosin Y electrode. *Solar Energy Materials & Solar Cells.* 2003;79(4): 495–505.
25. Li H, Cao L, Liu W, Su G, Dong B. Synthesis and investigation of TiO_2nanotube arrays prepared by anodization and their photocatalytic activity. *Ceramics International.* 2012;38(7): 1–4.
26. Ho SY, SuC, Kathirvel S, Li CY, Li WR. Fabrication of TiO_2nanotube–nanocube array composite electrode for dye-sensitized solar cells. *Thin Solid Films.* 2013;529: 123–127.
27. Chen X, Schriver M, Suen T, Mao SS. Fabrication of 10 nm diameter TiO_2nanotube arrays by titanium anodization. *Thin Solid Films.* 2007;515(24): 8511–8514.
28. Yathisha RO, Nayaka YA. Optical andelectrical properties oforganic dye sensitized Cr–ZnO andNi–CdO nanoparticles. *SN Applied Sciences.* 2020;2: 451.
29. Guo W, Ye J, Chang H, Yu C. Damage Characteristics Analysis of Laser Ablation Triple-Junction Solar Cells Based on Electroluminescence Characteristics. *Sensors.* 2024;24(15): 4886.
30. Miah MH, Khandaker MU, Rahman MB, Alam MNE, Islam MA. Band gap tuning of perovskite solar cells for enhancing the efficiency and stability: issues and prospects. *RSC Advances.* 2024;14: 15876–15906.
31. Tipparach U, Wongwanwatthana P, Sompan T, Saipin T, Krongkitsiri P. Preparation and Characterization of Nano-TiO_2 Thin Films by Sol-gel Dip-coating Method. *Chiang Mai University Journal of Natural Sciences. Special Issue on Nanotechnology.* 2008;7(1): 129–136.
32. Jiang K, Zhang J, Luo R, Wan Y, Liu Z, Chen J. A facile synthesis of Zn-doped TiO_2 nanoparticles with highly exposed (001) facets for enhanced photocatalytic performance. *RSC Advances.* 2021;11: 7627–7632.

MATERIALS PHYSICS AND MECHANICS RESEARCH ARTICLE

Submitted: May 15, 2025 **Revised: July 31, 2025** **Accepted: September 19, 2025**

Microstructure and nanomechanical properties of TaN coating prepared by RF magnetron sputtering

G. Saravanakumar [1], P. Gomathi [2], V. Bharathi [1], L. Ravikumar [1], G. Balakrishnan [3]✉

[1] Department of Mechanical Engineering, B.M.S. College of Engineering, Bengaluru, Karnataka, India

[2] Department of Mathematics, B.M.S. College of Engineering, Bengaluru, Karnataka, India

[3] Saveetha Institute of Medical and Technical Sciences, Saveetha Dental College and Hospital, Tamilnadu, India

✉ balaphysics76@gmail.com

ABSTRACT

In this work, TaN is coated on the high-speed steel substrates at 500 °C using radio frequency magnetron sputtering and its microstructural and nanomechanical properties are examined. The structural, surface morphology and mechanical properties are analyzed by X-ray diffraction, atomic force microscopy and nanoindentation, respectively. X-ray diffraction studies indicated the presence of hexagonal Ta_2N and cubic TaN phases at 5 sccm nitrogen flow at room temperature. It shows that the film prepared at 2 sccm and 500 °C revealed the strong intensity peak of FCC TaN phase, while the film prepared at 10 sccm and 500 °C showed that the broad peak demonstrating the nanocrystalline nature of the film. Atomic force microscopy analysis indicated the formation of crystallites of uniform size and homogeneous distribution. The surface roughness is ~ 2–6 nm in all the deposition conditions. The hardness of the TaN films has increased from 9.46 ± 1.15 to 30.05 ± 3.79 GPa with decreasing N_2 flow rate from 10 to 2 sccm. The microstructure depends on the preparation technique, processing parameters and nitrogen content in the films. TaN coating on high speed steel increased the hardness resulting the increase of wear resistance of the tool, leads to increase of the tool life.

KEYWORDS

tantalum nitride films • high speed steel • X-ray diffraction • atomic force microscopy • nanoindentation

Citation: Saravanakumar G, Gomathi P, Bharathi V, Ravikumar L, Balakrishnan G. Microstructure and nanomechanical properties of TaN coating prepared by RF magnetron sputtering. *Materials Physics and Mechanics*. 2025;53(5): 90–98.

http://dx.doi.org/10.18149/MPM.5352025_7

Introduction

Coating is an important process for the engineering components such as thermal barrier coatings for turbine engines, antireflection coating for many optoelectronic devices, wear resistant coatings for both cutting tools and the kitchen utensils. Hard coatings are developed to protect the materials from wear and corrosion and hence increased the life time of the components. The development of the hard coatings is forced by the constant requirements from the cutting tool industries. Few micron thick TiC coatings were deposited on cutting tools by chemical vapor deposition (CVD) to solve the problems in the cutting tool industry in 1969. It is observed that the metal carbide and nitride coatings can protect the materials from chemical and abrasive wear. Wear of the coating takes place as the cutting speed is increased. Most preferably Al_2O_3 coating is utlized to avoid oxidation. Bilayer coating of TiC and Al_2O_3 took the centre of attraction in industrial coating in 1975. These coatings protected the cutting boundaries

from the harsh environmental conditions. However, the CVD depositon technique is performed at high deposition temperature (900 °C), which causes poor rupture strength and toughness [1–6].

Physical vapour deposition (PVD) technique is an alternative technique to the CVD. The PVD coated TiN on the high speed steel (HSS) drill bits were the first industrial coatings in 1982. This technique produced crack free coating at lower deposition temperature of ~ 500 °C. TiN coating established by PVD method, led to the growth of TiCN coatings with increased hardness, but the problem encountered in the form of oxidation resistance. Hence, more attention has been focused on TiAlN system. Similarly, there was an increase of nanostructured coatings with hardness of more than 40 GPa. In the present scientific world, there are more than 100 different coatings available, which suits the specific requirement and demands of the modern industries with enahnced life time of components. Moreover, the cutting tool industries constantly searching for higher cutting speeds, which needs higher hot hardness and better oxidation resistance. Hardness, oxidation resistance and toughness are the three main factors, in the hard coating industries [7–9]. HSS-M2 type is the popular high speed steel replaces T1 high speed in most applications due to its better properties. Because of its low resistivity, structural integrity with Si, and wear-resistance capabilities, the cubic metastable phase TaN is favoured as a diffusion barrier for Cu interconnections in microelectronics. HSS materials are used in many applications such as cutting tools, gear cutters, milling cutters, tool bits, and drills due to its superior wear resistance and excellent hardness [10–12].

For the TaN films with low nitrogen, the hardness of the material is microstructure dependent. The hardness is increased with the decrease of crystallite size. TaN coatings are known for their hardness, wear and oxidation resistant, thermal stability and inertness. The recent research on tantalum nitride thin films has shown that they could be useful as extremely hard coatings [13–15]. Because of their superior wear resistance, TaN are applied to steel as protective coatings. Many research work on TaN is completed on their applications in thinfilm resistors and diffusion barriers. Few works is carried out on their applications in hard and wear resistant coatings. The scope of the present work is to increase the properties such as hardness and wear resisting behaviour of HSS with TaN coating. Increases hardness and wear resisting characteristics will increase the life time of the cutting tools (HSS). Different surface modification technologies are available to provide high wear-resistance and corrosion-resistance, thermal resistance and increasing hardness of the surface of the material. Among the many deposition techniques, the magnetron sputtering technology is widely used because of its advantages such as high deposition rate, purity of the films, stoichiometry, good adhesion of film, low pressure operation, uniform deposition on substrates and wide range of materials can be deposited. The work is carried out to increase the hardness and wear resisting behaviour of the HSS using nanostructured TaN coating and hence, increase the life time of the cutting tools (HSS) [13,16,17].

Materials and Methods

High speed steel

HSS are ferrous based alloys having the elements such as W, Mo, Cr, V, and Co. HSS materials are primarily used for cutting tools, since they have the capacity to retain a high hardness at high cutting speed. The elements present in the HSS are teseted and the values are (wt. %) C = 0.866, Mn = 0.652, Si = 0.944, P = 0.023, S = 0.023, Al = 0.039, Cr = 2.98, Ni = 0.393, Mo = 3.51, V = 1.32, Ti = 0.006, W = 4.67, Cu = 0.138, Co = 0.777, Fe = 84.436.

TaN coatings are deposited on HSS substrates by radio frequency (RF) reactive magnetron sputtering. Pure Ar and N_2 are used as sputtering with reactive gases and mirror finished. HSS are used as substrates with a hardness of 727 HV. The HSS substrates are 20 × 20 × 5 mm^3 in size, cleaned thoroughly and fixed on a substrate holder cum heater. The base vacuum of the chamber is about 3 × 10^{-6} mbar. The tantalum interlayer is deposited for 10 min using direct current (DC) power supply (360 V, 0.30 Amp) to improve the adhesion strength. Then, TaN thin films are deposited using the RF power of 100 W. The other deposition parameters are given in Table 1. The stylus profilometer is used to find the thickness of the films. The crystallinity of the films is analysed by X-ray diffractometer (PANalytical Xpert Pro) using CuKα1 (λ = 0.15406 nm) radiation. Surface topography and surface roughness are investigated using atomic force microscopy (Digital Instruments Nanoscope IIIa AFM) in non-contact mode. The hardness of the coatings is investigated using a nanoindenter (Hysitron Model-TI 950 Tribo Indenter) equipped with a Berkovich diamond indenter. The maximum indentation depth is ~ 70 nm.

Table 1. Deposition parameters

RF sputtering power, W	100
Argon flow rate, sccm	30
Nitrogen flow rate, sccm	2, 5 and 10
Substrates	HSS and Si (100)
Substrate temperature, °C	500
Interlayer	Tantalum
Deposition time, h	1
Target	Tantalum
Base vacuum, mbar	3.0 × 10^{-6}
Deposition pressure, mbar	3.0 × 10^{-2}
Substrate to target distance, mm	80

Results and Discussion

Microstructural studies

X-ray diffraction (XRD) pattern of the TaN films deposited on HSS substrates is shown in Fig. 1. The thickness of the coating is ~ 2 μm. Tantalum nitride has different stable and metastable phases. The films are deposited under four different conditions. The film prepared at 10 sccm N_2 flow rate and 500 °C shows broad peak indicating the nanocrystalline nature of the film. The film prepared at 5 sccm N_2 flow rate and room temperature revealed peaks at angles 33.4, 35.6, 41.2, 47.8, 56.5, 62.0 and 68.7º corresponding to the hexagonal Ta_2N (110) (JCPDS File No: 39-1485) and FCC TaN (111),

(200), (220) and (311) phases (JCPDS # 49-1283). The film deposited at 5 sccm and 500 °C shows the peaks at angles 62.1 and 69.2° indicating the FCC structured TaN (220) and (311) phase [18–21]. The film deposited at 2 sccm and 500 °C shows the very strong peak at 69.1° reveals the FCC TaN phase with (311) orientation. These studies indicate that 2 and 5 sccm at 500 °C indicate the formation of FCC TaN phases. At room temperature and 5 sccm nitrogen flow, both Ta_2N and TaN phases are observed. When adding nitrogen during the deposition, it strongly influences the phase composition, microstructure and properties. The increase in N_2 partial pressure increases the reaction probability between N_2 and Ta, and the TaN content in the film increases. The crystallinity of the films increased with the decrease of N_2 partial pressure. As the N_2 partial pressure, decreased from 10 to 2 sccm, the (311) reflection is stronger corresponding to the FCC TaN phase.

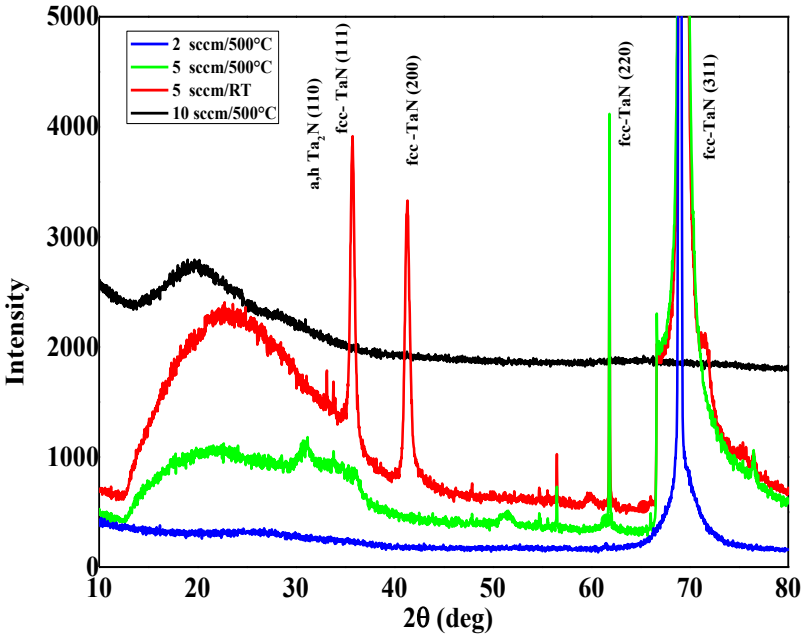

Fig. 1. XRD pattern of TaN films deposited on HSS-M2 substrates at 500 °C with different nitrogen flow rates

Michaela Grosser et al. [22] studied the phase composition, chemical and electrical properties of TaNx films with different nitrogen content. Aditya Aryasomayajula et al. [9] studied the TaN films deposited using pulsed DC magnetron sputtering method and the XRD studies showed the amorphous nature at low sputtering power. Bernoulli et al. [23] analyzed the effect of N_2 and Ar flow rate on structure and hardness of TaN and a transition from amorphous TaN to FCC TaN was observed. Elangovan et al. [14] prepared TaN films using pulsed DC magnetron sputtering and the XRD studies revealed the occurrence of α and β Tantalum in the films prepared in pure Argon atmosphere. The FCC TaN structures occurred for 2 sccm N_2 flow rate and cubic TaN for 5–25 sccm of N_2 with argon at 773 K. Nie et al. [19] prepared TaN films by reactive RF magnetron sputtering under various Ar/N_2 pressure and observed the changes from BCC tantalum to a mixture of hexagonal Ta_2N, and FCC TaN. Based on the microstructure, the property can be tuned for our applications. The phase formation is

either Ta_2N or TaN phase in the present work depending on the nitrogen flow rate. XRD peaks for the films shows the TaN phase, Ta_2N and TaN mixed phase and amorphous/nanocrystalline phase with the decrease in N_2 content. Therefore, it shows a structural dependence with respect to the nitrogen flow rate.

The surface topography and roughness of the films are investigated using AFM. The typical 3D images of the prepared films on silicon substrates with 3 × 3 μm^2 size are shown in Fig. 2. Atomic force microscopy (AFM) analysis of TaN coatings on silicon substrates at ambient temperature and 500 °C reveals significant differences in surface morphology and microstructural characteristics. The TaN coatings deposited at room temperature have a surface that is clearly granular, with small, tightly packed grains that have clear edges. The surface topography shows a fairly nanoscale structures with grain sizes that can be seen between 25–30 nm. The height distribution histogram for the room temperature sample shows a narrow, symmetrical distribution, which means that the surface properties are the same. On the other hand, the TaN coating deposited at 500 °C has a surface shape that is very different. The higher deposition temperature has made it easier for grains to grow, resulting in larger, more discrete crystallites. The surface topography shows a better three-dimensional grain structure with distinct height differences than the room temperature sample. The 3D surface representation clearly shows the increased roughness of the surface and more defined grain boundaries. Individual grains exhibit enhanced faceting and greater height variations, indicating superior crystalline formation. The height distribution histogram for the 500 °C sample shows a wider distribution with a slight asymmetry. This means that the surface is more uneven and the height changes more throughout the scanned area. The sample, deposited at room temperature has a surface roughness of ~ 2–3 nm, while the surface roughness was ~ 4–6 nm for the sample deposited at 500 °C. The thermal energy

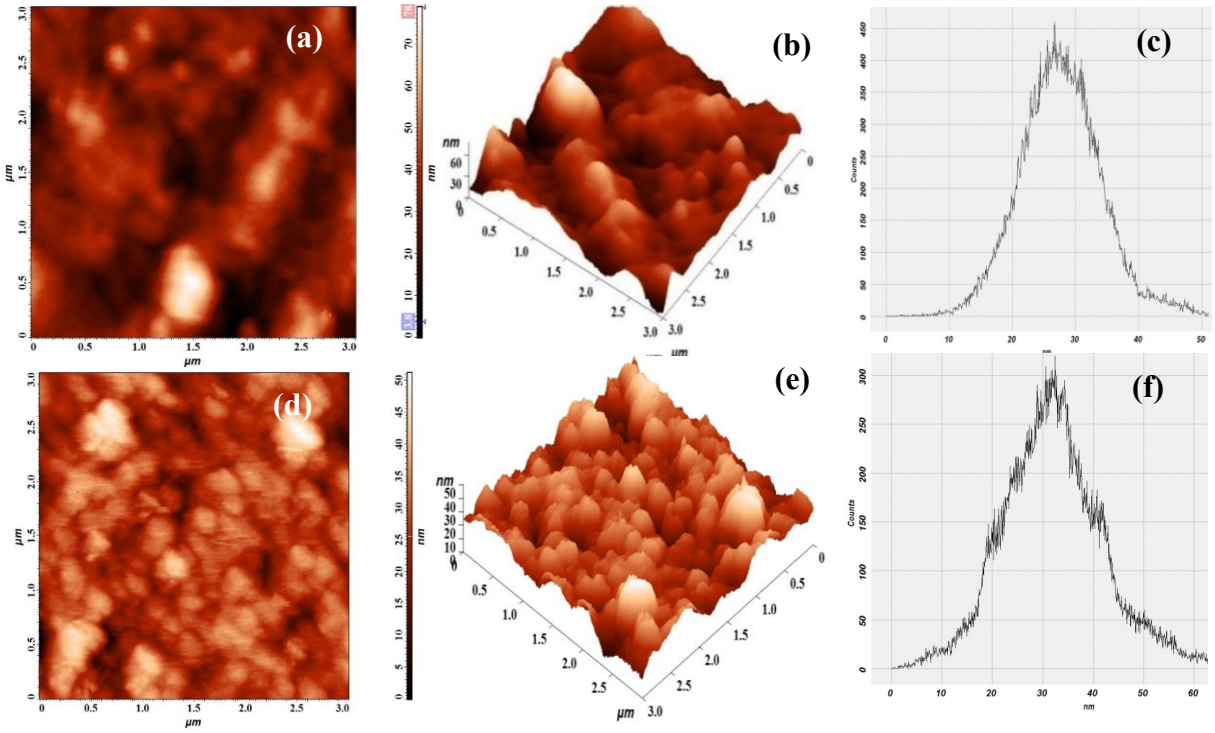

Fig. 2. (a,d) 2D, (b,e) 3D AFM images with (c,f) histogram of the TaN films deposited on Si at RT and 500 °C

is low at room temperature, the nucleation density is high, and grain growth is limited, which makes the microstructure less hard. At 500 °C, more thermal energy makes atoms move easily, which causes grains to merge and grow, resulting in larger grains with better crystallinity and higher hardness. The results are in concurrent with our XRD results [18,24–26].

Mechanical properties

The indentation studies are performed to a depth of 70 nm and ten indentations (Fig. 3) are carried out on each sample and the mean value is calculated. The microstructures, such as crystallite size, columnar structure, voids, film purity are the major components in deciding the properties. It is noticed that the hardness of the films is increased with the decrease of crystallite size. In the present work, N_2 flow rate is varied from 2 to 10 sccm and the mechanical property is found to be varied systematically (Table 2). For the TaN deposited at 10 sccm flow rate revealed the hardness of 9.46 ± 1.15 GPa, while at 5 sccm flow rate at 500 ºC indicated the hardness of 17.21 GPa, whereas the film deposited at 2 sccm flow showed the hardness of 30.05 ± 3.79 GPa. This clearly indicates that the hardness increased from 9.46 ± 1.15 to 30.05 ± 3.79 GPa with the decrease of N_2 flow rate.

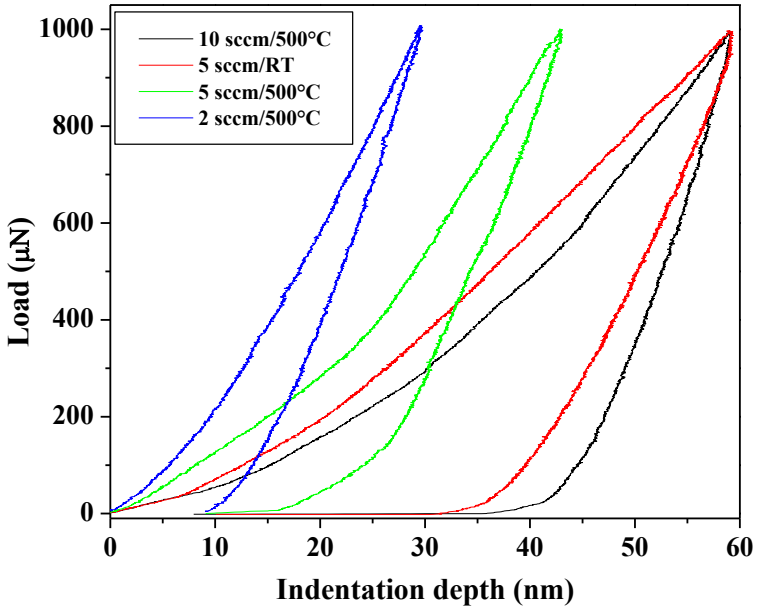

Fig. 3. Nanoindentation curves of TaN thin films deposited at different N_2 flow rates

Table 2. Nitrogen flow rates versus hardness of the films

Sample	Nitrogen flow rate, sccm	Nitrogen content, %	Substrate temperature, deg	Hardness, GPa	Elastic modulus, GPa
A	10.00	25.00	500	9.46 ± 1.15	229.80 ± 11.40
B	5.00	14.00	RT	10.44 ± 1.20	198.90 ± 14.45
C	5.00	14.00	500	17.21 ± 1.80	332.80 ± 19.31
D	2.00	6.00	500	30.05 ± 3.79	346.40 ± 24.00

Nie et al. [19] deposited the TaN films at different N_2 partial pressure range 0.0–30.0 % and the highest hardness of 27.8 GPa is obtained for the film prepared at 10 % N_2 partial pressure. The TaN films with low nitrogen, the hardness shows a structural

dependence. The decrease of crystallite size causes the hardness increased from 16 to 24 GPa. The processing settings and techniques of preparation determine the characteristics of the material. Research on tantalum thin films has shown that they can be used as extremely durable coatings [27–29]. Westergard [10] found that the TaN samples possess the hardness of 2250 to 3300 HV range and found to increase with N_2 flow rate. Yang et al. [6] reported the hardness and elastic modulus of 26 and 237.1 GPa, respectively for the TaN layer deposited using RF power of 150 W. Firouzabadi et al. [30] deposited the tantalum nitride films and found the formation of hexagonal Ta_2N and cubic TaN with increasing nitrogen flow rate. The present results are similar with the results obtained from other research groups [19,28–30]. The selection among these coatings (TiN, CrN, TiAlN, and TaN) is contingent upon the particular application. Although γ-Ta_2N exhibits superior hardness, TiN (31 ±4 GPa) provides commendable hardness with defined process settings. TiAlN (25–35 GPa) provides an optimal equilibrium with improved thermal stability, whereas CrN (18–25 GPa), despite its relative softness, may be favoured for applications having superior toughness with reduced residual stress. The enhanced hardness of specific TaN phases render them appealing for cutting tools and wear-resistant applications.

The TaN are of FCC structure and exhibit the strong covalent bonding with high bond density. The crystallized structure of FCC offers isotropic mechanical characteristics and dense atomic packing results in high cohesive energy, and the Ta_2N crystallizes in a hexagonal close-packed arrangement, which has the metallic character by the increased content of tantalum. The reduced level of nitrogen leads to reduced Ta_2N covalent bonds and increased anisotropic mechanical behaviour by layered hexagonal structure. TaN phase exhibited the greater hardness due to the nitrogen content and the structure whereas Ta_2N phase exhibited the lower hardness. In practice, TaN should be used when high hardness and wear resistance are needed, whereas Ta_2 N phase should be used when the toughness is needed.

Conclusions

Tantalum nitride coatings are deposited on HSS and silicon substrates using RF reactive magnetron sputtering technique. The thickness of the coating is ~ 2 μm. The microstructure and mechanical properties are studied at different N_2 flow rate. The hardness of the uncoated HSS is 727 HV. The XRD studies revealed the polycrystalline hexagonal Ta_2N and cubic TaN phases. The crystallite sizes increased with the decrease of N_2 partial pressure. The peak orientation changes as the nitrogen flow rate varied. The 3D AFM images show the formation of nanocrystallites with uniform distribution. The surface roughness is ~ 2–6 nm for the films. The nanoindentation studies indicated the hardness of 9.46 ± 1.15 GPa for the films deposited at 10 sccm N_2 flow rate, while it is 30.05 ± 3.79 GPa at 2 sccm N_2 flow rate. It is found that decrease in nitrogen content increases the hardness value of the coated sample. Also, the hardness is 17.21 ± 1.80 GPa at a substrate temperature of 500 °C, while it is 10.44 ± 1.20 GPa at room temperature. Hence, the TaN coating on high speed steel contributes to the increase of hardness. The increase of hardness value, resulting increase of wear resistance of the tool, and hence increasing the tool life time.

CRediT authorship contribution statement

G. Saravanakumar: conceptualization, methodology, software; **P. Gomathi**: experimental work, manuscript draft; **Vasanth Bharathi**: characterization of the samples and interpretation; **L. Ravikumar**: experimental work and supervision; **G. Balakrishnan**: writing, sample analysis and review.

Conflict of interest

The authors declare that they have no conflict of interest.

References

1. Rointan F. Bunshsh, Donald M. Mattox. *Handbook of Deposition Technologies For Films and Coatings Science*. New Jersey, USA: Noyes Pub.; 1982.
2. Bisht AK, Vaishya RO, Walia RS, Singh G. Nitrides ceramic coatings for tribological applications: A journey from binary to high-entropy compositions. *Ceram. Int.* 2024;50(6): 8553–8585.
3. Kaygorodov AS, Mamaev AS. Substrate influence on the mechanical properties of TiC/a-C coatings. *Materials Physics and Mechanics.* 2017;30(1): 35–39.
4. Feng HP, Hsu CH, Lu JK, Shy YH. Effects of PVD sputtered coatings on the corrosion resistance of AISI 304 stainless steel. *Mater. Sci. Eng. A.* 2003;347(1–2): 123–129.
5. Jiang H, Wang C, Zhang W, Si X, Li Y. Influences of Film Thickness on the Electrical Properties of TaNx Thin Films Deposited by Reactive DC Magnetron Sputtering. *Mater. Sci. Technol.* 2010;26(7): 597–600.
6. Yang YH, Chen DJ, Wu FB. Microstructure, hardness, and wear resistance of sputtering TaN coating by controlling RF input power. *Surf. Coat. Tech.* 2016;303: 32–40.
7. Grosser M, Seidel H, Schmid U. Microstructure and mechanical properties of sputter deposited tantalum nitride thin films after high temperature loading. *Thin Solid Films*. 2017;629: 69–78.
8. Chen Y, Zhang J, Gou H, Wang X, Chen Y, Guo H. Tantalum nitride thin film with a nearly zero temperature coefficient of resistance synthesized by magnetron co-sputtering. *Vacuum.* 2024;222: 113092.
9. Bend A, Kandadai VAS, Petersen JB, Jasthi BK. Effect of deposition pressure on the microstructure, mechanical, and corrosion properties of tantalum nitride thin films deposited by reactive pulsed laser deposition. *Vacuum.* 2025;238: 114228.
10. Singh V, Sharma RK, Sehgal R. An experimental investigation on nanomechanical and nanotribological behaviour of tantalum nitride coating deposited on Ti6Al7Nb alloy. *Tribol. Int.* 2024;194: 109461.
11. Aryasomayajula A, Valleti K, Aryasomayajula S, Bhat DG. Pulsed DC magnetron sputtered tantalum nitride hard coatings for tribological applications. *Surf. Coat. Tech.* 2006;201(7): 4401–4405.
12. Guo X, Niu Y, Chen M, Sun W, Zhu S, Wang F. Stoichiometry and tribological behavior of thick Ta(N) coatings produced by direct current magnetron sputtering (DCMS). *Appl. Surf. Sci.* 2018;427: 1071–1079.
13. Aryasomayajula A, Gupta MK, Janarthanaam SK. Studies on Tantalum Nitride (TaN) Hard Coatings on Turning Tools by DC Magnetron Sputtering Technique. In: *ASME 2005 International Mechanical Engineering Congress and Exposition.* ASME; 2008. p.101–104.
14. Elangovan T, Murugeshan S, Mangalaraj, D, Kuppusami P, Shabhana Khan, Sudha C, Ganesan V, Divakar R, Mohandas E. Synthesis and high temperature XRD studies of tantalum nitride thin films prepared by reactive pulsed dc magnetron sputtering. *J. Alloys. Compd.* 2011;509(22): 6400–6407.
15. Li X, Wang J, Li W, Liu P, Wang S, Li J, Mi B, Zhang G. Advancements in tantalum nitride-based films: A review. *J. Alloys Compd.* 2025;1020: 179427.
16. TC Li, BJ Lwo, NW Pu, SP Yu, CH Kao. The effects of nitrogen partial pressure on the properties of the TaNx films deposited by reactive magnetron sputtering. *Surf. Coat. Tech.* 2006;201(3–4): 1031–1036.
17. Yu H, Liang W, Miao Q, Yin M, Jin H, Sun Y, Xu Y, Chang X. Study on the wear resistance and thermodynamic stability of (MNbTaZrTi)N (M = Cr, Hf) high-entropy nitride coatings at elevated temperatures. *Surf. Coat. Tech.* 2025;497: 131792.
18. Lin JC, Chen G, Lee C. Growth of Tantalum Nitride Films on Si by Radio Frequency Reactive Sputtering: Effect of N2/Ar Flow Ratio. *Journal of The Electro Chemical Society.* 1999;146(5): 1835–1839.

19. Nie HB, Xu SY, Wang SJ, You LP, Yang Z, Ong CK, Li J, Liew TYF. Structural and electrical properties of tantalum nitride thin films fabricated by using reactive radio-frequency magnetron sputtering. *Appl. Phys. A.* 2001;73: 229–236.
20. Gladczuk L, Patel A, Demaree JD, Sosnowski M. Sputter deposition of bcc tantalum films with TaN underlayers for protection of steel. *Thin Solid Films.* 2005;476(2): 295–302.
21. Dobkowska A, Lofaj F, García MAG, Martinez DC, Kulikowski K, Paradiso A, Idaszek J, Gubicza J, Jenei P, Kabátová M, Kvetková L, Lisnichuk M, Inoue Sh, Kawamura Y, Święszkowski W. Structural, mechanical, corrosion, and early biological assessment of tantalum nitride coatings deposited by reactive HiTUS. *Surf. Coat. Tech.* 2024;493: 131267.
22. Grosser M, Münch M, Brenner J, Wilke M, Seidel H, Bienert C, Roosen A, Schmid U. Study on microstructural, chemical and electrical properties of tantalum nitride thin films deposited by reactive direct current magnetron sputtering. *Microsyst Technol.* 2010;16: 825–836.
23. Bernoulli D, Müller U, Schwarzenberger M, Hauert R, Spolenak R. Magnetron sputter deposited tantalum and tantalum nitride thin films: An analysis of phase, hardness and composition. *Thin Solid Films.* 2013;548: 157–161.
24. Riekkinen T, Molarius J, Laurila T, Nurmela A, Suni I, Kivilahti JK. Reactive sputter deposition and properties of TaxN thin films. *Microelectronic Engineering.* 2002;64(1–4): 289–297.
25. Lee WH, Lin JC, Lee C. Characterization of tantalum nitride films deposited by reactive sputtering of Ta in N_2/Ar gas mixtures. *Mater. Chem. Phys.* 2001;68(1–3): 266–271.
26. Alontseva D, Russakova A, Prokhorenkova N, Krasavin A, Borisov Y, Voinarovych S, Kyslytsia O. Development of microplasma spraying technology for applying biocompatible coatings. *Materials Physics and Mechanics.* 2018;39(1): 102–110.
27. Xu S, Munroe P, Xu J, Xie ZH. The microstructure and mechanical properties of tantalum nitride coatings deposited by a plasma assisted bias sputtering deposition process. *Surf. Coat. Tech.* 2016;307: 470–475.
28. YI Chen, BL Lin, YC Kuo, JC Huang, LC Chang, YT Lin. Preparation and annealing study of TaNx coatings on WC-Co substrates. *Appl. Surf. Sci.* 2011;257(15): 6741–6749.
29. Zemtsova EG, Morozov NF, Semenov BN, Valiev RZ, Smirnov VM. Mechanical properties of nanostructured titanium with bioactive titanium-organic nanocoating. *Materials Physics and Mechanics.* 2017;32(3): 253–257.
30. Firouzabadi SS, Naderi M, Dehghani K, Mahboubi F. Effect of nitrogen flow ratio on nano-mechanical properties of tantalum nitride thin film. *J. Alloys and Compds.* 2017;719: 63–70.

MATERIALS PHYSICS AND MECHANICS RESEARCH ARTICLE

Submitted: August 19, 2025 **Revised: September 30, 2025** **Accepted: October 16, 2025**

Microwave and infrared electromagnetic shields based on aluminum-containing polymer film

O.V. Boiprav [1] ✉, N.V. Bogush [1], V.V. Lobunov [1], V.V. Soloviev [2]

[1] Belarusian State University of Informatics and Radioelectronics, Minsk, Republic of Belarus

[2] Belarusian State Academy of Communications, Minsk, Republic of Belarus

✉ smu@bsuir.by

ABSTRACT

The technology of development microwave and infrared electromagnetic shields based on double-layer metalized polymer film and synthetic non-woven fibrous material is proposed. This technology consists in heat pressing of the construction, which is two fragments of the said fibrous material, between which fragments of the said film are uniformly distributed. The characteristics of electromagnetic radiation absorption and reflection in the frequency range of 0.7–17.0 GHz of the shields samples of various types developed in correspondence with the proposed technology are presented. The sample of each type differed in the number of fragments of double-layer metalized polymer film included in their composition (namely, the ratio between the total area of surface areas covered with double-layer metalized polymer film fragments and the total area of surface areas not covered with such fragments). In addition, the results of assessing the change in temperature of the front and back surfaces of the shields samples of each type as a result of the impact of infrared electromagnetic radiation on the first of the said surfaces are presented. It was found that electromagnetic shields developed in correspondence with the proposed technology are multi-band electromagnetic radiation absorbers in the frequency range of 1.6–17.0 GHz, which is their key advantage over their analogues. Such shields could be used for selection in the rooms zones for standing equipment sensitive to the microwave and thermal noise.

KEYWORDS

absorption • aluminum-containing polymer film • electromagnetic shield • polyurethane matrix • infrared range microwave range • reflection

Citation: Boiprav OV, Bogush NV, Lobunov VV, Soloviev VV. Microwave and infrared electromagnetic shields based on aluminum-containing polymer film. *Materials Physics and Mechanics*. 2025;53(5): 99–107. http://dx.doi.org/10.18149/MPM.5352025_8

Introduction

In order to create optimal conditions for the electronic devices functioning, it is required to protect them from the influences of electromagnetic radiation in both the microwave [1–5] and infrared [6–10] wavelength ranges. This is because that the influence of infrared electromagnetic radiation on electronic device components, as well as the influence of microwave electromagnetic radiation on them, lead to their premature failure. The following are prerequisites for premature failure of electronic device components due to influence of infrared electromagnetic radiation [11–15]: microscale deformation; changes of the volt–ampere characteristics parameters; changes of the electrical conductivity values.

To protect electronic devices components from the influence of microwave and infrared electromagnetic radiation, it is necessary to use microwave and infrared electromagnetic shields. The following types of such shields are currently known:

Publisher: Peter the Great St. Petersburg Polytechnic University

1. Textile material with a polyurethane coating, onto which a silver layer is applied using the magnetron sputtering method [16]. The electromagnetic radiation reflection coefficient value of this material in the microwave wavelength range is high value. The emissivity value of this material in the infrared wavelength range is low.
2. Hydrophilic PET fabric with a nanofiber coating based on PVA–co–PE, onto which a two–layer SiO2/Al film is applied using the magnetron sputtering method [17]. This fabric is characterized by high electrical conductivity and the presence of roughness. The size of this fabric roughness is comparable to the length of electromagnetic waves in the visible and infrared ranges.

The main disadvantage of shields [16,17] is their low manufacturability, which is caused by the following disadvantages of magnetron sputtering [18–20]: plasma instability; inability to achieve high–speed sputtering at low temperatures for strong magnetic materials due to magnetic flux limitations. In addition, of the electromagnetic radiation reflection coefficient values of these shields in the microwave wavelength range [16,17] are high. In this regard, these shields can be a source of passive electromagnetic interference in the specified wavelength range.

In connection with the above, the aim of the presented work was defined as the proposition and experimental confirmation of the technology for the development of microwave and infrared electromagnetic shields with the following properties in comparison with analogues: higher manufacturability; lower electromagnetic radiation reflection coefficient values in the microwave wavelength range (higher values of the electromagnetic radiation absorption coefficient in the specified wavelength range) [16,17]; developing the shields experimental samples developed in the correspondence with the proposed technology; assessment of the electromagnetic radiation absorption coefficient values in the microwave range of the developed shields samples; assessment of the change in the temperature of the front and back surfaces of the developed shields samples as a result of the impact on the first of the specified surfaces of infrared electromagnetic radiation.

Materials and Methods

The proposed technology includes the following operations:
1. Cutting out two same fragments of synthetic non–woven material. The dimensions and shape of such fragments are defined by the requirements to dimensions and shape of the electromagnetic shield being developed.
2. Cutting out fragments of double–layer metalized polymer film in correspondence with the following conditions: the fragments length and width should not exceed 3.0 and 1.0 cm, respectively; the fragments total area should be *C* % of the area of the fragments cut as a result of operation 1.
3. Uniform chaotic distribution of the double–layer metalized polymer fragments (operation 2), over the surface of one of the synthetic non–woven material fragments (operation 1).
4. Placing the other synthetic non–woven material fragment (operation 1) on top of the distributed double–layer metalized polymer fragments (operation 3).

5. Keeping the obtained construction in the heat press in correspondence with the following conditions: duration of 10.0 min; temperature of the heat press of ~ 250.0 ºC.

Double–layer metalized polymer film was used like the main component for the developing shields in the correspondence with the proposed technology due to the following reasons [21–23]: high electrical conductivity; high infrared electromagnetic radiation reflection coefficient.

Four types of shields samples were manufactured for the study. The type 1 sample was the reference one. It was a fragment of double–layer metalized polymer film. The types 2, 3 and 4 samples were developed in the correspondence with the proposed technology. Each of the samples of the listed types differed in the *C* value (Table 1).

Table 1. Characteristics of manufactured shields samples of the types 2, 3 and 4

Sample	*C*, %
Type 2 sample	50.0
Type 3 sample	65.0
Type 4 sample	75.0

The reference sample (the type 1 sample) was manufactured due to the following reasons:

1. to obtain the electromagnetic radiation absorption and transmission characteristics and surface temperature for the double–layer metalized polymer film, on the base of which the types 2, 3 and 4 samples were manufactured;
2. to define the difference between the electromagnetic radiation absorption and transmission characteristics and surface temperature of the double–layer metalized polymer film and the types 2, 3 and 4 samples manufactured on the base of this film (on the base of this difference it's possible to establish in what degree electromagnetic radiation absorption coefficients values of the types 2, 3 and 4 samples greater than electromagnetic radiation absorption coefficients values of the double–layer metalized polymer film, on the base of which these samples were manufactured).

To assess the electromagnetic radiation absorption coefficient values in the microwave range of the manufactured shields samples, the following was implemented.

1. The electromagnetic radiation reflection and transmission coefficients values by power (S11, dB and S21, dB respectively) in the frequency range 2.0–17.0 GHz were measured. The setup used in course of such measurements including the following components (Fig. 1): panoramic meter of transmission and reflection coefficients SNA 0.01–18; two horn antennas P6–23M with aperture size 351.0 × 265.0 mm^2 (type of the indicated antennas polarization is linear one). The measurements were carried out in correspondence with the method described in [24]. The measurements were carried out in the frequency range 0.7–17.0 GHz. This frequency range is associated with the operating frequencies of base stations of mobile communications, equipment used to build wireless information systems, radar stations, satellite systems, microwave ovens which together are sources of external electromagnetic fields for electronic devices [25–29].
2. The electromagnetic radiation reflection and transmission coefficients values (*R* and *T* respectively in relevance units (further – rel. units)) were calculated. The following equations are used in course of such calculations: $R = 10^{S_{11/10}}$, rel. units; $T = 10^{S_{21/10}}$, rel. units.

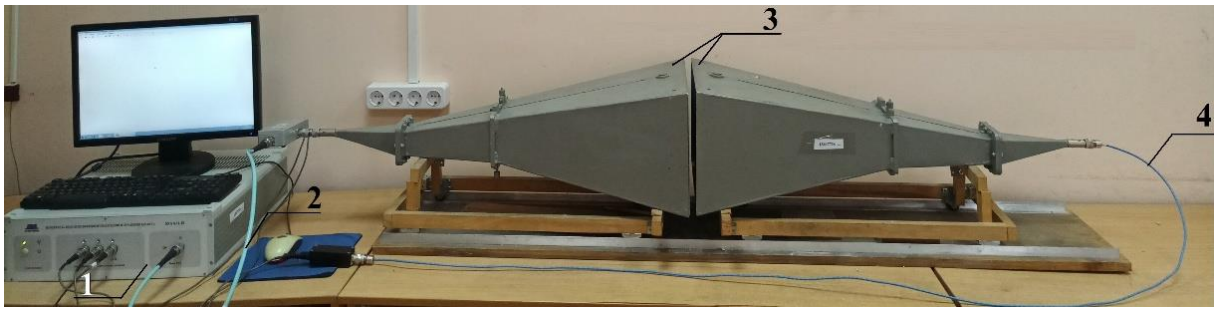

Fig. 1. Photo of the setup used in course of electromagnetic radiation reflection and transmission coefficients values measurements (1 – panoramic meter of transmission and reflection coefficients SNA 0.01–18; 2, 4 – coaxial waveguide; 3 – horn antennas P6–23M)

3. The electromagnetic radiation absorption coefficients values (*A*, rel. units) were calculated with use of the following equation: $A = 1 - R - T$, rel. units.

The technique presented in [30] was used to assess the change in the temperature of the front and back surfaces of the manufactured shields samples as a result of the impact of infrared electromagnetic radiation on the first of the specified surfaces. The conditions for performing the assessment were as follows: surface temperature of the used infrared electromagnetic radiation source of 70.0 ± 2.0 ºC; duration of exposure of the sample to infrared electromagnetic radiation of 60.0 ± 1.0 min; air temperature of 20.0 ± 1.0 ºC.

MobIR M4 thermal imaging camera, infrared electromagnetic radiation source based on MR16 halogen lamps, and C–01 electronic stopwatch were used during the assessment.

Results and Discussion

Results of measuring of S11 and S21 values of the types 1–4 samples on the base of which A values of these samples have been calculated are systematized in Table 2. *A* characteristic in the frequency range 0.7–17.0 GHz of the types 1–4 samples are presented on Fig. 2. As it can be seen from Fig. 2(a), *A* values in the frequency range 0.7–2.0 GHz of the electromagnetic shields samples developed in the correspondence with the proposed technology decrease from 0.2–0.6 to 0.2–0.45 rel. units, if the *C* value characteristic for these samples increases from 50.0 % till 65.0 or 75.0 %. This is because *R* values in the frequency range 0.7–2.0 GHz of such samples increase from 0.25–0.7 to 0.5–0.7 rel. units if the *C* value characteristic for these samples increases from 50.0 % till 65.0 or 75.0 % (Fig. 3(a)).

As can be seen from Fig. 2(b), if the *C* value characteristic for the samples of electromagnetic shields developed in the correspondence with the proposed technology increases from 50.0 till 65.0 % *A* values of such samples: decrease from 0.2–0.75 to 0.1–0.65 rel. units in the frequency range 2.0–7.5 GHz; increase from 0.2–0.6 to 0.3–0.7 rel. units in the frequency range 7.5–17.0 GHz. This explains *R* values of such samples under the specified condition increase from 0.1–0.7 to 0.25–0.85 rel. units in the frequency range 2.0–17.0 GHz (Fig. 3(b)); *T* values in the frequency range 7.5–17.0 GHz of the samples with $C = 50.0$ % is greater than *T* values in the specified frequency range of the samples with $C = 65.0$ %.

Table 2. Results of measuring of S_{11} and S_{21} values of the types 1–4 samples

Frequency, GHz	Type 1 sample		Type 2 sample		Type 3 sample		Type 4 sample	
	S_{11}, dB	S_{21}, dB	S_{11}, dB	S_{21}, dB	S_{11}, dB	S_{21}, dB	S_{11}, dB	S_{21}, dB
2.0	−0.2	−44.3	−1.4	−12.8	−0.7	−10.6	−4.7	−19.7
3.0	−0.6	−37.0	−5.1	−10.3	−2.8	−12.2	−0.7	−14.3
4.0	−1.1	−37.0	−4.0	−6.0	−2.4	−12.5	−1.5	−13.9
5.0	−2.7	−33.5	−5.1	−5.9	−4.2	−10.6	−3.1	−11.2
6.0	−4.1	−25.3	−11.3	−7.9	−5.9	−11.0	0.0	−12.8
7.0	−0.3	−29.1	−5.7	−7.6	−3.1	−7.2	−6.6	−12.4
8.0	−0.4	−28.8	−2.6	−5.6	−2.5	−9.0	−2.6	−11.7
9.0	−3.6	−27.0	−5.8	−6.0	−3.8	−10.5	−3.1	−14.6
10.0	−1.8	−28.5	−5.8	−6.7	−4.7	−11.0	−4.2	−14.0
11.0	−3.5	−28.9	−6.9	−6.3	−5.4	−11.0	−2.4	−16.8
12.0	−4.5	−25.2	−8.8	−7.0	−5.4	−10.7	−5.1	−16.0
13.0	−4.1	−27.2	−3.9	−8.4	−4.6	−11.8	−0.3	−15.6
14.0	−3.5	−19.6	−3.6	−7.9	−4.0	−11.4	−4.8	−17.2
15.0	−8.2	−18.2	−4.5	−7.8	−3.6	−12.8	−7.2	−17.3
16.0	−9.4	−14.7	−4.0	−6.4	−5.0	−12.2	−1.7	−18.4
17.0	−5.8	−12.7	−8.6	−6.1	−6.3	−12.1	−1.0	−15.9

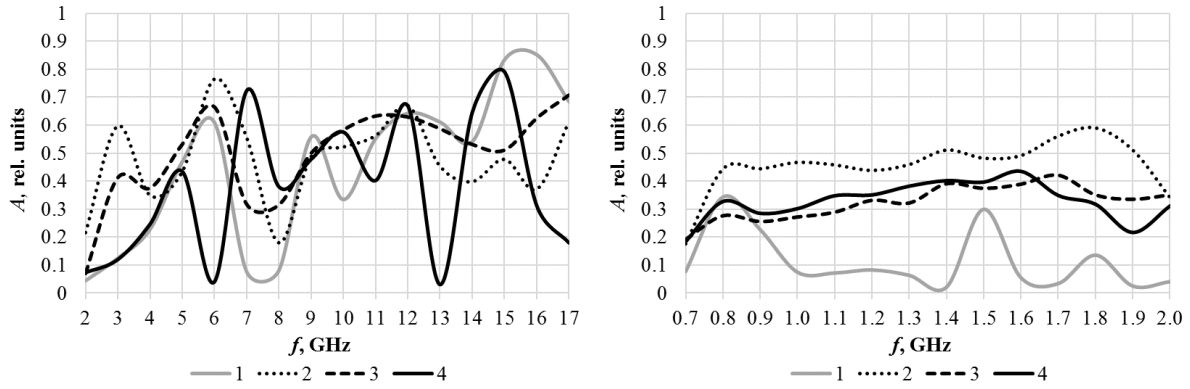

(a) (b)

Fig. 2. Graphs of the dependence of *A* characteristic on the frequency range (a) 0.7–2.0 and (b) 2.0–17.0 GHz of the types 1–4 samples (curves 1–4 respectively)

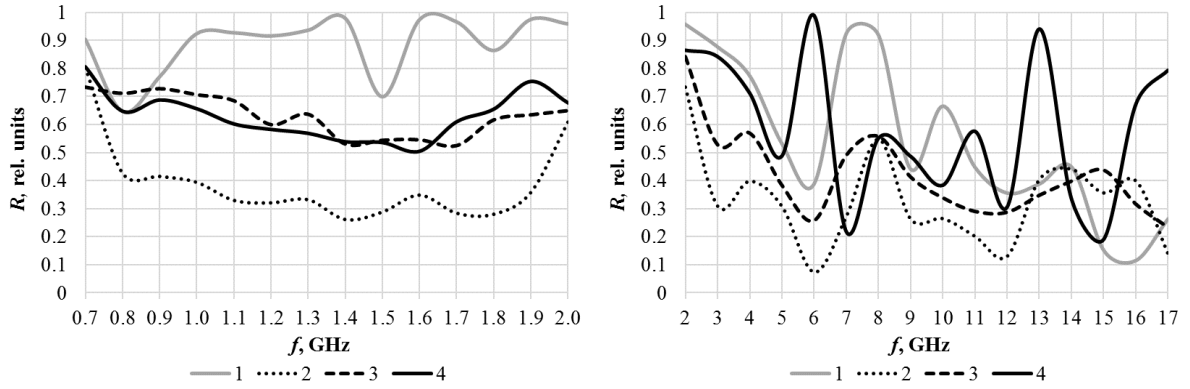

(a) (b)

Fig. 3. Graphs of the dependence of *R* characteristic on the frequency range (a) 0.7–2.0 and (b) 2.0–17.0 GHz of the types 1–4 samples (curves 1–4 respectively)

As can be also seen from Fig. 2(b), if the *C* value characteristic for the electromagnetic shields samples developed in the correspondence with the proposed technology increases from 50.0 till 75.0 % *A* values of such samples: decrease from 0.2–0.75 to 0.1–0.6 rel. units in the frequency range 2.0–7.0 GHz and from 0.55–0.65 to 0.05–0.6 rel. units in the frequency range 10.5–13.5 GHz and from 0.4–0.6 to 0.2–0.4 rel. units in the frequency range 16.0–17.0 GHz; increase from 0.2–0.6 to 0.35–0.75 rel. units in the frequency range 7.0–10.5 GHz and from 0.4–0.5 to 0.4–0.8 rel. units in the frequency range 13.5–16.0 GHz. This is due to *R* values of such samples under the specified condition increase from 0.1–0.7 to 0.2–0.99 rel. units in the frequency range 2.0–17.0 GHz (Fig. 3(b)), and *T* values in the frequency ranges 7.0–10.5 and 13.5–16.0 GHz of the samples with *C* = 50.0 % is greater than *T* values in the specified frequency ranges of the samples with *C* = 75.0 %.

It also seen from Fig. 2, that *A* values of the electromagnetic shields samples developed in the correspondence with the proposed technology is greater on 0.1–0.6 rel. units then that *A* values of the sample in the form of the fragment of double–layer metalized polymer film. Oscillations in the *R* characteristics of the samples may be due to the antiphase interaction of electromagnetic waves reflected from the sample surfaces and electromagnetic waves incident on them. Furthermore, this may be due to the dependence of the electrical conductivity of the double–layer metalized polymer film, which is to be used to fabricate the proposed electromagnetic shields, on the frequency of the electromagnetic radiation. Table 3 presents the values of effective absorption bands and bandwidths of the studied samples. It follows from Table 2, that the type 3 sample has the widest effective absorption band compared with the 1, 2 and 4 type samples.

Table 3. The values of effective absorption band and bandwidth of the studied samples

Sample	Effective absorption band, GHz	Effective absorption bandwidth, GHz
Type 1 sample	5.0–16.5 8.7–9.2 10.5–17.0	1.5 0.5 6.5
Type 2 sample	1.6–1.9 2.5–3.5 5.0–7.0 9.0–12.8 16.5–17.0	0.3 1.0 2.0 3.8 0.5
Type 3 sample	4.5–6.5 9.0–17.0	2.0 8.0
Type 4 sample	6.5–7.8 9.0–10.5 11.5–12.5 13.5–15.5	1.3 1.5 1.0 2.0

Graphic dependencies obtained from the results of assessing the change in temperature of the front and back surfaces of the manufactured shields samples as a result of exposure of the first of the indicated surfaces to infrared electromagnetic radiation are presented on Fig. 4. It follows from Fig. 4 that as a result of the increase from 50.0 to 75.0 % of *C* value, typical for shields samples developed in the correspondence with the proposed technology: the temperature of their front surface

increases from 45.0 ± 1.0 to 50.0 ± 1.0 ºC under the conditions in which the studies were conducted; the temperature of their back surface decreases from 36.0 ± 1.0 °C to 34.0±1.0 °C under the conditions in which the studies were conducted. This is due to the increase in the value of the electromagnetic radiation reflection coefficient in the infrared wavelength range of the above–mentioned shields. It should be noted that the temperature of the front surface of the type 1 sample under the conditions in which the studies were conducted is 52.0 ± 1.0 °C.

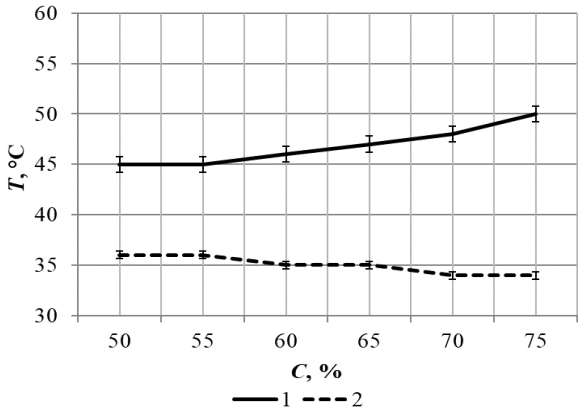

Fig. 4. Graphs of the dependence of the temperature of the front (curve 1) and back (curve 2) surfaces of the types 2–4 samples on the ratio *C*

Conclusions

Thus, electromagnetic shields developed in the correspondence with the proposed technology are multi–band absorbers of the electromagnetic radiation in the frequency range 1.6–17.0 GHz, which is one of their advantages compared to their analogues [16,17]. In addition, these shields, compared to their analogues [16,17], are more manufacturable. This is due to the fact that the time costs for their production are lower, and the degree of reproducibility of their manufacturing technology is higher.

Electromagnetic shields developed in correspondence with the proposed technology could be used for selection in the rooms zones for standing equipment sensitive to the microwave and thermal noises. In such cases they look like screens that must be attached to the frame made from radio transparency material.

CRediT authorship contribution statement

Olga V. Boiprav: writing – original draft, writing – review & editing; **Natalia V. Bogush**: investigation, validation; **Vadim V. Lobunov** : methodology, investigation; **Vladimir V. Soloviev** : formal analysis.

Conflict of interest

The authors declare that they have no conflict of interest.

References

1. Przesmycki R. Classification of the electromagnetic effects of information devices during high power microwave exposing. In: *2017 Progress in Electromagnetics Research Symposium – Fall (PIERS-FALL).* Singapore; 2017. p.357–363.
2. Batool S, Bibi A, Frezza F, Mangini F. Benefits and hazards of electromagnetic waves, telecommunication, physical and biomedical: a review. *European Review for Medical and Pharmacological Sciences.* 2019;23(7): 3121—3128.
3. Apakuppakul S, Methachittiphan N, Apiyasawat S. Effect of electromagnetic interference from smartphone on cardiac implantable electronic device (EMI-phone study). *Journal of Arrythmia.* 2022;38(5): 778—782.
4. Elmahaishi MF, Azis RS, Ismail I, Muhammad FD. A review on electromagnetic microwave absorption properties: their materials and performance. *Journal of Materials Research and Technology.* 2022;20: 2188—2220.
5. Hamouda SA, Amneenah NS. Electromagnetic interference impacts on electronic systems and regulations. *International Journal of Advanced Multidisciplinary Research and Studies.* 2024;4(1): 124—127.
6. Kataoka S, Atagi K. Prevention of IR interference from high frequency fluorescent lighting to IR remote-control systems. In: *Proceedings of 1995 IEEE Applied Power Electronics Conference and Exposition (APEC); 1995 March 5–9; Dallas, TX, USA.* 1995. p.785–789.
7. Kataoka S, Atagi K. Preventing IR interference between infrared waves emitted by high-frequency fluorescent lighting systems and infrared remote controls. *IEEE Transactions on Industry Applications.* 1997;33(1): 239—245.
8. Gayo E, de Fruto J. Interference filters as an enhancement tool for infrared thermography in humidity studies of building elements. *Infrared Physics & Technology.* 1997;38(4): 251—258.
9. Yoon Y, Hyeon S, Kim DR, Lee K-S. Minimizing thermal interference effects of multiple heat sources for effective cooling of power conversion electronics. *Energy Conversion and Management.* 2018;174: 218—226.
10. Ma J, Zheng H, Sun Y, Zhang Z, Wang X, Ding G. Temperature compensation method for infrared detection of live equipment under the interferences of wind speed and ambient temperature. *IEEE Transactions on Instrumentation and Measurement.* 2021;70: 3508709.
11. Schelling PK, Shi L, Goodson KE. Managing heat for electronics. *Materials Today.* 2005;8(6): 30—35.
12. Almubarak AA. The effects of heat on electronic components. *International Journal of Engineering Research and Application.* 2017;7(5): 52—57.
13. Cai L, Li P, Luo Q, Yan H, Zhai P, Gao P. Investigation of thermal radiation effects on thermoelectric module performance by an improved model. *Journal of Power Sources.* 2020;477: 228713.
14. Askerov SG, Gasanov MG, Kabdullayeva L. The influence of the metal microstructure on the breakdown mechanism of schottky diodes. *Materials Physics and Chemistry.* 2022;4(1): 1—6.
15. Beysembaeva BS, Ezhizhanskiy VD, Yarkin AE, Aseev EA, Reuta NS. Methods and means of ensuring the thermal regime of electronic equipment. *Reliability and Quality of Complex Systems.* 2024;(4): 96—102. (In Russian)
16. Wang J, Hu Q, Huang J, Li J, Lu Y, Liang T, Shen B, Zheng W, Song W. Multifunctional textiles enabled by simultaneous interaction with infrared and microwave electromagnetic waves. *Advanced Materials Interfaces.* 2022;9(12): 2102322.
17. Ye H, Liu Q, Xu X, Song M, Lu Y, Yang L, Wang W, Wang Y, Li M, Wang D. Construction strategy for flexible and breathable SiO2/Al/NFs/PET composite fabrics with dual shielding against microwave and infrared–thermal radiations for wearable protective clothing. *Polymers.* 2024;16(1): 6.
18. Mehr AK, Mehr AK. Magnetron sputtering issues concerning growth of magnetic films: a technical approach to background, solutions, and outlook. *Applied Physics A.* 2023;129(9): 662.
19. Garg R, Gonuguntla S, Sk S, Iqbal MS, Dadoa AO, Pal U, Ahmadipour M. Sputtering thin films: materials, applications, challenges and future directions. *Advances in Colloid and Interface Science.* 2024;330: 103203.
20. Borowski P, Mysliwiec J. Recent advances in magnetron sputtering: from fundamentals to industrial applications. *Coatings.* 2025;15(8): 922.
21. Pechen TM, Prudnik AM. Interaction of optical waves with a screening thin film aluminum coating having nickel nanoparticles. *Materials Physics and Mechanics.* 2018;39(1): 87—91.
22. Kassner ME. Recent developments in understanding the creep of aluminum. *Materials Physics and Mechanics.* 2018;40(1): 1—6.
23. Kumar D, Kumar P, Kaur K, Chalisgaonkar R, Singh SS, Gupta M. Investigation of aluminum metal matrix composite fabrication processes: a comparative review. *Materials Physics and Mechanics.* 2024;52(6): 154—170.

24. Boiprav O, Ayad H, Abdaljlil SA, Lynkou L, Abdulmawlay M. Charcoal- and foil-containing materials for radio electronic control systems protection from electromagnetic interferences. In: *2022 IEEE 21st International Conference on Sciences and Techniques of Automatic Control and Computer Engineering (STA).* 2022. p.299—304.
25. Hasanov MH, Atayev NA. Algorithm design nanosatellite based on radio frequency and optical communication. *Problems of Information Technology.* 2022;13(2): 61—68.
26. Hasanov MH, Mammadov FH, Sultanova S, Israfilova QA. Study of probability-time characteristics of GSM standard mobile telecommunication networks. *Herald of Azerbaijan Engineering Academy.* 2023;15(3): 80—89.
27. Hasanov MH, Mammadov FH, Orujova MY. Analysis of construction principles of fifth generation mobile communication networks (5G). *Herald of the Azerbaijan Engineering Academy.* 2024;16(2): 75—81.
28. Hammarin G, Norder P, Harimoorthy R, Chen G, Berntsen P, Widlund PO, Stoij C, Rodilla H, Swenson J, Branden G, Neutze R. No observable non-thermal effect of microwave radiation on the growth of microtubules. *Scientific Reports.* 2024;14: 18286.
29. Rawat K. Hazardous effect of use of microwave on human health. *International Journal of Innovative Research in Science, Engineering and Technology.* 2017;6(7): 20565—20572.
30. Boiprav OV, Lobunov VV, Lynkov LM, Al-Mashat EAA. Study of the interaction of electromagnetic radiation of the infrared wavelength range with radio absorbers based on metal-containing elements. *Aviation Materials and Technologies.* 2020;2(59): 89—94. (In Russian)

MATERIALS PHYSICS AND MECHANICS RESEARCH ARTICLE

Submitted: July 13, 2025 **Revised: September 30, 2025** **Accepted: October 30, 2025**

Work hardening behavior of AISI 321 austenitic stainless steel with different initial microstructures

M.S. Ghazani [1]✉, H.A. Rezai [2]

[1] Department of Materials Science Engineering, University of Bonab, Bonab, Iran

[2] Department of Materials Science Engineering, Sahand University of Technology, Tabriz, Iran

✉ m_shaban@ubonab.ac.ir

ABSTRACT

In the present investigation, different microstructures were obtained in AISI 321 austenitic stainless steel by cold rolling and subsequent annealing at different temperatures. The effect of initial microstructure on the work hardening behavior was analyzed using tensile analysis. At annealing temperatures of 700 and 800 °C, the stage I hardening is not apparent due to the high density of dislocations existed inside the austenite grains prior to tensile deformation. But the stage I hardening is seen in the ln(σ) ~ ln(ε) curves of the sample annealed at 900 °C and coarse grained one because the microstructures are consisted of equiaxed and dislocation free austenite grains. More detailed results were also obtained by differential Crussard-Jaoul analysis. This analysis indicated the occurrence of austenite to martensite transformation during tensile deformation of as received sample and that was annealed at 900 °C, which is distinguished by a positive slope in the ln(dσ/dε) vs. ln(ε) curves.

KEYWORDS

AISI 321 stainless steel • work hardening • cold rolling • annealing • tensile deformation

Citation: Ghazani MS, Rezai HA. Work hardening behavior of AISI 321 austenitic stainless steel with different initial microstructures. *Materials Physics and Mechanics*. 2025;53(5): 108–121.
http://dx.doi.org/10.18149/MPM.5352025_9

Introduction

For a work-piece to be suitable for utilization in a corrosive environment under external loads, the material used in its manufacture must have a combination of excellent corrosion resistance and outstanding mechanical properties [1]. Under these conditions, austenitic stainless steels are a good candidate. Despite these excellent properties, most of the austenitic stainless steels are susceptible to intergranular corrosion [2,3] and stress corrosion cracking [4]. In order to improve the resistance to intergranular corrosion and prevent sensitization, a sufficient amount of carbide forming elements such as titanium and niobium is added to their chemical composition. In Ti stabilized the AISI 321 austenitic stainless steel, a suitable amount of titanium (wt. %Ti =5 × wt. %C) is added to favor the formation of TiC precipitates which keeps chromium in solution at the austenite grain boundary area and improves resistance against the grain boundary sensitization [5].

Much research has been done on the corrosion resistance of this type of steel. For example, Lima et al. [6] studied the sensitization evaluation of austenitic stainless steels and reported that the stabilized steels (AISI 321 and AISI 347) are more resistant to sensitization than non-stabilized steels (ISI 304 and AISI 316). It was also concluded that niobium is more efficient stabilizing agent than titanium. Pardo et al. [7] studied the influence of Ti, C and N content of chemical composition on the intergranular corrosion

Publisher: Peter the Great St. Petersburg Polytechnic University

resistance of AISI 316Ti and AISI 321 stainless steels. It was demonstrated that the addition of Ti promotes intergranular corrosion resistance in stainless steels. Also, the reduction of carbon content to below 0.03 wt. % increases the sensitization resistance more than does Ti content.

Some research has also been done on the mechanical properties of the AISI 321 austenitic stainless steel. Zhao et al. [8] investigated the effect of solution treatment on microstructures and mechanical properties of the AISI 321 steel. They reported that the amount of sigma phase in the microstructure reaches to 18 wt. % after 1000 h service at 800 °C. It was concluded that the amount of sigma phase decreases from 18 to 2.6 wt. % with increasing the duration of solution annealing to 2 h. Also, it was shown that the size of austenite grains increases with solution annealing time which improves the fracture toughness in AISI 321 stainless steel. The strain hardening capacity measured by tensile testing is one of deformation characteristics of materials which determines the amount of uniform plastic deformation [9,10]. In materials with low strain hardening exponent, the onset of necking occurs earlier, and the total elongation and ductility decreases during tensile deformation [11]. This parameter also affects the toughness and workability of materials during metal forming processes. Dini et al. [12] investigated the effect of grain size on the work hardening behavior of high manganese austenitic steel and demonstrated that the optimum mechanical properties are achieved with varied work hardening capacities that can be obtained by changing the grain size. Also, it has been approved that the main reason for the low ductility of nanostructured materials is the low work hardening rate during uniform plastic deformation stage [13]. Therefore, Wang et al. [14] proposed three different strategies to achieve uniform tensile deformation in nanostructured metals. Producing bimodal or multi-modal grain size distribution is one of these methods. Considering the available literature, it is observed that the work hardening behavior of the AISI 321 stainless steel has been studied only in the work of Zhang et al. [15]. In this investigation, the difference in the work hardening behaviors of AISI 321 and Hadfield steels were attributed to the occurrence of twining in the Hadfield steel. Also, they declared that work hardening of the AISI 321 stainless steel is mainly resulted from dislocation interactions. They did not report any other microstructural evolution, such as austenite to martensite transformation (TRIP effect), that can affect the work hardening behavior of this steel. It is to be mentioned that our previous work [16] was mostly focused on post-deformation annealing's role on microstructure and mechanical properties of the cold-rolled AISI 321 stainless steel. In contrast, this work reports a thorough and detailed investigation of work hardening behavior by both Hollomon and differential Crussard–Jaoul (C–J) methods. In addition, the impact of different initial microstructures (coarse-grained, fine-grained, bimodal, and cold-worked) on absence or presence of visible hardening steps is described and the role of austenite-to-martensite transformation is highlighted (TRIP effect). These points have not been expressed in the literature and constitute the innovation of this study.

Materials and Methods

The chemical composition of the AISI 321 austenitic stainless steel used in the present study is represented in Table 1. In this type of stainless steels, chromium and nickel are

added to increase the corrosion resistance and stabilize the austenite phase respectively. Moreover, the addition of titanium by 0.3 wt. % prevents the sensitization of material to grain boundary corrosion through the formation of titanium carbide (TiC) precipitates instead of chromium carbide ($Cr_{23}C_7$) which depletes grain boundaries from chromium. The material was received in the form of a sheet with 10 mm thickness. The sheet was cut into smaller pieces with dimensions of 150 × 25 mm^2 to be suitable for cold rolling. All pieces were solution annealed at 1200 °C for 15 min and then quenched in water to obtain a fully austenitic structure. All samples were then rolled at room temperature with 80 % cross-section reduction. After cold rolling, samples were annealed for 15 min at 700, 800, and 900 °C.

Table 1. Chemical composition of the AISI 321 austenitic stainless steel

C	Si	Mn	Cr	Ni	Mo	Ti	N	Fe
0.036	0.421	1.910	17.154	8.620	0.374	0.303	0.013	bal.

Microstructure analysis was performed using optical microscopy after surface preparation by conventional metallographic procedure. For this reason, sample surfaces were ground with sandpapers of 100–2500 grit and then mechanically polished with 0.05-μm alumina suspension. To reveal grain structure, the electrolytic etching was used in the solution of 50 % nitric acid and distilled water by applying the current density of 0.1 mA/cm^2. Optical images were taken using Olympus PMG3 microscope. Tensile testing at room temperature was used for analyzing mechanical properties and work hardening behavior of cold rolled and annealed samples. Tensile samples were prepared according to ASTM E8 standard and tensile tests were conducted using Gotech AI-7000-LA20 testing machine with the cross-head speed of 0.1 mm/min. The work hardening behavior of cold rolled and annealed samples were then analyzed employing the Hollomon and differential C-J methods.

Results and Discussion

Tensile properties

Figure 1(a) shows the engineering stress-engineering strain curves of the AISI 321 austenitic stainless steel at different annealing conditions. As can be seen, the as received sample exhibit a lower tensile stress and higher elongation than the cold rolled and subsequently annealed samples. Also, exceptionally high value of tensile elongation observed during tensile testing as received sample, can be attributed to microstructural evolutions during deformation, and will be discussed later. For annealed samples, it is seen that the tensile strength increases and elongation to failure decreases with decreasing annealing temperature. The true stress-true strain curves obtained from engineering curves are shown in Fig. 1(b). These curves were plotted up to the strain corresponding to the maximum stress in the engineering stress-engineering strain curves. Obtained true stress-true strain curves were then used for evaluation of the work hardening behavior of the AISI 321 steel during tensile deformation. The tensile properties of the AISI 321 austenitic steel at different annealing conditions, obtained from engineering curves, are summarized in Table 2. The yield and tensile strengths of as received sample are 92 and 439 MPa respectively. The yield strength of as-received

sample is increased from 92 to 330, 586, and 800 MPa after cold rolling and annealing at 900, 800, and 700 °C respectively. Also, the tensile strength increases from 439 to 668, 956, and 1189 MPa by cold rolling and annealing at 900, 800, and 700 °C, respectively. The variations of tensile properties by cold rolling and annealing could be discussed considering the obtained microstructures.

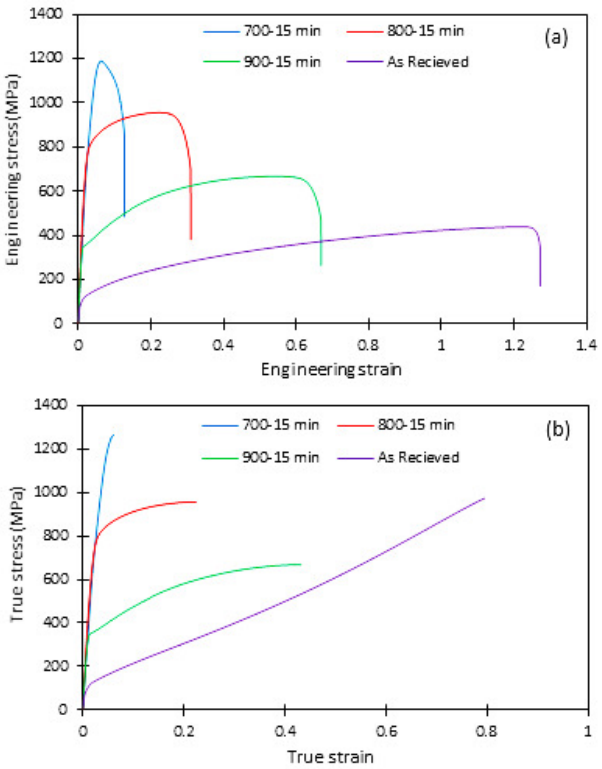

Fig. 1. Engineering stress vs. engineering strain (a), and true stress vs. true strain (b) curves of AISI 321 austenitic stainless steel after cold rolling and annealing at different temperatures

Table 2. Tensile properties of the as-received and cold rolled and annealed AISI 321 steels

Sample	Yield strength	Tensile strength	Total elongation, %	Uniform strain	Non-uniform strain	Hardening capacity	Uniform/non-uniform
700 °C	800 ± 12	1189 ± 20	13 ± 1	0.06	0.07	0.49	0.86
800 °C	586 ± 16	955 ± 13	31 ± 2	0.24	0.06	0.63	3.77
900 °C	330 ± 10	667 ± 12	67 ± 4	0.59	0.08	1.02	7.37
As-received	92 ± 8	439 ± 9	127 ± 6	1.23	0.04	3.78	30.75

Figure 2 shows the optical micrographs of the as-received and cold rolled and annealed samples. It is seen that the initial microstructure (Fig. 2(d)) is consisted of equiaxed austenite grains where their mean size was measured to be 120 μm with average intercept method. Fig. 2(c) shows the microstructure of the AISI 321 steel after cold rolling and annealing at 900 °C. This microstructure is also consisted of equiaxed austenite grains with the mean grain size of 5 μm. This uniform microstructure is obtained due to the occurrence of three different phenomena during annealing: static recrystallization in cold deformed austenite grains, martensite to austenite reversion and subsequent grain growth. The increase in strength after cold rolling and annealing at

900 °C is attributed to the reduction of mean grain size of austenite from 120 to 5 μm. It should be emphasis that the grain size strengthening follows the Hall-Petch relation in which the yield strength is proportional to the inverse of the square root of mean grain size ($\sigma_y = \sigma_0 + kd^{-1/2}$). According to Hall-Petch relation, the strength of material increases with decreasing grain size. It is worth to note that the number of dislocations at pile-ups decreases with grain refinement which produces smaller strain concentrations at the boundary with the nearing grain. Therefore, higher applied stresses are required to cause slip to pass to the neighboring grains through the grain boundary [17].

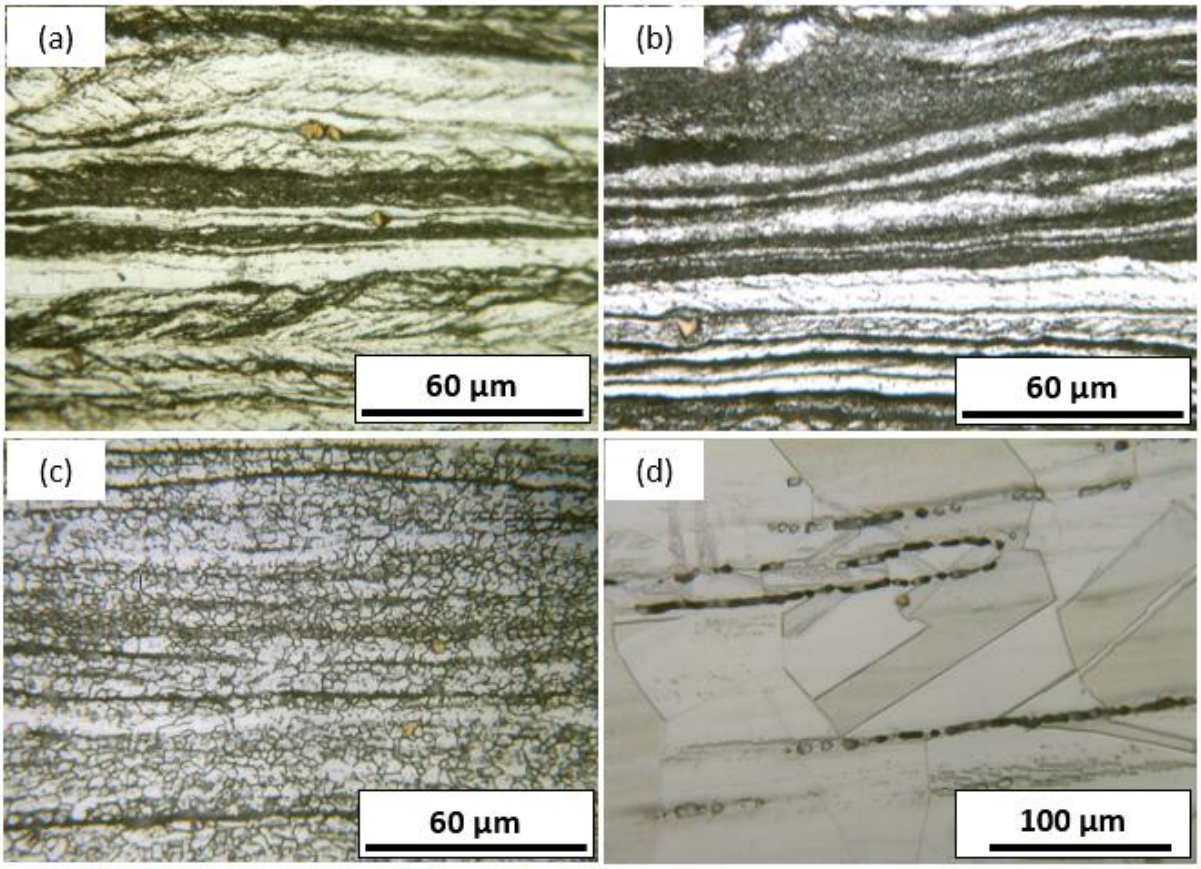

Fig. 2. Optical microstructures of AISI 321 austenitic stainless steel after cold rolling and annealing for 15 min at different temperatures: (a) 700 °C, (b) 800 °C, (c) 900 °C, and (d) initial coarse-grained sample

Figure 2(b) shows the microstructure after cold rolling and annealing at 800 °C for 15 min. The microstructure appears to consist of elongated austenite grains, together with ultrafine austenite grains formed by martensite reversion. The presence of relatively equiaxed and bright regions suggests that partial recrystallization might have occurred locally, although this cannot be confirmed with certainty using only optical metallography. Advanced characterization (e.g., electron backscatter diffraction (EBSD) or transmission electron microscopy (TEM)) would be necessary to unambiguously verify recrystallization. At this condition, the annealing time and temperature is probably not high enough for the sufficient growth of the ultrafine austenite grains, so that the bimodal grain size is produced. Whereas, annealing at 900 °C results in a uniform microstructure may be due to the intense growth of ultrafine austenite grains, after the martensite to

austenite phase transformation, so that their sizes are almost become equal to the mean size of the coarse austenite grains obtained by static recrystallization. Therefore, it could be mentioned that the increase in yield strength from 330 to 568 MPa and tensile strength from 668 to 956 MPa with decreasing the annealing temperature from 900 to 800 °C is mainly due to the refinement of equiaxed austenite grains. As it is seen in Fig. 2(a), the microstructure after annealing at 700 °C for 15 min is consisted of ultrafine austenite grains (dark regions) developed as a result of martensite to austenite transformation and elongated austenite grains (bright regions) with the traces of shear bands which indicates that the annealing temperature is not high enough to trigger static recrystallization inside cold worked grains. Therefore, increasing yield strength to 800 MPa and tensile strength to 1189 MPa by annealing at 700 °C is due to the effect of grain refinement and also higher dislocation density inside the elongated grains.

Hollomon analysis of work hardening behavior

In the present study, the Hollomon power low expression was used to describe the strain hardening characteristics of the AISI 321 austenitic stainless steel at different annealed conditions. The Hollomon equation is as follows [18]:

$$\sigma = k\varepsilon^n, \quad (1)$$

where ε is true strain, σ is true stress, n is the strain hardening exponent, and k is the strength coefficient. As it is evident, by writing the logarithmic form of the above equation, it is possible to evaluate the strain hardening exponent (n) and the strength coefficient (k) from the slope and intercept of the curves, respectively. The logarithmic form of the Hollomon equation is written as below:

$$ln\,(\sigma) = ln\,(k) + n\,ln\,(\varepsilon). \quad (2)$$

Figure 3 shows the ln (σ) vs. ln (ε) curves obtained from the experimental true stress vs. true strain curves of the as received and the cold rolled and subsequently annealed samples. The obtained plots indicate that none of the samples exhibited the linear variation of the ln(σ) vs. ln(ε) with a unique value for strain hardening exponent (n). As can be seen, for samples annealed, after 80 % cold rolling, at 700 and 800 °C for 15 min, the two-stage work hardening behavior is evident where the value of work hardening exponent is higher at first stage compared with second stage (Fig. 3(a,b)). Also, for sample annealed at 900 °C for 15 min after cold rolling and as received coarse grained one, the two-stage work hardening behavior is obvious (Fig. 2(c,d)) but the strain hardening exponent in the second stage is higher than the first stage. The two-stage work hardening behavior of steels has been reported earlier by other researchers. Shin et al. [19] studied the variation of tensile behavior after aging heat treatment of precipitation hardened martensitic steel. They suggested that the plastic strain regimes can be divided into two different stages by a rapid increase in strain hardening followed by a comparatively lower increase. It was revealed in their investigation that the strain hardening exponents at the first and the second stages is associated with the Ni_3Al precipitates. Kosaka et al. [20] investigated the work hardening behavior of the ferritic steels containing fine carbides varied from 3 to 15 nm. They concluded that work hardening proceeds in two stages and the plastic strain at which the later stage starts during tensile deformation decreases with the increase in the diameter of carbides. It is worth to note that work hardening in FFC single

crystal materials occurs in three different stages based on the nature of the dislocation interactions during tensile deformation. Comparing the results obtained in this study with the work hardening behavior of FCC materials [21], it is inferred that the stage I is absent during tensile testing of all samples. It should be noted that the stage I work hardening is representative of the easy glide of dislocations at the beginning of plastic deformation of single crystal materials. At this step, dislocations can slip over a long distance on the primary slip system without interacting with other dislocations and obstacles. The stage I work hardening is characterized by the low values of strain hardening exponent. Whereas the stage I work hardening shown in Fig. 3(c,d) for sample annealed at 900 °C for 15 min and as received coarse gained one does not occur due to easy glide of dislocations. For polycrystalline materials such as the present steel, the initial stage of deformation is more appropriately attributed to early multiple slip, which provides deformation compatibility between grains, rather than easy glide on a primary slip system as in single crystals. The low strain hardening rate observed in the stage I of the present samples is therefore interpreted as resulting from limited dislocation interactions at the onset of multiple slip, prior to significant dislocation accumulation and forest hardening.

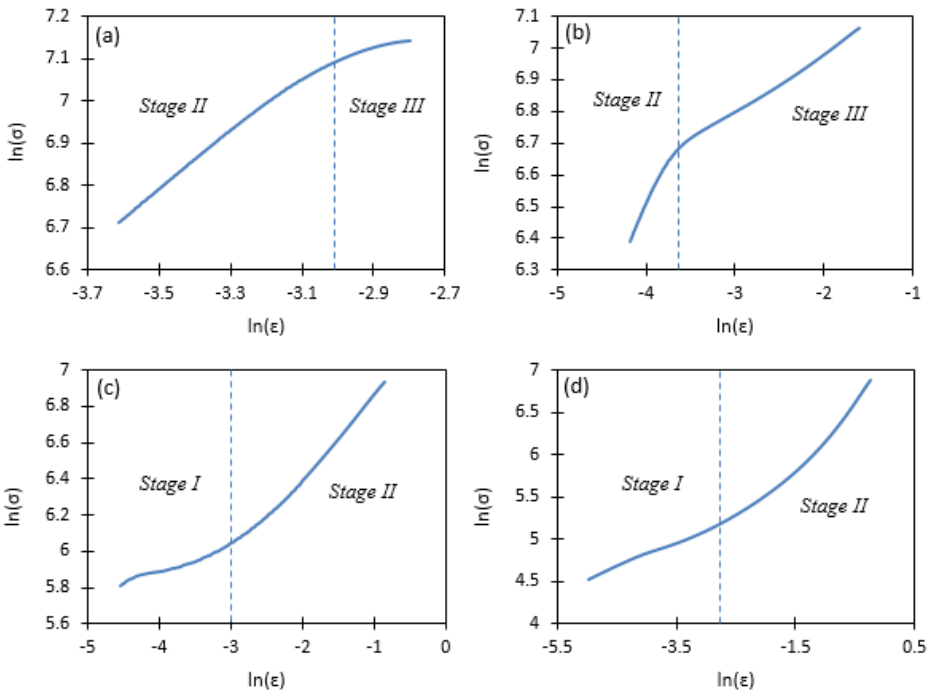

Fig. 3. ln(*σ*) vs. ln(*ε*) curves of the AISI 321 stainless steel after 80 % cold rolling and annealing for 15 min at temperatures of (a) 700 °C, (b) 800 °C, (c) 900 °C, and (d) the as received coarse grained sample in the annealed condition

As it is seen in Fig. 2(a), annealing at 700 °C for 15 min is not enough to transform the cold worked microstructure with high dislocation densities to the recrystallized and dislocation free austenite grains. Therefore, the dislocation tangles inside elongated grains may become an obstacle for generated dislocations during tensile testing which results in high levels of strain hardening at the initial stage of tensile deformation and the absence of the stage I work hardening. Also, some ultrafine austenite grains are evident in the primary elongated austenite grain boundaries which are the result of martensite to

austenite transformation. These ultrafine grains are also contributed in the high work hardening rate as previously reported by Del Valle et al. [22] for magnesium alloys processed by equal channel angular pressing. For sample annealed at 800 °C, Fig. 2(b), microstructure before tensile testing is composed of ultrafine, cold worked, and recrystallized austenite grains. In this case, the cold worked austenite and ultrafine equiaxed grains are responsible for the absence of the stage I work hardening. Whereas, for sample annealed at 900 °C for 15 min after cold rolling and initial coarse grained one, which has been annealed at 1200 °C, microstructures just before tensile testing are consisted of equiaxed dislocation free austenite grains due to the occurrence of static recrystallization and grain growth. In this case, the dislocation density inside grains is very low. For these two samples (coarse and equiaxed grain structure), the stage I of work hardening accompanies by the initiation of the stage II work hardening when the dislocation density inside each austenite grain increases and act as an obstacle for generated dislocations during continued deformation. Therefore, in the stage II, work hardening increases rapidly due to the interactions between dislocations on the activated secondary slip systems and those on the primary slip systems. A similar trend was observed during tensile deformation of the annealed AISI 321 and Hadfield steels in the work conducted by Zhang et al. [16]. For samples annealed at 700 and 800 °C, high density of dislocations which already existed inside elongated austenite grains, become an obstacle for generated dislocations so that the deformation process initiates from stage II hardening.

Table 3. Extracted data from the plots of ln(σ) vs. ln(ε) curves for the as received and annealed AISI 321 austenitic stainless steel

Annealing temperature, °C	Stage I	Stage II	Stage III	n_{I}	n_{II}	n_{III}	$\varepsilon_{I,II}$	$\varepsilon_{II,III}$
700	-	ln(σ)=0.6649ln(ε) +9.1199	ln(σ)=0.1559ln(ε) +7.5798	-	0.66	0.16	-	0.0485
800	-	ln(σ)=0.5715ln(ε) +8.7936	ln(σ)=0.1896ln(ε) +7.3613	-	0.57	0.19	-	0.0235
900	ln(σ)=0.1046ln(ε) +6.3101	ln(σ)=0.4663ln(ε) +7.3222	-	0.1	0.47	-	0.060	-
As-received	ln(σ)=0.271ln(ε)+ 5.9037	ln(σ)=0.8241ln(ε) +7.0103	-	0.27	0.82	-	0.135	-

The stage III work hardening initiates when the dislocation density inside grains reaches a critical value and the annihilation of dislocations by recovery become significant so that the work hardening rate decreases with further straining. For samples annealed at 700 and 800 °C, stage III work hardening is observed because the high density of dislocations exists prior to tensile deformation and further straining in the stage II increases dislocation density to a level that dislocation annihilation become predominant. But for sample annealed at the temperature of 900 °C and initial coarse grained one, dislocation density at the beginning of tensile deformation is very low and after the stage I (limited dislocation interactions at the onset of multiple slip) and stage II, remains in the lower levels so that the dislocation annihilation processes become insignificant compared with work hardening processes leading to the absence of the stage III work hardening. In Table 3, the results extracted from the ln(σ) vs. ln(ε)

curves are represented, which include the work hardening exponent at different stages of work hardening and corresponding transition strains.

Differential C-J analysis of work hardening behavior

Here, it is useful to emphasis that the change in the deformation mechanisms during tensile testing of materials results in the development of different stages in the true stress-true strain curves. In the case of the single crystals of FCC materials, as previously mentioned, variations of the true stress (σ) with true strain (ε) shows three distinct stages in the uniform plastic deformation region [23]. These stages are the stage I, stage II and stage III of work hardening which relate respectively to the easy glide of dislocations on primary slip systems, high work hardening rate due to the activation of secondary slip systems, and the dynamic recovery of dislocations. Nevertheless, the changes in the deformation stages have not always an obvious effect on the tensile curves of polycrystalline materials. In this case, some forms of analysis are required to reveal different deformation stages using the data acquired from the rue stress- true strain curves [24]. Hollomon analysis in the previous section is the simplest of these methods. This analysis was previously used for prediction of the deformation stages in ferrite-martensite dual phase steel [25], but results showed a continuous decrease in the work hardening exponent (n) with strain and district stages was not revealed. Similar results were also reported by Umemoto et al. [26] for ferritic, martensitic, and bainitic single structure steels. In the present investigation, although the variations of the strain hardening exponent (n) with strain is near continuous (as seen in Fig. 3), but deformation stages can be approximately deduced from these plots. For precise analysis of the tensile stress- strain curves, the Crussard-Jaoul (C-J) method has been applied to many kinds of alloys and reasonable results have been obtained [25,27,28]. The differential C-J analysis of the work hardening behavior of materials is based on the Ludwik equation as below [29]:

$$\sigma = \sigma_0 + k_L \varepsilon^{n_L}, \tag{3}$$

where σ is true stress, ε is true strain, n_L is work hardening exponent, k_L and σ_0 are material constants. After differentiation, the above equation can be written as follows:

$$ln\left(\frac{d\sigma}{d\varepsilon}\right) = ln(k_L n_L) + (n_L - 1)\ln\varepsilon. \tag{4}$$

Before analyzing the tensile true stress- true strain curves using the differential C-J method, it should be mentioned that the ln(dσ/dε) vs. ln(ε) curves for polycrystalline materials comprises four distinct stages as reported by Reed-Heel et al. [30] for polycrystalline nickel. The typical form of the ln(dσ/dε) vs ln(ε) curves for polycrystalline materials with different stages is shown in Fig. 4. During the initial accommodation stage, multiple slip starts at largest grains and spreads in to finer grains with further straining. The stage I begins when all grains deform simultaneously by multiple slip. Therefore, the slope of the ln(dσ/dε) vs. ln(ε) curves increases when the stage I initiates. It is worth to note that stage I in the description of the work hardening behavior of poly-crystals differs fundamentally from the stage I of single crystals where the crystal deforms by easy glide of dislocations on primary slip system. In the stage II dislocation slip occurs on a single slip system with hardening effect of the dislocations on the secondary systems [31]. During this stage, the in-grain subdivision is a predominant phenomenon. It is worth

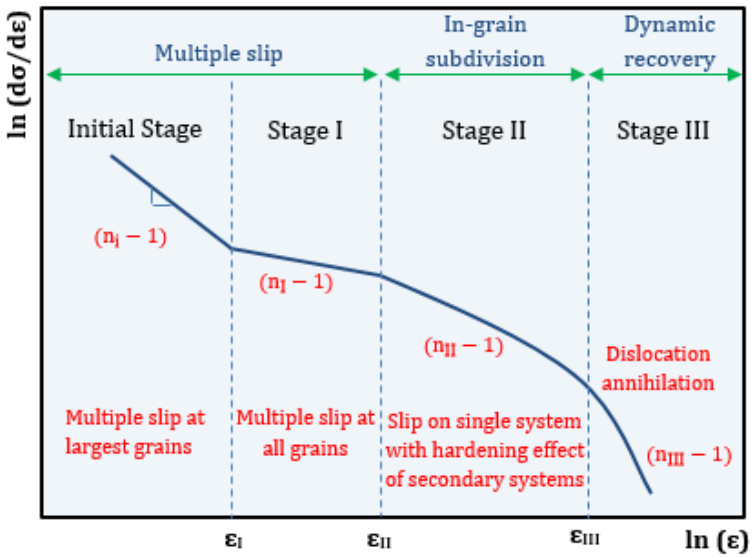

Fig. 4. Typical form of the ln(dσ/dε) vs. ln(ε) curves for polycrystalline materials. Based on [30]

to note that grain subdivision inside large austenite grains is primarily driven by multiple slip activity, which ensures deformation compatibility and promotes the gradual formation of dislocation substructures and misoriented sub-boundaries. This process is not confined to a particular stage of work hardening but occurs continuously from the very early stages of deformation until ultrafine-grained structures are eventually formed. The slope of the ln(dσ/dε) vs ln(ε) curve decreases when stage II initiates. Similar to work hardening behavior of single crystals, stage III is characterized by the occurrence of dynamic recovery due to the annihilation of dislocations. So, the slope of the ln(dσ/dε) vs. ln(ε) curve decreases when the stage III starts.

The differential C-J analysis of the true stress- true strain data for annealed samples was carried out using the Ludwik equation and the results are shown in Fig. 5. For the sample annealed at 700 °C for 15 min, as seen in Fig. 5(a), the three-stage hardening behavior is detected. Inspection of the microstructures of annealed samples in Fig. 2 reveals that after 15 min annealing at 700 °C (Fig. 2(a)), the microstructure is mainly composed of elongated austenite grains with cold deformed characteristics and some ultra-fine grains resulted from the reversion of deformation induced martensite. It is also obvious that the fraction of ultrafine-grained austenite is much less than the fraction of elongated grains where the occurrence of recovery is expected during annealing. As it is clear, the initial work hardening stage is not observed in the ln(dσ/dε) vs. $n\varepsilon$ curve of the sample annealed at 700 °C. This stage is observed when the initial microstructure of tensile sample is consisted of equiaxed grains with normal size distribution. The initial stage occurs with lower work hardening characteristics when the multiple slip starts only at larger grains. This stage accompanied with the stage I hardening when multiple slip occurs at all grains simultaneously. As the microstructure mainly consisted of cold deformed grains with high dislocation density which arranged in pileups, the initial stage is not observed and deformation starts with the occurrence of multiple slip at the elongated grains resulting to the stage I hardening.

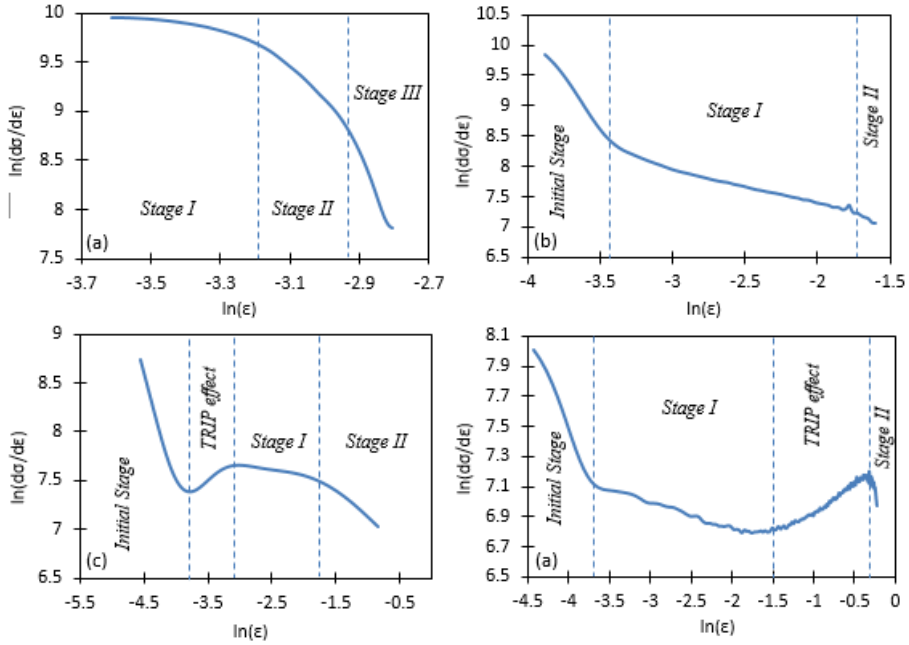

Fig. 5. Differential C-J analysis of the true stress-true strain curves of the AISI 321 austenitic stainless steel after annealing for 15 min at different temperatures: (a) 700 °C, (b) 800 °C, (c) 900 °C, and (d) initial coarse-grained steel

During the stage II, grain subdivision is predominant at elongated grains and also deformation of - ultra-fine austenite grains start with increasing the tensile stresses. As the work hardening capacity declines with grain refinement, the work hardening rate decreases in the stage II compared with the stage I. Finally, the stage III initiates when the dislocation annihilation occurs inside grains and work hardening rate decreases (Fig. 5(a)). For the sample annealed at 800 °C, as shown in Fig. 5(b), the ln(dσ/dε) vs. ln(ε) curve comprises three different stages. Comparing this curve with Fig. 3, it is deduced that the initial stage occurs with the characteristics of the multiple slip in large grains and accompanies with the stage I of work hardening due to the occurrence of multiple slip in all grains. This work hardening characteristics can be verified considering the initial microstructure of tensile sample (Fig. 2(b)). As said in the previous section, the microstructure after annealing at 800 °C is consisted of elongated austenite regions with the recrystallized features and also ultra-fine austenite grains due to the reversion of deformation induced martensite. Comparing this microstructure with Fig. 2(a), it is concluded that the size and volume fraction of ultra-fine austenite grains are increased with increasing the annealing temperature. Also, the static recovery inside elongated austenite grains is replaced by static recrystallization. In the presence of large austenite grains with low dislocation densities, due to static recrystallization, in conjunction with the ultra-fine grains, the plastic deformation starts with initial stage (high decrease rate of the work hardening) and accompanies with the stage I hardening, where the plastic deformation occurs simultaneously in ultra-fine and recrystallized austenite with different grain sizes.

Finally, the stage II hardening initiates at the final stage of the uniform plastic deformation region. This stage is characterized by the predominance of the subdivision of large austenite grains in the recrystallized regions (Fig. 2(b)) with the occurrence of single slip. So, the work hardening rate decreases in the stage II compared with

the stage I. As shown in Fig. 2(c,d), for samples annealed at 900 °C and initial coarse grained one, the trend similar to the behavior of the sample annealed at 800 °C is observed with this exception that the increase in the work hardening rate is noticed in some portion of the ln(dσ/dε) vs. ln(ε) curves. This increase in the rate of work hardening is attributed to the transformation of austenite phase to martensite during tensile testing which is known as TRIP effect.

Similar behavior has been reported by Cai et al. [32] for transformation induced plasticity (TRIP) steel with the chemical composition of Fe-0.18C-11Mn-3.8Al. They also explained that the superior tensile ductility is achieved in TRIP steels when the occurrence of austenite to martensite transformation is delayed. As can be seen in Fig. 5(c) the austenite to martensite transformation (TRIP) occurs in the early stage of uniform plastic deformation region for sample annealed at 900 °C. But for initial coarse-grained sample (Fig. 5(d)) this transformation is delayed and occurs in the later stage of the uniform plastic deformation region. This difference is attributed to the difference in the mean grain size of the austenite phase before the occurrence of TRIP phenomenon. As the austenite grain size of the sample annealed at 900 °C is lower than the initial annealed one, the dislocation density inside grains reaches to the critical value with higher rates than the coarse-grained sample. So, the TRIP effect is seen at the early stages of the uniform plastic deformation region. The total elongation of 127 % in initial coarse-grained sample is achieved due to the occurrence of TRIP at the later stages of the uniform plastic deformation region. The lower elongation of 67 % for sample annealed at 900 °C compared with as received sample is due to the lower austenite mean grain size and also the occurrence of TRIP at the early stages of plastic deformation. It is also worth to note that the stage III hardening is not observed during tensile deformation of initial coarse grained (Fig. 5(d)) and annealed samples at 800 and 900 °C (Fig. 5(b,c)).

As previously explained by Flinn et al. [33], the stage III hardening is expected when the high levels of plastic deformation could be imposed on sample before the necking during tensile testing. In the case of the sample annealed at 700 °C, the microstructure just before tensile testing is composed of elongated austenite grains with the characteristics of the cold work state (Fig. 2(a)). So, the initial dislocation density is high enough to trigger dislocation annihilation process during tensile deformation. Whereas, in samples annealed at 800 and 900 °C and initial coarse grained one, the microstructure mainly consisted of equiaxed and recrystallized austenite grains with low levels of dislocation densities. Therefore, the dislocation density during tensile testing does not reach to a value for the annihilation process to occur extensively.

Conclusions

In the present investigation, the AISI 321 austenitic stainless steel was cold rolled with 80 % reduction and then annealed at 700, 800, and 900 °C for 15 min to produce different initial microstructures for subsequent analysis. Then, the work hardening behaviors of annealed samples were analyzed using room temperature tensile testing. The main results are as follows:

1. In the Holomon analysis, all samples with different initial microstructures showed two-stage work hardening behavior. The absence of the stage I hardening in all samples and

the stage III hardening in sample annealed at 900 °C and as received specimen was confirmed by this analysis.
2. The stage III of hardening is not apparent in sample annealed at 900 °C and coarse grained one. The reason for this observation is that the density of dislocations in the sample at the final stages of the tensile testing does not reach to the critical value necessary for dynamic recovery to occur.
3. In the C-J analysis, the initial hardening stage, which is the indication of multiple slip at large grains, is not observed in the sample annealed at 700 °C for 15 min. At this annealing temperature, the microstructure is mainly consisted of elongated austenite grains with high density of dislocations which arrange in the form of dislocation cells and ultrafine grains resulted from martensite to austenite reversion. At other annealing conditions, the initial stage is observed due to the presence of large austenite grains in microstructures.
4. The stage III work hardening in the C-J analysis was observed only for the sample annealed at 700 °C. This is due to the high density of dislocations existed inside austenite grains before tensile testing.
5. The positive slop in the $\ln(d\sigma/d\varepsilon)$ vs. $\ln(\varepsilon)$ curves of the sample annealed at 900 °C and coarse grained one is attributed to the occurrence of austenite to martensite transformation (TRIP effect) which results in higher ductility and elongation to failure at these conditions.

CRediT authorship contribution statement

Mehdi Shaban Ghazani **:** writing – review & editing, writing – original draft, conceptualization, methodology; **Hesam Asghar Rezaei** **:** experimental design, sample preparation, investigation, analyses.

Conflict of interest

The authors declare that they have no conflict of interest.

References

1. Verma J, Taiwade RV. Effect of welding processes and conditions on the microstructure, Mechanical properties and corrosion resistance of duplex stainless steel weldments—A review. *J. Manuf. Process.* 2017;25: 134–152.
2. Kina AY, Souza VM, Tavares S, Pardal J, Souza J. Microstructure and intergranular corrosion resistance evaluation of AISI 304 steel for high temperature service. *Mater. Charact.* 2008;59(5): 651–655.
3. Singh R, Chattoraj I, Kumar A, Ravikumar B, Dey P. The effects of cold working on sensitization and intergranular corrosion behavior of AISI 304 stainless steel. *Metall. Mater. Trans. A.* 2003;34: 2441–2447.
4. Anita T, Pujar M, Shaikh H, Dayal R, Khatak H. Assessment of stress corrosion crack initiation and propagation in AISI type 316 stainless steel by electrochemical noise technique. *Corros. Sci.* 2006;48(9): 2689–2710.
5. Tiamiyu A, Eduok U, Szpunar J, Odeshi A. Corrosion behavior of metastable AISI 321 austenitic stainless steel: Investigating the effect of grain size and prior plastic deformation on its degradation pattern in saline media. *Sci. Rep.* 2019;9: 12116.
6. Lima A, Nascimento A, Abreu H, de Lima-Neto P. Sensitization evaluation of the austenitic stainless steel AISI 304L, 316L, 321 and 347. *J. Mater. Sci.* 2005;40: 139–144.
7. Pardo A, Merino M, Coy A, Viejo F, Carboneras M, Arrabal R. Influence of Ti, C and N concentration on the intergranular corrosion behaviour of AISI 316Ti and 321 stainless steels. *Acta. Mater.* 2007;55(7): 2239–2251.
8. Yanhui Z, Haitao M, Lai W, Changhai S, Chao G. Effect of solution treatment on microstructures and mechanical properties of AISI 321 service. *Acta Metall. Sin. (Engl. Lett.).* 2011;24(3): 243–248.

9. Yu C, Kao P, Chang C. Transition of tensile deformation behaviors in ultrafine-grained aluminum. *Acta. Mater.* 2005;53(15): 4019–4028.
10. Rybin VV, Ushanova EA, Zolotorevsky NY, Ermakova NY. Study of copper work-hardening behavior on a single sample experienced inhomogeneous dynamic deformation. *Materials Physics and Mechanics.* 2015;24(3): 253–258.
11. Y. Wang, E. Ma, Strain hardening, strain rate sensitivity, and ductility of nanostructured metals. *Mat. Sci. Eng. A.* 2004;375–377: 46–52.
12. Dini G, Najafizadeh A, Ueji R, Monir-Vaghefi S. Tensile deformation behavior of high manganese austenitic steel: The role of grain size. *Mater. Design.* 2010;31(7): 3395–3402.
13. Ma E. Instabilities and ductility of nanocrystalline and ultrafine-grained metals. *Scr. Mater.* 2003;49(7): 663–668.
14. Wang Y, Ma E. Three strategies to achieve uniform tensile deformation in a nanostructured metal. *Acta. Mater.* 2004;52(6): 1699–1709.
15. Zhang W, Wu J, Wen Y, Ye J, Li N. Characterization of different work hardening behavior in AISI 321 stainless steel and Hadfield steel. *J. Mate. Sci.* 2010;45: 3433–3437.
16. Rezaei H, Ghazani MS, Eghbali B. Effect of post deformation annealing on the microstructure and mechanical properties of cold rolled AISI 321 austenitic stainless steel. *Mat. Sci. Eng. A.* 2018;736: 364–374.
17. Meyers MA, Mishra A, Benson DJ. Mechanical properties of nanocrystalline materials. *Prog. Mater. Sci.* 2006;51(4): 427–556.
18. Zheng M, Li ZM. Strain-Hardening effect on critical strain assessment of pipe plastic bending at buchling. *Materials Physics and Mechanics.* 2020;44(1): 48–60.
19. Shin JH, Jeong J, Lee JW. Microstructural evolution and the variation of tensile behavior after aging heat treatment of precipitation hardened martensitic steel. *Mater. Charact.* 2015;99: 230–237.
20. Kosaka N, Funakawa Y. Work hardening in ferritic steel containing ultra-fine carbides, *ISIJ Int.* 2016;56(2): 311–318.
21. Šesták B, Seeger A. The Relationship between the Work-Hardening of BCC and FCC Metals. *Phys. Status. Solidi. B.* 1971;43(1): 433–444.
22. Del Valle J, Carreño F, Ruano OA. Influence of texture and grain size on work hardening and ductility in magnesium-based alloys processed by ECAP and rolling. *Acta. Mater.* 2006;54(6): 4247–4259.
23. Rollett AD, Kocks U. A review of the stages of work hardening. *Solid State Phenom.* 1993;35–36: 1–18.
24. Gronostajski Z. The constitutive equations for FEM analysis. *J. Mater. Process. Technol.* 2000;106(1–3): 40–44.
25. Das D, Chattopadhyay PP. Influence of martensite morphology on the work-hardening behavior of high strength ferrite–martensite dual-phase steel. *J. Mater. Sci.* 2009;44: 2957–2965.
26. Umemoto M, Tsuchiya K, Liu Z, Sugimoto S. Tensile stress-strain analysis of single-structure steels. *Metall. Mater. Trans. A.* 2000;31(7): 1785–1794.
27. Colla V, De Sanctis M, Dimatteo A, Lovicu G, Solina A, Valentini R. Strain hardening behavior of dual-phase steels. *Metall. Mater. Trans. A.* 2009;40: 2557.
28. Kumar SS, Raghu T. Tensile behaviour and strain hardening characteristics of constrained groove pressed nickel sheets. *Mater. Design.* 2011;32(8–9): 4650–4657.
29. Afrin N, Chen D, Cao X, Jahazi M. Strain hardening behavior of a friction stir welded magnesium alloy. *Scr. Mater.* 2007;57(11): 1004–1007.
30. Reed-Hill R, Cribb W, Monteiro S. Concerning the analysis of tensile stress-strain data using log dσ/dεp versus log σ diagrams, *Metall. Mater. Trans. B.* 1973;4: 2665–2667.
31. Raabe D, Zhao Z, Mao W. On the dependence of in-grain subdivision and deformation texture of aluminum on grain interaction. *Acta. Mater.* 2002;50(17): 4379–4394.
32. Cai Z, Ding H, Xue X, Jiang J, Xin Q, Misra R. Significance of control of austenite stability and three-stage work-hardening behavior of an ultrahigh strength–high ductility combination transformation-induced plasticity steel. *Scr. Mater.* 2013;68(11): 865–868.
33. Flinn J, Field D, Korth GE, Lillo TM, Macheret J. The flow stress behavior of OFHC polycrystalline copper. *Acta. Mater.* 2001;49(11): 2065–2074.

MATERIALS PHYSICS AND MECHANICS RESEARCH ARTICLE

Submitted: October 10, 2025 **Revised: November 1, 2025** **Accepted: November 17, 2025**

Modeling of vibro-magnetic-abrasive finishing tools and analysis of their influence on the surface quality of cutting ceramics

V.I. Burlakov [1], G.Yu. Burlakova [1], V.G. Artiukh [2], D.A. Kitaeva [2] ✉, N.V. Korihin [2]

[1] Pryazovskyi State Technical University, Mariupol, Russia

[2] Peter the Great St. Petersburg Polytechnic University, St. Petersburg, Russia

✉ dkitaeva@mail.ru

ABSTRACT

A model of a tool for machining cutting ceramics is proposed with an aim to provide a detailed analysis of its durability. The development of effective abrasive materials capable of operating under extreme conditions is discussed. The use of tools made from diamond-containing composite materials is necessitated by the exceptional hardness of diamonds. While many researchers have investigated finishing processes, the combination of vibrational and electromagnetic components to achieve a high-quality and productive lapping process for superhard ceramics has not been previously accomplished. The process of synthetic diamond manufacturing is described.

KEYWORDS

superhard materials • workpiece processing • diamond-containing composite materials • tool life high-performance workpiece processing • wear process

Funding. *This work has been supported by the grant of the Russian Science Foundation, RSF 25-19-00921.*

Citation: Burlakov VI, Burlakova GYu, Artiukh VG, Kitaeva DA, Korihin NV. Modeling of vibro-magnetic-abrasive finishing tools and analysis of their influence on the surface quality of cutting ceramics. *Materials Physics and Mechanics*. 2025;53(5): 122–131.
http://dx.doi.org/10.18149/MPM.5352025_10

Introduction

A critical scientific and technical challenge is the selection of an abrasive tool for the vibro-magnetic-abrasive finishing (VMAF) of cutting ceramics that ensures high quality of the machined surface and extends the service life of ceramic tools [1–3].

The process involves subjecting the processing medium and workpieces in the vibration machine's chamber to a constant magnetic field perpendicular to the plane of the medium's circulatory movement. Vibration drives the medium, aligning the ferromagnetic abrasive, Al_2O_3 granules, and synthetic diamonds (adhered to the granules) along the magnetic field lines. The dense abrasive packing prevents workpiece collision. Vnukov Y.N. [4] studied ceramic cutting plate processing and advanced tools. Kozyrev N.V. et al. [5] investigated synthetic diamond production. Liao Y.S. and Lin H.V. [6] explored advanced tool creation. Rogov V.A. and Shkarupa M.I. [7] compared mechanical processing of superhard materials by grinding. Lebedev V.A. and Dyachenko EA. [8] modeled vibro-abrasive finishing performance. Novikov N.V. and Klimenko S.A. [9] designed superhard material tools. Suslov A.G. [10] also contributed to tool research. Malinin P.V. et al. [11] studied centerless grinding preparation. Skryabin V.A. et al. [12] researched fine-media finishing. Skryabin V.A. and Svechnikova G.I. [13] experimentally studied finishing productivity for various profiles. Zubarev Y.M. and Yuryev V.G. [14]

designed abrasive tools and grinding operations. Volkovsky A.A. and Makarov V.F. [15] assessed surface quality in flat grinding. Rodionov I.V. and Kambulov S.V. [16] investigated burr removal on small parts via vibro-abrasive machining. Losev A.V. et al. [17] emphasized the need for finishing technologies in engineering. Zverovshchikov V.Z. and Zverovshchikov A.E. [18] worked with free abrasives. Tamarkin M.A. et al. [19] used free abrasives. Qi J. et al. [20] simulated grinding. Kazakov D.V. et al. [21] worked in abrasive grain environments. Tishchenko E.E. et al. [22] engaged in finishing. Rowe V.B. [23] studied modern material cutting processes. Wang G. et al. [24] formed profiles in abrasive media.

Residual tensile stresses play a key role in ceramic fracture, while compressive stresses are most detrimental. Thus, tensile stresses can be beneficial in machining, whereas compressive stresses must be eliminated. This study aims to maximize tool life by minimizing residual stresses and utilizing their presence during processing.

Material and Methods

In the cutting mode, friction occurs in several ways: chips rub against the tool's rake face, the flank face rubs against the workpiece, leading to wear, tool blunting, and the need for re-sharpening. This applies to edged tools. Abrasive machining can be viewed as material removal by individual grains; more grains result in higher quality and productivity. The concept of tool life also applies to abrasive tools, defined as the total operating time between the start of material removal and its practical cessation. Tool life for turning inserts is 30–90 min, depending on the tool and workpiece materials, cutting conditions, geometry, and machining environment. Abrasive tool life depends on the workpiece material, machining parameters, and abrasive type. This study focuses on the durability of corundum and synthetic diamond mixtures.

Cutting tool wear differs from general machine part wear due to the high chemical purity of the contact surfaces and the extreme pressure and temperature in the cutting zone [4]. Avoiding critical wear is essential to prevent tool failure, reduce repair effort, and extend service life. Excessive flank wear also increases surface roughness.

Tool wear in metal cutting involves abrasive, diffusion, and adhesive mechanisms. The dominant mechanism depends on the tool and workpiece properties and cutting conditions, including speed [5]. Specialized metalworking tools offer advantages through their edge geometry and processing technology, enabling efficient, high-quality machining. Using diamond abrasive tools mitigates but does not eliminate wear, merely delaying it. Abrasive tools wear during machining, with the rate and nature of wear depending on the workpiece and tool materials, and operating conditions. Abrasive tool performance is determined by its hardness — the ability to retain grains. Grains wear through abrasion and fracture, which are natural under grinding conditions [6].

When machining superhard ceramics with diamond tools, the lack of self-sharpening increases cutting forces, negatively affecting the surface layer. Controlling this impact through variable oscillations reduces cutting forces and preserves tool geometry. This approach is also applicable to the less-understood free abrasive method. Total abrasive wear comprises grinding wear and layer removal. Wear is quantified by the mass, volume, or area of removed particles, termed mass, volumetric, or surface wear, respectively [7].

Practical experience shows that the choice of tools and parameters affects not only

accuracy, roughness, and productivity but also tool consumption, wear resistance, and processing cost [8]. New abrasive materials can reduce tool consumption and enable unique processing. High-quality machines require high-quality tools. Their rational use unlocks modern equipment's potential, justifying the investment in advanced tooling [9]. Wear-resistant tools boost productivity by reducing setup time. Multifunctional tools minimize the tool range and machine time per operation [10]. The life of superhard material tools depends on the same factors as carbide-tipped tools, with proper sharpening and edge preparation being critical.

Results and Discussion

When processing cutting plates using vibration processing with free diamond abrasive average durability (Fig. 1) increased several times compared to the abrasive material made from mixture of monocorundum and 15 % additive of the artificial diamonds of ASM 20/14 brand (synthetic diamond micropowder) and processing with the abrasive material made from the monocorundum alone, that can be seen on Fig. 1.

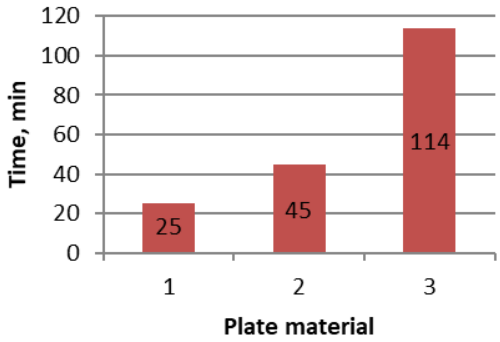

Fig. 1. Dependence of cutting plate durability on type of material:
1 – monocorundum; 2 – monocorundum + 15% ASM 20/14; 3 – monocorundum + 15 % UDD

As can be seen from Fig. 1, tool life turned out to be most acceptable when processed with a mixture of monocorundum with 15 % addition of UDD (ultradisperse diamond) brand artificial diamond materials. This is relatively new nanomaterial that is ultra-dispersed detonation synthesis diamond. The diamond was obtained using a developed technology which involved subjecting an ampoule containing a carbon material (usually graphite) to shock compression at pressures exceeding 10^5 atm during the detonation of an explosive charge, which was accompanied by heating to several thousand degrees. Under these conditions, carbon recrystallized into diamond, i.e., the essence of the method was to use the energy of an explosion to create conditions under which phase transition of graphite into diamond occurred. A 20-fold excess of copper or nickel powder was added to the ampoule to quickly remove heat to prevent the diamond from turning back into graphite when pressure dropped. The resulting product contained micron-sized diamond particles and was used for technical purposes, for example, as effective abrasive for rough grinding of parts [8].

As stated above, the tool's durability was determined by time of its continuous operation until complete failure i.e., breakdown. A series of experiments were conducted which made it possible to determine that over time the amount of material removed from

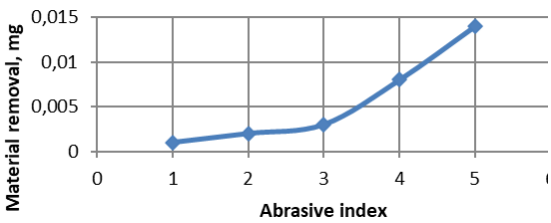

Fig. 2. Material removal from applied abrasive material (mixture): 1 – monocorundum; 2 – monocorundum + white corundum; 3 – monocorundum + 15 % ASM 20/14; 4 – monocorundum + 15 % AC6; 5 – monocorundum + 15 % UDD

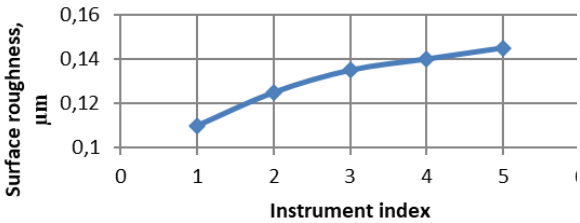

Fig. 3. Dependence of surface quality on used abrasive material (mixture): 1 – monocorundum; 2 – monocorundum + white corundum; 3 – monocorundum + 15 % ASM 20/14; 4 – monocorundum + 15 % AC6; 5 – monocorundum + 15 % UDD

the surface of the plate began to noticeably decrease. Analysis of the graph presented in Fig. 2 shows that not only durability of the tool itself must be taken into account but also removal of material being processed when using different abrasives.

Tool management also addresses the problems of using old tools that prematurely fail or fail to perform the required operations. Furthermore, automated production systems place higher demands on metal-cutting tools [9]. For example, an expensive tool may be damaged if, during operation of an end mill, one of non-resharpenable carbide inserts fails prematurely. In this regard, the task of increasing the tool life is a critical objective.

Since the main factor influencing tool wear is cutting temperature, the thermophysical characteristics of the tool material, which significantly affect the cutting influencing temperature, also influence tool wear. Thus, a 15 % addition of diamond abrasive material to monocorundum significantly increases the service life of cutting tools, which is essential for the domestic industry. Along with increase in tool life, quality of machined surface also improved [10]. The graph presented in Fig. 3 clearly confirms the above statement.

From the graph presented in Fig. 3 it is clear that productivity increases proportionally with the cutting ability of abrasive tool. Contact parameters are linear pressing force of abrasive tool [8]. The use of diamond-based technology significantly enhances capabilities of manufacturing industry. Using diamond tools ensures high-quality processing of any surface, providing high productivity and guaranteed reliability.

During the chip removal process at the diamond machining of ceramics individual diamond grains are combined with ferromagnetic component. Study of nature of ceramic surface damage by diamond grains revealed that a grain leaves a clear mark at both the beginning and the end of a scratch without obvious chips along edges. Being sufficiently hard, the diamond grain begins to cut off chips immediately upon contact with material. Middle part of scratch, however, has significant breakouts along its entire length at edges. Appearance of chips when a certain depth of grain penetration is reached is explained by the fact that with an increase in cutting depth, more cutting edges the of diamond grain become engaged, as a result of which micro-cutting forces in zone of its contact with sample material increase and, along with formation of highly dispersed chips, large areas of breakouts are observed. Forces that arise during finishing determine stability of abrasive tool, quality of processing and allow selection of rational technical parameters [11].

Condition of the surface layer is significantly influenced by the cutting forces when machining ceramics. Understanding the patterns of these forces allows for informed selection of the optimal machining conditions. Nature of cutting force changes can also be used to assess physical phenomena occurring in machining zone.

Abrasive wear is caused by the workpiece acting on tool's contact surfaces, where hard particles in the material scratch the tool, acting as micro-cutters. Due to high hardness of CBN (cubic boron nitride) particles, abrasive wear of tool depends on amount of hard abrasive. This abrasive wear of tool can also be associated with phenomenon of "self-wear" [12]. Source of particles that cause "self-wear" is rounded section of cutting edge of tool. Particles are removed from this area due to fatigue and adhesive interaction with workpiece material. They form a wavy pattern when they reach contact surfaces of tool. This mechanism determines wear.

Although diamond abrasive wears out due to the specific nature of process, it does not stop because the magnetic field presses the sample against the tool. Sufficiently high pressure in cutting zone causes resulting powder to act as a lapping paste. It results in the processing of a harder material with a softer material, a process achieved using vibro-magnetic-abrasive method.

Knowing the wear rate of the abrasive material allows for determining how long it will take for the machining process to transition to lapping mode even with soft material. This approach to wear ensures consistent performance on ceramics with virtually any type of abrasive material. So, the hypothesis that it is impossible to process a hard material with a softer material is not always confirmed. It is also important to note that abrasive wear which is the wear of a material under action of an abrasive should not be confused with the wear of an abrasive material. The former occurs as a result of the action of a hard abrasive on the part and the latter occurs when a soft abrasive is applied to a harder surface [13].

In a free state powder crystallizes into spherical microparticles which correspond to the thermodynamically most favorable form with minimum surface area and maximum volume. The process resembles lapping when using VMAF as the primary operation for machining superhard ceramics. Lapping is the machining of the surface layers of a part with a tool. During the lapping process the tool is pressed against the surface of the part with a force of 100–200 N that leads to a decrease in roughness and an increase in wear resistance.

Initial magnetic-abrasive mixture is held by magnetic forces (when magnetic field of installation is turned on) caused by the magnitude of the magnetic field in working space. Samples of cutting plates made of polycrystalline boron nitride (PCBN) are oriented in the space of the working zone according to the principle of least resistance to movement when vibrations are applied and when performing translational movements they pass through a compacted magnetic-abrasive layer performing surface treatment. Unbound powder grains move inside the working chamber [25–27]. The magnetic field forms a cutting tool with controlled rigidity from a ferromagnetic abrasive powder mass in accordance with its functional purpose. Each surface of PCBN samples being machined is in contact with the magnetic-abrasive layer [14].

It is impossible to use only traditional abrasive materials as cutting tools in vibro-magnetic-abrasive machining because they must have not only abrasive but also high magnetic properties. The key property of magnetic abrasive powders is the strength of

the bond between ferromagnetic and abrasive components. This bond significantly influences the stability of powder grains under thermal and mechanical loads. The microhardness, particle shape, manufacturing processability and cost of magnetic abrasive powder are also important. Thus, powders of ferroalloys, iron, cermets and other substances are used as cutting elements in VMAF which are selected depending on the material of the workpieces, the condition of their surface and the initial roughness.

A portion of magnetic abrasive powder is held by magnetic forces caused by the magnitude of the magnetic field in working space when magnetic field is turned on. Samples are pressed against the abrasive material and superhard ceramic is machined because the workpiece moves up or down. This removes excess material and creates a surface with a new microrelief. The frictional forces between the grains help the magnetic field to hold the powder within the working gap [15].

Each processed surface of the sample is in contact with a grain. The surface is subject to cutting force (if the grain has embedded itself in the surface and is performing microcutting or grinding the against sample surface) and friction force. These forces tend to capture the contacting grain along with moving workpiece and return it relative to its own center of inertia. The movement of grains along workpiece surface and their rotation are impeded by the surrounding grains, which under the influence of the magnetic field, compact and form columns of ferromagnetic powder.

If during gradual deepening of cutting grain into the surface being machined cutting force exceeds resistance of grain to rotation from the environment surrounding it or if obstacle in the form of increased microroughness or hard foreign inclusion appears on the path of the rubbing grain (cutting) then such grain returns and new sections and new cutting edges come into contact with the workpiece grain. By these turns intermittent nature of lines called traces of abrasive cutting on the surface of the workpiece can be explained.

A distinctive feature of abrasive cutting in VMAF is observed sharp changes in productivity of process when the processing conditions change. The unique cutting tool formed by the magnetic field from magnetic abrasive powder is characterized by increased elasticity. The depth of penetration of each grain into the surface being processed (and, therefore, volume of material cut by it), in the result of stable equilibrium in each individual case between the forces pressing the grain to the surface being processed and the forces of resistance of the workpiece material to the introduction of

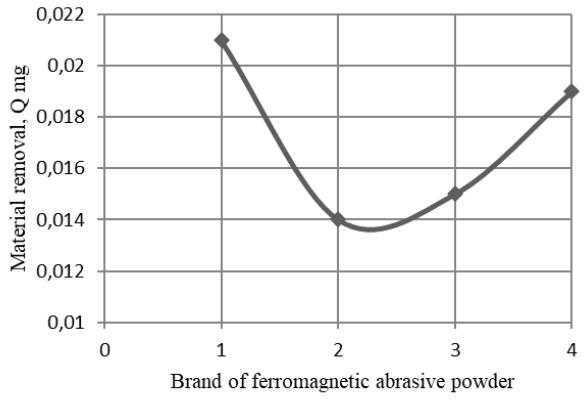

Fig. 4. Dependence of processing performance on dispersion of powder FEROMAP: 1 – FEROMAP 630/400 μm; 2 – FEROMAP 400/315 μm; 3 – FEROMAP 315/200 μm; 4 – FEROMAP 200/100 μm

the grain [16]. In order to determine grain size several observations were made during processing. The purpose of this was to determine the degree of dependence of processing productivity on the grain size of the abrasive (Fig. 4).

Previous studies have shown that when processing with powders such as FEROMAP 630/400 μm, FEROMAP 400/315 μm, FEROMAP 315/200 μm and FEROMAP 200/100 μm better surface quality was obtained than when using powders such as DCK 630/400 μm, DCK 630/400 μm and round-shaped powders such as POLYMAM-M 400/315 μm and PR R6M5 300/250 μm. Moreover, all of these powders have poor cutting properties. Therefore, FEROMAP powders of varying fineness were used for the studies [17].

Experiments have shown that FEROMAP 630/400 μm proved to be the best but use of the vibration force almost eliminated differences. This happened because without the use of vibration, the grain size played the primary role but it was vibration component that became decisive in choosing more productive and less expensive material. This is why FEROMAP 200/100 μm was chosen as the primary cutting material. During VMAF electric currents can be induced in them when the poles of the magnetic inductor act on electrically conductive powders and when samples are moved within working space relative to abrasive columns. The reasons for the appearance of induction currents can also be periodic changes in the magnetic flux density in the working space if inductor creates magnetic field [18].

Induction currents of workpiece influence the magnitude and the distribution of the magnetic field in working gap because they are always directed in such a way that their own magnetic field prevents a change in the external magnetic field that generates them. According to functional purpose of magnetic field, in each specific case, all known magnetic-abrasive machining schemes can be divided into five groups one of which has the following meaning where magnetic field forms cutting tool with controlled rigidity from a powder ferromagnetic abrasive mass and creates cutting forces. Other schemes are not functionally suitable for VMAF.

The process of vibro-magnetic-abrasive machining is a process in which material removal begins simultaneously with the activation of vibration and the creation of a magnetic field in the processing area. Determining the forces acting during VMAF is important for understanding the material removal mechanism because forces directly influence formation of the finished surface [19].

Surface quality was determined using a non-contact interference 3D profilograph the "Micron-alpha" [28]. The quality of the cutting edge surface is formed during finishing operations but pre-processing and preparation process also affect surface quality due to the technological inheritance of the original properties of the workpiece at all stages of its processing [29,30]. Surface roughness is determined by the adopted machining method which characterizes the size, shape and direction of the machining strokes. Cutting conditions influence formation of surface roughness [20,22].

Looking at examples of surfaces of superhard ceramic samples, it can be concluded that after processing with DCK 630/400 μm surface has randomly located features and large scratches. The number of scratches decreased sharply and they became less chaotic after processing the same sample with the POLYMAM-M 400/315 μm. This indicates that

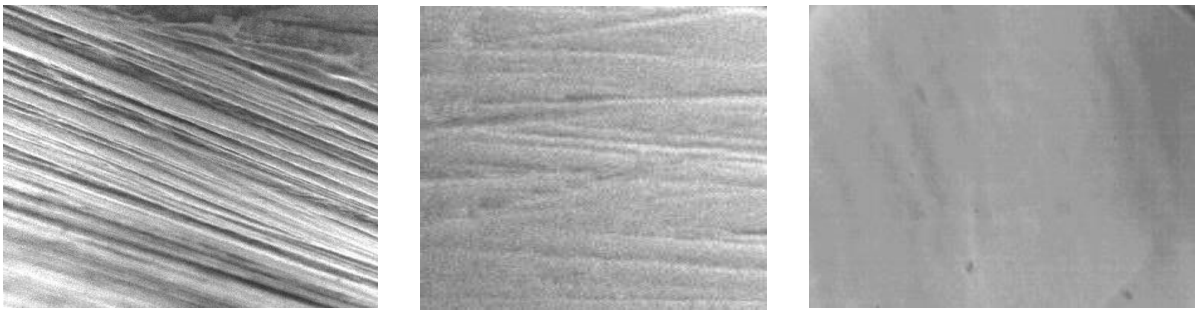

(a) (b) (c)

Fig. 5. Surfaces of superhard ceramic samples treated with VMAF using various ferromagnetic abrasive materials (×500): (a) by DCK 630/400 μm; (b) POLYMAM-M 400/315 μm; (c) by FEROMAP 200/100 μm

some processing of superhard ceramics took place but it was not possible to achieve the required surface roughness [21]. Figure 5 shows fragments of surfaces that have been treated with the VMAF.

Thus, when processing with DCK 630/400 μm (Fig. 6(a)) surface microrelief changed for the better; when processing with POLYMAM-M 400/315 μm (Fig. 6(b)) microrelief became better; when processing with FEROMAP 200/100 μm (Fig. 6(c)) surface acquired quasi-homogeneous characteristics which is an indicator of high-quality processing. These indicators show that quality of processing of FEROMAP 200/100 μm has significantly increased compared to the other ferromagnetic materials [23,24].

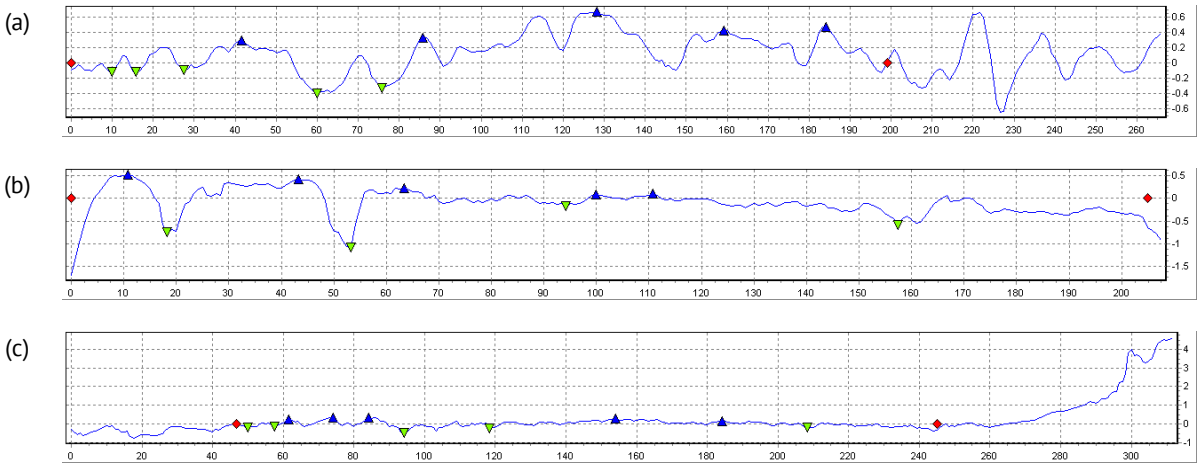

Fig. 6. Profilograms of the cutting ceramic surface after treatment by:
(a) DCK 630/400 μm; (b) POLYMAM-M 400/315 μm; (c) FEROMAP 200/100 μm

Conclusions

Only abrasive particles with spheroidal grain shape can be recommended for use as a magnetic abrasive tool. In addition, it can be used to provide increased polishing and strengthening capacity due to grinding of the treated surface that will be realized to lesser extent when using abrasive powders with different particle shape, performing primarily micro-cutting and dispersion of material from the surface of the workpiece.

FEROMAP 200/100 μm is the most suitable for processing superhard ceramics because after its action, the plate surface looks quasi-homogeneous and has the least roughness. The durability of cutting ceramic tools increases by almost 2–2.5 times.

CRediT authorship contribution statement

Viktor I. Bulakov: conceptualization; **Galina Yu. Burlakova:** conceptualization; **Viktor G. Artiukh**: investigation; **Daria A. Kitaeva**: data curation; **Nikolay V. Korihin**: data curation.

Conflict of interest

The authors declare that they have no conflict of interest.

References

1. Samantaraya D, Lakade S. Optimization of Machining Parameters in Hard Turning of Automotive Gears with PCBN tool using Taguchi Method. *International Review of Mechanical Engineering.* 2021;15(5): 278–286.
2. Zelinko A, Welzel F, Biermann D, Maiboroda V. Tool type and macrostructure for magnetic abrasive finishing of flat surfaces on CNC machine tools. *Production Engineering.* 2022;16: 523–533.
3. Al-Samarai RA, Al-Douri Y. *Metal Surface Engineering: Developed Tribology.* CRC Press; 2025.
4. Vnukov YN. *Progressive machining tool and methods for improving its quality.* Moscow: Mashinostroenie; 2008. (In Russian)
5. Kozyrev NV, Sysolyatin SV, Sakovich GV. Synthesis of ultrafine diamonds from alloys of TNT with polycyclic nitramines. *Combustion, Explosion and Shock Waves.* 2006;42: 486–489.
6. Liao YS, Lin HV. Mechanism of minimum quantity lubrication in high-speed milling of hardened steel. *International Journal of Machine Tools and Manufacture.* 2007;47(11): 1660–1666.
7. Rogov VA, Shkarupa MI. Comparative analysis of mechanical processing of super hard materials by grinding. *Technology of mechanical engineering.* 2009:5: 12–16. (In Russian)
8. Lebedev VA, Dyachenko EA. Model of productivity of vibroabrasive finishing and cleaning processing. In: Babichev AP. (Ed.). *Issues of vibration technology.* Rostov-on-Don, Russia: Don State Technical University; 2004. p.17–20. (In Russian)
9. Novikov NV, Klimenko SA. (Ed.) *Tools made of superhard materials.* Moscow: Mashinostroenie; 2014. (In Russian)
10. Suslov AG. (Ed.) *Technologist's Handbook.* Moscow: Innovative Mechanical Engineering; 2019. (In Russian)
11. Malinin PV, Bochkarev PY, Ulyanova LD, Shalunov VV. Improving the technological preparation of centerless grinding operations. *University proceedings. Volga region. Engineering sciences.* 2022;(4): 147–160. (In Russian)
12. Skryabin VA, Skhirtladze AG, Rybakov YV. New method of finishing treatment of parts with free fine-dispersed media. *Technology of Metals.* 2003;(2): 16–17. (In Russian)
13. Skryabin VA, Svechnikova GI. Experimental studies of performance of finishing abrasive processing of parts with different profiles. *Mashinostroitel.* 2011;(4): 18–22. (In Russian)
14. Zubarev YM, Yuryev VG. *Abrasive tools. Development of grinding operations.* Moscow: Mechanical Engineering; 2018. (In Russian)
15. Volkovsky AA, Makarov VF. Assessment of the quality of the treated surface during flat grinding of CFRP. *Bulletin of PNRPU. Mechanical engineering, materials science.* 2023;25(1): 73–82. (In Russian)
16. Rodionov IV, Kambulov SV. Study of possibility of removing burrs on parts with small dimensions using vibroabrasive machining. *Young researcher of Don.* 2018;4(13): 56–62. (In Russian)
17. Losev AV, Loseva OA, Dmitrevskaya YS. Need to use finishing and cleaning technologies in mechanical engineering. *Young Researcher of Don.* 2009;1: 34–46. (In Russian)
18. Zverovshchikov VZ, Zverovshchikov AE. Dynamic characteristics of compacted mass of working load during volumetric centrifugal processing of parts. *University proceedings. Volga region. Technical sciences.* 2007;1: 140–150. (In Russian)

19. Soloviev AN, Tamarkin MA, Tho NV. Finite element modeling method of centrifugal rotary processing. *Vestnik of Don State Technical University*. 2019;19(3): 214–220. (In Russian)
20. Qi J, Zhang D, Li S, Chen B. A micro-model of the material removal depth for the polishing process. *The International Journal of Advanced Manufacturing Technology*. 2016;86: 2759–2770.
21. Tamarkin MA, Tishchenko EE, Kazakov DV, Isaev AG. Ensuring reliability of technological processes of finishing and hardening centrifugal-rotational processing with steel balls. *Vestnik Mashinostroeniya*. 2017;(1): 80–83. (In Russian)
22. Tamarkin MA, Tishchenko EE, Melnikov AS. Technological foundations for optimizing finishing and hardening processes of parts in granular working environments. In: *Innovations in mechanical engineering. Proceedings of the X International Scientific and Practical Conference, 26-29 November 2019, Kemerovo*. Gomel: KSTU named after T.F. Gorbachev; 2019. p. 555–562. (In Russian)
23. Rowe WB. *Principles of Modern Grinding Technology*. 2nd ed. William Andrew; 2013.
24. Wang G, Zhou X, Yang X, Zhou H, Chen G. Material removal profile for large mould polishing with coated abrasives. *The International Journal of Advanced Manufacturing Technology*. 2015;80: 625–635.
25. Mo P, Chen J, Chen C, Hu Q, Pan X, Xiao L, Lin F. Study on the composition, microstructure and mechanical properties of PCBN composites synthesized by TiN–AlN–Ti combined with cBN. *Journal of Materials Science*. 2022;57: 17481–17490.
26. Zou Q, Dong P, Li Y, Li Sh, Dai L, Wu D, Luo Y. Effect of Sintering Temperature on Microstructure and Properties of PcBN Composites. *Journal of Materials Engineering and Performance*. 2025;34: 4494–4501.
27. Mo P, Chen J, Wang P, Pan X, Zhang J, Li K, Chen C. Effect of synthesis pressure on the properties of PcBN composites. *Diamond and Related Materials*. 2024;150: 111697.
28. Burlakov VI, Artiukh VG, Kitaeva DA, Korihin NV. Machinability of nitride ceramics with abrasive powders and their addition to diamond powder. *Materials Physics and Mechanics*. 2025;53(4): 99–110.
29. Krasnitckii SA, Sheinerman AG, Gutkin MYu. Brittle vs ductile fracture behavior in ceramic materials at elevated temperature. *Materials Physics and Mechanics*. 2024;52(2): 82–89.
30. Bolotov AN, Novikova OO, Novikov VV. Effect of loading on tribotechnical characteristics of antifriction diamond-bearing mineral ceramics. *Materials Physics and Mechanics*. 2025;53(2): 104–112.

MATERIALS PHYSICS AND MECHANICS RESEARCH ARTICLE

Submitted: August 16, 2025 **Revised: September 15, 2025** **Accepted: October 23, 2025**

Influence of dispersed inorganic fillers on the properties of vulcanized rubber based on ethylene propylene diene monomer rubber SKEPT-40

E.N. Egorov ✉, **N.I. Kol'tsov**

I.N. Ulyanov Chuvash State University, Cheboksary, Russia

✉ enegorov@mail.ru

ABSTRACT

The influence of various powder inorganic fillers (carbon black P 803, P 324 and N 220, silica ZC-120) on the rheometric properties of the rubber compound, physico-mechanical and performance properties of vulcanized rubber based on ethylene propylene diene monomer rubber SKEPT-40, used for rubberizing metal surfaces, was studied. The rubber compound under study based on the above rubber included a vulcanizing agent (sulfur), vulcanization accelerators (2-mercaptobenzthiazole and tetramethylthiuram disulfide), vulcanization activators (zinc white and stearic acid) softener (industrial oil I-8A). It was found that vulcanized rubber with a content of 60.0 parts per hundred parts of rubber (phr) of carbon black N 220 has high physico-mechanical properties, the smallest changes in tensile strength, elongation at break and weight after exposure to aggressive acid-base environments and good frost resistance.

KEYWORDS

carbon black P 803, P 324 and N 220 • silica ZC-120 • ethylene propylene diene monomer rubber SKEPT-40 vulcanized rubber • rheometric • physico-mechanical and performance properties

Citation: Egorov EN, Kol'tsov NI. Influence of dispersed inorganic fillers on the properties of vulcanized rubber based on ethylene propylene diene monomer rubber SKEPT-40. *Materials Physics and Mechanics*. 2025;53(5): 132–139.
http://dx.doi.org/10.18149/MPM.5352025_11

Introduction

It is known [1–8] that dispersed inorganic fillers make it possible to regulate the technological properties of rubber compounds and the physico-mechanical properties of vulcanizates. In [1], the effect of Zeosil 1165 PM silicon dioxide modified with the organosilane coupling agent bis-(3-triethoxysilylpropyl) tetrasulfane (TESPT) on the rheometric properties of a rubber compound and the physico-mechanical properties of vulcanized rubber based on natural rubber (NR) was investigated. It was shown that the introduction of modified silicon dioxide into the rubber compound leads to an improvement in the rheometric, rheological of the rubber compound, and physico-mechanical properties of the vulcanized rubber. In [2], it was shown that binary fillers with a silica to graphite powder ratio of 1:1 in an amount of only 20.0 phr provide excellent mechanical properties and improved resistance to thermooxidative aging of composites based on NR compared to single fillers. In [4], the influence of hollow polymer microspheres Expancel 909 DU 80, Expancel 043 DUT 80, Expancel 920 DET 40d25, Expancel 920 DUT 40, Expancel 930 MB 120 and Lega Foam 120 MB in an amount of 5.0 phr on the rheometric properties of the rubber compound, the physico-mechanical and performance properties of oil-resistant rubber was studied. It was found that

Publisher: Peter the Great St. Petersburg Polytechnic University

vulcanized rubber containing Expancel 043 DUT 80 microspheres has the best physico-mechanical properties, high wear resistance and resistance to the effects of aggressive hydrocarbon environments. In [8], the influence of the amount of 5.0, 10.0, 15.0 and 20.0 phr was considered. The effect of montmorillonite on the physico-mechanical properties of vulcanizates based on a mixture of natural rubber/styrene-butadiene rubber in a ratio of 50/50 phr was studied. It was shown that the tensile strength of the filled vulcanized rubber reached its maximum value (11.2 MPa) when the montmorillonite content was 15.0 phr.

As a rule, fillers are used to improve the elastic-strength and performance parameters and the chemical resistance of vulcanized rubbers to the action of aggressive acidic and alkaline environments [9–22]. In the rubber industry, rubber compounds based on ethylene propylene diene monomer rubbers are of practical interest, which are characterized by a balanced resistance to the effects of temperatures [23] and oxidation by ozone [24–27]. Despite the achieved results, in connection with increasing requirements, it remains important to develop rubbers that are resistant to temperature effects and highly resistant to alkaline and acidic environments. To eliminate these shortcomings, dispersed powder fillers are introduced into rubber compounds, of which the effective are carbon black [28–34] and silica [35–38]. Therefore, research on the creation of high-quality rubbers based on ethylene propylene diene monomer rubbers, resistant to the effects of temperatures and aggressive environments, using dispersed inorganic fillers is relevant. In this article, the influence of carbon black P 803, P 324, N 220, and silica ZC-120 as fillers on the rheometric properties of the rubber compound, physico-mechanical, and performance properties of vulcanized rubber based on ethylene propylene diene monomer rubber SKEPT-40, often used in the rubber industry, was studied [39,40].

Material and Methods

The rubber compound included ethylene propylene diene monomer rubber SKEPT-40 with a Mooney viscosity ML_{1+4} (100 °C) = 38, ethylene and dicyclopentadiene content of 56 and 6 wt. %, as well as the following ingredients: vulcanizing agent (sulfur), vulcanization accelerators (2-mercaptobenzothiazole and tetramethylthiuram disulfide), vulcanization activators (zinc white and stearic acid), softener (industrial oil I-8A). Carbon black P 324, N 220 and P 803, as well as silica ZC-120 were used as fillers. Carbon black P 324 and N 220 are powders of a deep black color with a particle size of 0.028–0.036 and 0.024–0.033 μm, bulk density of 340 and 355 kg/m^3, a specific surface area of 75–82 and 106–114 m^2/g, and a dibutyl phthalate absorption of 100 ± 5 and 113 ± 7 cm^3/100 g, respectively. Carbon black P 803 is a dark gray powder with a particle size of 9–320 μm, bulk density of 320 kg/m^3, specific surface area of 14–18 m^2/g, dibutyl phthalate absorption of 83 ± 7 cm^3/100 g. Silica ZC-120 is a white powder with a particle size of 0.005–0.015 μm, silicon dioxide content of 97 %, specific surface area of 105–135 m^2/g, a pH (5 % aqueous suspension) of 6–8.

The rubber compound was prepared on LB 320 160/160 laboratory mills at a roll surface temperature of 60–70 °C for 25 min. The rheometric properties of the rubber compound were studied on an MDR 3000 Basic rheometer at 150 °C for 60 min in

accordance with ASTM D2084-79. To determine the physico-mechanical properties, the rubber compound was vulcanized at a temperature of 150 °C for 60 min in a PV-100-3RT-2-PCD vulcanization press. The elastic strength properties were determined according to [42] Shore A hardness was measured in accordance with [43]. Rebound elasticity was determined according to [44]. Relative residual compression deformation (RCD) was determined according to [45]. Change in tensile strength, relative elongation at break and hardness after thermal-oxidative aging in air was determined according to [46]. The change in conditional tensile strength, relative elongation at break and hardness after exposure to liquid aggressive environments was determined according to [47]. The change in mass after exposure to liquid aggressive environments was found according to [47]. The frost resistance coefficient for elastic recovery after compression was determined according to [48].

Results and Discussion

Four variants of rubber compounds were studied, containing carbon black P 324, N 220, P 803 and silica ZC-120 in the amount of 60.00 phr (traditional formulation). For each variant of rubber mixture, vulcanization curves were recorded at 150 °C for 60 min. The research results are shown in Fig. 1.

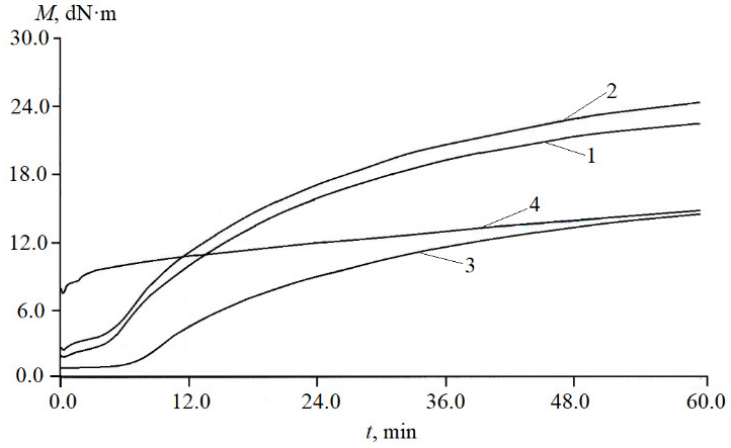

Fig. 1. Vulcanization curves of rubber compound (curve numbers correspond to variant numbers)

The rheometric parameters determined on the basis of the obtained vulcanization curves are given in Table 1. It follows from Table 1 that for variant 3 of the rubber compound containing P 803 carbon black as a filler, a significant increase in the scorch time is observed, which may negatively affect the productivity and quality of the final product. At the same time, variant 4 is characterized by the lowest scorch time. The difference between the torques is directly proportional to the degree of chemical crosslinking of the vulcanizate. Thus, the vulcanizate of variant 2 containing N 220 carbon black as a filler should be characterized by a high degree of crosslinking and have better strength properties.

After vulcanization of the rubber compound, the main physico-mechanical properties of the vulcanizates were determined and are given in the Table 1. The Table shows that variant 2 demonstrates the better physico-mechanical characteristics compared to other variants of vulcanizates, which is explained by the smaller particle

Table 1. Results of the study of the properties of various variants of rubber compounds and vulcanizates

Fillers, indicators	Variants			
	1	2	3	4
Carbon black P 324, phr	60.0	–	–	–
Carbon black N 220, phr	–	60.0	–	–
Carbon black P 803, phr	–	–	60.0	–
Silica ZC-120, phr	–	–	–	60.0
Rheometric properties of rubber compound				
M_H, dN·m	22.51	24.33	14.37	17.51
M_L, dN·m	2.24	3.11	1.02	8.65
ΔM, dN·m	20.27	21.22	13.35	8.86
t_s, min	3.31	3.27	8.57	0.50
t_{90}, min	43.17	43.79	46.50	50.36
Physico-mechanical properties of vulcanizates				
f_p, MPa	14.6 ± 0.7	14.6 ± 0.6	6.0 ± 0.3	5.4 ± 0.3
ε_p, %	356 ± 17	362 ± 19	294 ± 14	682 ± 32
H, units Shore A	72 ± 1	77 ± 1	62 ± 1	68 ± 1
S, %	36 ± 1	37 ± 1	54 ± 1	40 ± 1
RCD at 25 % compression (125 °C × 24 h), %	32.0 ± 1.1	20.0 ± 0.7	30.0 ± 0.9	41.0 ± 1.4
Changes in the physico-mechanical properties of vulcanizates after aging in air (125 °C × 24 h)				
Δf_p, %	+(1.0 ± 0.1)	+(1.0 ± 0.1)	+(1.0 ± 0.1)	+(7.0 ± 0.3)
Δε_p, %	-(15.0 ± 0.6)	-(9.0 ± 0.4)	-(30.0 ± 1.3)	-(52.0 ± 2.1)
ΔH, units Shore A	+(9 ± 1)	+(7 ± 1)	+(8 ± 1)	+(10 ± 1)
Changes in physico-mechanical properties and mass of vulcanizates in a 20 % NaOH solution (23 °C × 24 h)				
Δf_p, %	+(6.0 ± 0.2)	+(3.0 ± 0.1)	+(5.0 ± 0.2)	+(10.0±0.4)
Δε_p, %	+(24.0 ± 0.8)	+(10.0 ± 0.3)	+(18.0 ± 0.6)	+(14.0±0.5)
ΔH, units Shore A	+(1 ± 1)	+(3 ± 1)	-(1 ± 1)	+(3±1)
Δm, %	0.17 ± 0.01	0.13 ± 0.01	0.18 ± 0.01	0.25 ± 0.01
Changes in physico-mechanical properties and mass of vulcanizates in a 20 % HCl solution (23 °C × 24 h)				
Δf_p, %	+(10.0 ± 0.4)	+(2.0 ± 0.1)	-(5.0 ± 0.2)	+(3.0 ± 0.1)
Δε_p, %	+(12 ± 0.4)	+(6.0 ± 0.2)	-(54.0 ± 2.1)	+(56.0 ± 2.3)
ΔH, units Shore A	+(1 ± 1)	-(2 ± 1)	-(1 ± 1)	-(7 ± 1)
Δm, %	0.43 ± 0.01	0.42 ± 0.01	0.46 ± 0.01	0.45 ± 0.01
Frost resistance of vulcanizates				
K_B	0.32 ± 0.01	0.34 ± 0.01	0.40 ± 0.01	0.31 ± 0.01

Note: M_H is maximum torque; M_L is minimum torque; ΔM is difference between the maximum and minimum torques; t_s is scorch time; t_{90} is optimum cure time; f_p is tensile strength; ε_p is elongation at break; H is hardness; S is rebound elasticity; RCD is relative residual compression deformation; Δf_p, Δε_p and Δm are relative changes in the tensile strength, elongation at break and mass; ΔH is change in hardness; K_B is the coefficient of frost resistance by elastic recovery after compression.

size and larger specific surface area of the N 220 carbon black used in this variant compared to P 324 and P 803 carbon black, as well as by the poor dispersion of ZC-120 silica in the rubber matrix [41]. At the same time, vulcanizates of variants 3 and 4 have low values of conventional tensile strength and hardness, which limits their use in conditions where high strength and reliability of materials are required. However, variant 4 is characterized by a good indicator of elongation at break. Vulcanizate of variant 2, containing carbon black N 220 as a filler, is characterized by the lowest value of relative residual compression deformation, which indicates its high elastic properties.

The table also shows the results of the study of changes in the physico-mechanical properties and hardness of vulcanizates after thermal aging in air. As can be seen, the stable physico-mechanical properties are found in the vulcanizate of variant 2 of the rubber compound containing carbon black grade N 220. It shows a slight change in the tensile strength, as well as in the elongation at break after thermal aging in air.

The changes in the physico-mechanical properties and weight of the vulcanizates after exposure to aggressive environments were further investigated: 20 % aqueous solutions of NaOH and HCl at 23 °C for 24 h (see Table 1). The data obtained show that the best resistance in a 20 % HCl solution is demonstrated by the vulcanizate of variant 2, which is characterized by the smallest changes in strength and elongation.

Table 1 also shows the results of the study of the frost resistance of the vulcanizates, determined by their elastic recovery after a single 20 º% compression for 5 min at –50 ºC. As can be seen, all vulcanizates have high frost resistance coefficient values, which indicates the ability to maintain elasticity and physico-mechanical properties at extremely low temperatures, allowing them to be used in cold climates.

Conclusions

The objects of the study were a rubber compound and vulcanized rubber on its basis, obtained by sulfur vulcanization of ethylene propylene diene monomer rubber SKEPT-40 in the presence of vulcanization accelerators (2-mercaptobenzothiazole and tetramethylthiuram disulfide), vulcanization activators (zinc white and stearic acid), a softener (industrial oil I-8A) and various inorganic fillers (carbon black P 803, P 324, N 220 and silica ZC-120) in an amount of 60.0 phr. The rubber compound was prepared on laboratory rollers LB 320 160/160, and then its rheometric properties were determined on a rheometer MDR 3000 Basic. The vulcanized rubber was obtained by vulcanizing the rubber compound in a P-V-100-3RT-2-PCD vulcanization press. The resulting vulcanizates were tested for their physical and mechanical properties (elastic strength properties, Shore A hardness, rebound elasticity, and relative compressive strain), as well as their performance properties (changes in tensile strength, elongation at break, and hardness after thermal-oxidative aging in air, changes in mass after exposure to liquid aggressive environments, and frost resistance).

These results allow us to formulate the following conclusions:

1. The rubber compound containing N 220 carbon black exhibits a large difference between the maximum and minimum torques, which is directly proportional to the degree of chemical crosslinking and the strength properties of the vulcanizate.
2. The vulcanizate containing carbon black N 220 has better and more stable physico-mechanical properties compared to vulcanizates containing carbon blacks P 324, P 803 and silica ZC-120, which explained by the smaller particle size and higher specific surface area of carbon black N 220 compared to carbon black P 324 and P 803, as well as poor dispersion of silica ZC-120 in the rubber matrix. For the vulcanizate containing carbon black N 220, an insignificant change in the conventional tensile strength is observed, as well as the relative elongation at break after thermal aging in air, exposure to aggressive acid-base environments, and high frost resistance.

3. Recommendations for the practical application of the results: a rubber mixture consisting of ethylene propylene diene monomer rubber SKEPT-40 and containing 60.0 phr carbon black N 220, can be recommended for rubberizing the surfaces of tanks used for transporting and storing acid-base solutions.
4. A possible direction for further research is to study the effect of carbon black N 220 on rubber based on other ethylene propylene diene monomer rubbers, such as S 501A and S 505A.

CRediT authorship contribution statement

Evgeniy N. Egorov **:** writing – review & editing, writing – original draft, conceptualization, investigation; **Nikolay I. Kol'tsov** **:** writing – review & editing, writing – original draft, conceptualization, supervision, data curation.

Conflict of interest

The authors declare that they have no conflict of interest.

References

1. Rombaldi SH, Pierozan NJ, Brandalise RN. Influence on mechanical and rheometric properties through different methods of chemical modification of silica applied to natural rubber compounds. *Journal of Elastomers and Plastics.* 2021;53(2): 165–187.
2. Alam MN, Kumar V, Potiyaraj P, Lee DJ, Choi J. Mutual dispersion of graphite–silica binary fillers and its effects on curing, mechanical, and aging properties of natural rubber composites. *Polymer Bulletin.* 2022;79(5): 2707–2724.
3. Shahamatifard F, Rodrigue D, Park KW, Frikha S, Mighri F. Natural rubber nanocomposites: effect of carbon black/multi-walled carbon nanotubes hybrid fillers on the mechanical properties and thermal conductivity. *Polymer-Plastics Technology and Materials.* 2021;60(15): 1686–1696.
4. Egorov EN, Sandalov SI, Kol'tsov NI, Voronchikhin VD. Study of the effect of polymeric microspheres on the properties of oil and petrol resistant rubber. *Journal of Siberian Federal University. Chemistry.* 2024;17(3): 376–382. (In Russian)
5. Marzocca AJ, Garraza ALR, Anbinder S, Macchi C, Somoza A. Changes in the mechanical, micro-, and nano-structural properties of reinforced vulcanized natural rubber compounds: their dependence on the SiO_2/CB ratio. *Rubber Chemistry and Technology.* 2022;95(1): 58–81.
6. Honorato LR, Visconte LLY, Nunes RCR. Effect of different cure systems on natural rubber/nanocellulose nanocomposites in rheological, physical-mechanical, aging, and mechanical properties. *Journal of Elastomers and Plastics.* 2022;54(5): 676–692.
7. Amrollahi A, Razzaghi-Kashani M, Hosseini SM, Habibi N. Carbon black/silica hybrid filler networking and its synergistic effects on the performance of styrene-butadiene rubber composites. *Polymer Journal.* 2022;54(7): 931–942.
8. El Mogy SA, Lawandy SN. Enhancement of the cure behavior and mechanical properties of nanoclay reinforced NR/SBR vulcanizates based on waste tire rubber. *Journal of Thermoplastic Composite Materials.* 2024;37(2): 520–543.
9. Zaeimoedin TZ, Aziz AKC, Kamal MM. Improving filler dispersion and physical properties of epoxidised natural rubber/silica compound by using dual fillers and coupling agent in mixing process. *Malaysian Journal of Analytical Sciences.* 2014;18(3): 604–611.
10. Shiva M, Akhtari SS, Shayesteh M. Effect of mineral fillers on physico-mechanical properties and heat conductivity of carbon black-filled SBR/butadiene rubber composite. *Iranian Polymer Journal.* 2020;29: 957–974.
11. Egorov EN, Kol'tsov NI. Influence of glass fibers on the physico-mechanical and performance properties of rubber based on general and special purpose caoutchoucs. *Materials Physics and Mechanics.* 2024;52(1): 126–131.
12. Kumar V, Alam MN, Manikkavel A, Song M, Lee DJ, Park SS. Silicone rubber composites reinforced by carbon nanofillers and their hybrids for various applications: A review. *Polymers.* 2021;13(14): 2322.
13. Roy K, Debnath SC, Potiyaraj P. A critical review on the utilization of various reinforcement modifiers in filled rubber composites. *Journal of Elastomers and Plastics.* 2019;52(2): 167–193.

14. Braihi AJ, Jawad AJ, Kadhum AAH, Aljibori HSS, Al-Amiery AA. Chemical resistance of NR/SBR rubber blends for surfaces corrosion protection of metallic tanks in petrochemical industries. *Koroze a Ochrana Materiálu.* 2020;64(2): 65–71.
15. Kazemi H, Mighri F, Rodrigue D. A review of rubber biocomposites reinforced with lignocellulosic fillers. *Journal of Composites Science.* 2022;6(7): 183.
16. Wang Z, An Q, Jiao L, Lu P, Qu Y, Xu Z, Sun W, Li Y. Preparation and properties of fluorosilicone composites with thermal conductivity and chemical resistance through modification of filler and matrix. *Polymer Degradation and Stability.* 2024;225: 110823.
17. Omar MF, Ali F, Jami MS, Azmi AS, Ahmad F, Marzuki MZ, Muniyandi SK, Zainudin Z, Kim MP. A Comprehensive Review of Natural Rubber Composites: Properties, Compounding Aspects, and Renewable Practices with Natural Fibre Reinforcement. *Journal of Renewable Materials.* 2025;13(3): 497–538.
18. Egorov EN, Sandalov SI, Kol'tsov NI. Influence of basalt fibres on the physical-mechanical, performance and dynamic properties of rubber for rail pads. *Chemistry for Sustainable Development.* 2023;31(4): 362–366. (In Russian)
19. Ushmarin NF, Egorov EN, Kol'tsov NI. Influence of microspheres on properties of aggressive resistant rubbers. *Izvestiya vysshikh uchebnykh zavedeniy khimiya khimicheskaya tekhnologiya [ChemChemTech].* 2021;64(2): 49–55. (In Russian)
20. Zou Y, Yao YF, Zhang R, Zhao YH, Cao J, Xu YX. Biobased recyclable rubbers with shape memory, self-welding, and damping properties by cross-linking epoxidized natural rubber with succinic anhydride. *ACS Sustainable Chemistry and Engineering.* 2023;11(51): 18123–18130.
21. Ridho MR, Agustiany EA, Rahmi DnM, Madyaratri EW, Ghozali M, Restu WK, et al. Lignin as green filler in polymer composites: development methods, characteristics, and potential applications. *Advances in Materials Science and Engineering.* 2022;2022(1): 1363481.
22. Ushmarin NF, Egorov EN, Sandalov SI, Kol'tsov NI. Influence of polymeric microspheres on rubber properties for coating metal surfaces. *Russian Journal of General Chemistry.* 2023;93: 734–739.
23. Kumar SP, Prabhakaran G, Vishvanathperumal S. Influence of Modified Nanosilica on the Performance of NR/EPDM Blends: Cure Characteristics, Mechanical Properties and Swelling Resistance. *Journal of Inorganic and Organometallic Polymers and Materials.* 2024;34: 3420–3442.
24. Bizhani H, Katbab AA, Lopez-Hernandez E, Miranda JM, Lopez-Manchado MA, Verdejo R. Preparation and characterization of highly elastic foams with enhanced electromagnetic wave absorption based on ethylene-propylene-diene-monomer rubber filled with barium titanate/multiwall carbon nanotube hybrid. *Polymers.* 2020;12(10): 2278.
25. Costa NL, Hiranobe CT, Cardim HP, Dognani G, Sanchez JC, Carvalho JAJ, Torres GB, Paim LL, Pinto LF, Cardim GP, Cabrera FC, dos Santos RJ, Silva MJ. A Review of EPDM (Ethylene Propylene Diene Monomer) Rubber-Based Nanocomposites: Properties and Progress. *Polymers.* 2024;16(12): 1720.
26. Li C, Wang Y, Yuan Z, Ye L. Construction of sacrificial bonds and hybrid networks in EPDM rubber towards mechanical performance enhancement. *Applied Surface Science.* 2019;484: 616–627.
27. Ghoreishi A, Koosha M, Nasirizadeh N. Modification of bitumen by EPDM blended with hybrid nanoparticles: Physical, thermal, and rheological properties. *Journal of Thermoplastic Composite Materials.* 2020;33(3): 343–356.
28. Fan Y, Fowler GD, Zhao M. The past, present and future of carbon black as a rubber reinforcing filler–A review. *Journal of Cleaner Production.* 2020;247: 119115.
29. Robertson CG, Hardman NJ. Nature of carbon black reinforcement of rubber: Perspective on the original polymer nanocomposite. *Polymers.* 2021;13(4): 538.
30. Egorov EN, Sandalov SI, Kol'tsov NI. Study of the influence of dispersed fillers on properties of rubber for gaskets of rail fastening. *Materials Physics and Mechanics.* 2023;51(6): 119–126.
31. Zhang H, Wang C, Zhang Y. Preparation and properties of styrene-butadiene rubber nanocomposites blended with carbon black-graphene hybrid filler. *Journal of Applied Polymer Science.* 2015;132(3): 41309.
32. Jovanović V, Samaržija-Jovanović S, Budinski-Simendić J, Marković G, Marinović-Cincović M. Composites based on carbon black reinforced NBR/EPDM rubber blends. *Composites Part B: Engineering.* 2013;45(1): 333–340.
33. Xu T, Jia Z, Li J, Luo Y, Jia D, Peng Z. Study on the dispersion of carbon black/silica in SBR/BR composites and its properties by adding epoxidized natural rubber as a compatilizer. *Polymer Composites.* 2018;39(2): 377–385.
34. Ismail H, Omar NF, Othman N. Effect of carbon black loading on curing characteristics and mechanical properties of waste tyre dust/carbon black hybrid filler filled natural rubber compounds. *Journal of Applied Polymer Science.* 2011;121(2): 1143–1150.
35. Egorov EN, Ushmarin NF, Sandalov SI, Grigor'ev VS, Kol'tsov NI, Voronchikhin VD. Study of the effect of silica filler Silica 1165 on the properties of rubber for rail fastening gaskets. *Journal of Siberian Federal University. Chemistry.* 2022;15(1): 110–117 (In Russian)

36. Liu H, Yang L, Liu X, Cao JP, Zhang J, Luo Z, Gao, Z. Silicon dioxide nanoparticle decorated graphene with excellent dispersibility in natural rubber composites via physical mixing for application in green tires. *Composites Part B: Engineering.* 2023;258: 110700.
37. Bera A, Sarkar K, Ganguly D, Ghorai SK, Hore R, Kumar N, Amarnath SKP, Chattopadhyay S. Recent advancements in silica filled natural rubber composite: A green approach to achieve smart properties in tyre. *Journal of Polymer Research.* 2024;31(4): 122.
38. Khan H, Amin M, Ali M, Iqbal M, Yasin M. Effect of micro/nano-SiO_2 on mechanical, thermal, and electrical properties of silicone rubber, epoxy, and EPDM composites for outdoor electrical insulations. *Turkish Journal of Electrical Engineering and Computer Sciences.* 2017;25(2): 1426–1435.
39. Kablov VF, Keibal NA, Kochetkov VG, Novopoltseva OM, Kryukova DA, Urzhumov DA, Tokar' VP. Research on Elastomeric Fire-and Heat-Protection Materials Containing Plasma-Treated Microspheres. *Polymer Science, Series D.* 2024;17: 286–290.
40. Davydova ML, Shadrinov NV, Fedorova AF, Khaldeeva AR, Sokolova MD. Studying the Stability of Ethylene-Propylene Rubbers under Thermocycling in Different Working Media. *Polymer Science, Series D.* 2025;18: 239–244.
41. Bokobza L. Elastomer Nanocomposites: Effect of Filler–Matrix and Filler–Filler Interactions. *Polymers.* 2023;15(13): 2900.
42. Russian State Standard. GOST 270-75. *Rubber. Method of the determination elastic and tensile stress-strain properties*. Moscow: Standardinform; 2008. (In Russian)
43. Russian State Standard. GOST 263-75. *Rubber. Method for the determination of Shore A hardness.* Moscow: Standards Publishing; 1989. (In Russian)
44. Russian State Standard. GOST 27110-86. *Rubber. Method for determination of rebound elasticity on the Shob type machine*. Moscow: Standards Publishing; 1987. (In Russian)
45. Russian State Standard GOST 9.029-74. *Unified system of corrosion and ageing protection. Vulcanized rubbers. Method of testing of resistance to ageing under static deformation of compression*. Moscow: Standards Publishing; 1982. (In Russian)
46. Russian State Standard. GOST 9.024-74. *Unified system of corrosion and ageing protection. Rubbers. Methods of heat ageing stability determination.* Moscow: Standards Publishing; 1975. (In Russian)
47. Russian State Standard. GOST 9.030-74 (method B). *Unified system of corrosion and ageing protection. Vulcanized rubbers. Method of testing resistance to attack by corrosive media in limp state.* Moscow: Standardinform; 2008. (In Russian)
48. Russian State Standard. GOST 13808-79. *Rubber. Method for the determination of low temperature resistance according to elastic rebound after compression*. Moscow: Standards Publishing; 1978. (In Russian)

MATERIALS PHYSICS AND MECHANICS RESEARCH ARTICLE

Submitted: July 5, 2025 **Revised: September 1, 2025** **Accepted: November 12, 2025**

Dynamic fracture of concretes with basalt and limestone aggregate at different temperatures

N.S. Selyutina [1,2]✉, **D.D. Khairetdinova** [1,3]

[1] St. Petersburg State University, St. Petersburg, Russia

[2] Institute for Problems in Mechanical Engineering of the Russian Academy of Science, St. Petersburg, Russia

[3] St. Petersburg State University of Aerospace Instrumentation, St. Petersburg, Russia

✉ nina.selutina@gmail.com

ABSTRACT

The dynamic strength of concrete subjected to variable thermal and velocity conditions is examined, predicated on the incubation time criterion and the thermal fluctuation theory of strength. A salient feature of this criterion is the invariant characteristic time, serving as a quantification of the loading rate. Model validation is accomplished through a comparative analysis of predicted outcomes against empirical data obtained from concrete specimens incorporating basalt, gravel, and limestone aggregates. It is shown that the characteristic relaxation time of concretes increases within the temperature interval of 20 to 800 °C and decreases at temperatures above ~ 800 °C. The temperature dependence of the characteristic relaxation time for concrete with basalt, limestone and gravel aggregate, determining the intensity of the relaxation process, is predicted based on proposed model.

KEYWORDS

dynamic strength • characteristic time • temperature • strain rate • activation energy

Funding. *The study was supported by the Russian Science Foundation (RSF grant 22-11-00091_P).*

Citation: Selyutina NS, Khairetdinova DD. Dynamic fracture of concretes with basalt and limestone aggregate at different temperatures. *Materials Physics and Mechanics*. 2025;53(5): 140–149. http://dx.doi.org/10.18149/MPM.5352025_12

Introduction

Temperature and strain rate are key parameters affecting the quasi-static and dynamic strength of concrete. With an increase in the rate of deformation and a fixed temperature, a positive velocity sensitivity of the material is observed, i.e. the dynamic strength increases with the rate of deformation and exceeds the value of static strength. Furthermore, for certain types of concrete [1,2], the commonly held view that both static and dynamic strength decrease with rising temperature above room temperature [3] does not consistently hold across all temperature ranges. In such cases, the quasi-static and dynamic strength of concrete [1,2] above room temperature initially decreases at 200 °C, increases at 400 °C and then declines again at 600 and 800 °C. However, even at these higher temperatures, the strength remains greater than at 200 °C, relative to the values measured at room temperature. The rate of increase of dynamic strength with strain rate with increasing temperature above room temperature may decrease or increase depending on the chemical reactions occurring at a given temperature and different microstructure depending on temperature, as shown in Table 1.

Publisher: Peter the Great St. Petersburg Polytechnic University

Table 1. Reasons for increase (+) or decrease (-) of static strength of concrete at different temperatures

C-S-H= $CaSO_4$+H_2O		–
gel decomposition C-S-H		
20–400 °C	Evaporation of free and capillary water inside concrete.	–
~ 400 °C	C_3S (C_2S) + H_2O → C-S-H-gel+ $Ca(OH)_2$	+
	The process of dehydration [4–6] and shrinkage of the C-S-H gel, which strengthens the bond between the aggregate and the cement paste and partially compensates for the loss of strength caused by their difference in deformation.	
400–600 °C	$Ca(OH)_2$→CaO+H_2O	–
	Increase in the difference in deformation between the aggregate and concrete paste and decomposition $Ca(OH)_2$.	
< 600 °C	$CaCO_3$→CaO+CO_2	–
	$CaCO_3$ begins to decompose and the aggregate becomes loose.	

At constant temperature during high-speed deformation [7–9], the water content in the samples influences the strength of concrete. Concrete with 0 % water saturation exhibits higher strength under static loads, and water-saturated concrete demonstrates greater strength under dynamic loads. Under static conditions, the phenomenon can be attributed to hydrostatic pressure in water-saturated concrete samples. Conversely, under dynamic conditions, the influence of hydrostatic pressure on concrete strength increases, which leads to a slowdown in the incubation processes during micro-cracking.

The application of thermal fluctuation theory of strength is often used to predict the strength of concrete and other composite materials [10–14]. Although concrete appears robust, temperature fluctuations during service can significantly reduce its lifespan [15]. Thermal stresses caused by temperature variations must always be considered during the design phase of concrete components. Furthermore, the incorporation of alternative materials to enhance sustainability—such as recycled concrete, slag, and plastic aggregates—inevitably affects concrete's thermal response [16–19]. Key observations include:

1. Recycled concrete aggregates exposed to cyclic thermal loading develop microcracks in the interfacial transition zones, reducing strength [20,21].
2. Slag aggregates, due to their high density, improve thermal resistance, minimizing strength loss at elevated temperatures [22].
3. Plastic aggregates lead to significant strength loss under high temperatures as the plastic particles melt [23,24].

In this paper, a method is proposed for predicting the increase in both static and dynamic strength of concrete with rising temperature, based on the incubation time criterion [7,25,26], while incorporating the thermofluctuation mechanism of fracture [12–14,27–29]. By introducing the concept of incubation time and applying the standard equations of thermofluctuation strength theory, the model enables estimation of a material's dynamic strength across a wide range of deformation rates and temperatures. The proposed model demonstrates good predictive capability for the strength of concrete containing limestone and basalt aggregates under varying thermal and speed conditions. It is shown that the characteristic relaxation time decreases with increasing temperature up to approximately 1000 K, after which it begins to increase — an anomalous behavior for this parameter.

Incubation time criterion

The instability of strength characteristics in brittle materials under high-speed deformation has been observed in dynamic experiments involving rocks and concrete [1,2,30]. Predicting the distinctive strain rate dependence of material strength across a wide range of strain rates remains one of the central challenges in fracture dynamics. In this paper, a structural-temporal approach previously proposed in studies [7,25,26] is employed to calculate material strength at varying strain rates. Dynamic strength σ_d is defined as the maximum value of the ultimate stress achieved in a sample when it is loaded until fracture. Within the framework of the structural-temporal approach, the fracture condition is expressed as follows:

$$\frac{1}{\tau}\int_{t-\tau}^{t}\left(\frac{\sigma(t')}{\sigma_c}\right)^{\alpha} \mathrm{d}t' \le 1, \qquad (1)$$

where τ is the incubation time of fracture, $\sigma(t)$ is the time dependence of the stresses in the sample (at the place of fracture), σ_c is the static compressive strength, α is the parameter characterizing the sensitivity of the material to the level of force field intensity that causes compression fracture. Within the framework of the structural-temporal approach, when determining the ultimate strength σ_{ul}, condition (1) is written for each of the loads. In this case, the set of material characteristics α, τ, σ_c differs for the cases of tension and compression. In this work, the strain rate dependence of the compressive strength of concrete is considered. The fracture time t_* is determined from the condition in which the inequality (1) transforms into equality. The incubation time is the characteristic time of relaxation. In the case of fracture, the physical nature of the incubation time is associated with the relaxation processes of micro-cracking before macro-fracture.

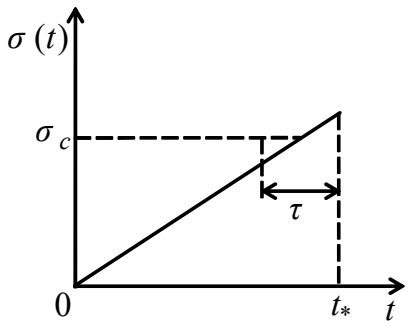

Fig. 1. Temporal dependence of stress for slow linear loading

Fracture criterion (1) implies the existence of an incubation period, preceding a macroscopic failure of the material. In this context, an incubation process is an essential component of the overall fracture process and occurs under both quasi-static and fast impact loads. The presence of this fracture incubation period gives rise to specific phenomena under dynamic loading, most notably the well-established strain-rate dependence of material strength. As one of the simplest interpretations of the fracture incubation time, let us consider an example of fracture caused by a slow (t_*>>τ) linearly growing tensile stress $\sigma(t) = \dot{\sigma}\, t\, H(t)$, where $\dot{\sigma}$ = const and $H(t)$ is the Heaviside step function. Substituting linear expression for $\sigma(t)$ into (1), we can calculate the time to

fracture $t_* = \sigma_c/\dot{\sigma} + 0.5\,\tau$ and a value of the critical stress at the moment of fracture $\sigma_{ul} = \sigma(t_*) = \sigma_c + 0.5\,\dot{\sigma}\,\tau$, where σ_c is the tabulated value of the material static strength. In the case of very slow stress growth $(\dot{\sigma}\,\tau)/\sigma_c << 1$, the ultimate stress does not differ much from the static strength $\sigma_{ul} \approx \sigma_c$. The obtained expressions show that according to Eq. (1) the material remains intact at the moment when the static strength limit is achieved $t_c = \sigma_c/\dot{\sigma}$. It is crucial that before the onset of the macroscopic rupture of the material, preparatory processes having a characteristic temporal period τ evolve in the material structure (Fig. 1).

The main advantage of using the structural-temporal approach is the introduction of the incubation time parameter, which is invariant with respect to the loading history $\sigma(t)$. According to the notion of the incubation time, two concrete specimens with different fibre volume fractions have different incubation time values. The incubation time is determined by approximation methods based on an experimental set of strength and strain rate values. The least squares method is used in this study. The loading of concrete samples in both static and dynamic experiments, as shown in the previous studies [7,25,26], is carried out according to the linear function of deformation in time.

The time dependence of the stresses in the sample has the following form:

$$\sigma(t) = E\dot{\varepsilon}tH(t), \tag{2}$$

where E is Young's modulus, $\dot{\boldsymbol{\varepsilon}}$ is the strain rate, and $H(t)$ is the Heaviside function. It is noted that wave processes are neglected when measuring the dynamic strength in experiments [1–3] on a split Hopkinson pressure bar, where long-term load pulses are set. Therefore, when assessing strength in a wide range of strain rates based on the structural-temporal approach (1), wave effects are also neglected.

Let us recall that, according to the given definition of strength above, for the case of linear loading, the strength is defined as $\boldsymbol{\sigma_{ul}} = \boldsymbol{\sigma}(\boldsymbol{t_*}) = \boldsymbol{E\dot{\varepsilon}t_*}$. Substituting Eq. (2) into the equality condition (1), the dependence of the fracture time on the strain rate $\boldsymbol{t^*}(\dot{\boldsymbol{\varepsilon}})$ is determined:

$$\boldsymbol{t_*}(\dot{\boldsymbol{\varepsilon}}) = \begin{cases} \left((\boldsymbol{\alpha}+\boldsymbol{1})\left(\frac{\boldsymbol{\sigma_c}}{\boldsymbol{E\dot{\varepsilon}}}\right)^{\boldsymbol{\alpha}}\boldsymbol{\tau}\right)^{\frac{1}{\alpha+1}}, & \dot{\boldsymbol{\varepsilon}} \geq \sqrt[\alpha]{\boldsymbol{\alpha}+\boldsymbol{1}}\,\frac{\boldsymbol{\sigma_c}}{\boldsymbol{E\tau}} \quad (\boldsymbol{t_*} \leq \boldsymbol{\tau}), \\ \frac{\boldsymbol{\sigma_{ul}^{sol}}}{(\boldsymbol{E\dot{\varepsilon}})^{\boldsymbol{\alpha}+\boldsymbol{1}}}, & \dot{\boldsymbol{\varepsilon}} < \sqrt[\alpha]{\boldsymbol{\alpha}+\boldsymbol{1}}\,\frac{\boldsymbol{\sigma_c}}{\boldsymbol{E\tau}} \quad (\boldsymbol{t_*} > \boldsymbol{\tau}), \end{cases} \tag{3}$$

where $\boldsymbol{\sigma_{ul}^{sol}}$ is the solution to the following equation with respect to $\boldsymbol{\sigma_{ul}}$:

$$(\boldsymbol{\sigma_{ul}})^{\boldsymbol{\alpha}+\boldsymbol{1}} - (\boldsymbol{\sigma_{ul}} - \boldsymbol{E\dot{\varepsilon}\tau})^{\boldsymbol{\alpha}+\boldsymbol{1}} = (\boldsymbol{\alpha}+\boldsymbol{1})\boldsymbol{E\dot{\varepsilon}\tau\sigma_c^{\alpha}}. \tag{4}$$

Then, by substituting the obtained dependence $\boldsymbol{t_*}(\dot{\boldsymbol{\varepsilon}})$ (Eq. (3)) into $\boldsymbol{\sigma_{ul}}$, the dependence of the ultimate strength on the strain rate has the following form:

$$\boldsymbol{\sigma_{ul}}(\dot{\boldsymbol{\varepsilon}}) = \begin{cases} \left((\boldsymbol{\alpha}+\boldsymbol{1})\boldsymbol{E\dot{\varepsilon}\tau\sigma_c^{\alpha}}\right)^{\frac{1}{\alpha+1}}, & \dot{\boldsymbol{\varepsilon}} \geq \sqrt[\alpha]{\boldsymbol{\alpha}+\boldsymbol{1}}\,\frac{\boldsymbol{\sigma_c}}{\boldsymbol{E\tau}} \quad (\boldsymbol{t_*} \leq \boldsymbol{\tau}), \\ \boldsymbol{\sigma_{ul}^{sol}}(\dot{\boldsymbol{\varepsilon}}), & \dot{\boldsymbol{\varepsilon}} < \sqrt[\alpha]{\boldsymbol{\alpha}+\boldsymbol{1}}\,\frac{\boldsymbol{\sigma_c}}{\boldsymbol{E\tau}} \quad (\boldsymbol{t_*} > \boldsymbol{\tau}). \end{cases} \tag{5}$$

In the case of α = 1, Eq. (5) is written explicitly:

$$\boldsymbol{\sigma_{ul}}(\dot{\boldsymbol{\varepsilon}}) = \begin{cases} \sqrt{\boldsymbol{2E\dot{\varepsilon}\tau\sigma_c}}, & \dot{\boldsymbol{\varepsilon}} \geq \frac{\boldsymbol{2\sigma_c}}{\boldsymbol{E\tau(T)}} \quad (\boldsymbol{t_*} \leq \boldsymbol{\tau}), \\ \boldsymbol{\sigma_c} + \frac{\boldsymbol{1}}{\boldsymbol{2}}\boldsymbol{E\dot{\varepsilon}\tau}, & \dot{\boldsymbol{\varepsilon}} < \frac{\boldsymbol{2\sigma_c}}{\boldsymbol{E\tau(T)}} \quad (\boldsymbol{t_*} > \boldsymbol{\tau}). \end{cases} \tag{6}$$

Thus, Eq. (6) provides a simple description of the ultimate stress across a wide range of strain rates. To estimate the incubation time τ and the amplitude parameter α, the least

squares method is used on a set of experimental data referring to critical stresses and corresponding strain rates. In [7], the process of fracture within the framework of the structural-temporal approach, written at $\alpha = 1$, is considered at various scale levels, and the characteristic of τ is determined at a given scale level. Establishing a set of material parameters $\boldsymbol{\sigma_c}$, E, τ makes it possible to construct a non-linear relationship.

Hybrid model

In this section, we define the temperature dependencies for the characteristic relaxation time $\tau(T)$ and introduce them on the basis of the thermofluctuation theory of strength [27,31,32]. In this case, the intensity of the relaxation process is usually considered as a process with an exponential dependence on temperature [27]. The canonical form of the Zhurkov formula has the form (7) for estimating the temperature dependence of the intensity of relaxation processes:

$$\boldsymbol{\tau(T) = \tau_a \exp\left(\frac{U_0 - \delta\sigma}{kT}\right)}, \quad (7)$$

where τ (T) is the effective time to reach a state close to equilibrium (such a movement of the system towards equilibrium is called relaxation) [27], T is temperature, $\boldsymbol{\tau_a}$ is the period of oscillation of atoms in a solid ($\boldsymbol{\tau_a}$=10^{-12}...10^{-13} s), $\boldsymbol{U_0}$ is the initial activation energy in the unstressed state of the body (the activation energy of interatomic bonds), δ is the structural coefficient that characterizes the velocity of decrease in activation energy with increasing stress under fracture, k = 8.314 J/(K·mol) is the Boltzmann's universal gas constant. The value of the barrier $U(T)$ under the assumptions presented in the work [33] is determined from the measured dependence of ln $\tau_e(1/T)$:

$$\boldsymbol{U(T) = kT \ln\left(\frac{\tau_e}{\tau_a}\right)}, \quad (8)$$

where $\boldsymbol{\tau_e}$ is the effective time to reach a state close to equilibrium (such movement of the system towards equilibrium is the relaxation) [27]. Equation (8) showed good agreement with experimental data in the papers [14,34,35] for concrete with sand aggregate in various temperature ranges from -40 to +60 °C [14]; from -5 to -25 °C [34]; from -40 to 0 °C [35].

Based on studies on the long-term strength of concrete in the temperature range from -40 to +60 °C in work [14], it was established: (1) the activation energy of fracture is independent of applied stress and temperature and is equal to 162.8 kJ/mol; (2) the pre-exponential constant, which characterizes the average time between successive thermal oscillations, depends on both stress and temperature; (3) the higher the temperature, the less the effect of stress. In the paper [14], it was proposed to use Zhurkov's formula Eq. (7) in the following generalized form:

$$\boldsymbol{\tau(T) = \tau_a \sigma(T) \exp\left(\frac{U_0}{kT}\right)}. \quad (9)$$

In [36,37], Zhurkov's formula (Eqs. (7) and (9)) and the structural-time approach [29] were applied to determine the strength dependencies during spall fracture:

$$\boldsymbol{\tau(T) = \tau_a \, exp\left(\frac{U_0 - \delta\sigma}{kT}\right) - \frac{t_i}{2}}, \quad (10)$$

where $\boldsymbol{t_i}$ is the pulse duration. In this paper, the intensity of the relaxation process is proposed to be written as decreasing and increasing exponential dependencies:

$$\boldsymbol{\tau(T) = \tau_a \exp\left(\frac{U_0}{kT}\right) + \tau_1 \exp\left(\frac{T_m}{T - T_m}\right)}, \quad (11)$$

where T_m is the melting temperature, τ_1 is material's constant.

Velocity dependencies of the strength of concretes with basalt and limestone aggregate

Within the framework of the incubation time criterion, theoretical dependencies of strength on the strain rate were developed for concretes produced with limestone aggregate (concrete L), gravel aggregate (concrete G) and with basalt aggregate (concretes B1 and B2), based on experimental data [1–3]. Table 2 shows Mix proportions of concrete [1–3]. Dynamic and static experiments on compressive strength in [1,3] were carried out at different fixed temperatures: 20, 400, 650, 800, and 950 °C for concrete with basalt aggregate [3] and 20, 200, 400, 600, and 800 °C for concretes with limestone aggregate [1] and gravel aggregate [2]. For each temperature illustrated in Fig. 2, two theoretical strength dependencies on strain rate were plotted, indicated by solid lines: one curve intersected the minimum experimental point ($\dot{\varepsilon}$,σ_{ul}), while the other aligned with the maximum experimental point ($\dot{\varepsilon}$,σ_{ul}). As a result, the range of experimental values ($\dot{\varepsilon}$,σ_{ul}) was between these two theoretical dependencies. The values of Young's modulus and static strength for each temperature are set according to experimental data [1,3] from stress-strain relationships and take a fixed value for each temperature. The two theoretical dependencies of strength on the strain rate for concretes B1, B2 and L differed only in the fracture characteristic time, thereby setting the characteristic time interval for each temperature: from 80.8 to 135.4 μs at 20 °C; from 42.35 to 95 μs at 400 °C; from 19.4 to 64.1 μs at 650 °C; from 17.4 to 47.67 μs at 800 °C; from 88.6 to 227.3 μs at 950 °C for concretes B1 and B2; from 39.9 to 97.1 μs at 20 °C, from 60.1 to 82 μs at 200 °C, from 78.6 to 157.86 μs at 400 °C, from 122.5 to 181.46 μs at 600 °C, from 247.2 to 350.8 μs at 800 °C for concrete L and from 49.14 to 89.71 μs at 20 °C, from 39.92 to 67.28 μs at 200 °C, from 60.92 to 94.88 μs at 400 °C, from 121.54 to 128.14 μs at 600 °C, from 86.88 to 194.43 μs at 800 °C for concrete G. For the entire set of experimental values ($\dot{\varepsilon}$,σ_{ul}), the parameter of the average characteristic time is also determined for both concretes:

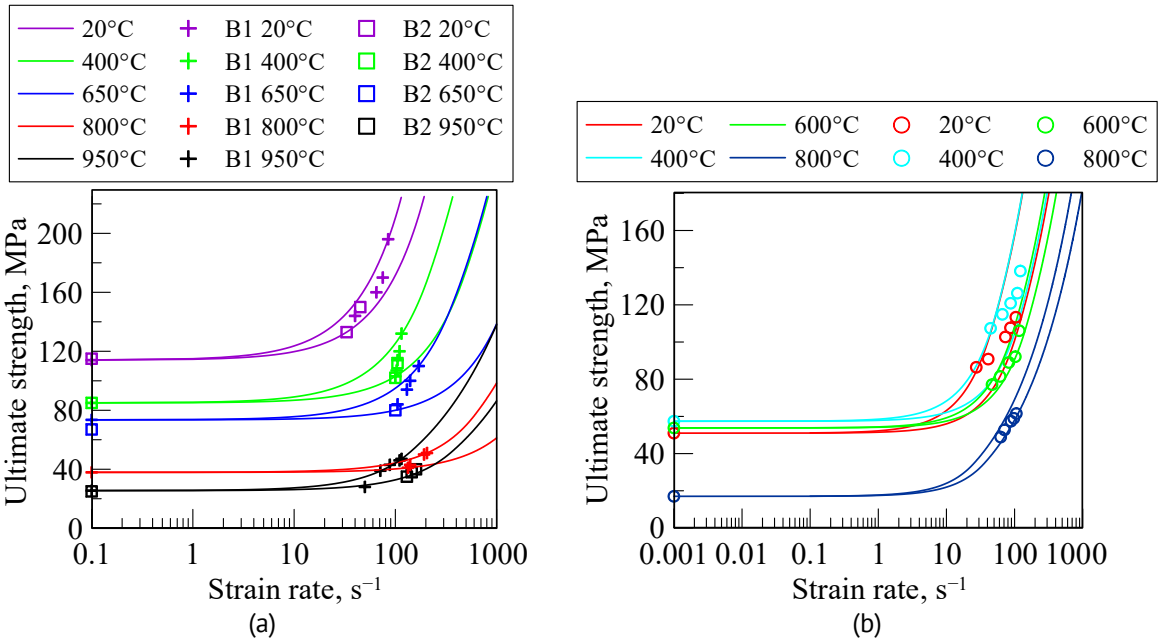

Fig. 2. The range of theoretical speed dependencies of concrete strength at different temperatures, plotted on experimental data by tests of concrete (a) B1 and B2 [3]; (b) L [1]

Table 2. Mix proportions of concrete [1,3]

Designation for this work	Concrete B1	Concrete B2	Concrete L	Concrete G
Reference	[3] (concrete C)	[3] (concrete B)	[1]	[2]
Water, kg/m^3	166	179	180	180
Cement, kg/m^3	442	391	371	600
Fly ash, kg/m^3	78	69	99	-
Sand, kg/m^3	689	689	672	668
Admixture, kg/m^3	5.3	3.5	5	9
Aggregate, kg/m	1125	1172	1008	1002
Material of aggregate	Basalt	Basalt	Limestone	Gravel

113.4 μs at 20 °C; 72.62 μs at 400 °C; 49.5 μs at 650 °C; 39.4 μs at 800 °C; 148.5 μs at 950 °C for concretes B1 and B2; at 68.5 μs 20 °C, 72.65 μs at 200 °C, 139.65 μs at 400 °C, 129.65 μs at 600 °C, 307.55 μs at 800 °C for concrete L and 69.9 μs 20 °C, 54.07 μs at 200 °C, 77 μs at 400 °C, 124.37 μs at 600 °C, 141.59 μs at 800 °C for concrete G.

We develop the temperature dependence of the incubation time using a hybrid model of Eq. (11) for the derived range of characteristic times, on the basis of which the theoretical dependencies of strength on the strain rate were calculated in Fig. 2. Parameters for the theoretical temperature dependencies of characteristic time: (black curve, B1 and B2) τ_1 =380 μs, U_0=2374 kJ/mol, T_m=1773 K; τ_1=250 μs U_0 = 195.3 kJ/mol, T_m=1500 K (red curve, concrete L) and τ_1=250 μs U_0 = 30 kJ/mol, T_m=1300 K . The obtained values of the activation energy for concrete are close to the value U_0= 162.8 kJ/mol obtained in [18] for concrete. As shown in Fig. 3, the incubation time for concretes with limestone and gravel aggregate increases with temperature, whereas for concrete with basalt aggregate, it initially decreases up to 800 °C and then increases. Figure 3 shows that the incubation time for concretes with limestone and gravel aggregate increases with temperature, whereas for concrete with basalt aggregate, it initially decreases up to 800 °C, after which it begins to increase.

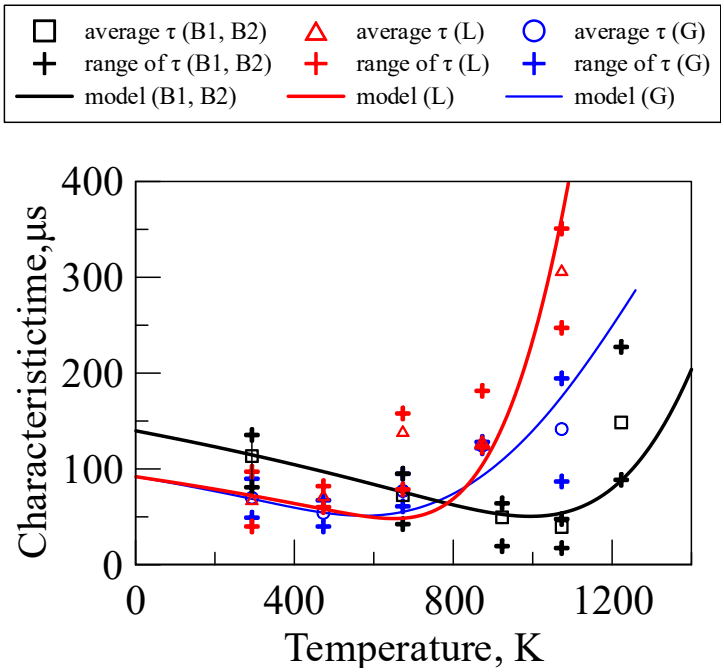

Fig. 3. Temperature dependencies of the characteristic time of concrete B1, B2, L and G

At high temperatures, the influence of inertial forces on the strength of the concrete is dominant, since the concrete structure has more cracks and an increased water content. The latter effect, combined with inertial forces, makes it possible to increase the characteristic and dynamic strength at the same time. The resulting effect is considered anomalous because the typical dependence at high temperatures is a decreasing function of relaxation time.

Conclusions

The rate dependences of concrete strength at different temperatures, plotted on experimental data by tests of concrete with basalt and limestone aggregate. were predicted based on the incubation time criterion. The proposed model accurately predicts the strength of concrete with limestone, gravel and basalt aggregates under varying temperature and loading rate conditions. Based on the incubation time criterion and the theoretical construct of thermofluctuation strength, two discrete temperature-dependent characteristic time functions were ascertained: one pertinent to concretes incorporating limestone and gravel aggregate and another specific to concrete with basalt aggregate. It is evinced by the inquiry that the influence of aggregate composition is exerted on both the velocity of dynamic strength enhancement and the characteristic relaxation time.

CRediT authorship contribution statement

Nina S. Selyutina: writing – review & editing, writing – original draft, the main idea, state of the problem, conceptualization, analysis of the result, hybrid model, supervision; **Diana D. Khairetdinova**: writing – original draft, analysis of the result, investigation.

Conflict of interest

The authors declare that they have no conflict of interest.

References

1. Su H, Xu J, Ren W. Experimental study on the dynamic compressive mechanical prop-erties of concrete at elevated temperature. *Materials & Design.* 2014;56: 579–588.
2. Li L, Zhang R, Jin L, Du X, Wu J, Duan W. Experimental study on dynamic compressive behavior of steel fiber reinforced concrete at elevated temperatures. *Construction and Building Materials.* 2019;210: 673–684.
3. Chen L, Fang Q, Jiang X, Ruan Z, Hong J. Combined effects of high temperature and high strain rate on normal weight concrete. *International Journal of Impact Engineering.* 2015;86: 40–56.
4. Ma Q, Guo R, Zhao Z, Lin Z, He K. Mechanical properties of concrete at high temperature - A review. *Construction and Building Materials.* 2015;93: 371–383.
5. Arioz O. Effects of elevated temperatures on properties of concrete. *Fire Safety Journal.* 2007;42(8): 516–522.
6. Pan Z, Sanjayan JG. Stress–strain behaviour and abrupt loss of stiffness of geopolymer at elevated temperatures. *Cement and Concrete Composites.* 2010;32(9): 657–664.
7. Selyutina NS, Petrov YuV. Dynamic strength and fracture of brittle materials under shock-wave loading. *Engineering Fracture Mechanics.* 2020;225: 106265.
8. Selyutina N, Smirnov I. Dynamic deformation and fracture of structured materials un-der high-rate loading. *Mechanics of Materials.* 2023;179: 104613.

9. Selyutina NS, Khairetdinova DD. Dynamic Fracture of Fibre-Reinforced Concrete Depending on the Shape and Material of the Reinforcing Fibre. *Journal of Dynamic Behavior of Materials.* 2025;11: 34–44.
10. Rudskoy AI, Bashkarev AY, Bessonova VY. Application of the thermofltuation theo-ry of strength to calculate the durability of adhesive joints on the example of granite-bitumen composites. In: *Systems Analysis in design and management: collection of scientific papers of the XXVI International scientific and practical conference, October 13-14, 2022*. 2022. p.507–520. (In Russian)
11. Revilla-Cuesta V, Hurtado-Alonso N, Manso-Morato J, Serrano-López R, Manso JM. Effects of temperature and moisture fluctuations for suitable use of raw-crushed wind-turbine blade in concrete. *Environmental Science and Pollution Research.* 2024;31(25): 37757–37776.
12. Kartashov EM. Advanced materials for extreme environments: Synthesis and characterization. *Fine Chemical Technologies.* 2021;16(6): 526–540.
13. Asadi I, Shafigh P, Hassan ZFBA, Mahyuddin NB, Thermal conductivity of concrete – A review. *Journal of Building Engineering.* 2018;20: 81–93.
14. Iskakbayev AI, Teltayev BB, Yestayev KZ, Abu BD. Long-term strength of asphalt concrete and its applications. *Construction and Building Materials.* 2020;244: 118325.
15. Ferronato N, Fuentes Sirpa RC, Guisbert Lizarazu EG, Conti F, Torretta V. Construction and demolition waste recycling in developing cities: management and cost analysis. *Environmental Science and Pollution Research.* 2023;30(9): 24377–24397.
16. Xu GT, Liu MJ, Xiang Y, Fu B. Valorization of macro fibers recycled from decom-missioned turbine blades as discrete reinforcement in concrete. *Journal of Cleaner Production.* 2022;379: 134550.
17. Xu J, Xiong W, Guo X, Lai T, Liu Y, Ying W. Properties of using excavated soil waste as fine and coarse aggregates in unfired clay bricks after dry-wet cycles. *Case Studies in Construction Materials.* 2022;17: e01471.
18. Çeçen F, Aktaş B, Özbayrak A. Decarbonization of the concrete railway sleeper pro-duction: bringing the low-dosage pozzolanic cement usage in the sleeper production via novel laminated CFRPU reinforcement technique. *Materials Today Sustainability.* 2023;23: 100455.
19. Li L, Yu H, Zhou S, Dao V, Chen M, Ji L, Benhelal E. Activation and utilization of tailings as CO_2 mineralization feedstock and supplementary cementitious materials: a critical review. *Materials Today Sustainability.* 2023;24: 100530.
20. Revilla-Cuesta V, Skaf M, Santamaría A, Espinosa AB, Ortega-López V. Self-compacting concrete with recycled concrete aggregate subjected to alternating-sign temperature variations: thermal strain and damage. *Case Studies in Construction Materials.* 2022;17: e01204.
21. Munoz Perez SP, Salazar Pretel TM, Villena Zapata LI. Mechanical properties of a soil improved with recycled demolition concrete for the construction of shallow foundations. *Materials Physics and Mechanics.* 2023;51(1): 168–178.
22. Beaucour AL, Pliya P, Faleschini F, Njinwoua R, Pellegrino C, Noumowé A. Influence of elevated temperature on properties of radiation shielding concrete with electric arc furnace slag as coarse aggregate. *Construction and Building Materials.* 2020;256: 119385.
23. Tariq KA, Rehman MU, Ghafran R, Kamran I, Haroon M. Physio-mechanical and thermal properties of concrete produced by partial replacement of sand with plastic fines. *Proceedings of the Pakistan Academy of Sciences: A.* 2021;57(3): 61–68.
24. Erofeev VT, Korotaev SA, Vatin NI. Deformation and Heat-Insulating Characteristics of Light Concrete on Porous Burned Binder Under Heating. *Materials Physics and Mechanics.* 2023;51(1): 33–41.
25. Petrov YV, Gruzdkov AA, Bratov VA. Structural-temporal theory of fracture as a multiscale process. *Phys Mesomech.* 2012;15: 232–237.
26. Petrov YV, Smirnov IV, Volkov GA, Abramian AK, Bragov AM, Verichev SN. Dynamic failure of dry and fully saturated limestone samples based on incubation time concept. *Journal of Rock Mechanics and Geotechnical Engineering.* 2017;9(1): 125–134.
27. Solov'eva YV, Starenchenko SV, Starenchenko VA. Energy of Activation of the Plastic Deformation of Ni_3Ge Single Crystals with Different Orientations of the Axis of Compression. *Bulletin of the Russian Academy of Sciences: Physics.* 2020;84: 1582–1585.
28. Goldenberg BG, Rakshun YV, Bugaev SV, Meshkov OI, Tsybulya SV. Designing a Technological Station for Synchrotron Radiation on the VEPP-4M. *Bulletin of the Russian Academy of Sciences: Physics.* 2019;83: 129–133.
29. Glebovskii PA, Petrov YV. Kinetic interpretation of the structural-time criterion for fracture. *Phys. Solid State.* 2004;46: 1051–1054.

30. Smirnov I, Konstantinov A. Evaluation of critical stresses for quasi-brittle materials at various loading rates. *Materials Physics and Mechanics.* 2020;44(2): 210–220.
31. Zhurkov SN. Kinetic Concept of the Strength of Solids. *Int J Fract.* 1965;1: 311–323.
32. Regel VR, Slutsker AI, Tomashevskiy EE. *Kinetic Nature of Solid Body Strength.* Moscow: Nauka; 1974. (In Russian)
33. Slutsker AI, Polikarpov YI, Vasil'eva KV. Determination of the activation energy for complicated relaxation processes. *Physics of the Solid State.* 2002;44: 1604-1610.
34. Gubach LS, Fisher EK. About the use of kinetic theory of solid bodies strength in investigation of asphalt concrete service life in conditions of low temperatures. In: *Efficiency Increase for the Use of Cement and Asphalt Concretes in Siberia. Interuniversity Collection.* 1979. p.3-9. (In Russian)
35. Nickolskiy YuE, Pisklin VM, Shestakov VN. About long-term strength of asphalt concrete within the interval of temperatures from 233 to 273 K. In: *Efficiency Increase for the Use of Cement and Asphalt Concretes in Siberia. Interuniversity Collection.* 1979. p.10–17. (In Russian)
36. Zhurkov SN. Kinetic concept of the strength of solids. *Int J Fract.* 1984;26: 295–307.
37. Suhir E, Kang SM. Boltzmann–Arrhenius–Zhurkov (BAZ) model in physics-of-materials problems. *Modern Physics Letters B.* 2013;27(13): 1330009.

MATERIALS PHYSICS AND MECHANICS RESEARCH ARTICLE

Submitted: July 30, 2025 **Revised: August 28, 2025** **Accepted: October , 2025**

Structural response of reinforced, steel fiber reinforced and prestressed geopolymer concrete beams subjected to transverse loading

T.Q.K. Lam [1] ✉, K.S. Sreekeshava [2], S. Kumar [3], C. Bhargavi [2], B.N. Skanda Kumar [2], G. Gayathri [2], Y.R. Suresh [2]

[1] Faculty of Civil Engineering, Mien Tay Construction University, Vinh Long, Vietnam

[2] Jyothy Institute of Technology, Affiliated to Visveswaraya Technological University, Belagavi, India

[3] Bureau veritas, Bangalore, India

✉ lamkhai@mtu.edu.vn

ABSTRACT

The workability of the geopolymer concrete mixes was evaluated in accordance with prevailing code of practice. Furthermore, regression analysis was carried out to establish correlations among the strength properties. Fly ash was considered as the primary binder, activated with NaOH and Na_2SiO_3 solutions. The beam mixes were selected based on trial combinations that achieved the highest compressive strength of 41.63 MPa at a water-fly ash ratio of 0.23. To investigate the structural performance, beams of generally reinforced, steel fiber reinforced and prestressed geopolymer concrete with comparable geometries were fabricated and tested under two-point loading. The results revealed that steel fiber reinforced and prestressed geopolymer concrete beams exhibited 14 and 32 % higher ultimate strength, respectively, as compared with generally reinforced geopolymer concrete beams. Moreover, beam stiffness improved by 22 % (steel fiber reinforced geopolymer concrete) and 25 % (prestressed geopolymer concrete). All the beam types satisfied serviceability limits, with deflections below the code-specified span/250 ratio at cracking load. Strain measurements indicated reductions of 10 % in steel fiber reinforced geopolymer concrete and 40 % in prestressed geopolymer concrete relative to generally reinforced geopolymer concrete, with maximum strains of 0.036 (steel fiber reinforced geopolymer concrete), 0.035 (prestressed geopolymer concrete) and 0.030 (generally reinforced geopolymer concrete). Ductility ratios were observed to improve by 6–7 % in both steel fiber reinforced geopolymer concrete and prestressed geopolymer concrete beams. Crack analysis revealed that the flexural failures were predominant in generally reinforced and steel fiber reinforced geopolymer concrete beams, while prestressed geopolymer concrete beams exhibited shear-dominated failures with diagonal tension cracks.

KEYWORDS

stiffness • geopolymer • deflection • polymerization • alkalinity

Citation: Lam TQK, Sreekeshava KS, Kumar S, Bhargavi C, Skanda Kumar BN, Gayathri G, Suresh YR. Structural response of reinforced, steel fiber reinforced and prestressed geopolymer concrete beams subjected to transverse loading. *Materials Physics and Mechanics*. 2025;53(5): 150–163.
http://dx.doi.org/10.18149/MPM.5352025_13

Introduction

The geopolymer concrete (GPC) is produced by blending geopolymer binders with certain aggregates. These binders are formed by chemically activating aluminosilicate rich-source materials using alkaline solutions. This leads to formation of polymeric structures with characteristics comparable to natural rocks [1]. Owing to their superior durability,

fire resistance, mechanical strength and strong adhesion between the aggregates and steel reinforcement, these binders have emerged as sustainable alternative to ordinary Portland cement (OPC) [2]. The increasing interest in GPC is attributed to its nature friendly properties, having potential to reduce carbon emissions, while delivering high performance structural properties [3].

Multiple industrial by-products such as fly-ash, silica fume, ground granulated blast furnace slag (GGBS), metakaolin, sawdust and rice husk ash have been considered as precursors in synthesis of geopolymers [4]. These source materials can be used individually or in combination, with mix proportions. The proportions are often selected through trial optimisation or based on past experimental evidence to meet structural performance requirements.

In this investigation, fly ash has been employed as primary binder, activated with a 14M NaOH solution and Na_2SiO_3 solution in the ratio of 1:2.5. Manufactured sand (M-sand) and crushed stone (10–12 mm) served as fine and coarse aggregates respectively. A polycarboxylate-based superplasticiser (Glenium 220R, BASF) was used at 2 % by weight of the binder to ensure adequate workability. It shall be not4ed that previous studies have shown that workability and strength of GPC are governed by water-geopolymer solid ratio, with strength generally increasing at lower water content [5,6]. Full strength maturity of GPC is typically achieved through thermal curing for 24 h at 65–70 °C [7].

The strength relationships of GPC are mostly compared with established standards for conventional concrete. For compressive-tensile correlations, ACI-318-08 [8] proposes $f_t = 0.59\sqrt{f_{ck}}$, while CIB-FIB [9] and Neville [10] suggest $f_t = 0.30\sqrt{f_{ck}}$ and $f_t = 0.23\sqrt{f_{ck}}$, respectively. Similarly for compressive-flexural correlations, IS 456-2000 [11], Aci-318 and BS 8110 [12] provide relationships such as $f_r = 0.70\sqrt{f_{ck}}$, $f_r = 0.62\sqrt{f_{ck}}$ and $f_r = 0.60\sqrt{f_{ck}}$. Although such empirical expressions exist for OPC-based systems, equivalent validated models for GPC-mainly when modified with fibers-remain limited.

Steel fibers, when randomly distributed in the matrix, arrest crack propagation and improve both post-cracking strength and ductility [13]. Research works have shown that, while the inclusion of fibers may moderately affect compressive strength with variations of about 3 at 0.25 % fiber content and 8 at 1 % [14], it significantly enhances flexural and tensile performance [15–17]. The load bearing capacity after cracking increases due to the bridging action of fibers, which alters the failure mechanism from brittle to ductile [18]. It must as well be noted that incorporating steel fibers reduces the workability of fresh concrete, necessitating optimisation of fiber volume based on trial data [19–22]. Correlation models for fiber-reinforced OPC concrete have as well been proposed [23–25], but their direct applicability to fiber reinforced GPC has not been comprehensively validated.

Although previous studies confirm the potential of GPC as a sustainable alternative to OPC and list out the beneficial role of steel fibers in improving tensile and flexural behaviour, limited research has been done on the comparative structural performance of generally reinforced (GR-GPC), steel fiber reinforced (SFR-GPC) and prestressed GPC (PS-GPC) beams under flexural loading. Further, the development of reliable correlation models to evaluate the strength parameters of fiber-reinforced GPC is still in its early stages. These gaps restrict the wider applications of GPC in structural members

requiring high ductility, stiffness and load carrying efficiency. This study hence aims to investigate and compare the mechanical and flexural performance of GR-GPC, SFR-GPC and PS-GPC beams and establish their suitability for structural applications.

Materials and Methods

Geopolymer concrete mixtures were prepared by varying the percentage of fly-ash as the primary binder. The workability of each mixture was evaluated in accordance with the relevant code of practice. Regression analysis was performed to establish correlation among the strength parameters. The mixture that achieved the maximum compressive strength was selected for fabrication of generally reinforced beams.

To study the effects of fiber, steel fiber reinforced GPC mixtures (SFR-GPC-M) were prepared by incorporating barying fiber volume fractions (0.5, 1 and 1.5 %) into the optimised GPC mixture. The SFR-GPC mixture that demonstrated the best performance in terms of compressive, tensile and flexural strength was chosen for beam casting. Prestressed beams (PS-GPC) and generally reinforced beams (GR-GPC) were also fabricated using optimised GPC-M.

To ensure a statistical reliability and minimise experimental error, three beams were cast and tested in each category (GR-GPC, SFR-GPC and PS-GPC). The sample size of three was chosen in line with common practice in structural experimental studies, where triplicate specimen provide sufficient reproducibility and allow for identification of outliers. All the beams were of identical dimensions, enabling direct comparisons.

The beams were subjected to a four-point bending test to examine flexural performance. Structural parameters such as cracking load, ultimate load, stiffness, ductility, strain distribution and crack pattens were recorded and analysed.

Basic material testing

The source material employed in this study was Class F fly ash sourced from Raichur Thermal Power Corporation Limited (RTPCL), Karnataka, India. The fly ash confirmed to IS 3812 2003 (part 1&2) [26]. Its chemical and physical properties are presented in Table 1. The scanning electron microscopy (SEM) image of the fly ash shown in Fig. 1.

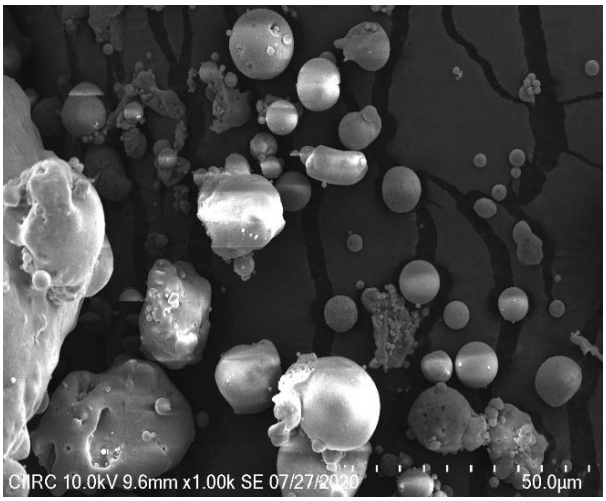

Fig. 1. Scanning electron microscopy image of fly ash (5000 Magnification)

Table 1. Attributes of fly ash

Sr. No	Details	Attributes
1	Relative density	2.08
2	Blain's air permeability, m^2/kg	329.00
3	Silicon Di Oxide (SiO_2), wt. %	63.01
4	Aluminium Oxide (Al_2O_3), wt. %	31.60
5	$SiO_2 + Al_2O_3 + Fe_2O_3$, wt. %	94.61

Laboratory grade sodium hydroxide (NaOH) flakes are used to prepare the alkaline solution. The physical and chemical properties are shown in Table 2. Alkaline liquid preparation involved the utilization of laboratory-grade sodium silicate (Na_2SiO_3). Its properties are summarized in Table 3. Steel fibers were produced from regular drawn steel wires cut into lengths. Their properties are given in Table 4.

Table 2. Attributes of sodium hydroxide

Sr. No	Description	Attributes
1	Appearance	Flake
2	Specific gravity	1.39
3	Sodium hydroxide, wt. %	97.4
4	Sodium carbonate, wt. %	1.6

Table 3. Attributes of sodium silicate

Sr. No	Description	Attributes
1	Flow	Viscous
2	Specific gravity	1.35
3	SiO_2, wt. %	58.25
4	Mg_2O, wt. %	8.10
5	Water content, wt. %	32.80

Table 4. Attributes of steel fibre

Sr. No	Description	Attributes
1	Dimensions, mm^2	36.00 × 0.60
2	Relative density	7.85
3	Elastic Modulus, GPa	200.00
4	Aspect ratio	60.00

A high-performance superplasticizers based on polycarboxylic ethers, marketed under the trade name Glenium 220R (BASF Construction Chemicals), was used in the trial mixes. The admixture confirms to IS 9103:1999 [27]. For improved workability, a dosageof 1–2 % by mass of fly ash was adopted.

Mix proportion and preparation of concrete

The density of GPC varies between 2350 to 2460 kN/m^3 [28]. Trial concrete mixes were formulated by adjusting the percentage of fly ash while maintaining a constant concrete density. The alkaline activator solution consisted of 14 M NaOH and Na_2SiO_3 prepared one day prior to mixing with fixed water content of 130 L/m^3 [29]. To maintain stability, the prepared NaOH solution was stored in air-tight, high-density polyethylene containers at room temperatures. This prevented carbonation and ensured consistency in molarity.

A polycarboxylate ether-based superplasticizer Glenium 220R was added in the range of 1–2 % by mass of fly ash to improve the workability. The mix proportions are presented in Table 5. Figure 2 presents the methodology of preparation and curing of GPC specimen including their casting, specimen after 24 h of setting and specimen arranged inside hot air curing chamber (HACC) for thermal c using at 65 °C for 24 h.

(a) (b) (c)

Fig. 2. Preparation and curing of geopolymer concrete specimens: (a) casting process showing the placement of fresh GPC into moulds in layers followed by compaction; (b) demoulded cube, cylinder, and prism specimens after 24 h of setting; (c) specimens arranged inside the hot air curing chamber (HACC) for thermal curing at 65 ºC for 24 h

Table 5. Mix proportions

Trials	Percentage of fly ash	*FA*, kg/m^3	*ca*, kg/m^3	*fa*, kg/m^3	NaOH, kg/m^3	Na_2SiO_3, kg/m^3	Water to fly ash ratio
GPC-M_1	15.5	314.6	991.72	779.03	89.82	224.4	0.41
GPC-M_2	17.2	356.58	968.4	760.6	89.82	224.41	0.36
GPC-M_3	19.1	398.29	944.08	742.7	89.82	224.4	0.32
GPC-M_4	21.3	439.03	921.4	721.8	89.82	224.4	0.29
GPC-M_5	23.1	479.83	898.6	704.66	89.82	224.4	0.27
GPC-M_6	25.2	522.42	873.12	682.2	89.82	224.4	0.24
GPC-M_7	27	563.16	851.56	667.4	89.82	224.4	0.23
GPC-M_8	29.3	606.57	828	650.59	89.82	224.4	0.21
GPC-M_9	30.9	645.48	804.4	636.3	89.82	224.4	0.18
FA is fly ash, ca is coarse aggregates, fa is fine aggregates							

Casting and curing of GPC

The fresh concrete mixtures as indicated in above Table 5 were poured into moulds following the mixing process. Cylindrical and cube specimens were formed in three layers, while prismatic specimens were formed in two layers. Each layer was compacted by applying manual strokes with a tamping bar and vibration on a vibrating table for 15 to 20 sec.

Following the casting process, the test specimens were covered with a polyethylene sheet, as illustrated in Fig. 2, in order to reduce water evaporation. For a period of 7 days, the specimen was allowed to rest [30]. Following a resting period, all specimens underwent temperature curing in a hot air curing chamber (HACC), as depicted in Fig. 2. Details regarding the arrangement, construction, performance, and technical specifications

of the HACC are elaborated elsewhere [31]. Curing of all specimens was conducted at 65 °C for a duration of 24 h [32]. Subsequently, the specimens were cooled at room temperature for 20 to 24 h prior to testing.

Mechanical strength of hardened concrete

The compressive, split tensile and flexural strengths of hardenend geopolymer concrete mixtures are summarized in Table 6 and further illustrated in Figs. 3 and 4. The compressive strength (f_c) was determined from cube specimen of 150 × 150 × 150 mm^3, the split tensile strength (f_t) from cylindrical specimen of height of 300 mm and diameter of 150 mm and the flexural strength (f_r) from prismatic specimen of size of 350 × 150 × 150 mm^3.

Table 6. Strength attributes of GPC-Mixtures

Mixtures	Strength in compression (f_c), MPa	Strength obtained from split tensile test (f_t), MPa	Strength obtained after transverse loading (f_r), MPa
GPC-M_1	24.45	2.35	3.62
GPC-M_2	28.52	2.46	3.98
GPC-M_3	30.48	3.17	4.10
GPC-M_4	33.78	3.58	4.32
GPC-M_5	36.43	3.97	4.78
GPC-M_6	37.78	4.32	5.12
GPC-M_7	41.63	4.44	5.60
GPC-M_8	35.64	3.88	4.76
GPC-M_9	29.15	3.01	4.21

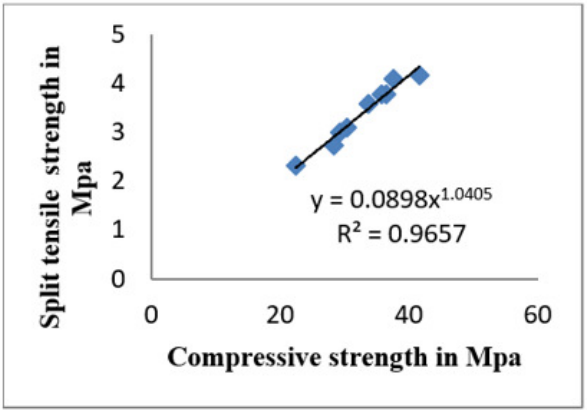

Fig. 3. Dependence strength obtained from split tensile test (f_t) on strength in compression (f_c)

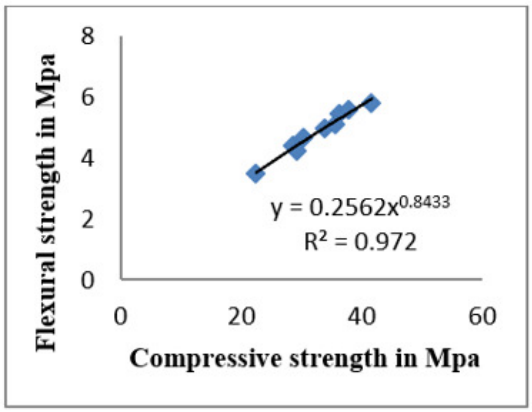

Fig. 4. Dependence strength obtained after transverse loading (f_r) on strength in compression (f_c)

The relationships between these concrete strengths were established through regression analysis, as illustrated in the equations:

$$f_t = 0.898 f_c^{1.040}, \quad (1)$$

$$f_r = 0.256 f_c^{0.843}. \quad (2)$$

The design with the largest flexural strength among the various mixtures was chosen for the production of fiber-reinforced Geopolymer concrete. The strength of fiber-reinforced concrete is influenced by various factors [33]. The selected type of fibers was added with selected mix GPC-M7 by varying volume fraction with selected aspect ratio of 60 [34]. The steel fiber added geopolymer concrete mixtures (SF-GPC-M) are depicted

in Table 7. The correlation of strength parameters f_{tf} and f_{rf} of SF-GPC-M, mixtures on fibre fraction V_f are illustrated in Figs. 5 and 6.

Table 7. Attributes of strength of SF-GPC-Mixtures

Mixtures	Fiber volume fraction (V_f), %	Compressive strength (f_{cf}), MPa	Split tensile strength (f_{tf}), MPa	Flexural strength (f_{rf}), MPa
SF – GPC - M_1	0.3	35.40	5.38	5.46
SF – GPC - M_2	0.34	33.92	5.65	5.61
SF – GPC - M_3	0.5	33.15	5.75	5.85
SF – GPC - M_4	0.8	32.54	5.15	6.06
SF – GPC - M_5	1.0	30.95	6.01	6.13
SF – GPC - M_6	1.2	30.18	5.25	6.33
SF – GPC - M_7	1.4	29.48	5.12	5.93

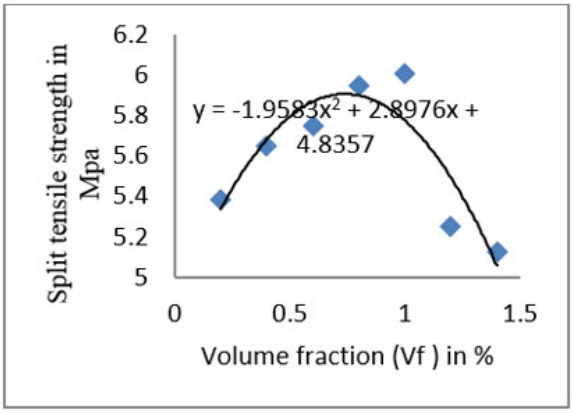

Fig. 5. Dependence split tensile strength (f_{tf}) on fiber volume fraction (V_f)

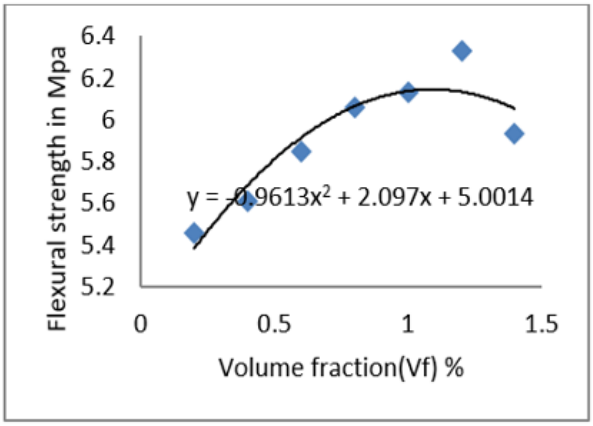

Fig. 6. Dependence flexural strength (f_{rf}) on fiber volume fraction (V_f)

The correlation of strength parameters f_{tf} and f_{rf} of SF-GPC-M mixtures on f_{cf} are illustrated in Figs. 7 and 8 respectively. The compressive strength, flexural strength and split tensile stength of SF-GPC-M mixtures over GPC-M_7 mix indicated in Figs. 9–11, respectively.

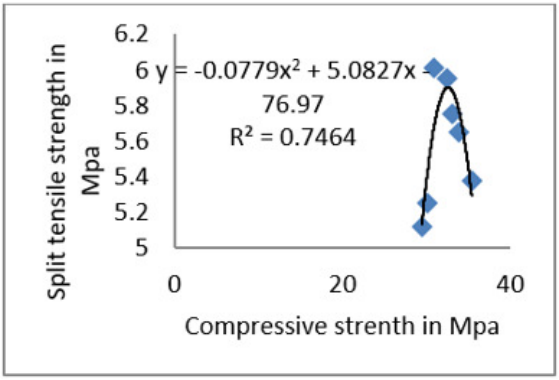

Fig. 7. Dependence split tensile strength (f_{tf}) on compressive strength (f_{cf})

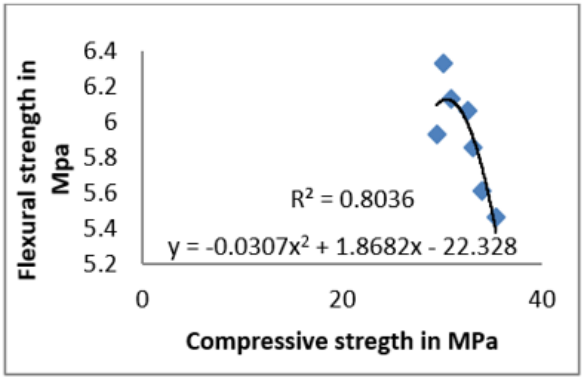

Fig. 8. Dependence flexural strength (f_{rf}) on compressive strength (f_{cf})

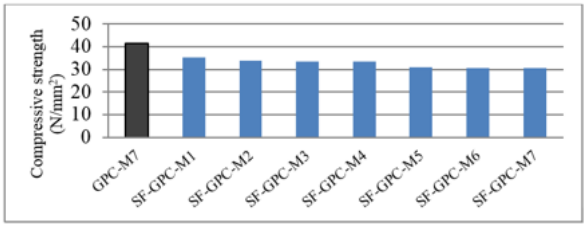

Fig. 9. Compressive strength of steel fiber-geopolymer concrete mixes over geopolymer concrete-M_7

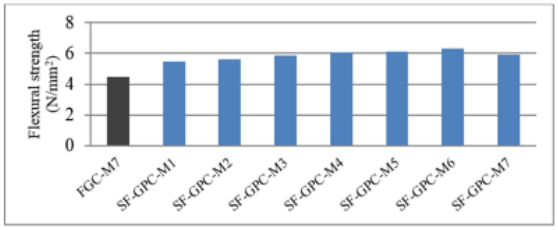

Fig. 10. Flexural strength of steel fiber-geopolymer concrete mixes over geopolymer concrete-M_7

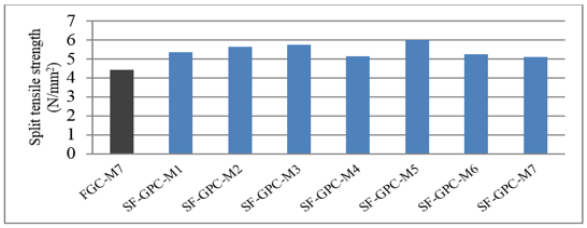

Fig. 11. Split-tensile strength of steel fiber-geopolymer concrete mixes over geopolymer concrete-M_7

Mechanical strength of steel fiber-GPC-mixtures with aspect ratio of 60 is shown in the equations:

$$f_{tf} = -1.95{V_f}^2 + 2.89V_f + 4.83, \quad (3)$$

$$f_{rf} = -0.961{V_f}^2 + 2.10V_f + 5.0, \quad (4)$$

$$f_{tf} = -0.078{f_{cf}}^2 + 5.1f_{cf} - 77.0, \quad (5)$$

$$f_{rf} = -0.030{f_{cf}}^2 + 1.86f_{cf} - 22.0\,. \quad (6)$$

Manufacturing of beams

The mix, FGC-M7 was selected due to optimum compressive strength and as well as flexural strength for manufacturing of GR-GPC and PS-GPC beams. The mix SF-GPC-M6 with volume fraction of 1.2 % was selected for SFR-GPC beam due to higher flexural strength among the mixes. All the aforesaid types of the beams were manufactured with same size. Figure 12 illustrates the dimensions of the beam and reinforcement details for Generally Reinforced-GPC and Steel Fiber Reinforced-GPC beams. The form work arrangements for beam were prepared for afore said types of beams as indicated in Fig. 13. The reinforcements were placed in the form work shown Fig. 14.

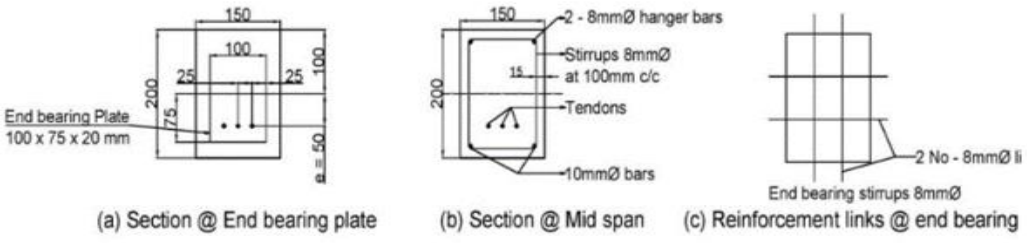

Fig. 12. GR-GPC and SFR-GPC beams reinforcement

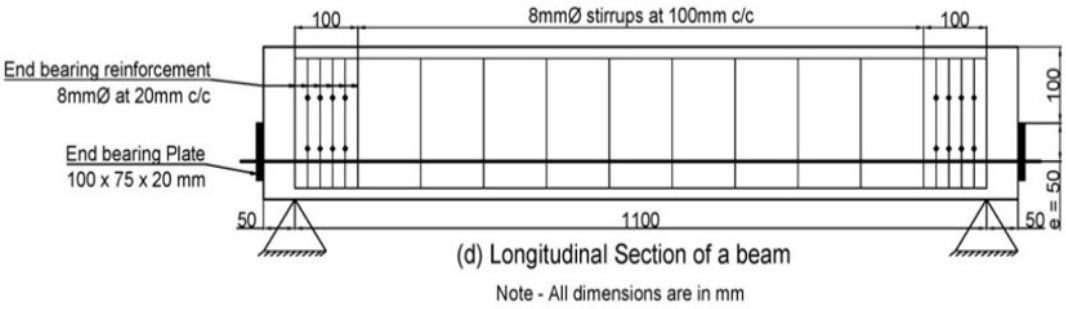

Fig. 13. Reinforcement detailing for PS-GPC beams

Fig. 14. Formwork arrangement

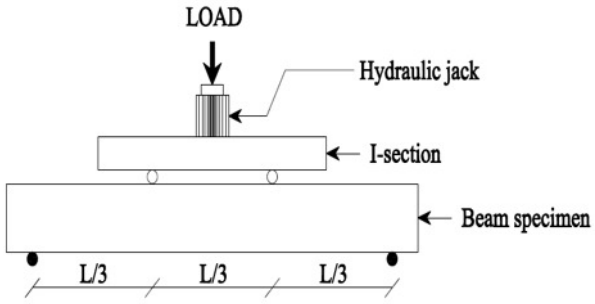

Fig. 15. Schematic of two-point loading

The concrete preparation process was conducted as detailed in the next section. Fibers were introduced into the mixer machine after blending the fine and coarse aggregates, but prior to incorporating fly ash to prepare the SF-GPC mixtures. Concrete was poured where each layer of concrete was compacted by using tamping rod. The concrete surface was leveled properly by using straight edge. A flexible PVC tube with a diameter of 10 mm was utilized as a sheathing, positioned at a specified eccentricity to accommodate the tendons. Proper care has been taken to avoid the concrete passing into the duct or sheathing of PS-GPC beams while placing and compacting the concrete in the form work. Manufactured beams were kept for three days as the rest period and temperature cured at 65 ºC for 24 h in HACC.

Post tensioning operation

The high strength steel tendons diameter of 7 mm was used to transfer the prestressing force. The barrel and wedges were used to anchor the tendons over the mild steel bearing plate. To withstand the bursting force generated during the post-tensioning process, bearing plates or end plates measuring 100 × 75 × 20 mm^3 were employed. After the temperature curing process, the beams were removed from the high alumina cement concrete (HACC), and the tendons were inserted into the duct. The prestress staple gun of 40 tonnes capacity was used to transfer the tension force in tendons. The required amount of prestress force of 35 kN is transferred to tendons and anchored with barrels and wedges. The details of top and bottom reinforcement (non-prestressed steel) are similar for all types of the beam as shown in reinforcement detail. The effect of non prestressing steel is not discussed in these investigations.

Beams testing

All beams underwent testing using the two-point loading method. The loading process is as depicted in Figs. 15 and 16. The beams were supported on a loading frame with a capacity of 50 tonnes, and the load was incrementally applied. The beam deflection was measured. Demountable mechanical gauges, with a gauge length of 200 mm and capable of measuring up to 8 microstrains, were used, as shown in Fig. 17. Cracks in the beam were marked and observed, as illustrated in Fig. 18.

Fig. 16. Test setups for beam

Fig. 17. Strain measurement at 0.42 x_u

Fig. 18. Marking of cracks

Results and Discussion

The experimental test outcomes averaged are given in Table 8. The load versus deflection at the centre of the span are presented in the graph, shown in Fig. 19. The strain measured at the depth of 0.42 x_u shown in Fig. 20. The comparison of load–deflection and load–strain responses (Figs. 19 and 20) indicates that PS-GPC consistently exhibited superior performance compared to SFR-GPC and GR-GPC. The peak load of PS-GPC was about 20–25 % higher than SFR-GPC and 35–40 % higher than GR-GPC, while SFR-GPC showed an improvement of 10–15 % over GR-GPC. In terms of deformation characteristics, PS-GPC sustained nearly 15–20 % higher deflection and 20–25 % higher strain than SFR-GPC, and 25–35 % higher deflection and 30–35 % higher strain than

Table 8. Experimental test results

Beam	Average peak load, kN	Deflection Δ_y, mm	Stiffness, kN/m	Intial crack strain	Failure load, kN	Ultimate load deflection Δ_u, mm	Failure strain	Ratio of ductility Δ_u/Δ_y
GR-GPC	47	3.25	14.46	0.010	74	10.45	0.030	3.21
SFR-GPC	55	3.08	17.85	0.009	86	10.25	0.035	3.37
PS-GPC	68.6	3.52	19.48	0.006	100	12.03	0.036	3.41

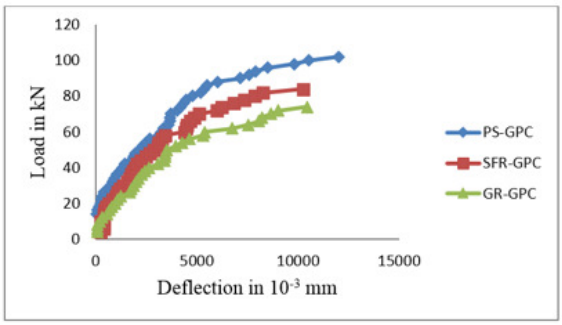

Fig. 19. Comparison of load versus deflection

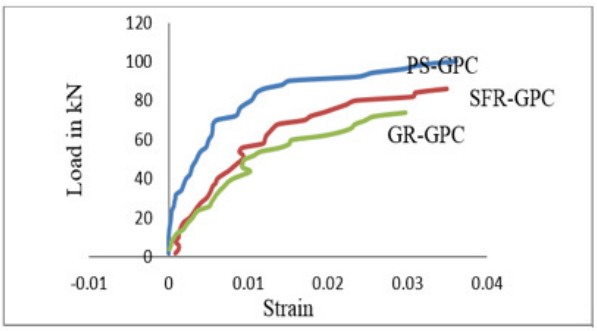

Fig. 20. Load versus strain at 0.42 x_u depth

GR-GPC. These variations clearly demonstrate that the incorporation of precipitated silica significantly enhances both load-carrying capacity and ductility of geopolymer concrete, followed by steel fiber reinforcement, whereas glass reinforcement resulted in relatively lower improvements.

The observed crack patterns (Figs. 21–23) highlight distinct modes of failure among the GR-GPC, SFR-GPC, and PS-GPC beams. In GR-GPC beams (Fig. 21), flexural cracks initiated at the tension face and propagated vertically towards the compression zone, indicating a typical brittle flexural failure with limited energy absorption. In contrast, SFR-GPC beams (Fig. 22) exhibited enhanced tenacity, as the presence of steel fibers enabled gradual dissipation of energy through multiple fine cracks. This crack-bridging effect delayed the localization of damage and improved ductility compared to GR-GPC. On the other hand, PS-GPC beams (Fig. 23) carried higher loads but developed sudden, wider cracks beyond the limiting yield stresses of the bottom layers. The failure mode in these beams was characterized by combined shear-flexural cracking, demonstrating the higher stiffness of the matrix but reduced crack control in comparison with fiber-reinforced counterparts. Overall, flexural failure dominated in GR-GPC and SFR-GPC beams, while PS-GPC beams exhibited a shear-flexural failure mode.

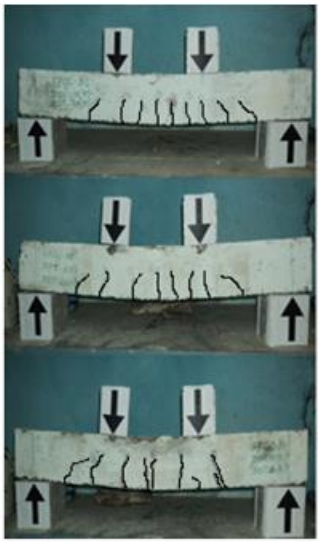

Fig. 21. Pattern of failure of GR-GPC beam

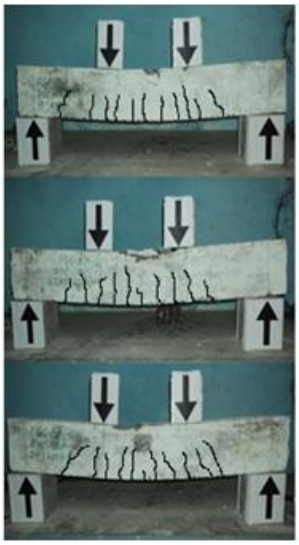

Fig. 22. Pattern of failure of SFR-GPC beams

Fig. 23. Pattern of failure of PS-GPC beams

Conclusions

Based on the experimental investigation on generally reinforced (GR-GPC), steel fiber reinforced (SFR-GPC), and pre-stressed (PS-GPC) geopolymer concrete beams, the following conclusions can be drawn:

1. SFR-GPC and PS-GPC beams achieved approximately 14 and 32 % higher peak load capacity, respectively, compared to GR-GPC beams.
2. The stiffness of SFR-GPC and PS-GPC beams was found to be 22 and 25 % higher, respectively, than that of GR-GPC beams.
3. All beam types exhibited deflections within the permissible limits specified by the Span/250 ratio under elastic conditions, up to or just before the onset of cracking.
4. At maximum load in the elastic region, SFR-GPC and PS-GPC beams recorded approximately 10 and 40 % lower strain values, respectively, than GR-GPC beams. The maximum strain values observed were 0.036 for SFR-GPC, 0.035 for PS-GPC, and 0.030 for GR-GPC beams.
5. Both SFR-GPC and PS-GPC beams demonstrated improved ductility, with ductility ratios of 6–7 % higher than GR-GPC beams.
6. GR-GPC and SFR-GPC beams exhibited predominantly flexural cracking, although SFR-GPC showed a greater number of finer cracks due to the crack-bridging action of fibers. In contrast, PS-GPC beams displayed combined shear-flexural failure, with diagonal tension cracks indicating the dominance of shear in the failure mechanism.

Overall, the study demonstrates that the incorporation of steel fibers and the use of pre-stressing significantly enhance the structural performance of geopolymer concrete beams in terms of strength, stiffness, ductility, and crack control. These findings support the application of advanced geopolymer composites in structural elements, contributing to the development of more durable and sustainable infrastructure.

CRediT authorship contribution statement

T.Q.K. Lam: writing – review & editing, writing – original draft; **K.S. Sreekeshava**: conceptualization, original draft; **S. Kumar**: supervision, investigation and conceptualization; **C. Bhargavi**: writing-review and editing, investigation; **B.N. Skanda Kumar:** visualization, testing; **G. Gayathri**: review and editing, supervision; **Y.R. Suresh**: supervision, investigation and data curation.

Conflict of interest

The authors declare that they have no conflict of interest.

References

1. Davidovits J. Geopolymers. *Journal of Thermal Analysis.* 1991;37(8): 1633–1656.
2. Lloyd N, Rangan BV. Geopolymer concrete with Fly Ash. In: Zachar J, Claisse P, Naik TR, Ganjian E. (eds.) *Proceedings of the Second International Conference on Sustainable Construction Materials and Technologies, 28–30 June 2010, Ancona, Italy.* UWM Center for By-Products Utilization; 2010. p.1493–14504.
3. Nair A, Aditya SD, Adarsh RN, Nandan M, Dharek MS, Sreedhara BM, Prashant SC, Sreekeshava KS. Additive Manufacturing of Concrete: Challenges and opportunities. *IOP Conference Series: Materials Science and Engineering.* 2020;814: 012022.

4. Nuruddin MF, Malkawi AB, Fauzi A, Mohammed BS, Al-Mattarneh HM. Geopolymer concrete for structural use: Recent findings and limitations. *IOP Conference Series: Materials Science and Engineering.* 2016;133: 012021.
5. Anilkumar S, Sreekeshava KS, Bhargavi C. Studies on Optimization of Fly Ash, GGBS and Precipitated Silica in Geopolymer Concrete. *Construction Materials.* 2025;5(2): 29.
6. Rangnath RV, Saleh M. Some optimal values in Geopolymer concrete incorporating fly ash. *Indian Concrete Journal.* 2008;82(10): 26–35.
7. Hardjito D, Rangan BV. *Development and properties of low-calcium fly ash-based Geopolymer concrete.* Faculty of Engineering Curtin University of Technology. Research Report GC 1, 2005.
8. ACI Committee 318. *Building Code Requirements for Structural Concrete and Commentary.* American Concrete Institute; 2008.
9. Comité Euro-International du Béton (CEB). *Evaluation of the Time Dependent Behaviour of Concrete.* Lausanne: CEB; 1991. Bulletin No. 199.
10. Neville AM. *Properties of Concrete.* 4th ed. Essex: Longman Group Ltd.; 1995.
11. Indian Standards. IS 456:2000. *Indian Standard Code of Practice for Plain and Reinforced Cement Concrete.* New Delhi: Bureau of Indian Standards; 2000.
12. British Standards Institution. BS 8110-1:1985. *British Standard Structural Use of Concrete: Code of Practice for Design and Construction.* London: British Standards Institution; 1985.
13. Bencardino F, Rizzuti L, Spadea G, Swamy RN. Stress-Strain Behavior of Steel Fiber-Reinforced Concrete in Compression. *Journal of Materials in Civil Engineering.* 2008;20(3): 255–263.
14. Ganesan N, Indira PV, Santhakumar A. Engineering properties of steel fibre reinforced geopolymer concrete. *Advances in Concrete Construction.* 2013;1(4): 305–318.
15. Song PS, Hwang S. Mechanical properties of high-strength steel fiber-reinforced concrete. *Construction and Building Materials.* 2004;18(9): 669–673.
16. Bernal S, de Gutierrez R, Delvasto S, Rodriguez E. Performance of Geopolymeric Concrete Reinforced with Steel Fibers. In: *Proceedings of the 10th Inorganic-Bonded Fiber Composite Conference (IIBCC 2006), 15-18 November 2006, Sao Paulo, Brazil.* New-York: Curran Associates, Inc.; 2006. p.220–232.
17. Kumar S, Rajendra S, Sreekeshava KS. Assessment of the shear strength of fly ash-based geopolymer concrete. In: Vinyas M, Loja A, Reddy KR. (eds.) *Advances in Structures, Systems and Materials. Lecture Notes on Multidisciplinary Industrial Engineering.* Singapore: Springer; 2020. p.277–286.
18. Al-Majidi MH, Lampropoulos A, Cundy AB. Steel fibre reinforced geopolymer concrete (SFRGC) with improved microstructure and enhanced fibre-matrix interfacial properties. *Construction and Building Materials.* 2017;139: 286–307.
19. Ramadoss P, Nagamani K. Investigation on the tensile strength of high-performance fiber reinforced concrete using statistical methods. *Computers and Concrete.* 2006;3(6): 389–400.
20. Mohammadi Y, Singh SP, Kaushik SK. Properties of steel fibrous concrete containing mixed fibres in fresh and hardened state. *Construction and Building Materials.* 2008;22(5): 956–965.
21. Bisht M, Iqbal MA, Kamran K, Bratov V, Morozov NF. Numerical study of thin UHPC targets response against ballistic impact. *Materials Physics and Mechanics.* 2022;50(1): 74–88.
22. Erofeev VT, Korotaev SA, Vatin NI. Deformation and Heat-Insulating Characteristics of Light Concrete on Porous Burned Binder Under Heating. *Materials Physics and Mechanics.* 2023;51(1): 33–41.
23. Xu B, Shi HS. Correlations among mechanical properties of steel fiber reinforced concrete. *Construction and Building Materials.* 2009;23(12): 3468–3474.
24. Hueste MBD, Chompreda P, Trejo D, Cline DBH, Keating PB. Mechanical properties of high-strength concrete for prestressed members. *ACI Structural Journal.* 2004;101(4): 457–465.
25. Thomas J, Ramaswamy A. Mechanical Properties of Steel Fiber-Reinforced Concrete. *Journal of Materials in Civil Engineering.* 2007;19(5): 385–392.
26. Indian Standards. IS 3812-1:2003. *Indian Standard Specification for Pulverized Fuel Ash.* New Delhi: Bureau of Indian Standards; 2003.
27. Indian Standards. IS 9103:1999. *Indian Standard Concrete Admixtures — Specification.* New Delhi: Bureau of Indian Standards; 1999.
28. Bhargavi C, Sreekeshava KS, Sunagar P, Dharek MS, Ganesh CR. Mechanical Properties of Steel and PolypropyleneFiber Reinforced Geopolymer Concrete. *Journal of Mines, Metals and Fuels.* 2023;71(7): 984–989.
29. Hardjito D, Wallah SE, Sumajouw DMJ, Rangan BV. On the development of fly ash-based geopolymer concrete. *ACI Materials Journal.* 2004;101: 467–472.

30. Pradeepa J, Kumar S, Ravindra PM. Cost-effective curing arrangement for geopolymer concrete specimens. *International Journal of Emerging trends in Engineering and Development.* 2012;2(7): 227–233.
31. van Jaarsveld JGS, van Deventer JSJ, Lukey GC. The effect of composition and temperature on the properties of fly ash and kaolinite-based Geopolymers. *Chemical Engineering Journal.* 2002;89(1-3): 63–73.
32. Karunanithi S, Anandan S. Flexural Toughness Properties of Reinforced Steel Fibre Incorporated Alkali Activated Slag Concrete. *Advances in Civil Engineering.* 2014; 2014(1): 719436.
33 Li Z, Zhang Y, Zhou X. Short Fiber Reinforced Geopolymer Composites Manufactured by Extrusion. *Journal of Materials in Civil Engineering.* 2005;17(6): 624–631.
34. Kumar S, Pradeepa J, Ravindra PM, Rajenda S. Experimental approach to study the properties of fiber reinforced fly ash based geopolymer concrete. *International Journal of Informative & Futuristic Research.* 2015;2(8): 2625–2635.

MATERIALS PHYSICS AND MECHANICS RESEARCH ARTICLE

Submitted: June 29, 2025 Revised: September 1, 2025 Accepted: November 12, 2025

Concrete column performance enhanced by 3D-printed honeycomb, chiral auxetic, and re-entrant lattices via FDM and DLP methods

M. Hematibahar [1], R.S. Fediuk [2,3]✉, N.I. Vatin [4], A. Milani [5], A. Tahmasebi [5], O. Kordi [5], M. Kharun [6], G.R. Fediuk [2], A.O. Shangutov [7], Y.K. Gitman [8]

[1] Department of Architecture, Restoration and Design, RUDN University, Moscow, Russia

[2] Far Eastern Federal University, Vladivostok, Russia

[3] Vladivostok State University, Vladivostok, Russia

[4] Peter the Great St. Petersburg Polytechnic University, St. Petersburg, Russia

[5] Tarbiat Modares University, Tehran, Iran

[6] Moscow State University of Civil Engineering, Moscow, Russia

[7] Perm Military Institute of the National Guard Troops of the Russian Federation, Perm, Russia

[8] Perm State Humanitarian Pedagogical University, Perm, Russian Federation

✉ roman44@yandex.ru

ABSTRACT

This study addresses a gap in the literature by investigating the reinforcement of mini-columns with 3D-printed lattice structures to improve the mechanical performance of cementitious materials for structural applications. Three reinforcement patterns honeycomb, re-entrant auxetic, and chiral auxetic were designed and fabricated using two additive manufacturing methods: fused deposition modeling (FDM) and digital light processing (DLP). Polylactic acid was used for FDM, and photopolymer resin for DLP printing. Each pattern was printed in both cylindrical and hyperboloid geometries and embedded into concrete mini-columns. The objective was to evaluate their influence on compressive strength, flexural behavior, and strain performance. Testing, including ultrasonic pulse velocity, was conducted to assess internal integrity. Results show that the type, placement, and geometry of the reinforcement significantly influenced mechanical performance, with DLP-printed structures providing higher resolution and improved interfacial bonding. Among the patterns, the re-entrant auxetic geometry yielded the highest enhancement in compressive strength up to 18 % compared to unreinforced samples, demonstrating the potential of auxetic designs in structural reinforcement.

KEYWORDS

fused deposition modeling • digital light processing • auxetic structure • spent coffee grounds • peanut shell

Funding. *This research was funded by the Ministry of Science and Higher Education of the Russian Federation within the framework of the state assignment No 075-03-2025-256 dated 16 January 2025, Additional agreement No 075-03-2025-256/1 dated 25 March 2025, FSEG-2025-0008.*

Citation: Hematibahar M, Fediuk RS, Vatin NI, Milani A, Tahmasebi A, Kordi O, Kharun M, Fediuk GR, Shangutov AO, Gitman YK. Concrete column performance enhanced by 3D-printed honeycomb, chiral auxetic, and re-entrant lattices via FDM and DLP methods. *Materials Physics and Mechanics*. 2025;53(5): 164–180. http://dx.doi.org/10.18149/MPM.5352025_14

Introduction

There are different types of reinforced concrete and cementitious materials with fibers, rebar, and other materials [1–4]. There is a new way to reinforce concrete via 3D-printing (3DPRC) [5]. To understand the scope of this field, Wan et al. [6] used a 3D-printed

reinforcement in water, so that when the beam breaks, the self-healing material can repair the concrete. Another example is the 3DPRC under flexural cyclic loading; they found that the maximum crack width was 20–80 μm [7]. Other samples investigated the auxetic cementitious composites (ACCs). They used reinforced cementitious materials with four types of auxetic patterns: "re-entrant" (RE), "rotating-square" (RS), "chiral" (CR), and "missing-rib" (MR). They understand RE has 853 % highest ductility. Moreover, if the water-to-binder ratio decreased from 0.4 to 0.3, then the compressive strength increased by more than 18.5 % [8]. Salazar et al. [9] reinforced an ultra-high-performance concrete (UHPC) beam with a 3D printed lattice. It has been observed that certain types of ultra-high-performance concrete (UHPC) reinforced with 3D-printed lattice structures exhibit higher compressive and flexural strengths than other samples. The literature review aims to present the current state of 3D-printed reinforced concrete (3PRC) technology. Although still emerging, this technology shows significant potential for enhancing performance in both civil engineering and materials science applications. At the same time, substantial efforts have been directed toward optimizing its structural performance and fabrication processes.

To find the best pattern and shape for a concrete beam, Hematibahar et al. [10] first added a hyperboloid structure to concrete to determine its compressive, tensile, and flexural strengths. They found that the hyperboloid shell structure cannot affect tensile strength; however, it does affect concrete strain. Later, the concrete beam was optimized using various 3D-printed truss types. They printed four types of trusses (Pratt, Howe, Warren, and Warren with vertical members) with the fused deposition modeling (FDM) technique. Reinforced concrete with a 3D-printed Warren truss increased in flexural strength by more than 18 %. Although the flexural strength of the beam increased with the addition of Warren trusses to concrete, the strain condition was strain-softening [11]. Finally, Hematibahar et al. [12] find optimized strain-hardening 3DPRC. They reinforced cementitious materials with honeycomb, 3D honeycomb, grid, and triangle at different distances from the bottom of the cementitious beam. Overall, they found that although the triangle and 3D-printed reinforced cementitious improved flexural strength more than the control sample, the Honeycomb pattern increased the beam's flexural strength and changed the reinforced cementitious's strain behavior to strain-hardening. Therefore, pattern, distance, and placement method are the best ways to choose the real pattern. Most studies focused on changing the concrete bearing and capacity in "concrete or cementitious beam". For example, Xu et al. [13] analyzed different types of 3D-printed reinforced concrete with a mesh pattern under three-point bending of a concrete beam. In another example, Meng et al. [14] investigated a special geometry with auxetic behavior in both in-plane and out-of-plane directions, resulting in a 1.7 times higher compaction energy than that of conventional cement-based materials. Finally, the current research focused on improving the compressive and flexural strength of concrete beams, either by creating new theories or by filling scientific gaps. To fill the gap of previous studies, this paper decides to reinforced the mini column for the first time after optimize the pattern and distance in the cementitious beam.

This article endeavors to reinforce the cementitious beam using four three-pattern types (honeycomb, re-entering auxetic (RE), chiral auxetic (CA). This study aims to conduct extensive research on cyclic loading, reinforced beams, and tension beams. Also, the

current study aimed to examine mechanical properties, including compression testing for each reinforced type, and to conduct nondestructive tests.

Material and Methods

Materials

Table 1 illustrates the mixture design of the concrete samples used in this study. The components were cement, water, marble powder, straw powder, microsilica, and superplasticizer (SP). Table 2 presents the microsilica chemical composition derived from X-ray fluorescence (XRF) analysis. This analysis was examined using a Philips PW 2404 device.

Table 1. Mixture design for samples in this study (kg/m^3)

Cement	Water	Marble powder	Straw powder	Microsilica	SP
500	154	1400	100	100	12.32

Table 2. Microsilica chemical composition (wt. %).

SiO_2	91.55
Al_2O_3	1.024
K_2O	1.73
MgO	1.02
Na_2O	0.52
Fe_2O_3	0.59
CaO	0.45
SO_3	0.35
P_2O_3	0.14
Cl	0.105
MnO	0.074
Zn	0.014
Pb	0.009
Rb	0.005
Sr	0.005
Cu	0.003
Ga	0.002
L.O.I	2.37

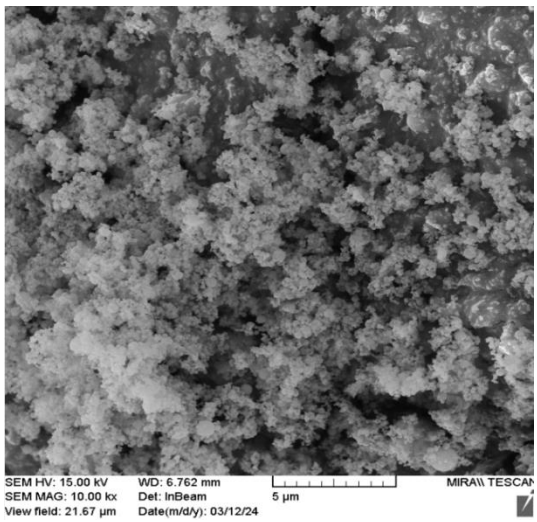

Fig. 1. Scanning electron microscopy (SEM) image of microsilica microstructure

Marble powder can help mitigate many environmental hazards, such as air pollution [15]. In addition, 10 % of marble added to cementitious materials increases the compressive strength [16] (Fig. 1). Microsilica (silica fume) can increase the calcium silicate hydrate (CSH) formation process in the hydration time. For example, some studies added silica fume to cement and found that it can improve concrete compressive strength by rapidly increasing CSH formation [17]. In another experiment, Shooshpasha et al. [18] found that silica fume can fill voids in cement paste and increase the material's durability. Superplasticizer can reduce water content and improve the mechanical properties of concrete [19]. SP affected the concrete compressive strength and other mechanical properties [20].

Methods

Etymology. In this project, researchers aim to test a new engineering method that will make it easier for engineers to build columns in the future. Hence, this team introduced this technology to the world for the first time and selected the name "Sotun" for it. "Sotun" is the Persian translation of "column" in English. Since it is difficult to repeat the "Sotun" word, the project will be called STN.

FDM and DLP methods. There are two types of 3D primary samples, using FDM (fused deposition modeling) and DLP (digital light processing). DLP enables the automated production of customized 3D parts using digital models. This technology has played an important role in industries such as aerospace, medicine, design, and engineering over the past 40 years. High accuracy in DLP can be achieved by selecting appropriate process parameters (such as layer thickness, printing direction, curing time and temperature, and laser power) and suitable materials. This study investigates the effects of these parameters on mechanical properties, including tensile strength, hardness, and surface roughness [21]. DLP is a precision 3D printing technology that uses an ultraviolet (UV) laser to solidify a liquid photopolymer resin layer by layer (Table 3). This process causes localized polymerization and the formation of complex structures by controlled laser irradiation into the resin reservoir. DLP is particularly used in the production of prototypes and industrial parts due to its high precision and excellent surface finish. Parameters such as laser power, layer thickness, and curing temperature directly affect the quality of the final product [22].

Table 3. Parameters of 3D-printed samples for DLP method

Printing resolution, mm	Infill, %	Exposure time, s
0.05	100	2.5

Rapid prototyping is done with technologies such as 3D printing and additive manufacturing. In additive manufacturing, materials are layered on top of each other to create the final product. One of the most widely used methods in this field is FDM, in which the selection of process parameters, such as temperature and speed, directly affects the quality of the manufactured parts. This method is expanding day by day across industries and research, especially in PLA-based applications, due to its advantages such as low cost, high quality, and short production time [23].

3D-printed samples were fabricated using Quantum 3D printer with the following printing parameters: nozzle diameter of 0.4 mm, raster width of 0.6 mm, layer height of 0.3 mm, and 100 % infill (Table 4). Creality PLA+ filament was used for all prints. Due to the complexity of the sample geometries, extensive support structures were required during printing and were carefully removed afterward. The samples consisted of two general shapes: cylindrical and hyperboloid cylinders with a 5-degree angle from the vertical axis. Each shape featured three different wall patterns: honeycomb, chiral auxetic, and re-entrant.

Table 4. Parameters of 3D-printed samples for FDM method

Nozzle diameter, mm	Printing speed, mm/s	Layer height, mm	Infill, %	Raster diameter, mm
0.4	30	0.3	100	0.6

3D-printing pattern. In this study, three types of reinforcement patterns, honeycomb (HC), re-entrant auxetic (RE), and chiral auxetic (CA) were used to fabricate mini columns via 3D-printing. Each pattern was designed in both cylindrical and hyperboloid geometries. Figure 2 illustrates the pattern types, their geometrical configurations, and the corresponding printed structures.

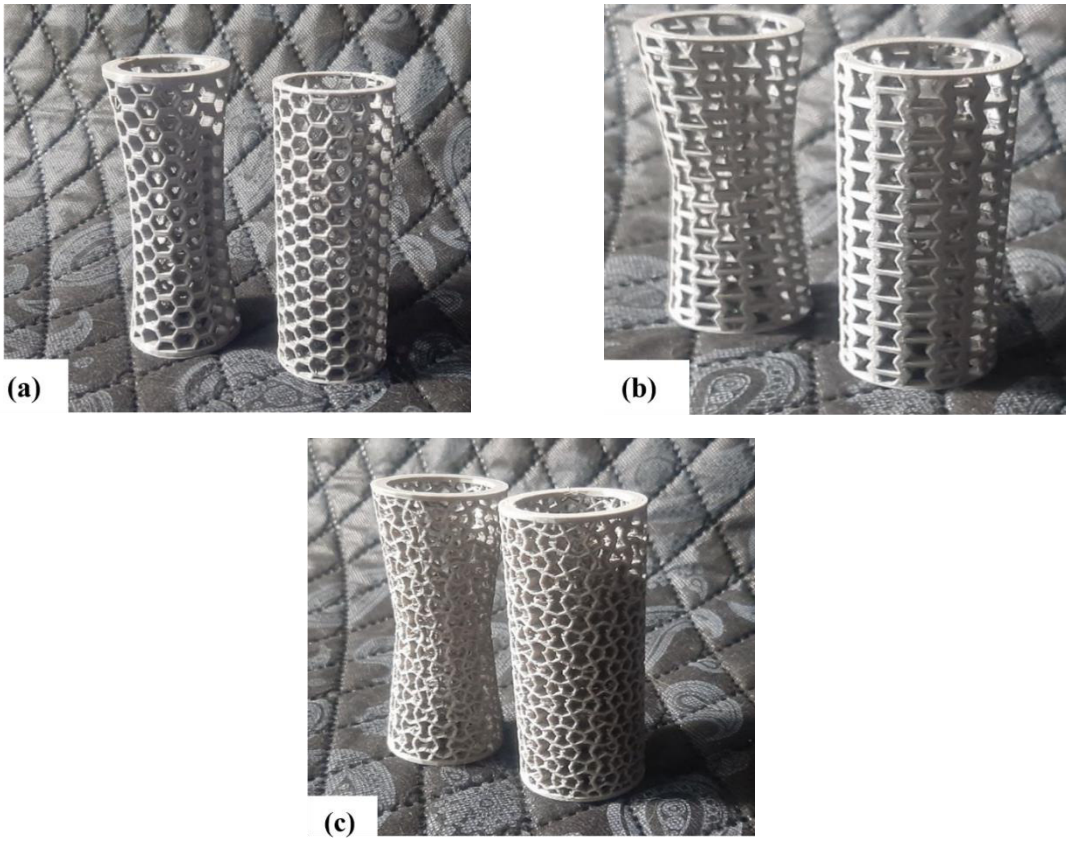

Fig. 2. Reinforcement pattern types used in this study: (a) honeycomb (HC), (b) re-entrant auxetic (RE), and (c) chiral auxetic (CA), each shown in both cylindrical and hyperboloid geometries

Each reinforced 3D print is divided into two samples: the hyperboloid with an 85° angle and the cylinder. The 85° specimens were created to understand the hyperboloid behavior with maximum effect under compressive loading. The diameter of each mini

column is 5.5 cm, and its height is more than 11 cm. According to Fig. 2, the 3D-printed reinforcement had a 1.5 cm cover over the external cementitious materials.

Figure 3 shows the research method. Firstly, the cementitious materials were mixed by hand until the mixture was ready for embedding in the molds. Finally, three types of reinforcement were placed in the molds, and cementitious material was embedded within them.

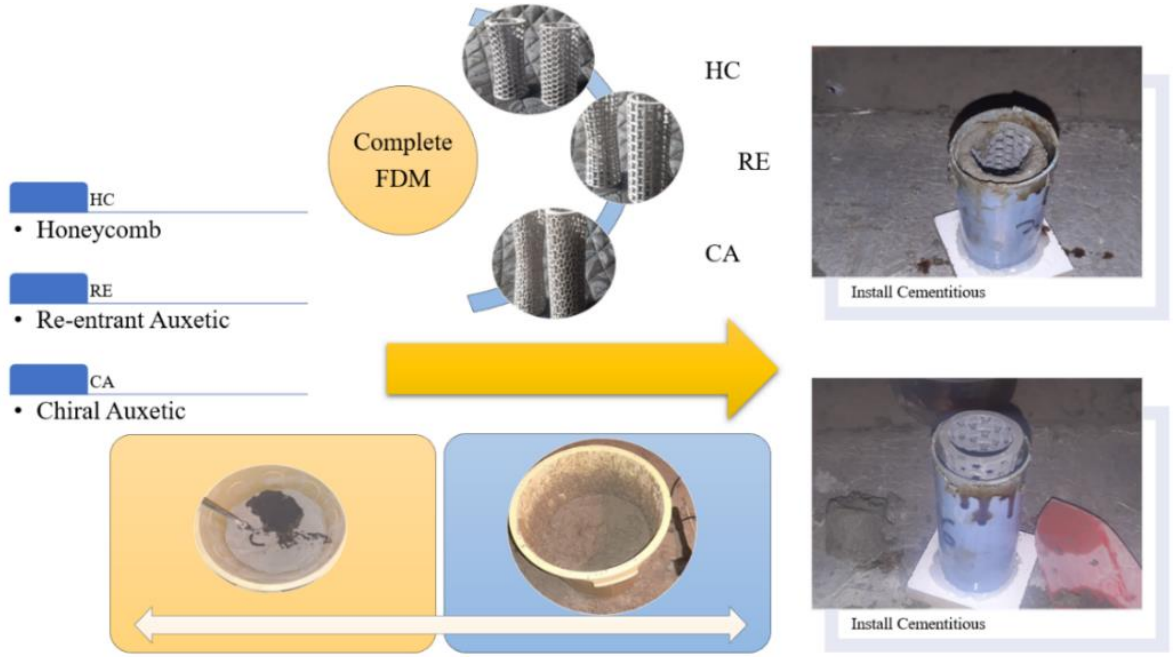

Fig. 3. Step-by-step process of embedding 3D-printed reinforcement structures into concrete molds for mini-column fabrication

Experimental methods. To determine the mechanical properties of concrete and mini-columns, as well as to conduct nondestructive testing, the following specimens were tested (Fig. 4): concrete 5 × 5 × 5 cm^3 cubes according to ASTM C109 [24]; reinforced cement columns under compressive loading according to ASTM C39/C39M-21 [25].

The following tests were carried out: displacements at three points of the columns, recorded by sensors installed at these three points to detect buckling; compressive strength of each specimen according to ASTM C39/C39M-21 [25].

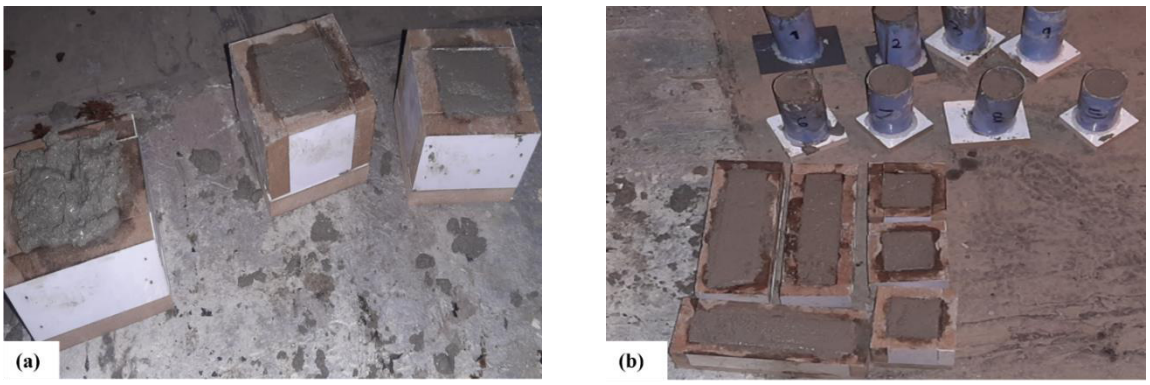

Fig. 4. (a) Cubical (5 × 5 × 5 cm^3) and rectangular concrete specimens prepared as reference samples; (b) specimens placed under standard curing conditions

Results and Discussion

In this section, three cases were investigated: the compressive strength of the control sample, the reinforced concrete column using the FDM method, and the reinforced concrete column using the DLP method.

Compressive strength

The structure formation of composite concrete columns with 3D-printed inclusions (honeycombs, chiral auxetics, and re-entrant lattices) occurs through the formation of a hierarchical internal architecture, where polymer metastructures manufactured using FDM or DLP methods act as permanent formwork or a deformation framework that determines the spatial organization of the stress-strain state in the hardening concrete. The cell geometry determines local zones of stress concentration and redistribution, and interfacial interactions at the polymer-cement stone boundary affect the integrity and crack resistance of the system. However, full structural formation is limited by the incompatibility between the physical and mechanical properties of the components and the lack of chemical adhesion, which requires further optimization of the compositions and co-printing technologies.

The compressive strength of the control specimen is 113 MPa; in fact, the control specimen was reinforced without any pattern. This high strength, which is twice that of traditional concrete, opens the broadest prospects for the development of these materials.

FDM Method

This section presents the result of concrete reinforcement using FDM method.

CA samples. Considering Fig. 5, if the CA sample is used as the reinforced sample, the compressive strength decreased at 85 and 90 degrees. Figure 5(a) shows that the compressive strength increases to a point where it reaches its maximum value (84.91 MPa). After reaching the maximum compressive strength, the material fails, and the strength decreases. Changes in the slope of the graph can indicate structural changes or internal cracks in the material. Figure 5(b) shows a compressive strength of 105.58 MPa. According to Fig. 5(b), the influence of 3D-printed reinforcement is observed.

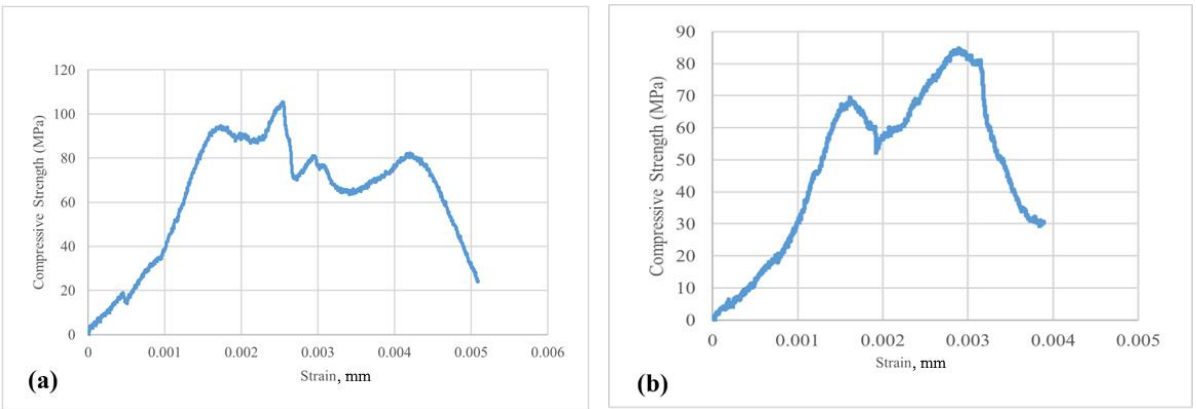

Fig. 5. CA sample. (a) CA85, (b) CA90

HC sample. According to Fig. 6, the compressive strength of the samples increased by more than 50 % for both types of reinforced concrete mini columns. In fact, according to Fig. 6, the compressive stress-strain curve of HC85 shows less strain hardening than that of HC90.

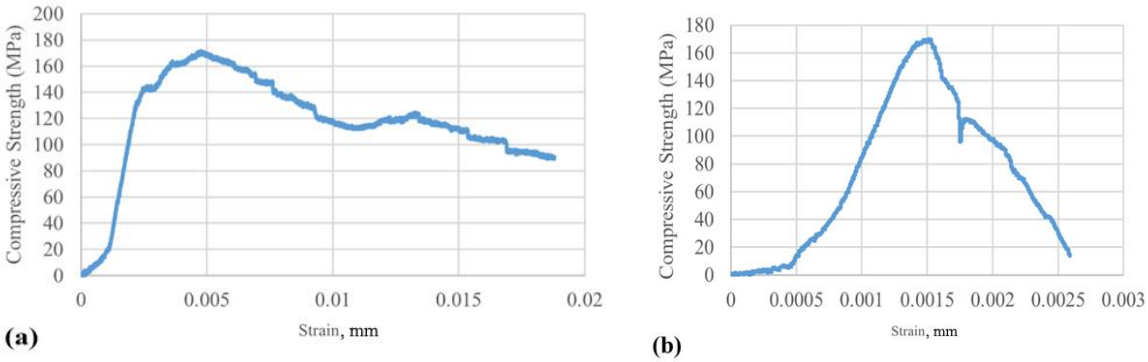

Fig. 6. HC sample: (a) HC85, (b) HC90

Carefully studying Fig. 6, we note some interesting features. Columns with honeycomb reinforcement are much more effective than columns with chiral auxetic reinforcement for two reasons. First, they show up with compressive strengths up to 2 times higher. Second, a much smaller degree of dependence of compressive strength on the angle of inclination of reinforcement in columns is noted (171 MPa for 85 degrees and 169 MPa for 90 degrees).

RE Sample. According to Fig. 7, if re-entrant (RE) reinforcement is added to concrete, the compressive strength increases by more than 267 % for RE with 85 degrees and 77 % for RE with 90 degrees.

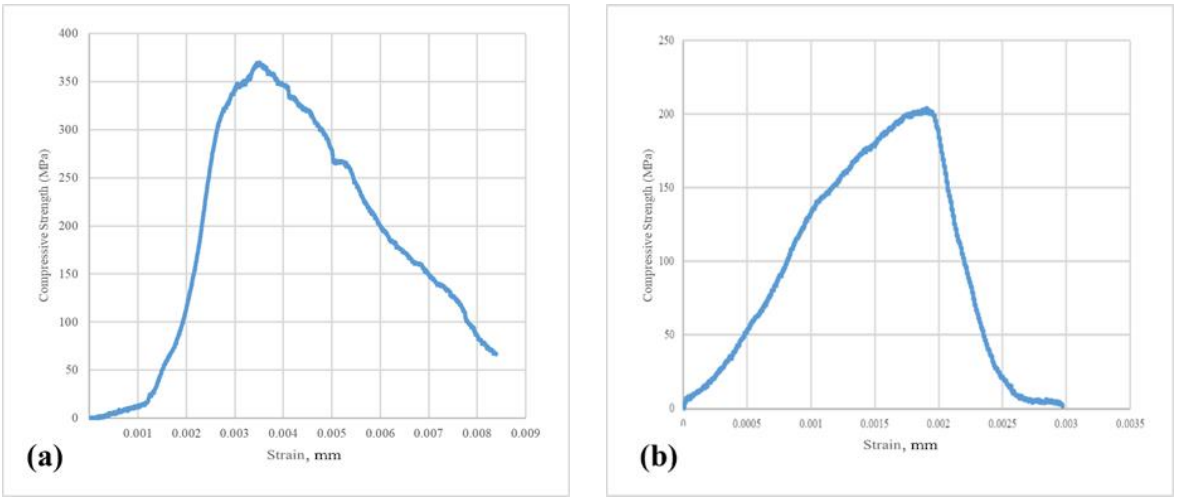

Fig. 7. RE sample: (a) RE85, (b) RE90

This reinforcement can be considered the most effective type compared to chiral auxetic and honeycomb reinforcements. Achieving a high compressive strength (369 MPa) enables these columns to be used in the most heavily loaded and critical structures. On the other hand, there is a significant spread in compressive strength values

of 170 MPa (from 369 to 199 MPa) if the column reinforcement angle is changed by 5 degrees (from 85 to 90 degrees).

The compressive strength of all samples except HC-90, HC-85, and CA-90 is lower than that of the other samples. Considering Fig. 6, if concrete is reinforced with RE-90, the concrete compressive strength improved by more than 42 % compared to the control sample. Moreover, if concrete is reinforced with 25 %, its compressive strength will improve.

However, in the previous structures, the reinforced concrete beam was found to be the rational type, as concrete beams are honeycombed structures. This study found that the sensible way to reinforce concrete columns is with RE90 and CA85 concrete. RE type of concrete known as "re-entrant" and CA type of concrete known as "chiral". The use of honeycomb-reinforced CA concrete can significantly alter column properties. The CA form can change the concrete from compressive to tensile and can also reduce its tensile strength. Hence, all types of concrete, if reinforced with concrete by CA at an angle of 85 degrees [26]. Therefore, adding CA to concrete can increase the compressive strength at 85 degrees, but at 90 degrees, the compressive strength decreased to 87 MPa.

Understanding the re-entry structure is very important because the structure must be re-entered (RA). In this type of structure, it is essential to observe the energy dissipation [27]. According to the combination of Figs. 7 and 9, if RE was washed for less than the special amount (the less-than-control sample), the STN improved by more than 42 %. However, if RE was reinforced with 90°, the STN improved by more than 42 %. In fact, the cement must increase the concrete's plasticity (Fig. 8). This ratio is also the same for Chorial too [28]. Different types of materials must be used. First, there are organic materials such as cellulose Nanocrystals, Inorganic materials such as gusted twisted, and organic-inorganic materials such as protein MOF [29].

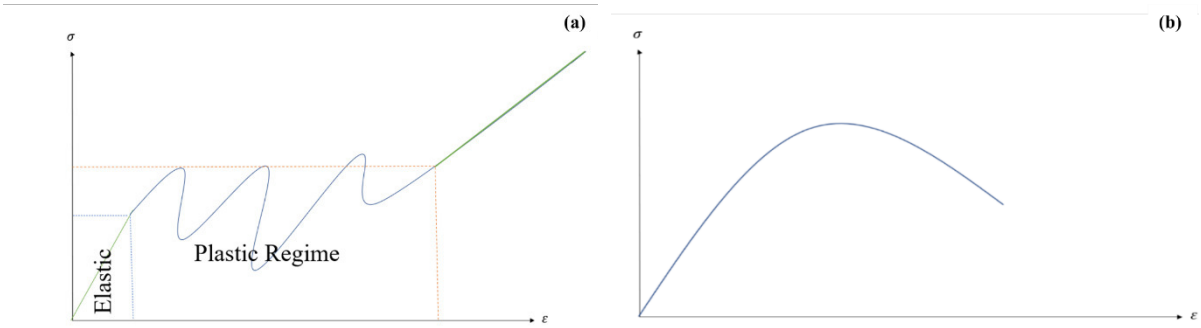

Fig. 8. Stress-strain curve of (a) RE under compression, (b) concrete

Considering the current study, horizontal resistance (F_y) can be considered in three conditions:

$$F_y = \left\{ \begin{matrix} Concrete.stiffnes.has.to.be.more.than.Plastic.system. \\ Concrete.stiffnes.is.equal.with.Plastic.system. \\ Concrete.stiffnes.is.less.than.Plastic.system. \\ \vdots \end{matrix} \right\}. \quad (1)$$

Considering the investigation, the algorithmic system of this article was based on Eq. (1). To find the best form of compressive stiffness of concrete, it has to be greater than the plastic system (RE90, RE85, and CA85). Moreover, if the system had been

balanced, the RE85 configuration would have been appropriate. As shown in Fig. 7, conventional concrete must improve the failure resistance of the specimen without inducing additional brittleness [30,31]. Considering Fig. 6, the conventional concrete has been cracked in shear types. Moreover, RE, HC, and RC had resistance against concrete, whereas shear compressive. Other elements illustrate torsional strength; it means that shear strength changes to twisting.

CA cracked hardly and assisted concrete very soon; overall, concrete, CA, and cementitious materials show complete failure. Overall, 90 degrees is better than 85 degrees. The most interesting situation is twisted concrete from compressive strength and shear conflicts. Meanwhile, twisted reinforced concrete. Overall, the maximum indexes were pattern, degree of pattern, negative possessions, etc.

DLP samples

In this section, the reinforced concrete fabricated using the DLP method is investigated.

CA samples. According to Fig. 9, the compressive strength has improved by more than 326 % for DLP method and CA shape with a 90-degree hyperboloid. For specimen CA90, the reinforcement is directly engaged, whereas in CA85 the concrete is first subjected to compressive loading.

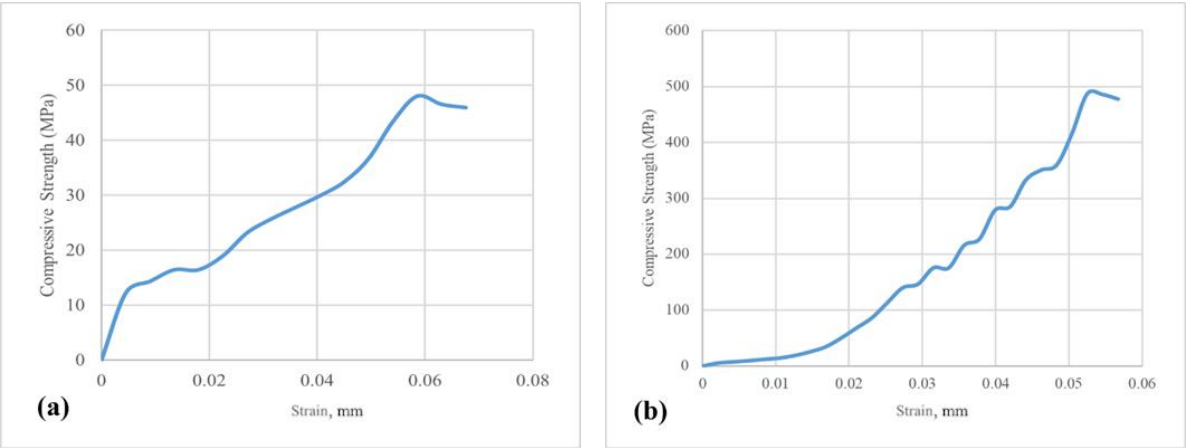

Fig. 9. CA sample: (a) CA85, (b) CA90

In the additive manufacturing of SA reinforcement using DLP methods, the most interesting feature is the strength under compression of the columns. Firstly, the maximum compressive strength of 488 MPa is achieved at a reinforcement angle of 90 degrees. On the other hand, if the angle is reduced by 5 degrees, the compressive strength decreases by an order of magnitude (48 MPa). This decrease necessitates careful design and strict control of reinforcement quality.

HC Sample. Considering Fig. 10, the compressive strength decreased for HC90 and improved for HC85. However, DLP-printed samples for honeycomb reinforcement are twice as effective (in terms of compressive strength) as FDM-printed samples. This effectiveness suggests the importance of the research results presented in this article, which confirm the difficulty of predicting the achievement of target compressive-strength values using various additive technologies to produce reinforcement cages of different geometries.

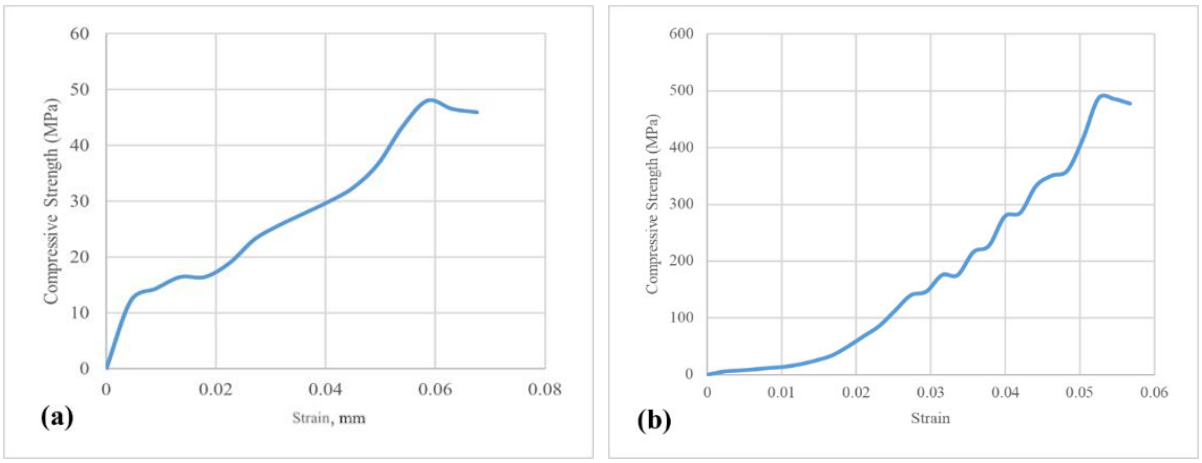

Fig. 10. HC sample: (a) HC85, (b) HC90

RE Samples. According to Fig. 11, the compressive strength increases by more than 30 % compared to conventional concrete samples. Despite the lower results compared to FDM, it is worth noting the lower dependence on the reinforcement angle (142 and 139 MPa at 85 and 90 degrees, respectively).

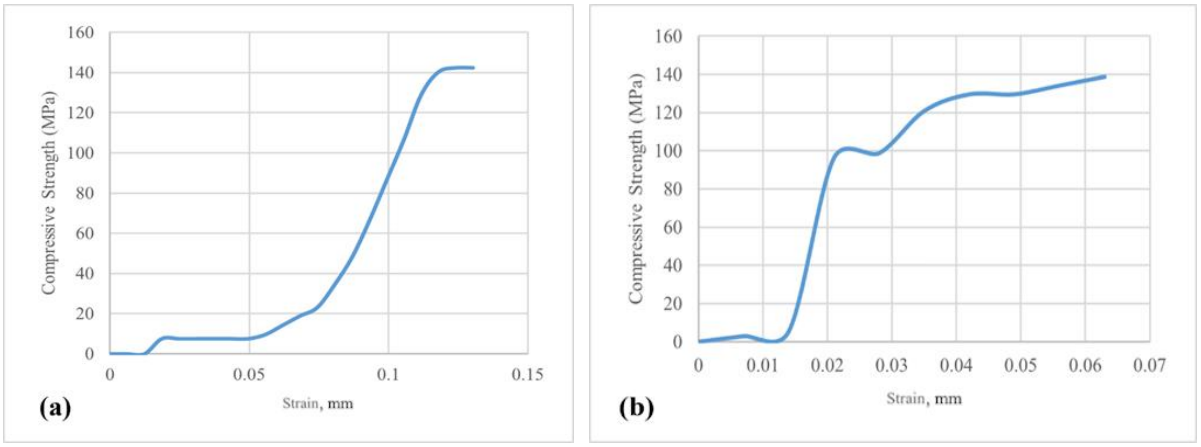

Fig. 11. RE sample: (a) RE85, (b) RE90

Failure types

This part drives to two sections; the first part is about the failure of all samples. Moreover, the second part is nondestructive testing for buckling STN.

Failure types of concrete. Two types of concrete failure have been shown in Fig. 12: the cube surface has been separated, and the next layer of concrete has failed. In STN columns, if different types of concrete have failed under compression, first the concrete cover separated, and then the maximum tension was on the inside of the reinforced concrete. Moreover, reinforced concrete prevents shear cracks (Fig. 13(c,d,e). Figure 13(c) illustrates most of the concrete locked into the STN, Honeycomb structure. It should be understood that if reinforcement with different types of concrete, such as Honeycomb and other structures, is added, it shows better deformations and higher energy (85 degrees) than other (90 degrees).

Golias et al. [32] studied the carbon FRP column cladding of reinforced concrete beams under cyclic loading and found that, if the column was reinforced with CFRP cladding, shear cracks increased. Chandramouli et al. [33] used fiber-reinforced concrete and a hybrid double-skin tubular column within concrete. They analyzed the fiber angle and fiber thickness of the concrete tube. The results show that as fiber thickness and steel increased, compressive strength improved. Overall, stripping reinforced columns away from concrete columns can increase the compressive strength; at the same time, concrete falls till concrete. The concrete in the tension and pressure zones cracks, not only in columns, but also in beams, when loads are applied [34].

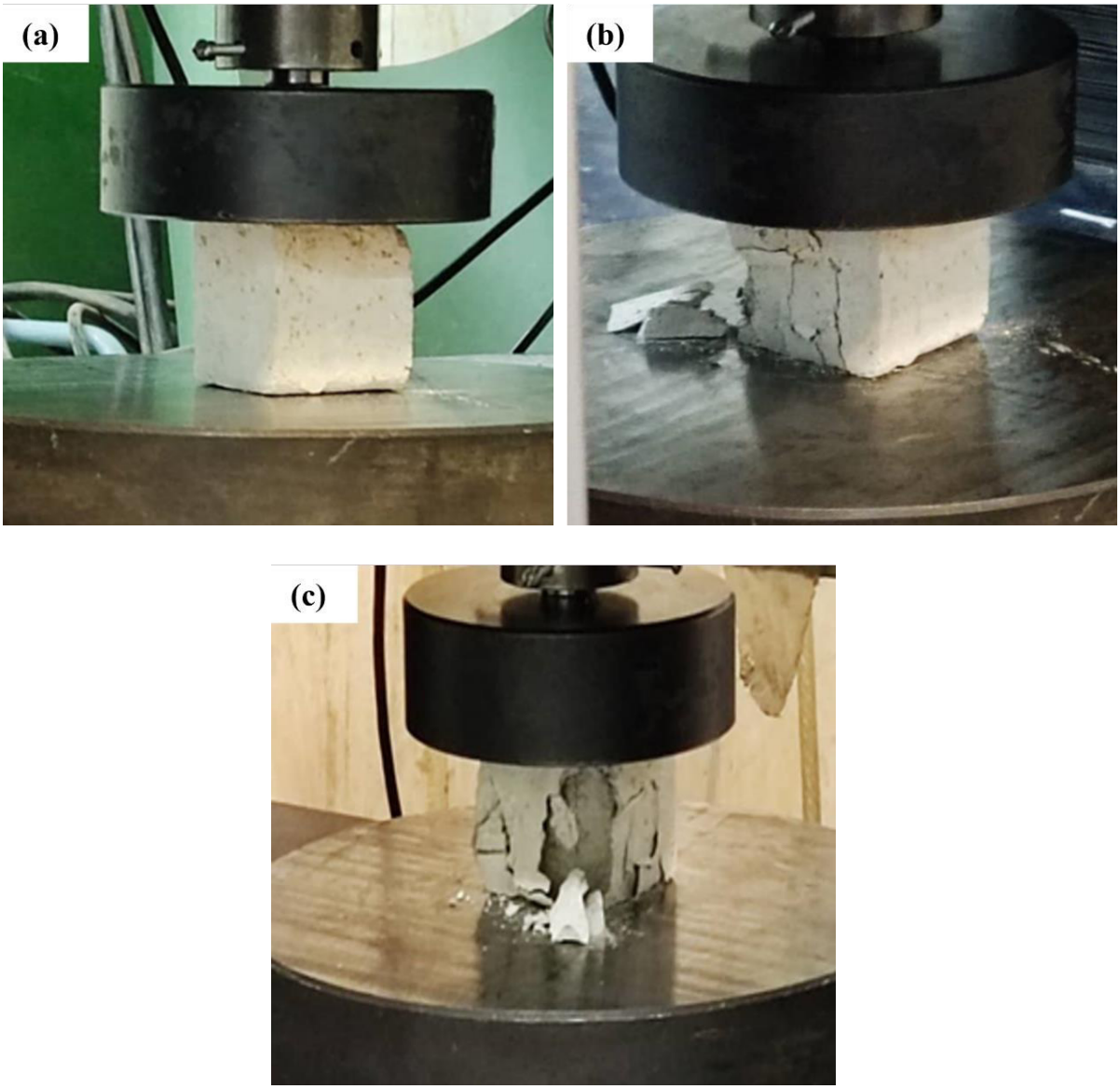

Fig. 12. Compression the cube samples: (a) cube samples under loading; (b) under loading and cracking; (c) failure of cube samples

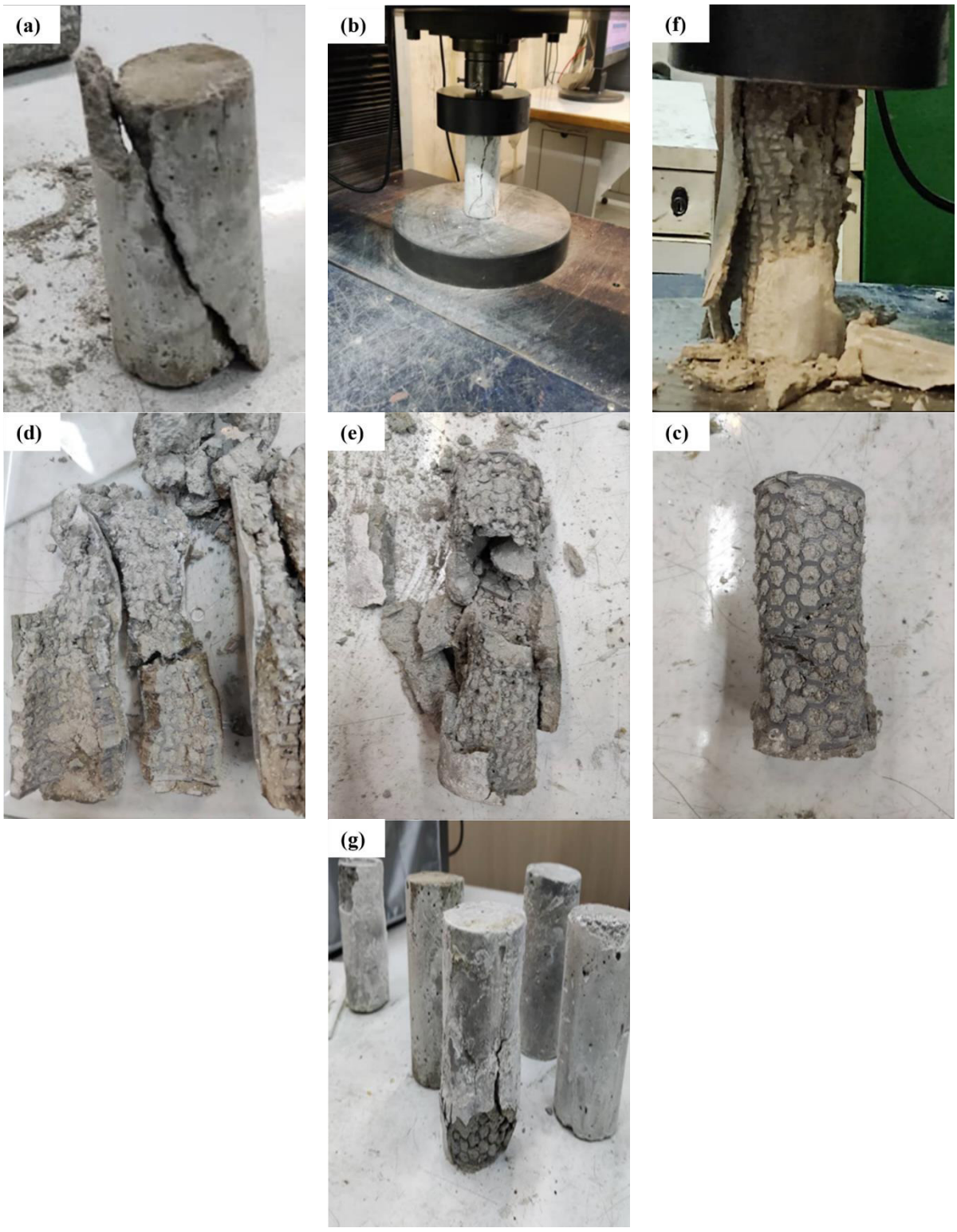

Fig. 13. Failure of STN concrete; (a) control sample;(b) control sample; (c) honeycomb; (d) different of styles of reinforced concrete; (e) RE-85; (f) CA-90; (g) failures of different concrete samples

Summary of results

This study investigated the effect of 3D-printed reinforcement patterns, including honeycomb, recursive auxetic, and chiral auxetic structures, on the mechanical performance of small concrete columns. The findings indicate significant differences in

compressive strength, failure modes, and strain behavior based on the geometry and location of the reinforcements. The results are discussed in the context of previous research and practical applications.

The RE pattern, especially the RE85 and RE90 specimens, showed the greatest improvement in compressive strength (267 and 77 %, respectively). These results are consistent with previous studies that emphasized the high energy absorption and ductility of eutectic structures under compression [27]. The uniform stress distribution in the recursive geometry is likely responsible for this improvement. In contrast, the CA pattern produced different results: the CA85 specimen increased strength by 165 %, while the CA90 specimen decreased it. These results suggest that the angle of reinforcement placement (85° vs. 90°) plays a key role in load carrying, probably due to differences in stress redistribution and buckling resistance [26]. The honeycomb (HC) pattern, which performed well in previous studies on beams [12,30], showed a moderate improvement (50 %) in columns. This difference highlights the importance of the specific design of stiffeners for different structural elements (beams vs. columns) and loading conditions.

The 85° hyperbolic design performed better than the 90° cylindrical specimens in all models (RE85 vs. RE90). This result supports the hypothesis that angled reinforcements are better able to restrain shear stresses and delay crack propagation, as observed in hyperbolic shell structures [10]. The failure modes also confirmed that the 85° reinforced columns had a more ductile behavior, whereas the 90° columns failed abruptly due to localized shear cracks.

The DLP-printed CA90 specimen showed a significant increase of 326 % in compressive strength, which was much higher than that of the FDM-printed specimens. This result indicates the influence of printing accuracy and material density on structural performance. The high accuracy of DLP probably maintains the integrity of the eutectic geometry better under load. However, the HC and RE patterns in the DLP method showed less improvement, indicating that material brittleness or adhesion between concrete and DLP polymers may need to be optimized [30].

Destructive tests showed that the reinforced columns had greater resistance to shear cracking than the control specimens. For example, the HC pattern confined the concrete within its cells, preventing complete collapse. These findings are consistent with studies on FRP-reinforced columns [32,34], but 3D-printed reinforcements offer greater design flexibility and environmental benefits. For example, eutectic patterns can reduce material consumption while maintaining strength, which is consistent with sustainable construction goals [16,35-46].

This study focused on small columns; generalizing the results to real columns requires further investigation of printability and cost-effectiveness. Long-term durability under cyclic loading and environmental conditions (such as humidity and temperature) needs to be tested. Future research could explore hybrid reinforcements or multi-material printing to improve surface adhesion.

The production and implementation of these mini-columns in large-scale construction open up broad prospects for the development of small businesses in the regions, consistent with earlier studies.

Although the use of 3D-printed auxetic and re-entrant structures for strengthening concrete columns demonstrates promising mechanical properties (increased impact

strength, negative Poisson's ratio, and controlled deformation), their practical implementation in construction practice is currently limited by technological, economic, and regulatory barriers. Future research should focus on scalability, material compatibility, and standardization to translate these innovations from the laboratory to the construction site.

Conclusions

This study provides valuable insights into the use of 3D-printed reinforced concrete (3PRC) to enhance the mechanical properties of mini-columns. The investigation of three distinct reinforcement patterns, namely honeycomb (HC), re-entrant auxetic (RE), and chiral auxetic (CA), shows that the geometry and placement of reinforcement significantly influence the performance of cementitious materials under compression and flexural loads. The results demonstrated that RE90 and CA85 reinforcement patterns increased the compressive strength of the concrete by more than 40 % compared to the control sample, with RE90 showing the greatest improvement. On the other hand, HC-90 and CA90 patterns resulted in lower compressive strength, highlighting the importance of selecting optimal patterns for reinforced concrete structures. Nondestructive testing and failure analysis revealed that reinforced columns exhibited greater resistance to shear cracking and improved energy absorption. This study fills a gap in existing research by focusing on optimizing 3D printing techniques for concrete reinforcement, specifically for mini-columns. The study offers practical implications for the design of more efficient, durable, and sustainable concrete structures in future civil engineering applications.

CRediT authorship contribution statement

Mohammad Hematibahar: writing – review & editing, writing – original draft; **Roman S. Fediuk**: conceptualization, writing – original draft; **Nikolai I. Vatin**: investigation, writing – original draft; **Amirali Milani**: supervision, writing – original draft; **Ahmadreza Tahmasebi:** data curation, writing – original draft; **Omid Kordi**: writing – review & editing, writing – original draft; **Makhmud Kharun**: conceptualization, writing – original draft; **German R. Fediuk**: investigation, writing – original draft; **Anton O. Shangutov**: supervision, writing – original draft; **Yelena K. Gitman**: data curation, writing – original draft.

Conflict of interest

The authors declare that they have no conflict of interest.

References

1. Vatin NI, Hematibahar M, Gebre T. Impact of Basalt Fiber Reinforced Concrete in Protected Buildings: A Review. *Frontiers in Built Environment*. 2024;10: 1407327.
2. Momeni K, Vatin N, Hematibahar M, Gebre T. Repair Overlays of Modified Polymer Mortar Containing Glass Powder and Composite Fibers-Reinforced Slag: Mechanical Properties, Energy Absorption, and Adhesion to Substrate Concrete. *Frontiers in Built Environment*. 2024;10: 1479849.

3. Hematibahar M, Kharun M, Beskopylny A, Stel'makh S, Shcherban E, Razveeva I. Analysis of Models to Predict Mechanical Properties of High-Performance and Ultra-High-Performance Concrete Using Machine Learning. *Journal of Composites Science*. 2024;8: 287.
4. Chiadighikaobi PC, Hematibahar M, Kharun MA, Stashevskaya N, Camara K. Predicting Mechanical Properties of Self-Healing Concrete with Trichoderma Reesei Fungus Using Machine Learning. *Cogent Engineering*. 2024;11: 2307193.
5. Hematibahar M, Hasanzadeh A, Kharun M, Beskopylny AN, Stel'makh SA, Shcherban' EM. The Influence of Three-Dimensionally Printed Polymer Materials as Trusses and Shell Structures on the Mechanical Properties and Load-Bearing Capacity of Reinforced Concrete. *Materials*. 2024;17(14): 3413.
6. Wan Z, Xu Y, Zhang Y, He S, Šavija B. Mechanical Properties and Healing Efficiency of 3D-Printed ABS Vascular Based Self-Healing Cementitious Composite: Experiments and Modelling. *Engineering Fracture Mechanics*. 2022;267: 108471.
7. Sun R, Han L, Zhang H, Ge Z, Guan Y, Ling Y, Schlangen E, Šavija B. Fatigue Life and Cracking Characterization of Engineered Cementitious Composites (ECC) under Flexural Cyclic Load. *Construction and Building Materials*. 2022;335: 127465.
8. Xu Y, Savija B. Auxetic Cementitious Composites (ACCs) with Excellent Compressive Ductility: Experiments and Modeling. *Materials & Design*. 2024;237: 112572.
9. Salazar B, Aghdasi P, Williams ID, Ostertag CP, Taylor HK. Polymer Lattice-Reinforcement for Enhancing Ductility of Concrete. *Materials & Design*. 2020;196: 109184.
10. Hematibahar M, Hasanzadeh A, Vatin N, Kharun M, Shooshpasha I. Influence of 3D-Printed Reinforcement on the Mechanical and Fracture Characteristics of Ultra High-Performance Concrete. *Results Eng*. 2023;19: 101365.
11. Chiadighikaobi PC, Hasanzadeh A, Hematibahar M, Kharun M, Mousavi MS, Stashevskaya NA, Adedapo Adegoke M. Evaluation of the Mechanical Behavior of High-Performance Concrete (HPC) Reinforced with 3D-Printed Trusses. *Results Eng*. 2024;22: 102058.
12. Hematibahar M, Milani A, Fediuk R, Amran M, Bakhtiary A, Kharun M, Mousavi MS. Optimization of 3D-Printed Reinforced Concrete Beams with Four Types of Reinforced Patterns and Different Distances. *Engineering Failure Analysis Journal*. 2025;168:109096.
13. Xu Y, Zhang H, Gan Y, Savija B. Cementitious Composites Reinforced with 3D Printed Functionally Gradedpolymeric Lattice Structures: Experiments and Modelling. *Additive Manufacturing*. 2021;39: 101887.
14. Meng Z, Xu Y, Xie J, Zhou W, Bol RJM, Liu QF, Šavija B. Unraveling the Reinforcing Mechanisms for Cementitious Composites with 3D Printed Multidirectional Auxetic Lattices Using X-Ray Computed Tomography. *Materials & Design*. 2024;246: 11331.
15. Oza RB, Kangda MZ, Agrawal MR, Vakharia PR, Solanki DM. Marble Dust as a Binding Material in Concrete: A Review. *Material Today: Proceedings*. 2022;60: 421–430.
16. Basha SA, Shaikh FUA. Suitability of Marble Powders in Production of High Strength Concrete. *Low-Carbon Materials and Green Construction* 2023;1: 27.
17. Shooshpasha I, Hasanzadeh A, Kharun M. Effect of Silica Fume on the Ultrasonic Pulse Velocity of Cemented Sand. International Conference on Engineering Systems, *Journal of Physics: Conference Series*. 2020;1687: 012017.
18. Shooshpasha I, Hasanzadeh A, Kharun M. The Influence of Micro Silica on the Compaction Properties of Cemented Sand. *IOP Conference Series: Materials Science and Engineering*. 2019;675: 012002.
19. Pereira P, Evangelista L, de Brito J. The Effect of Superplasticizers on the Mechanical Performance of Concrete Made with Fine Recycled Concrete Aggregates. *Cement and Concrete Composites*. 2012;34: 1044–1052.
20. Puertas F, Santos H, Palacios M. Polycarboxylate Superplasticiser Admixtures: Effect on Hydration, Microstructure and Rheological Behaviour in Cement Pastes. *Advances in Cement Research*. 2005;17: 77–89.
21. Husna A, Ashrafi S, Tomal AA, Tuli AT, Rashid AB. Recent Advancements in Stereolithography (SLA) and Their Optimization of Process Parameters for Sustainable Manufacturing. *Hybrid Advances*. 2024;7: 100307.
22. Melchels FPW, Feijen J, Grijpma DW. A Review on Stereolithography and Its Applications in Biomedical Engineering. *Biomaterials*. 2010;31(24): 6121–6130.
23. Patel R, Desai C, Kushwah S, Mangrola MH. A Review Article on FDM Process Parameters in 3D Printing for Composite Materials. *Materials Today Proceedings*. 2022;60: 2162–2166.
24. ASTM International. *ASTM C 109. Standard Test Method for Compressive Strength of Hydraulic Cement Mortars (Using 2-in. or [50-Mm] Cube Specimens)*. ASTM; 2017.
25. ASTM International. *ASTM International. ASTM C39/C39M-21, Standard Test Method for Compressive Strength of Cylindrical Concrete Specimens*. ASTM; 2021.

26. Jiao G, Yan G. Design and Elastic Mechanical Response of a Novel 3D-Printed Hexa-Chiral Helical Structure with Negative Poisson's Ratio. *Materials & Design*. 2021;212: 110219.
27. Rad MS, Hatami H, Ahmad Z, Karimdoost Yasuri A. Analytical Solution and Finite Element Approach to the Densere-Entrant Unit Cells of Auxetic Structures. *Acta Mechanica*. 2019;230: 2171–2185.
28. Kumar Choudhr N, Panda B, Shanker Dixit U. Energy Absorption Characteristics of Fused Deposition Modeling 3D Printed Auxetic Re-Entrant Structures: A Review. *Journal of Materials Engineering and Performance*. 2023;32: 8981–8999.
29. Levkina EV, Titova NY. The Analysis of the Financial Condition of Small Business and the Ways of its Development in the Primorsky Territory. *IOP Conference Series: Earth and Environmental Science*. 2019;272(3): 032185.
30. Shcherban' EM, Stel'makh SA, Mailyan LR, Beskopylny AN, Smolyanichenko AS, Chernil'nik AA, Elshaeva DM, Beskopylny NA. Structure and Properties of Variatropic Concrete Combined Modified with Nano- and Micro-silica. *Construction Materials and Products*. 2024;7(2): 3.
31. Hematibahar MH, Kharun M, Fediuk RS, Vatin NI, Porvadov MG, Sabitov LS. Predicting the flexural strength of 3D-printed geopolymer reinforced concrete using machine learning techniques. *Materials Physics and Mechanics*. 2025;53(4): 22–34.
32. Golias E, Schlüter FE, Spyridis P. Strengthening of Reinforced Concrete Beam-Column Joints by Means of Fastened C-FRP Ropes. *Structures*. 2024;66: 106811.
33. Chandramouli P, Jayaseelan R, Pandulu G. Axial Compression Behaviour of Hybrid Composite FRP–Concrete–Steel Double-Skin Tubular Columns with Various Fibre Orientations. *Case Studies in Construction Materials*. 2022;17: e01326.
34. Petropavlovskaya VB, Petropavlovskii KS, Novichenkova TB, Klyuev SV, Vasilev YE, Ignatyev AA. Fine-grained cement concrete with compressed structure, modified with basalt technogenic highly dispersed powder. *Construction Materials and Products*. 2025;8(4): 2.
35. Fediuk R, Smoliakov A, Muraviov A. Mechanical properties of fiber-reinforced concrete using composite binders. *Advances in Materials Science and Engineering*. 2017;2017(1): 2316347.
36. Moonphukhiao A, Samran B, Chaiwichian S. Preparation and characterization of geopolymer/activated carbon composite materials used as a bone substitute material. *Materials Physics and Mechanics*. 2025;53(1): 150–158.
37. Fediuk RS, Smoliakov AK, Timokhin RA, Batarshin VO, Yevdokimova YG. Using thermal power plants waste for building materials. *IOP Conference Series: Earth and Environmental Science*. 2018;87(9): 092010.
38. Klyuev SV, Ayubov NA, Fomina EV, Ageeva MS, Klyuev AV, Nedoseko IV. Influence of carbon black additives and finely ground waste from stone wool production on characteristics of cement systems. *Construction Materials and Products*. 2025;8(4): 8.
39. Fediuk R. Reducing permeability of fiber concrete using composite binders. *Special Topics and Reviews in Porous Media*. 2018;9(1): 79–89.
40. Ham S, Jong Han J, Kim J. Chiral Materials for Optics and Electronics: Ready to Rise? *Micromachines*. 2024;24: 528.
41. Fediuk RS, Lesovik VS, Liseitsev YL, Timokhin RA, Bituyev AV, Zaiakhanov MY, Mochalov AV. Composite binders for concretes with improved shock resistance. *Magazine of Civil Engineering*. 2019;85(1): 28–38.
42. Momeni K, Vatin N, Hematibahar M, Gebre T. Differences between 3D Printed Concrete and 3D Printing Reinforced Concrete Technologies: A Review. *Frontiers in Built Environment*. 2025;10: 145062.
43. Fediuk RS, Yevdokimova YG, Smoliakov AK, Stoyushko NY, Lesovik VS. Use of geonics scientific positions for designing of building composites for protective (fortification) structures. *IOP Conference Series: Materials Science and Engineering*. 2017;221(1): 012011.
44. Kharun M, Alaraza HA, Hematibahar M, Al Daini R, Manoshin AA. Experimental Study on the Effect of Chopped Basalt Fiber on the Mechanical Properties of High-Performance Concrete. *AIP Conference Proceedings*. 2022;2559(1): 050017.
45. Fediuk RS, Lesovik VS, Mochalov AV, Otsokov KA, Lashina IV, Timokhin RA. Composite binders for concrete of protective structures. *Magazine of Civil Engineering*. 2018;82(6): 208-218.
46. Ayoub T, Alaa Hasan H, Sheikh MN, Hadi NSM. Effect of CFRP Strip Tie Configurations on the Behavior of GFRP Reinforced Concrete Columns under Different Loading Conditions. *Structures*. 2024;69: 1072426.

MATERIALS PHYSICS AND MECHANICS

53 (5) 2025

УЧРЕДИТЕЛИ

Санкт-Петербургский политехнический университет Петра Великого
Адрес: 195251, Санкт-Петербург, Политехническая ул., д. 29

Институт проблем Машиноведения Российской академии наук
Адрес: 199178, Санкт-Петербург, Большой пр-кт В.О., д. 61

ИЗДАТЕЛЬ

Санкт-Петербургский политехнический университет Петра Великого
Адрес: 195251, Санкт-Петербург, Политехническая ул., д. 29

Журнал зарегистрирован в Федеральной службе по надзору в сфере связи, информационных технологий и массовых коммуникаций (РОСКОМНАДЗОР), свидетельство ПИ №ФС77-69287 от 6 апреля 2017 года.

АДРЕС И ТЕЛЕФОН РЕДАКЦИИ

199178, Санкт-Петербург, Большой пр-кт В.О., д. 61

Тел. редакции: +7(812)552 77 78, доб. 224

E-mail редакции: mpmjournal@spbstu.ru

Компьютерная верстка Л.И. Гузилова

Подписано в печать 15.12.2025 г. Выход в издания в свет: 30.01.2026 г.
Формат 60x84/8. Печать цифровая
Усл. печ. л. 10,0. Тираж 100. Заказ___.
Цена: Бесплатно

Отпечатано в **Издательско-полиграфическом центре Политехнического университета Петра Великого**
Адрес: 195251, Санкт-Петербург, Политехническая ул., 29
Тел.: +7(812)552 77 17

MPM SCIENTIFIC JOURNAL

MPM, Vol. 53, No. 5, 2025